SUBSTRATE SUPPORTED METAL STRIP ANTENNAS FOR MONOLITHICALLY FABRICATED MILLIMETRE WAVELENGTH ARRAYS

by

Andrew J. Parfitt, BE(Hons)

A thesis submitted in fulfilment of the requirement for the degree of

Doctor of Philosophy

in

The University of Adelaide

Department of Electrical and Electronic Engineering

Faculty of Engineering

November, 1992

To my parents

Contents

Abstract

Practical realization of radar and communication systems that exploit the millimetre-wave part of the electromagnetic spectrum by using high gain antenna systems that may be electronically beam steered, challenges both current design knowledge and technological capability. Progress and achievement on both these frontiers is ultimately judged in relation to such considerations as cost-effectiveness and reliability, as well as specified millimetre-wave performance requirements. Increasingly stringent system requirements have focussed attention on the design of phased array antennas, and cost-effective implementation of such arrays for millimetre wavelength operation requires extensive use of integration, especially if each antenna element is to have amplifiers and other components such as switches as well as phase shifters associated with it. The research presented in this thesis addresses the problem of designing phased arrays at millimetre-wavelengths with antenna elements that are fabricated on the substrates of monolithic microwave integrated circuits (MMICs).

Fundamental to the need for design knowledge is the development of accurate and versatile analytical tools. After reviewing appropriate architectures for MMIC based phased arrays, and the implications of the architecture on the choice of antenna elements, a class of antennas is identified which consist of metal conductors supported on finite size dielectric substrates that may be electrically thick. A numerical solution to the electric field integral equations formulated for these structures has been developed for calculating the impedance and radiation characteristics of elements and arrays. The method can be applied to the entire antenna structure, which is specified in terms of the geometric and constitutive parameters associated with both the radiating and feeding parts. In this way uncertainties due to gross idealizations for analytical reasons are minimized, and the accuracy of designs that take account of all practical aspects of the structure can be tested with measurements.

Application of the method, subsequent to testing it with experimental measurements, has demonstrated its accuracy for a variety of antenna element and array problems. Useful information has been obtained which reveals the influence of the

fields within the dielectric parts of the structure on the antenna characteristics in sufficient detail to enable engineering design that exploits these effects to optimize performance. Accurate design is essential to the realization of MMICs because there is no cost-effective way of adjusting the individual components in such an assembly after fabrication.

From the results obtained, it is concluded that the substrate supported metal strip antennas described in this thesis satisfy the requirements for MMIC based phased arrays, and exhibit useful characteristics.

Statement of Originality

This work contains no material which has been accepted for the award of any other degree or diploma in any university or other tertiary institution and, to the best of the author's knowledge and belief, contains no material previously published or written by another person, except where due reference has been made in the text.

The author gives consent to this copy of his thesis, when deposited in the University Library, being available for loan and photocopying.

Andrew J. Parfitt

Acknowledgements

The author would like to express his sincere gratitude to his supervisors, Dr. Donald W. Griffin and Dr. Peter H. Cole, for their guidance and support throughout the course of this research, and for the time they devoted to many aspects of the work.

The work was supported financially by research grants from The Australian Research Council and The Australian Telecommunications and Electronics Research Board, and by way of a cadetship provided by the Australian Defence Science and Technology Organisation.

Many of the calculations on which this work is based were carried out using the Fujitsu VP2200 vector-supercomputer of the Australian National University Supercomputer Facility, through their external users scheme. The assistance of the Defence Science and Technology Organisation Microelectronics Section, and the Joint Microelectronics Research Centre of the University of New South Wales, in the fabrication of antenna elements is also recognized.

Thanks are also expressed to Mr. Gordon Allison and Mr. Geoff Pook for their expert technical assistance during the course of the experimental work.

List of Author's Related Publications

The following is a list of the author's publications which are related to the research reported this thesis.

Chapter 2

A.J. Parfitt and D.W. Griffin, "Monolithic microwave and millimetre wave integrated circuit antennas", Proceedings of IREECON International Convention, Melbourne, Australia, pp 169–172, Sept. 1989.

A.J. Parfitt and D.W. Griffin, "Integrated antenna elements for MMIC phased array radar modules: constraints and options", Proceedings of RADARCON 90, Adelaide, Australia, pp 391–397, Apr. 1990.

A.J. Parfitt, D.W. Griffin and P.H. Cole, "A chip scale approach to monolithic microwave integrated circuit antenna design for millimetre wavelengths", IEEE Antennas and Propagation Symposium, Chicago, IL, pp 1914–1918, July 1992.

Chapters 3 and 4

A.J. Parfitt and D.W. Griffin, "A single wire fed dipole on slab antenna for monolithic integration with microwave and millimetre wave circuits", IEEE Antennas and Propagation Symposium, Dallas, TX, pp 795–798, May 1990.

A.J. Parfitt, D.W. Griffin and P.H. Cole, "Analysis of a metal strip dipole antenna suitable for monolithic integration at millimetre wavelengths", Third Australian Symposium on Antennas, Sydney, Australia, p 46, Feb. 1991.

A.J. Parfitt, D.W. Griffin and P.H. Cole, "Theoretical and measured input admittance of a metal strip antenna contiguous with the edge of an electrically thick, finite size dielectric substrate", IEEE Antennas and Propagation Symposium, London, Ontario, pp 995–998, June 1991.

A.J. Parfitt, D.W. Griffin and P.H. Cole, "On the modelling of metal strip antennas contiguous with the edge of electrically thick, finite size dielectric substrates", IEEE Transactions on Antennas and Propagation, Vol. 40, No. 2, pp 134–140, Feb. 1992.

Chapter 5

A.J. Parfitt, D.W. Griffin and P.H. Cole, "Mutual coupling between metal strip dipoles on electrically thick, finite size dielectric substrates", IEEE Antennas and Propagation Symposium, Chicago, IL, pp 1906–1909, July 1992.

A.J. Parfitt, D.W. Griffin and P.H. Cole, "Mutual coupling between metal strip antennas on finite size, electrically thick dielectric substrates", to appear in IEEE Transactions on Antennas and Propagation, Jan. 1993.

Chapter 6

A.J. Parfitt, D.W. Griffin and P.H. Cole, "Computer aided design of monolithic integrated circuit antennas and arrays", IREECON International Convention, Sydney, Australia, pp 680–683, Sept. 1991.

A.J. Parfitt, D.W. Griffin and P.H. Cole, "Active impedance computation for an infinite array of monolithic integrated circuit antennas", IEEE Antennas and Propagation Symposium, Chicago, IL, pp 1010–1013, July 1992.

A.J. Parfitt, D.W. Griffin and P.H. Cole, "Numerical modelling of infinite arrays of composite dielectric and conducting antenna elements", ACES/TEAM International Workshop, Melbourne, Australia, p 145, August 1992.

A.J. Parfitt, D.W. Griffin and P.H. Cole, "Design of a new monolithically integrated array for millimetre wavelengths", Asia Pacific Microwave Conference, Adelaide, Australia, pp 35–38, August 1992.

A.J. Parfitt, D.W. Griffin and P.H. Cole, "Analysis of infinite arrays of substrate supported metal strip antennas", accepted for publication in IEEE Transactions on Antennas and Propagation.

Appendix B

A.J. Parfitt, D.W. Griffin and P.H. Cole, "Measuring the radiation pattern of a resonant dipole antenna in the presence of an electrically thick finite size dielectric substrate – a method that satisfies theoretical assumptions", IEEE Antennas and Propagation Symposium, London, Ontario, pp 1206–1209, June 1991.

Appendix E

A.J. Parfitt and D.W. Griffin, "Analysis of the single wire fed dipole antenna", IEEE Antennas and Propagation Symposium, San Jose, CA, pp 1344–1347, June 1989.

List of Principal Symbols

Symbol	Description
a	ratio of radiating mode currents on folded dipole arms
a, b	rectangular waveguide cross-sectional dimensions
a_n, b_n	surface current expansion constants on metal strip
a_e	equivalent-radius of thin-wire approximation
c	speed of light in a vacuum
c_n, d_n, e_n	volume polarization current expansion constants in dielectric
C_j	diode junction capacitance
C_p	diode packaging capacitance
d_x, d_y	element spacings in arrays
D	on-axis antenna directivity
e	electronic charge
E_{cm}	elements of subvector $\mathbf{E_c}$
E_x, E_y, E_z	electric field components
$\vec{E}^{\mathrm{i}}$	incident electric field
$\vec{E}^{s}$	scattered electric field
$\vec{E}^{\mathrm{total}}$	total electric field in dielectric
$\mathbf{E}$	vector of electric field excitations
$\mathbf{E_c}$, $\mathbf{E_d}$	subvectors of $\mathbf{E}$
$\mathbf{E_{c,MN}}$, $\mathbf{E_{d,MN}}$	subvectors of $\mathbf{E}$ for infinite array
f_n	line current expansion constants on wire conductors
F_x	electric vector potential
$\mathcal{F}_c$, $\mathcal{F}_d$	operators for terms of the moment matrix
G	antenna gain
G_0	on-axis antenna gain at resonance

$G(\vec{r}, \vec{r}')$	Green's function
H	height of substrate
H_x, H_y, H_z	magnetic field components
i_d, i_f, i_t	folded dipole equivalent model currents
I_d, I_f, I_t	folded dipole mode currents
I'_d, I'_f, I'_t	folded dipole equivalent model currents
I_i	current at port i
$I_{i,\text{open}}$	current at port i with other ports open circuit
$I_{i,\text{short}}$	current at port i with other ports short circuit
$I_{i,\text{odd}}$	current at port i with odd symmetry excitation
$I_{i,\text{even}}$	current at port i with even symmetry excitation
I_j	diode junction current
$I_{j,dc}$	diode junction current (direct current)
$I_{j,\omega}$	diode junction current (fundamental frequency)
I_n	current on nth pulse expansion function
I_s	diode saturation current
$\mathbf{I_n}$	vector of feed port currents for n-element array
$\mathbf{I'_{n-1}}$	reduced vector of feed port currents
$\bar{\bar{\mathbf{I}}}_\mathbf{n}$	$n \times n$ identity matrix
$\mathcal{I}_1$, $\mathcal{I}_2$	Green's function integrals
$\vec{J}_c$	surface current density on metal strip
$\vec{J}_c^{\,t}$	$\vec{J}_c$ on top surface of conductor
$\vec{J}_c^{\,b}$	$\vec{J}_c$ on bottom surface of conductor
$\vec{J}_d$	volume polarization current density in dielectric
$\mathbf{J}$	vector of current densities
$\mathbf{J_c}$, $\mathbf{J_d}$	subvectors of $\mathbf{J}$
$\mathbf{J_{c,MN}}$, $\mathbf{J_{d,MN}}$	subvectors of $\mathbf{J}$ for infinite array

k	Boltzmann's constant (Appendix B)
k	propagation constant
k_0	free space propagation constant
k_x, k_y, k_z	dielectric waveguide propagation constants
$K(k)$	elliptic integral of the first kind with modulus k
l_c	y-directed segment length
l_n	length of nth pulse expansion function
L	length of metal strip antenna
L_p	diode packaging inductance
$\mathcal{L}_c$, $\mathcal{L}_d$	operators for scattered electric field
m, n	denote field and source points respectively
M, N	denote element position in arrays
n	diode ideality factor (Appendix B)
$\hat{n}$	unit vector normal to dielectric surface
n_c	number of metal strip segments in source region
n_d	number of dielectric segments in source region
n_f	number of segments on a feed line wire
n_g	number of grid intersection points
n_s	number of dielectric surface segments
n_x, n_y, n_z	number of segments in co-ordinate directions
N_c	total number of conductor segments
N_d	total number of dielectric segments
P_{av}	power density
P_d	power dissipated due to conductor losses
P_n	two-dimensional pulse basis function
$P_{n,MN}$	P_n for elements of array
P_n^1	one-dimensional pulse basis function

Q	junction charge
Q_n	three-dimensional pulse basis function
$Q_{n,MN}$	Q_n for elements of array
$\vec{r}$	position vector for location of field points
$\vec{r}'$	position vector for location of source points
R_a	antenna radiation resistance
R_{in}	total antenna input resistance
R_j	diode junction resistance
R_l	instrumentation load resistance
$R_{loss,c}$	feed point resistance due to conductor losses
$R_{loss,d}$	feed point resistance due to dielectric losses
R_s	diode series resistance (Appendix B)
R_s	conductor surface resistance
R_w	resistance of high-resistance leads
s	spacing between balanced transmission line conductors
s, s'	element spacings (Chapter 5)
$\mathbf{S_n}$	n-port scattering matrix
S_{ij}	ijth term of scattering matrix
S_c	surface of metal strip
S_c'	top and bottom surfaces of metal strip
S_d	surface of dielectric
S_{xy}, S_{yz}, S_{xz}	dielectric segment surfaces
ΔS_n	surface area of nth metal strip segment
t	substrate thickness
t_d	offset electrical delay
T	temperature
u, v	arbitrary rectangular co-ordinates

V_d	dielectric volume
V_i	ith port excitation voltage
V_j	diode junction voltage
$V_{j,dc}$	diode junction voltage (direct current)
$V_{j,\omega}$	diode junction voltage (fundamental frequency)
V_{rf}	high frequency voltage at antenna terminals
$\mathbf{V_n}$	vector of feed port excitation voltages for n-element array
$\mathbf{V'_{n-1}}$	reduced vector of feed port excitation voltages
w	metal strip width
$\hat{x}$, $\hat{y}$, $\hat{z}$	rectangular co-ordinate unit vectors
X_a	antenna reactance
Y	feed point active admittance in array
Y_d, Y_f, Y_t	folded dipole mode admittances
Z	feed point active impedance in array
$Z_{c,mn}$, $Z_{d,mn}$	moment matrix terms
Z_d	single dipole impedance for folded dipole decomposition
Z_{in}	folded dipole input impedance
Z_{ij}	self or mutual impedance terms relating to the ports i and j
Z_L, Z_0	transmission line characteristic impedance
Z_{L0}	free space transmission line characteristic impedance
Z_{oc}	measured monopolar impedance with other ports open circuit
Z_s	resonator end impedance
Z_{sc}	measured monopolar impedance with other ports short circuit
Z_t	transmission line mode impedance for folded dipole decomposition
$\mathbf{Z}$	moment matrix
$\mathbf{Z_{cc}}$, $\mathbf{Z_{dd}}$	submatrices of moment matrix
$\mathbf{Z_{cd}}$, $\mathbf{Z_{dc}}$	submatrices of moment matrix

$\mathbf{Z_n}$	port impedance matrix for n-element array
$\mathbf{Z'_{n-1}}$	reduced port impedance matrix
α, β, γ	unit normal terms
γ^2	folded dipole impedance step up ratio
Γ	diode voltage sensitivity (Appendix B)
Γ_n	active reflection coefficient for mode n
$\tan\delta$	dielectric loss tangent
ϵ_0	permittivity of free space
ϵ_r	relative permittivity of dielectric
$\dot{\epsilon}_r$	complex relative permittivity of dielectric
$\epsilon_{r\,\mathrm{eff}}$	transmission line effective dielectric constant
η_r	radiation efficiency
η_0	free space wave impedance
θ_n	beam-steer angle of mode n
ρ	junction charge density
$\rho_{n+\frac{1}{2}}$	charge density on offset pulse
ρ_c	surface charge density on conductor
ρ_d	surface charge density on dielectric
σ_c	conductivity of imperfect metallic conductor
σ_d	conductivity of imperfect dielectric
τ_u	dielectric surface identifier function
λ_g	guide wavelength in direction of propagation
λ_r	free space wavelength at antenna resonance
λ_0	free space wavelength
μ_0	permeability of free space
ω	angular frequency

List of Abbreviations

Abbreviation	Definition
EMC	Electromagnetic Coupling
FET	Field Effect Transistor
GaAs	Gallium Arsenide
HEMT	High Electron Mobility Transistor
LITA	Longitudinal Integration and Transverse Assembly
MMIC	Monolithic Microwave Integrated Circuit
SBD	Schottky Barrier Diode
TILA	Transverse Integration and Longitudinal Assembly

Chapter 1

Introduction

1.1 Millimetre Wave Phased Arrays

The exploitation of the millimetre-wave part of the electromagnetic spectrum for radar, communications and imaging systems has been receiving increasing attention over the past two decades. Although millimetre-wave systems will not replace microwave, optical or infrared systems for most applications, for some specific tasks a sufficient number of unique features attach to millimetre-wave systems to warrant this interest [1]. Advantages have been perceived in areas of both commercial and military significance, and are often related to the potential for high-resolution, compact systems, brought about by the short wavelengths. Propagation characteristics as well as large available bandwidth are other factors which may favour the use of millimetre wavelengths. A substantial body of literature, for example [1,2,3], serves to demonstrate that millimetre-wave systems are progressing beyond the conceptual stage to become a reality.

System performance often dictates the need for high gain antenna systems which may be electronically beam steered. Antenna gain and beamwidth requirements deter-

mine the antenna aperture, and the need for electronic beam steering focuses design on apertures filled with discrete elements with the phase of excitation at each element controlled so that the beam is formed in the required direction. At microwave frequencies, such *phased arrays* have been implemented using half-wave resonant dipole, or waveguide radiating elements [4], however, the use of planar printed circuit arrays of microstrip antennas is gaining popularity [5,6]. In the most versatile implementations of phased arrays, each antenna element is connected to a module which contains the appropriate electronic and electromagnetic circuits to perform the beam steering function. Other functions which are usefully performed by the module may include amplification, transmit/receive switching and frequency conversion. Such phased arrays are often referred to as *active arrays*. The complexity required for the implementation of active arrays frequently leads to high cost [7], and as a consequence their application has been restricted to only the most demanding of military systems. It is clear that if phased arrays, and in particular active arrays, are to be employed at millimetre-wavelengths, substantial cost-effectiveness must be achieved in relation to the millimetre-wave performance specifications.

High levels of integration in the form of monolithic microwave integrated circuits (MMICs) capable of operation at millimetre-wavelengths provides the strategy by which system realization will become feasible and cost-effective. The current status of MMIC technology is such that millimetre wave functional units are becoming available [8,9]. Developments in MMIC technology to the extent where the electronics of a phased array module may be fabricated on a single substrate will undoubtably provide further impetus to the implementation of millimetre-wave phased array systems. The benefits associated with MMIC fabrication at millimetre wavelengths are, however, not restricted to the necessity for cost-effective realization of the electronics. Because of the small physical dimensions at millimetre-wavelengths, monolithic fabrication of the antenna element on the same substrate as the electronics becomes feasible. This has the effect of simplifying the construction of the array and increasing the reliability of the module to antenna element interface, as well as further reducing the cost. These advantages are significant for large arrays where many thousands of elements may be

required.

Given the desirability of integrating the antenna element and the electronics, accurate design methods are needed for appropriate antenna elements and array architectures which are compatible with the approach. MMIC fabrication imposes constraints on the types of elements which may be employed, mainly due to the processes and materials used. Furthermore the choice of an appropriate architecture is governed by technological factors such as the available substrate area, yield, signal routing, electromagnetic shielding and heat removal, and is therefore also a factor in determining an appropriate antenna element. Finally, the degree of integration is a major consideration.

Wafer scale integration, in which many antenna elements and their associated electronics are fabricated on the surface of a MMIC substrate which is orientated to lie in the aperture plane of the array, is typically embodied as a planar array of microstrip dipoles, patches, or printed slot antennas [5,10]. Grid systems for achieving spatial power combining [11] and integrated horn antennas [12] are two other examples where wafer scale integration may be employed. Because of the constraint on element spacing, imposed by grating lobe conditions, the total area of each module and antenna element is restricted to approximately $\lambda_0^2/4$ in the aperture plane. For active arrays, therefore, it has been suggested that there are significant difficulties in realizing all the required functions as well as the antenna element within this area on a single wafer [5], and multi-layer approaches are typically proposed as a solution [13,14].

A chip scale approach offers an alternative method. Using appropriate architectures, the substrate area occupied by the antenna element does not in principle restrict the size of the MMIC module which drives it if the chip is orientated normal to the array aperture. In chip scale integration, individual modules are fabricated, each comprising a single antenna or subarray and its associated electronics. The chips are then arranged according to design in the aperture plane. This technique has been suggested by several authors [5,15,16,17], however, little progress has been reported regarding the detailed considerations for its implementation. Although it is necessary to fabricate many chips

and then to build up the array by assembling the chips and ensuring that each MMIC is appropriately housed, the significant gains and flexibility which are obtained in relation to the major constraints identified above are believed to warrant the additional construction effort. Some techniques for simplifying the construction problem have been suggested [15], and further consideration is given here to the practicalities which are involved.

Out of the considerations described above, this thesis first presents a detailed review of the nature and advantages of array architectures employing chip scale integration of the phased array module and antenna element. Arising from these considerations, a class of antenna elements, which may be described as *substrate supported metal strip antennas*, is proposed for careful study in order to assess the potential for millimetre-wave phased arrays fabricated in this manner. In the remainder of the thesis, a design method that can solve the significant electromagnetic design problems is developed for arrays of such antenna elements.

1.2 Substrate Supported Metal Strip Antennas

Substrate supported metal strip antennas form a general class of antennas suitable for MMIC fabrication using the chip scale approach described above. Possibly the most basic monolithically integrated radiating structure falls within this class, and consists of a half-wave resonant metal strip, contiguous with the end of an ungrounded extension of the MMIC substrate. Such antennas are economical in terms of the substrate area they occupy, and are found to satisfy the constraints imposed by the MMIC processes and array architecture considerations. To assemble the array, each ungrounded substrate extension, on which an antenna element or subarray is fabricated, is made to protrude through a slot in a metal ground plane. The substrates are therefore orientated normal to the array aperture as required.

At millimetre wavelengths, the substrates used in typical Gallium Arsenide MMIC

processes are electrically thick, and therefore the ungrounded substrates supporting the metal strip antennas described above are anticipated to have a significant effect on the design and performance of the elements and the array. A large body of literature deals with the problem of radiation by dipole antennas on electrically thick substrates of infinite lateral extent [18,19,20]. Much of this work deals with microstrip dipoles which are constructed on grounded substrates, however dipoles printed on substrates which form dielectric lenses have also been considered. Arrays of microstrip antennas, including microstrip patches, have been studied in considerable detail [21], and many of the effects which are due to the substrate geometry have been observed, and explanations put forward. A recent review of progress in the area of printed antennas and arrays is given in [22]. Some work has also been reported for substrates which have been truncated in one of the lateral directions [23], and for infinite arrays of antennas on substrates that are continuous in one lateral direction and periodically spaced in the other [24]. Finite size substrates in the form of separate chips, however, have not received attention beyond the case where the substrate is electrically thin [25]. Consequently the unsolved problems in this area present a considerable obstacle to the development of arrays that make use of substrate supported metal strip antenna elements. Due to the potential significance of metal strip antennas on finite size, electrically thick substrates to monolithically integrated phased arrays, the aim of this thesis is to redress this lack of information.

Because antennas which are fabricated monolithically cannot be economically tuned or adjusted after manufacture, and because the antenna elements are physically connected to the electronics associated with the module and may not be tested independently, accurate analytical models and numerical methods are required for design purposes. The antenna geometry as described above, comprising as it does a metal strip on a finite size three-dimensional dielectric region, precludes analysis by classical methods. Moreover, the antenna geometry is also such that the sizeable contributions to the analysis of planar geometries, which have been made in recent years in response to the proliferation of microstrip antennas and arrays, are not directly applicable to the problem. For these reasons, numerical methods which make no assumptions regarding

the nature of the fields in dielectric regions, for example that of [26], are attractive. In the work reported in this thesis, a method for analysing composite conducting and dielectric structures has been applied to the antennas under consideration. The method has been applied firstly to the element geometry, in order to reveal and identify the phenomena associated with the dielectric substrate, and then to entire structures which include both radiating and feeding parts. In this way gross idealizations for analytical purposes are minimized, and accurate design models can be obtained.

Practical measurements which support the theoretical studies are essential to test the numerical techniques. This is especially the case for the antenna structures considered here, since there is little or no reported work with which to compare results. Carefully designed experiments which verify the accuracy of the results, and demonstrate the application of the numerical techniques to engineering design, form an integral part of the work reported in this thesis.

Important information regarding the performance of antenna elements in an array environment may be obtained from the calculation or measurement of mutual coupling between elements. Because the cost of performing mutual coupling measurements increases with the number of elements in an array the need for accurate analytical techniques is acute. Considerations such as the complexity of the numerical algorithms required to extend the computation to mutual coupling, and the size of the computing resources necessary for an accurate solution to be obtained, are significant. An efficient mutual coupling analysis for substrate supported metal strip antennas is possible and is presented in this thesis. In addition to the insight obtained from mutual coupling analyses, the analysis of arrays of infinite extent reveals useful information about the scanning performance of a phased array [27]. For the large arrays that are under consideration in this thesis, the infinite array approach offers the possibility of accurate performance prediction for the majority of the elements that do not lie near the edge of the array. Effects such as surface wave excitation and scan blindness which are associated with the antenna element and array geometry often affect the performance of a phased array, and the prediction of such phenomena forms an important task in the design process. Furthermore, the flexibility to develop solutions to array problems

hinges on the availability of effective numerical techniques for modelling all of the details of the antenna element. In this thesis, techniques are described which achieve this flexibility for the class of MMIC antennas studied, and the array performance that is achievable is demonstrated.

The numerical analysis has revealed the effects which are associated with the electrically thick, finite size substrate that is present in the class of MMIC antenna elements described in this thesis. Several of the properties which have been identified are able to be exploited to optimize the radiation and impedance characteristics of the antenna element and the array, and designs that make use of these properties have been illustrated. For this reason, substrate supported metal strip antennas provide a level of performance which makes them highly attractive candidates for the practical implementation of millimetre-wave phased array systems.

1.3 Outline of the Thesis

This thesis is primarily concerned with the design of antenna elements for fabrication using MMIC technology, the ultimate aim being the realization of millimetre wavelength phased array antennas. The work reported here has particular relevance to operation in the frequency range from 30GHz to 100GHz, where microwave rather than optical techniques are predominant. The key issues involved in arriving at an appropriate architecture for such arrays are reviewed in Chapter 2. Because the advancement of MMIC technology is not influenced to any great extent by the special requirements of integrated antennas, attention is centred on the need to merge system, fabrication and antenna requirements. With this in mind, the chip scale approach to array construction has been identified as showing promise for practical implementation, and the various features associated with it are outlined and evaluated. Antenna elements which are compatible with chip scale integration are also reviewed in the light of the particular constraints of MMIC fabrication. A wide variety of antennas having an appropriate geometry have been described in the literature, however the constraints

associated with MMIC fabrication at millimetre wavelengths are found to restrict the applicability of many candidates. After examining some of the available options, the substrate supported metal strip dipole antenna is proposed as a simple solution, and the practical and analytical requirements for its exploitation are outlined. Such antennas have not received significant attention previously, especially for the case where the substrate is electrically thick.

In Chapter 3, a numerical analysis of the substrate supported metal strip antenna is developed. The problem is formulated in terms of surface currents on the metal strips and volume polarization currents in the dielectric substrate. The electric field integral equations for the structure are then solved using the method of moments. Care is taken to ensure that the electrically thick substrate is accurately modelled, and a computationally efficient algorithm which achieves this is developed. Results are obtained for an idealized antenna having a voltage excitation at an infinitesimal gap at the centre of the metal strip. In this way, the influence of the dielectric substrate on the impedance and radiation characteristics can be investigated. The numerical results are compared with measurements made on structures scaled to operate at microwave frequencies, and excellent agreement is obtained. Among the effects discovered which are attributable to the presence of the dielectric substrate, and which are predicted accurately by the analysis, are a reduction in resonant resistance, a physical shortening of the length of the metal strip for resonance, and the presence of cross-polarized radiation.

After developing a fundamental understanding of the interaction between the surface currents on the metal strip dipole and the volume polarization currents in the dielectric substrate, and how this interaction affects the antenna performance, the issue of feeding the antenna can be addressed. Feed structures and impedance matching are considered in Chapter 4, where the numerical analysis is extended to aid the development of practical antenna elements. The correct design of substrate supported metal strip folded dipoles fed by coplanar strip feed lines is described, and the design predictions are compared with measured results for antennas fabricated on RT Duroid and Gallium Arsenide substrates. The measurements were again conducted at microwave

frequencies on antennas with their dimensions scaled to simulate millimetre wavelength operation.

The volume polarization currents induced in the dielectric substrate have been shown to have an effect on the radiation characteristics of the antenna by introducing cross-polarized radiation. Because polarization performance may be an important system parameter [28], where excessive levels of cross-polarized radiation exist, steps must be taken to control the radiation characteristics in order to ensure that the widest range of applications exist for these antennas. In Chapter 4 it is shown how appropriate geometries for both the feed and the radiating structure can be chosen to reduce the level of cross-polarized radiation arising from the presence of the dielectric substrate. One particularly useful result obtained from the analysis of the complete antenna geometry is the partial cancellation caused by interference between the feed line radiation and radiation from the volume polarization currents induced in the substrate, thereby solving the dual problems of unwanted substrate and feed line radiation.

Two alternative antennas are also considered in Chapter 4. Firstly, an antipodal metal strip antenna and feed line is considered, where parts of the element and feed are constructed on opposite sides of the ungrounded substrate, and it is shown how the electrically thick substrate acts to create a high level of cross-polarization. Secondly, a novel single strip fed, substrate supported metal strip antenna, which occupies a relatively small substrate area, is introduced. The analysis of these alternative geometries illustrates the versatility of the numerical technique for design purposes.

Chapter 5 offers a solution to the problem of computing mutual coupling between substrate supported metal strip antennas. The numerical computations are performed on a Fujitsu VP2200 vector-supercomputer, and the mutual impedances obtained are found to agree well with the results of measurements on idealized structures. Application of the computed results to the design of practical two-element and three-element arrays, which are then constructed and tested at microwave frequencies, demonstrates further the accuracy of the mutual coupling calculations and their usefulness in practice. From the results it is noted that the use of electrically thick dielectric substrates

produces antenna elements which exhibit low mutual coupling. This fact is useful for MMIC based array design, and also suggests that electrically thick, finite size dielectric substrates may be employed at lower frequencies to reduce mutual coupling effects. Such techniques do not appear to have been previously explored.

The mutual coupling analysis described in Chapter 5 can only be applied directly to relatively small arrays due to the large computing resources required. For this reason, phased array analysis has frequently been undertaken by studying the theoretical scanning performance of an infinite array of antenna elements. Although practical arrays have finite dimensions, an array which is infinite in extent is known to exhibit properties which make it suitable for analysis, and the results are a good indication of the performance available from a large phased array. In Chapter 6 an infinite array of substrate supported metal strip antennas is analysed. The method developed is shown to be capable of modelling all the significant features of the radiating element and its feed, and is therefore able to accurately predict the performance of large practical arrays. The impedance and radiation characteristics of a substrate supported metal strip antenna element in an infinite array are computed as a function of the beam direction, and the scan blindness caused by the presence of the substrate as well as the feed line is investigated. It is shown how the common mode current, which is induced on the feed line as the beam is steered in space, can be controlled to obtain good scanning performance for a wide range of beam directions.

Using the numerical techniques that have been developed for phased array analysis, a fixed-beam array of single strip fed substrate supported metal strip antennas is investigated as an additional example. This example further demonstrates how the design method can be applied to solve array problems. In this case, particular symmetries are exploited to achieve an acceptable array radiation pattern, and the analysis is used to ensure that all of the design requirements are met.

From the extensive study described in this thesis, conclusions regarding the performance of substrate supported metal strip antennas employed in MMIC based arrays are drawn in Chapter 7. The relevance of this research to the the future development

of cost-effective millimetre wavelength phased arrays is highlighted and some areas for further research are identified.

In summary the major contributions to research made in this thesis are as follows:

- A logical framework for assessing the feasibility of MMIC based phased array antenna elements is given.
- The benefits associated with a chip scale approach to the integration of the antenna elements and the electronics of a phased array module are reviewed.
- A class of antenna element which has not previously received attention, comprising a metal strip antenna on a finite size, electrically thick substrate, is identified as being useful for the application described.
- An analysis of substrate supported metal strip antennas is developed which is able to take account of both the radiating and feeding parts of the structure, and which accurately models the finite size, electrically thick dielectric substrate.
- The effect of the dielectric substrate on the antenna performance is described, and some of the characteristics are exploited to optimize the antenna performance.
- Practical examples are used to illustrate solutions to design problems which occur for both isolated elements and arrays.
- Experimental measurements are used to test and verify the analytical models that are developed.

Chapter 2

Monolithic Integrated Array Architectures

2.1 Introduction and overview

The benefits associated with the use of printed circuit antennas in conjunction with integrated electronics have been recognized for many years, particularly with regard to systems designed to operate at millimetre wavelengths [19]. Antennas which are fabricated on hybrid or monolithic integrated circuits have been termed *integrated circuit antennas*, and offer the possibility of overcoming fabrication difficulties associated with the small electrical dimensions at millimetre wavelengths, increasing the reliability of the overall system, and reducing the complexity and losses incurred by the use of transmission line interconnections and feed networks. Many examples of integrated circuit antennas can be found in the literature, including antenna elements integrated with detector diodes for imaging arrays [19,29,30], antenna elements integrated with mixers for receivers [31,32], and antenna elements integrated with oscillators for spatial power combining arrays [33]. A wide variety of integrated circuit antennas have been

conceived and fabricated, ranging in complexity from adaptations of printed circuit antennas through to specially designed structures such as integrated horn antennas [12] and semiconductor antennas [34,35]. The diversity of these structures attests to the interest in the development of integrated antennas, and the extent to which they may be usefully employed has been widely explored.

As the level of sophistication of MMIC technology increases, active phased array systems for operation at millimetre wavelengths, employing MMICs which perform many or all of the functions associated with the front-end amplification, switching, frequency conversion and beam forming operations of a phased array, are becoming feasible [36,37,38,39]. The concept of an *array architecture* refers to the way in which the array is constructed, and includes the electromagnetic, thermal and mechanical aspects of the design. For reasons similar to those which motivated the development of integrated circuit antennas, array architectures which include antenna elements fabricated on a part of the MMIC substrate have practical potential [38,40,41]. Antennas which are formed as a component part of the MMIC during the sequence of wafer processing steps associated with MMIC fabrication are subject to the limitations of that technology, and are defined in this work as *MMIC antennas* in order to distinguish them from the more general class of integrated circuit antennas which are not necessarily required to satisfy the constraints imposed by a particular MMIC technology.

The potential of MMIC antennas is realized in the key area of relatively low production cost where large numbers of reliable sub-units are needed for an array. Although monolithic active array architectures present a complex and many faceted design problem, the advantages in terms of practical realization, and the predicted gains in performance over passive arrays, promise substantial rewards for successful solutions [42]. From the point of view of the antenna designer, there are many factors which will have an impact on the choice of antenna element to be fabricated, and which are closely related to system specifications and the decision to adopt a particular array architecture. In addition, the capabilities and limitations of MMIC technology itself may, to a significant extent, restrict the available solutions, presenting constraints which need to be addressed in the antenna and array design. The problems are formidable enough

that one commentator has recently observed that no truly monolithic array has yet been produced [6].

It is the intention of this chapter to put the antennas and arrays considered later in this thesis in the particular context of MMIC based active arrays. To this end, the important design issues relating to MMIC antennas and arrays are reviewed, and the basic array architectures are identified. After outlining the constraints and options associated with the different architectures, the application of the substrate supported metal strip antennas introduced in Section 1.2 to MMIC based active arrays is described. The considerations presented in this chapter suggest that these and other antennas and arrays having a similar geometry may provide a basis for the development of practical systems.

2.2 Design considerations for MMIC antennas and arrays

The key component in the realization of an active array is the *phased array module*, which may contain power amplifiers, low-noise amplifiers, switches and phase shifters, together with control circuits to implement beamforming and monitoring functions. A phased array module may be associated with a single antenna element or a group of elements, the latter referred to as a *subarray*. The use of MMIC technology to fabricate the phased array module offers significant advantages in terms of reliability, performance and system modularity. MMIC technology, soundly established at microwave frequencies [43,44], is being developed further to provide useful circuits and systems in the millimetre-wave range [45]. Economically viable commercial application of MMICs at these higher frequencies is likely, for the foreseeable future, to be based on existing state-of-the-art methodologies for production. Approaches employing more esoteric methodologies are less attractive where specialized processes are needed. Since the microelectronics industry is driven by influences wider than those interested in phased

array development, it is useful to observe that cost-effective solutions to array design which are able to make use of the most advanced existing technology have the greatest potential to become a reality.

The above considerations apply equally to the development of MMIC antennas for active arrays. The constraints placed on the antenna elements by the adoption of MMIC fabrication processes are summarized in Section 2.2.1. General requirements placed on the antenna element by system specifications are reviewed in Section 2.2.2, together with the important issues relating to the array architecture.

2.2.1 MMIC constraints

Substrate parameters The parameters associated with the substrate are an important consideration in the choice of a suitable antenna element. MMIC technology employs Gallium Arsenide (GaAs) substrates having a relatively high permittivity ($\epsilon_r = 12.9$). Semi-insulating GaAs, which would form the substrate material for a MMIC antenna, is a low-loss dielectric at millimetre wavelengths. The substrate thickness is determined by a number of considerations, including the need for mechanical strength and the characteristics of the active devices to be fabricated, and also dictates the width of the microstrip line interconnections for a given characteristic impedance. Typical 100 to 200μm substrates, although physically thin, are electrically thick at millimetre wavelengths; a factor which must be addressed in the choice and design of MMIC antenna elements. The majority of MMIC components are fabricated on grounded substrates, and a grounded substrate for active elements will therefore need to be present in any design. Ungrounded areas of substrate may be made available by removing the ground plane under a part of the MMIC if so desired.

Substrate area usage The substrate area occupied by the MMIC electronics is related to the complexity of the circuit. For a phased array module, many functions may need to be incorporated, and the substrate area will be correspondingly large.

Moreover, signal routing, control circuits, digital data bus lines and bias lines will also occupy substrate area. The need to accommodate on the MMIC substrate an antenna element and its feed network, both of which may be relatively large when compared with the area occupied by the MMIC electronics, will have a further impact on the availability and usage of substrate area. Because the module is constrained to a limited area in the array aperture plane, architectures which are able to fit all of the components, including the antenna element, into this limited area must be developed. The cost of building an array of MMIC antenna elements is also directly related to the area of substrate occupied by the antenna element, and physically small antenna and feed designs may be preferred for this reason.

Degree of integration The degree of integration relates to the way in which the phased array modules and antenna elements are implemented in an array using MMIC technology. *Wafer scale integration* is often proposed at millimetre wavelengths, and involves the replication of functional units many times on a single wafer in such a way that the entire wafer may be used to form part of the array [46]. Functional units may be a complete phased array module or part of a phased array module, depending on the array architecture chosen. In contrast, *chip scale integration* involves the fabrication of individual functional units which are diced from the wafer after manufacture and then assembled into the array [47].

Yield Questions regarding the number of functional units to be fabricated on a single wafer or chip need to be addressed to facilitate reliable fabrication. Problems associated with low yields from MMIC processes or interconnection failures may result in unacceptable thinning of the array and consequent degradation in performance.

Fabrication techniques A MMIC antenna element must be fabricated using the techniques and materials available in the MMIC process. Completely integrated structures are therefore limited to planar geometry antennas comprising dielectric and metal parts. Several layers of metallization and dielectric films are usually

available in MMIC processes, and may be exploited in the design of the antenna element.

Shielding and isolation Performance modelling of MMIC circuits under accurately defined conditions is an essential part of a MMIC design process. For circuits which operate in the presence of integrated antenna elements, space-wave and surface-wave radiation from the antenna must either be included in the modelling, or else appropriate shielding and isolation techniques used in the design of the MMIC housing. Additionally, spurious radiation from the MMIC electronics may also influence the performance of the antenna element. Array architectures which provide adequate housing for the MMIC electronics as well as mechanisms for efficient radiation from the integrated antenna are therefore desirable.

Interconnections Typically, the output terminal of the MMIC electronics, which is to be connected to the antenna element, takes the form of a microstrip transmission line. Methods for low-loss, high-reliability connection to a MMIC antenna element on the same wafer or chip may be achieved either i) by direct connection if the antenna has a suitable feed port, ii) via a balun transformer or microstrip transition it the antenna cannot be fed directly from a microstrip feed line or iii) by electromagnetic coupling (EMC) to the microstrip feed line without any actual connection required [5,48].

Testing and modelling Computer aided design of MMICs is becoming highly developed in order to accurately predict the performance of circuits and devices fabricated using increasingly sophisticated techniques [49]. Since the antenna element forms an integral part of the MMIC, independent testing of the antenna element or module electronics is not possible. For this reason, both the module and the antenna elements should be amenable to analysis that makes realistic assumptions regarding the environment in which each will operate. Any interaction between the module and the antenna element must therefore be well defined. The need for highly accurate MMIC antenna design models arises from these considerations and the fact that post-fabrication tuning is not feasible. Due to the high cost of the systems proposed, experimental measurements on complete arrays are

impractical, and therefore there is a critical need to avoid problems appearing at a late stage of development that may cause the array to be redesigned and refabricated.

2.2.2 System requirements and architectural considerations

Many of the constraints identified in Section 2.2.1 that are imposed on MMIC antennas have a direct impact on the achievable system performance. Engineering design involves the requirement to meet certain specifications, and the adoption of a particular technology is dependent on the potential for it to satisfy these specifications. Although the use of MMIC technology provides a widely accepted means of achieving cost-effective solutions to design problems at millimetre wavelengths, monolithic integration of antennas is still very much in the development stage [46]. It is therefore necessary for the array performance to be demonstrated in the context of proven architectures before fully integrated millimetre-wave arrays can progress to complete active array systems of many thousands of elements. Array architectures are sought which are able to meet the broad design objectives of proposed millimetre-wave phased array applications, and which conform to the constraints imposed by MMIC technology outlined above.

Some electrical considerations associated with the antenna element which underly design specifications are summarized below [5].

Bandwidth The choice of antenna element is influenced by the bandwidth over which the system is expected to operate. Substrate parameters, over which the designer of a MMIC antenna may have little control, can affect the bandwidth of the antenna element. In general, the millimetre-wave active arrays which have been proposed are intended to operate over bandwidths of only a few percent, however, factors such as the sensitivity of the antenna performance to manufacturing tolerances and environmental effects that are unable to be modelled in an analysis

may necessitate the design of antennas with wider bandwidths. Modern phased array system requirements also indicate a trend towards the use of wider bandwidths [50,51], and these may need to be addressed for future millimetre-wave arrays.

Scanning performance The maximum angular range over which the main beam of the antenna may be scanned is limited by several factors. The beamwidth of the antenna element must cover a sufficiently large angle to permit the required scan range to be achieved. The need to avoid grating lobes entering the field of view of the antenna element as the array is scanned then determines the maximum spacing between the elements in canonical array geometries with regularly spaced elements, and therefore defines the packing density required in the aperture plane. Scan blindness effects, which may be introduced by the excitation of surface waves propagating across the array aperture [5,52] or by scattering from feed lines [53], also limit the scan range.

Spurious radiation Radiation from feed networks can degrade the performance of the array by introducing cross-polarized radiation, increasing sidelobe levels or modifying the mutual coupling between elements. The use of a feed network that can be accurately modelled at the design stage of development is therefore an important factor in the choice and development of an array element.

Radiation pattern characteristics The quality of the radiation pattern of the antenna element may be measured by a number of parameters, including gain and radiation efficiency, cross-polarization performance and beamwidth. The issue of maintaining the quality of the radiation pattern as the beam of the array is scanned in space is also of concern.

Impedance characteristics An antenna element that presents close to a matched impedance to its feed network is necessary for efficient radiation. The impedance of an antenna element is, however, dependent on the array environment in which it operates, and is also a function of the beam steer angle of the array. This necessitates accurate design methods that take account of the array environment and in particular the mutual coupling between elements.

While the above design considerations are dependent on the application for which the array is intended, and are not unique to integrated antenna arrays, they serve to illustrate the wide range of factors which need to be taken into account in the development of MMIC antenna elements.

As well as the element design considerations set out above, some additional factors which are basic to the choice of the array architecture are listed below.

Power and signal distribution The requirement to distribute a synchronous source signal and control signals to a large number of phased array modules poses a considerable design challenge. Topologies which accommodate paths by which the electromagnetic power, digital control signals and bias voltages can be routed to each module or subarray are needed for a practical array implementation.

Construction The architecture of the array is largely governed by the manner in which the aperture plane is filled with the antenna elements. In the case of arrays incorporating MMIC antennas, the choice of architecture is also related to the physical and electrical characteristics of the antenna elements that are used. The choice of a particular architecture also has an impact on the degree of integration that may be achieved. Various configurations are described and evaluated in Section 2.3.

Heat removal Many of the active devices employed in MMIC technology, particularly FET devices, have a low efficiency. This results in the need to consider heat removal from the phased array module, and the provision of suitable paths for heat transfer form a part of the architectural considerations. Issues which need to be addressed include the thermal properties of the media surrounding the active devices, the availability of surfaces for heat transfer away from critical areas, and the desirability of ambient air cooling rather than forced air cooling or liquid cooling. The use of HEMT devices at millimetre wavelengths, with their increased efficiency, may also assist by reducing the heat generation [42].

All of the considerations outlined above are within the domain of the antenna de-

signer, since they have a significant impact on the choice of the technology, architecture and antenna element that is to be used. Ultimately the suitability of an antenna element and an array architecture for fabrication with MMIC technology is judged by how well the above constraints are satisfied in the light of the performance requirements of the array.

2.3 Basic architectures employing MMIC antenna elements

The array architecture that is chosen to implement a phased array that incorporates MMIC antennas depends on the antenna element geometry. In general, MMIC antennas may be classified into one of two types:

1. Antenna elements fabricated on the top surface of the grounded MMIC substrate. Such antenna elements must have the maximum of their radiation pattern on or close to the direction normal to the MMIC substrate. For the majority of array applications, the substrate itself extends continuously across the aperture plane of the array and encompasses a number of elements.

2. Antenna elements fabricated on a part of the MMIC substrate that has the MMIC ground plane removed. Such antenna elements must have the maximum of their radiation pattern on or close to the longitudinal axis of the MMIC, and may be termed *endfire elements*. The substrates are therefore orientated normal to, and form a periodic structure in, the aperture plane of the array. Each ungrounded part of the MMIC substrate may contain a single element or a linear array of elements.

MMIC array architectures for each of the above types of element are illustrated in Figure 2.1. Where the first type of element is employed, MMIC wafers orientated parallel

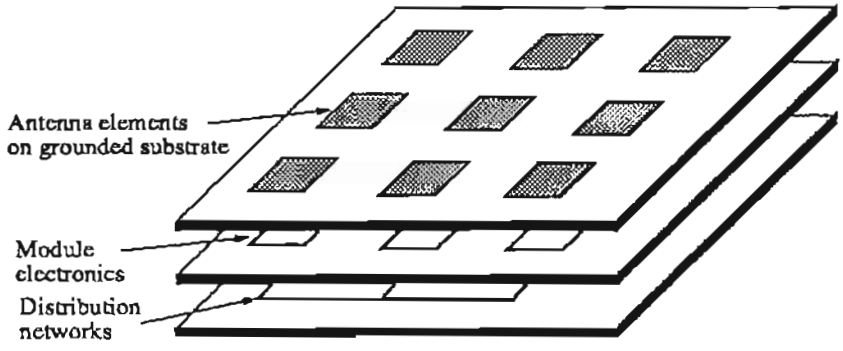

(a)

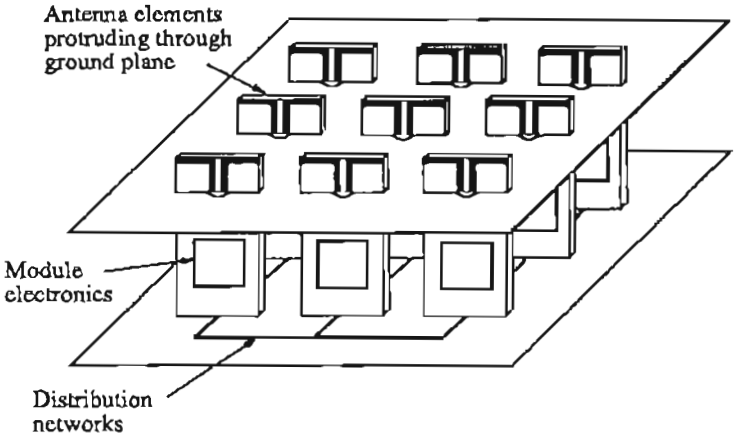

(b)

Figure 2.1: Integrated array architectures: (a) Transverse Integration and Longitudinal Assembly, and (b) Longitudinal Integration and Transverse Assembly. The boresight radiation direction of both arrays is vertical in the page.

to the transverse array aperture are stacked in the longitudinal direction to build the array. This architecture is therefore referred to as *Transverse Integration and Longitudinal Assembly* (TILA). Where the second type of element is employed, MMIC wafers orientated longitudinally to the array aperture are arranged in the transverse direction to build the array. Correspondingly, this architecture is referred to as *Longitudinal Integration and Transverse Assembly* (LITA). In this section, the merits and limitations of TILA and LITA architectures for MMIC arrays are summarized, and typical antenna elements compatible with each approach are identified. The issue of electromagnetic power distribution affects both architectures and is dealt with separately.

2.3.1 TILA arrays

Microstrip antenna technology, involving metal strips or patches separated by a dielectric layer from a metal ground plane, has been suggested as the basis for MMIC active arrays, and is suitable for use in TILA architectures. In the past, the desire for inexpensive, low-profile and easily fabricated planar arrays has motivated the development of microstrip antennas, and many examples of microstrip antennas can be found in the literature. Analytical methods for accurate design of both microstrip antenna elements and arrays of elements are well established, and considerable experimental testing of designs has been undertaken. For these reasons, antenna elements such as microstrip dipoles and patches, as well as printed slots, have been the first choice of the proponents of integrated active arrays.

For millimetre wavelength applications, various configurations of microstrip patches or dipoles having bandwidths of up to about 10% have been employed as array elements. In general low permittivity, thick substrates are preferred for larger bandwidths, however, monolithic fabrication on semiconductor substrates imposes a relatively high permittivity. Furthermore, if the antenna elements are to be fabricated on MMIC substrates, the actual substrate parameters may be prescribed by the fabrication process and materials employed, and consequently the substrate is likely to be electrically thick

at millimetre wavelengths. Where electrically thick substrates are employed, the issues relating to the excitation of surface waves and their effect on the radiation efficiency and mutual coupling between array elements need to be addressed [5].

The constraints associated with the antenna and array geometry of a TILA architecture need to be addressed directly. For a MMIC based active array, adequate substrate area must be available for the MMIC electronics as well as the antenna element, and various constructions for achieving this have been adopted or proposed. Subarrays incorporating several antenna elements together with the module electronics on the surface of a single MMIC have been designed and fabricated [37], however, all of the functions that are required for an operational phased array cannot be accommodated on the one substrate. Moreover, it has been found that interaction between the electronics and the antenna elements by way of spurious radiation and surface wave effects degrades the array performance.

In order to shield the antenna elements from the MMIC electronics a two sided geometry may be used [5], where each side of the structure is separated by the microstrip ground plane. Electromagnetic coupling through apertures in the ground plane is used to transfer millimetre-wave energy from the modules to the antenna elements. Such a structure also offers the possibility of using an alternative substrate material for the antenna array so that some degree of control over the antenna characteristics can be obtained. Arrays of this type are no longer fully monolithic arrays, and may be termed *hybrid arrays*. In the case of a hybrid array, an additional set of considerations related to the use of dissimilar materials in the array construction must be addressed. These include the effect of different material properties, and in particular different thermal characteristics which may cause material stresses to fracture the fragile MMIC wafers. Issues such as the ability to meet manufacturing tolerances and subsequent alignment are also important for hybrid arrays.

Additional substrate area may be obtained by using a multilayer TILA architecture such as that shown in Figure 2.1a [13]. Antenna elements on the top layer are excited from the MMIC electronics on the lower layers either by direct interconnection

between the layers or by electromagnetic coupling. At each layer, a given function or set of functions is implemented and duplicated many times such that when the layers are connected together, a complete subarray is obtained. Such architectures offer, in principle, the potential for completely monolithic arrays with each layer fabricated by wafer scale integration. It is noted, however, that a hybrid approach may still be adopted for the antenna elements if required. Multilayer structures offer the widest degree of flexibility in TILA architectures.

Assessment of the multilayer TILA architecture shown in Figure 2.1a has been undertaken, and has highlighted the areas which need special consideration [13,16,41, 42]. Among these are the following.

- The need to provide reliable interconnections. Many thousands of interconnections are required in a practical array, and these must extend between the layers making up the array as well as between modules on a given layer. Connections between layers may be physical connections, or in the case of millimetre-wave transmission lines electromagnetic coupling may be used to transfer electromagnetic energy between layers. Where physical connections are required, new techniques, such as the use of via holes filled with conducting ink [54], are necessary to ensure the reliability of the large number of interconnections. The routing of the millimetre-wave transmission lines, digital control signal lines and bias voltage lines on each layer in such a way as to minimize interference and cross-coupling of the signals also presents a considerable topological challenge. Optical techniques for phased arrays have recently received attention, and may prove useful in the area of signal distribution [55].

- The need to provide appropriate mechanisms for heat transfer. The provision of paths along which the heat generated by the active electronics can be removed from the array is essential to maintain the proper operation and long life of the array. In a TILA architecture, the active components of the MMICs are sandwiched within dielectric layers, and the ground planes of the MMICs are enclosed by these layers. If the thermal conductivity of the dielectric layers

is poor, the transfer of heat to the outer face at the back of the array may be inhibited, and a complex and expensive cooling system may be required to overcome this difficulty. Furthermore, steps must be taken to ensure that heat is not transferred to the array aperture, since heating could cause displacement of the elements leading to phase errors in the feeding of the elements, or stress damage to the antenna elements.

- Module failure and repair problems. Because the multilayer TILA architecture favours the fabrication of large subarrays constructed on several wafers, failures due to yield problems or damage may render large portions of the array unusable. The cost associated with the development of subarrays having a sufficient number of usable elements when the array is finally assembled, or else the cost of re-fabrication and repair of subarrays that do not have a high proportion of usable elements, may prove prohibitive.

Recent reports suggest that to a significant degree, these problems are still unsolved [42].

TILA architectures made up of several wafers, with each wafer providing a single function which is duplicated many times, have the potential for greatly simplifying the overall array construction, particularly where large subarrays are feasible. For this reason, many researchers are focussing work in this area. Technological limitations such as those described above are, however, likely to inhibit the fully monolithic realization of such arrays in the near future.

2.3.2 LITA arrays

An alternative to the TILA architecture is the LITA architecture shown in Figure 2.1b. In the LITA architecture, the MMIC antenna is integrated on the same substrate as the MMIC electronics forming the phased array module. The substrates are then orientated so that the elements protrude through a ground plane that shields the

MMIC electronics, and the modules extend back perpendicular to the ground plane. In Figure 2.1b, individual chips comprising a single module and its antenna element are illustrated, however, collinear arrays of several elements and their associated modules could also be constructed on a single chip. In either case, because all of the components of a phased array module are located on a single substrate, the LITA architecture is an example of chip scale integration.

The LITA architecture is derived from conventional approaches to active phased array design at microwave frequencies, which has in the past employed waveguide or resonant dipole antenna elements connected to individually housed phased array modules [7]. Tapered slotline arrays for millimetre-wave imaging applications also employ a LITA architecture [56], and have recently been analysed for phased array applications [57]. Hybrid approaches to LITA arrays have also been developed. In one example of a hybrid array, MMIC based components of a phased array module are mounted on a mother-board, which contains the feed and radiating elements [7]. Another hybrid array comprises a microstrip antenna array fed from behind the microstrip ground plane by MMIC phased array modules orientated perpendicular to it [58].

For a fully monolithic approach to LITA arrays, a variety of MMIC antennas are compatible [41]. For example, travelling wave antennas such as the tapered slotline antennas described above could be fabricated on an ungrounded part of the MMIC substrate, or dielectric rod antennas [59] could be formed by trimming an ungrounded extension of the MMIC substrate to the appropriate geometry [60]. Resonant antennas such as half-wave resonant dipoles [24,61], or dielectric resonators [62] are also candidates for MMIC antennas in LITA arrays. The suitability of a structure is, however, dependent on the constraints identified with regard to array performance and fabrication. Limitations on the physical size of elements for reasons of cost, the need to avoid introducing grating lobes into the array pattern or the need for a wide field of view, and also the requirement to avoid inappropriate fabrication techniques, may eliminate some of the potential structures. Furthermore, studies of antenna elements for millimetre wavelengths have suggested that the potential for low-loss fully dielectric structures is not necessarily realized in practice, and in fact such antennas may suffer from poor

quality radiation patterns that are difficult to control [63]. These considerations must be reviewed as part of the design process leading to the choice of an antenna element for a LITA array, however, assessment of the types of MMIC antenna element that may be suitable has not been as widely undertaken as for the TILA arrays described above.

There are some apparent advantages of LITA arrays which suggest that research into appropriate antenna elements may be fruitful. Among these are the following.

- Single wafer modules. The potential for fabricating fully functional, self-contained MMIC modules on a single chip has advantages in terms of the modularity of the overall system. Post-fabrication construction of the array allows pre-testing of entire modules or subarrays before the complete array is assembled. Additionally, the size of the subarray can be chosen according to the limitations on yield imposed by a particular MMIC process technology.

- Substrate area availability. The restrictions on substrate area are largely removed using the LITA architecture, since the MMIC substrates can extend back from the array aperture as far as is necessary to provide sufficient area for all of the module electronics. The limiting factor on substrate area is therefore set primarily by the size of the active area of the MMIC that can be fabricated reliably, and by the cost considerations associated with economical and efficient chip area usage.

- Signal routing flexibility. The use of single wafer modules alleviates the problem of critical alignment between several layers, needed in TILA architectures to couple electromagnetic energy between layers. Because the array assumes a three-dimensional rather than a two-dimensional geometry, an additional degree of freedom is available to route the digital control signals and bias voltages between the modules, leaving only the millimetre-wave transmission lines in the plane of the MMIC substrate. The use of the packaging and housing structure associated with the array assembly to distribute the digital control signals and bias voltages in such a way that they do not interfere with any of the electromagnetic circuits

is a possibility that is not readily available with the wafer sandwich of the TILA architecture.

- Heat removal mechanisms. The three-dimensional LITA architecture provides additional surface area through which the heat generated by the active devices on the MMICs may be removed. Because the ground planes of the MMICs are not sandwiched in layers, freedom exists to choose an appropriate intermodule medium which is conducive to efficient heat transfer to the outer surfaces of the array.

LITA architectures therefore offer some advantages for active arrays incorporating MMIC antenna elements. Appropriate methods for supporting and housing the MMIC modules are required to implement LITA architecture active arrays, taking into account the small dimensions of the array elements at millimetre wavelengths. Where collinear subarrays comprising several antenna elements and their associated modules are feasible, the magnitude of the assembly problem may be similar to, but much less concentrated than that of the TILA architecture array, and the full advantages of LITA architectures may be realized.

2.3.3 Array feeds

Common to both TILA and LITA architectures is the problem of designing a feed network to distribute millimetre-wave power to each of the modules of the array. The issue of power distribution is overviewed in [42], and the discussion here will be limited to MMIC array applications. Printed circuit antenna arrays have been constructed using *corporate feed networks* which aim to provide a feed port connection at each element from a single source by the use of constrained transmission lines and power dividers. Planar and volume corporate feeds are illustrated in Figure 2.2a and 2.2b respectively. A planar corporate feed could be used to distribute power to individual modules or subarrays in a TILA architecture, and the distribution network would

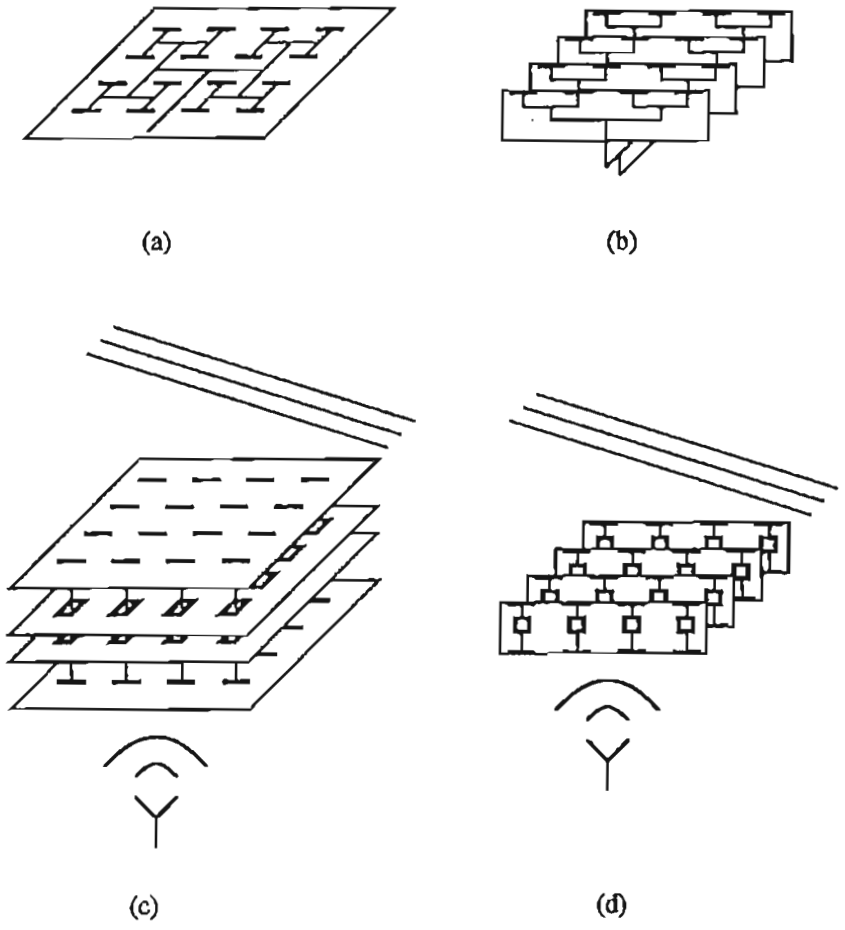

Figure 2.2: Examples of array feeds: (a) planar corporate feed, (b) volume corporate feed, (c) space fed active lens with TILA architecture and (d) space fed active lens with LITA architecture.

form one of the layers of the overall structure. Direct connection or electromagnetic coupling may be employed to transfer power to the modules from the feed network. Similarly, a volume corporate feed could be used to distribute power to individual modules in a LITA architecture that comprises collinear subarrays. In the case of the LITA architecture, however, two separate planar corporate feed networks are needed to make up the volume corporate feed; the first to distribute the power on each MMIC subarray, and a second to distribute power to each of the subarrays. Corporate feeds offer highly accurate power distribution to the array elements, provided that close tolerances can be held in fabrication and assembly on the variations between what should be identical paths to each element. Additionally, where a conformal array is required, the adoption of a corporate feeds network can result in a compact structure. For large arrays, however, the power dividers and transmission lines associated with corporate feed networks can introduce significant loss that must be compensated by increasing the gain of the active array amplifiers.

Space feeds offer an alternative method of power distribution. In Figure 2.2c, a TILA architecture *active lens* is illustrated. Millimetre-wave power is distributed spatially from a source antenna, and is received at each module by an antenna element on the reverse face to the array aperture. The feed is lossless except for spillover and reflection losses, and has the additional advantages of being inexpensive and simple to implement. A similar active lens implemented using a LITA architecture is illustrated in Figure 2.2d. Space feeds have been proposed as being especially useful for MMIC based active arrays operating at millimetre wavelengths, and various system implementations have been suggested [15]. Moreover, a space feed removes the need for precise alignment of the antenna subarrays to the feed network and the corresponding constraints on fabrication tolerances.

Although both TILA and LITA architectures may be designed with space feeds, the TILA architecture has the significant disadvantage that if a space fed active lens is required, both faces of the planar assembly are occupied by antenna arrays leaving no provision for a means of heat removal from active components. In contrast, the LITA architecture retains the facility for heat transfer because paths are available through

the side faces of the assembly. For this reason, research into LITA architectures is further stimulated.

2.4 A chip scale approach to antenna integration

In this thesis, antenna elements and arrays which are amenable to LITA architecture MMIC based arrays are the subject of research. Figure 2.3 illustrates schematically a chip scale approach to the construction of a LITA array of the substrate supported metal strip antennas introduced in Section 1.2. As illustrated, individual chips comprising a single module and antenna element are assembled to produce the array, a section of which is illustrated in Figure 2.3a. The antenna element, shown in Figure 2.3b, consists of a metal strip contiguous with the end of an ungrounded extension of the MMIC substrate. The metal strip antenna is designed to operate at its half-wave resonance, and is shown here with a coplanar strip feed line. The MMIC electronics of each module is housed behind the array ground plane, and the ungrounded extension of the substrate on which the metal strip antenna is fabricated is made to extend up to a quarter wavelength out of a slot in the module housing. It is clear that the general considerations outlined in Section 2.3.2 for LITA array architectures are satisfied. Because the architecture is such that the MMIC electronics is appropriately housed and shielded, for the purpose of design and analysis the antenna structure itself may be considered independently of the actual array construction used.

There are several reasons to suggest that the investigation of substrate supported metal strip antenna elements is warranted for application to millimetre wave arrays.

- The geometry is simple and readily fabricated using MMIC techniques.
- A composite conducting and dielectric structure is employed, and is therefore less likely to suffer from the problem of poor array radiation pattern control than a purely dielectric structure.

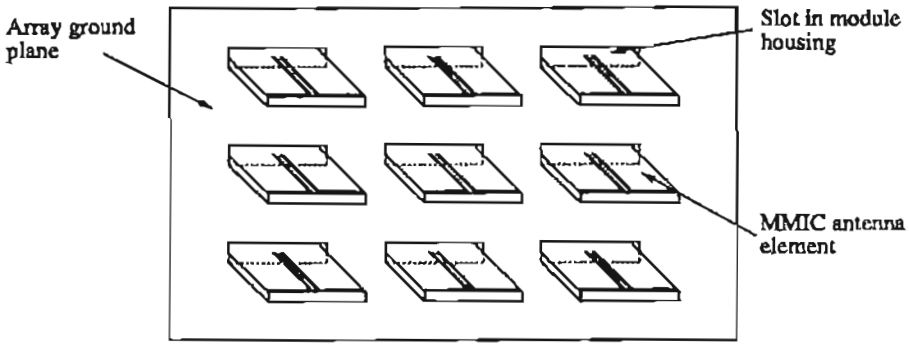

(a)

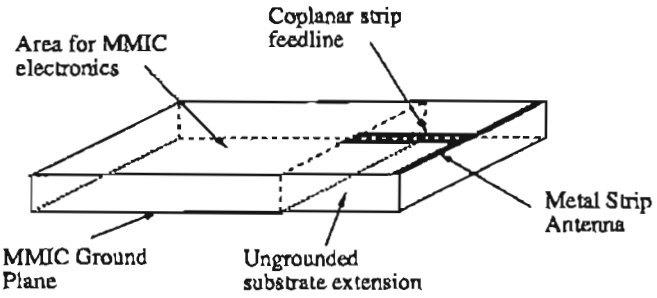

(b)

Figure 2.3: Chip scale antenna integration with substrate supported metal strip antennas: (a) a 3×3 segment of a large array and (b) a single antenna element of the type used in (a).

- Being a resonant structure, the element occupies a relatively small substrate area compared with travelling wave structures. Substrate area usage, and therefore cost, are kept to a minimum.
- The antenna dimensions are amenable to half-wavelength spacing between the elements in an array.

Such arrays, consisting of metal strip antennas on finite size, electrically thick substrates, have not been investigated in the past. Where similar geometries have been proposed, the substrates are usually assumed to be electrically thin, and air gaps between individual elements have not been considered. At millimetre wavelengths, the electrically thick, finite size, substrates employed in the antenna structures to be considered in this thesis are anticipated to have a large effect on the performance of the antenna elements and the array. No previous analysis of such structures appears to have been undertaken for the substrate thicknesses and geometries identified here, and the remainder of this thesis is aimed at providing a design procedure and using it to explore the features of the antenna elements and arrays.

Several aspects of the array assembly are now considered in order to illustrate the diverse means available to realize the structures in practice. Firstly, for the array described above, individual chips are fabricated and then mounted within rectangular metal housings. For a space fed active array, substrate supported metal strip antenna elements would protrude from both the front and rear sides of the assembly. Such a scheme is feasible at the lower end of the millimetre-wave band where the dimensions make the chips still reasonably manageable. Incorporated within the housing assembly would be appropriate control signal and bias paths. An alternative assembly, involving chips mounted on metalized ribbons which are bonded together in a honeycomb structure has also been proposed to simplify the construction and provide a means of obtaining dual polarization [15].

Where multi-module and multi-element MMIC chips are achievable, either due to improved reliability of the MMIC processes, or due to a reduced functionality require-

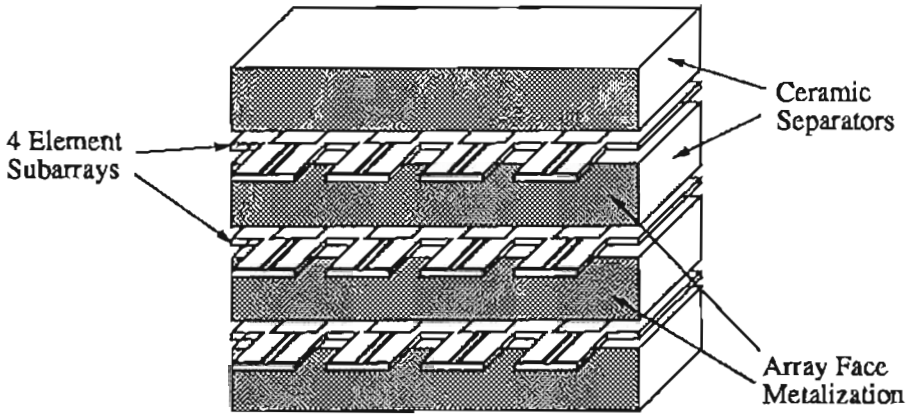

Figure 2.4: A subarray approach to monolithic integrated circuit arrays employing substrate supported metal strip antennas.

ment on the module, a subarray approach such as that illustrated in Figure 2.4 may be employed. In the construction shown, the ungrounded extensions of the substrates on which the antenna elements are fabricated are made to protrude from between ceramic separators which have metalized surfaces to produce the array ground plane. This layered approach to fabrication is similar to that proposed for TILA architectures. The modules of each subarray, however, are still self contained on a single chip, and no millimetre-wave connections are required between the layers, thereby avoiding the associated alignment problems. Because the chip scale approach is used, fewer inter-chip connections are required than for the layered TILA approach. The protruding part of the substrate between the elements of each collinear subarray is removed so that the array aperture is filled in the same way as the previous assembly. The analysis developed in this thesis is therefore common to both approaches. Additional layers of dielectric material extending underneath the substrate supported metal strip antenna may also be employed to increase the mechanical strength of the cantilever protrusions. Again, a space fed active lens system could be fabricated by incorporating antennas along both the front and the rear edges of the substrates shown in Figure 2.4. Assemblies similar to the one suggested here may be useful at frequencies up to and above 100GHz. The fabrication of subarrays of this type represents the ultimate realization

of the design research presented here, and offers promise for the realization of fully monolithic active arrays.

2.5 Summary

From the considerations outlined in this chapter, it is apparent that the array architecture has a considerable impact on the type of antenna element which may by used in an active array employing MMIC antenna elements. Various architectures have been described briefly in order to illustrate how substrate supported metal strip antennas may be used to achieve realizable active arrays satisfying the constraints imposed by MMIC fabrication. A LITA architecture which makes use of chip scale integration of the phased array modules and antenna elements is proposed as a viable alternative to the more commonly considered TILA geometries. A new subarray method is also proposed as a means of increasing the degree of integration attained from the use of the chip scale approach, and illustrates the range of possibilities available through the LITA approach.

This chapter has therefore provided the context in which the substrate supported metal strip antennas considered in this thesis may be employed, and has illustrated some of the benefits afforded the array designer by their use. Of course, many of the details of the fabrication of a practical array still require thorough investigation, in particular with regard to what a given MMIC process and technology is able to achieve. It is the purpose of this thesis, however, to provide a validated design procedure and methods for the engineering of significant improvements in the performance of MMIC antenna arrays that use substrate supported metal strip antennas. In this way, the options available in the design of active array antennas for millimetre wavelength applications that make full use of current advances in MMIC technology are widened.

Chapter 3

Substrate Supported Metal Strip Antennas - Analysis and Experiment

3.1 Introduction and overview

Classical antenna analysis can be classified according to the basic assumptions that may be made in idealizing practical design problems. Thus, much of the analysis of metal structures proceeds on the assumption that currents exist on infinitely conducting surfaces in an infinite homogeneous non-conducting medium which is often free space. In most analyses, the current distribution may not be assumed, and must be determined by use of techniques such as the method of moments [64]. The assumptions with regard to the material media, however, still hold for many practical structures. Where the antenna is to be operated close to the boundary between two semi-infinite media, one medium is often free space and the other medium assumes properties of earth or some other material. The special case of a perfectly conducting ground plane at the interface

is usually treated by means of images of the antenna structure which are assumed to be created by the presence of currents flowing on the sheet. Modifications to this *image theory* may be used where the interface is actually the surface of the earth. Another classification arises when stratification of the material medium as an idealization is a closer representation of the practical antenna assembly. The strata are usually assumed to be infinite in extent. Because waveguide propagation may occur in the strata as well as radiation in the free space and material media above and below the strata, analysis is more complicated. Microstrip antennas of the type described in Section 2.3.1 for use in TILA arrays, where the strata arise from one or more layers of dielectric on a metal ground plane, are one example in this category. An even more complex class of analytical design arises when it is not possible to assume strata that are infinite in *any* direction. Antenna structures comprising finite size dielectric and conducting regions, such as the substrate supported metal strip antennas described in Section 1.2 fall into this last category.

Both integral-equation methods and differential-equation methods may be used for the analysis of antenna structures. Differential-equation methods, comprising finite-element and finite-difference techniques, have been applied to radiation and scattering by two-dimensional and three-dimensional structures through the use of hybrid methodologies such as the finite-element–boundary-integral method described in [65]. More commonly, integral-equation methods have been employed for composite finite-size three-dimensional structures. Surface and volume formulations have been implemented for a variety of structures, and solved using iterative techniques [66,67,68,69]. The problem of appropriately modelling homogeneous dielectric regions has been addressed by the use of rooftop functions [70,71] resulting, however, in a more complex formulation of the problem and a larger computational overhead. Nyquist methods for the solution of integral equations have also been proposed for application to composite problems [72]. Because the rectangular geometry of the substrate supported metal strip antennas considered in this thesis may be relatively simply described using an integral-equation approach for calculation of both the near-field and far-field, a volume formulation employing rectangular pulse basis function expansions, similar in principle

to that described in [66], is employed for the analysis. A numerical implementation is developed here which is able to avoid the need for the more complex rooftop function formulation of the problem for the antennas considered. Furthermore, the relatively simple solution adopted here will be expanded later to deal with more detailed structures that include feed lines with remarkably little increase in computational overhead.

The basic geometry of the substrate supported metal strip antenna is analysed in this chapter. Feed lines, which are omitted from the analysis at this stage, are introduced in Chapter 4. The aim of the work presented in this chapter is to develop the modelling of substrate supported metal strip antennas for substrates which are electrically thick, and to verify the results by comparison with experimental measurements. Various assumptions made in the modelling are addressed, and the problem is formulated for efficient numerical solution. Finally, the analysis of the basic geometry allows the fundamental effects associated with the dielectric substrate to be identified and studied. The results which are obtained form the basis for the design of practical antenna elements.

3.2 Formulation and numerical implementation

3.2.1 Antenna geometry

The antenna element illustrated in Figure 2.3b consists of a metal strip contiguous with the end of a dielectric substrate which forms a rectangular cross-section dielectric waveguide of the type described in Appendix A. The hybrid TE^{y}_{11} mode, the characteristics of which are outlined in Appendix A, is the lowest order mode which may propagate in the substrate, and has its principal electric field component aligned with the axis of the metal strip antenna. Above the low-frequency cut-off of this mode, propagation in the substrate is therefore anticipated. The TE^{y}_{11} mode will not propagate in the grounded substrate of the MMIC since the anti-symmetry required about

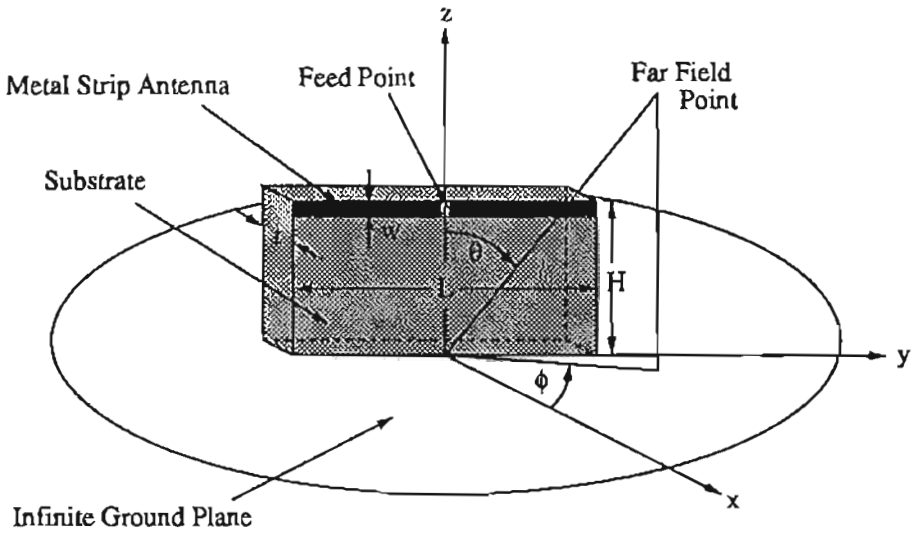

Figure 3.1: Idealized geometry used in the analysis.

the MMIC ground plane does not exist, and the principal electric field component is shorted by the MMIC ground plane. Below the cut-off frequency of the next higher order mode, the fields are therefore confined to the ungrounded part of the substrate. For frequencies of interest here, this condition is met. The MMIC substrate and the module housing together may also be regarded as forming a partially filled rectangular waveguide with the ungrounded substrate of the substrate supported metal strip antenna protruding from an aperture at the end of that waveguide. An investigation of the dominant mode of the partially filled waveguide for typical substrate thicknesses and aperture sizes shows that this too is cut-off at frequencies of interest [73]. For these reasons, and because the slot in the module housing through which the ungrounded substrate protrudes is physically and electrically small, as a simplified starting point for developing an analytical model the antenna is idealized to that shown in Figure 3.1, where a continuous ground plane is shown. The ground plane is considered to be infinite in extent, the metal strip is assumed to be excited by an ideal voltage source at the centre, and no feed structure is included.

The geometry shown in Figure 3.1 may be described as a metal strip antenna on a finite size dielectric slab. For a typical MMIC antenna, the electrical thickness of the

dielectric slab at millimetre wavelengths is large, and the correct modelling of the fields which are excited in the dielectric slab is important for accurate numerical results to be obtained.

3.2.2 Integral equation formulation

The electric-field integral-equations which relate to the geometry shown in Figure 3.1 are obtained from the boundary conditions associated with the tangential electric fields at the surface of the metal strip, and the conditions which determine the total electric field within the dielectric substrate. Denoting the incident electric field at location $\vec{r}$ as $\vec{E}^i(\vec{r})$, and the scattered electric field at location $\vec{r}$ as $\vec{E}^s(\vec{r})$, the electric-field integral equations are

$$\left[\vec{E}^i(\vec{r})\right]_{\tan} + \left[\vec{E}^s(\vec{r})\right]_{\tan} = 0 \quad \text{for } \vec{r} \in S_c \tag{3.1a}$$

$$\vec{E}^i(\vec{r}) + \vec{E}^s(\vec{r}) = \vec{E}^{\text{total}}(\vec{r}) \quad \text{for } \vec{r} \in V_d \tag{3.1b}$$

where S_c is the surface of the metal strip, V_d is the volume of the dielectric substrate, subscripts tan refer to electric field components tangential to S_c, and $\vec{E}^{\text{total}}(\vec{r})$ is the total electric field in V_d at location $\vec{r}$. Using the equivalence principle, the metal strip is replaced by its equivalent surface current $\vec{J}_c$ and the dielectric substrate by equivalent volume polarization currents $\vec{J}_d$, where all equivalent currents exist in free space [66]. The metal strip has a width which is narrow with respect to its length, and is also assumed in the analysis to be infinitesimally thin, such that the equivalent surface current $\vec{J}_c$ represents the total surface current on the metal strip. With these substitutions, the scattered electric field at location $\vec{r}$ may be written as

$$\vec{E}^s(\vec{r}) = \mathcal{L}_c\left\{\vec{J}_c\right\} + \mathcal{L}_d\left\{\vec{J}_d\right\}. \tag{3.2}$$

Expressions for the operators $\mathcal{L}_c$ and $\mathcal{L}_d$ are derived from vector and scalar potentials and are given below. From the relationship between the total electric field in the

dielectric and the volume polarization current,

$$\vec{E}^{\text{total}}(\vec{r}) = \frac{\vec{J}_d(\vec{r})}{j\omega\epsilon_0(\epsilon_r - 1)}, \tag{3.3}$$

where ω is the angular frequency, ϵ_0 the permittivity of free space and ϵ_r the relative permittivity of the dielectric slab. The dielectric is considered to be homogeneous, and for the moment lossless. Equation 3.1 therefore yields the coupled equations

$$-\left[\mathcal{L}_c\left\{\vec{J}_c\right\}\right]_{\tan} - \left[\mathcal{L}_d\left\{\vec{J}_d\right\}\right]_{\tan} = \left[\vec{E}^i(\vec{r})\right]_{\tan}, \quad \text{for } \vec{r} \in S_c, \tag{3.4a}$$

$$\frac{\vec{J}_d(\vec{r})}{j\omega\epsilon_0(\epsilon_r - 1)} - \mathcal{L}_c\left\{\vec{J}_c\right\} - \mathcal{L}_d\left\{\vec{J}_d\right\} = \vec{E}^i(\vec{r}), \quad \text{for } \vec{r} \in V_d. \tag{3.4b}$$

In the following analysis, primed co-ordinates refer to the position of sources and unprimed co-ordinates to the position of field components. The surface charge density on the metal strip, ρ_c, may be expressed in terms of the surface current as

$$\rho_c(\vec{r}\,') = -\frac{1}{j\omega}\vec{\nabla}\,' \cdot \vec{J}_c(\vec{r}\,') \tag{3.5}$$

and the operator $\mathcal{L}_c$ may be written as

$$\mathcal{L}_c\{\vec{J}_c\} = \frac{-j\omega\mu_0}{4\pi}\iint_{S_c}\vec{J}_c(\vec{r}\,')G(\vec{r},\vec{r}\,')ds' + \frac{\vec{\nabla}}{j\omega\epsilon_0 4\pi}\iint_{S_c}\vec{\nabla}\,' \cdot \vec{J}_c(\vec{r}\,')G(\vec{r},\vec{r}\,')ds' \tag{3.6}$$

where μ_0 is the permeability of free space. The free space Green's function $G(\vec{r},\vec{r}\,')$ is

$$G(\vec{r},\vec{r}\,') = \frac{\exp(-jk_0|\vec{r}-\vec{r}\,'|)}{|\vec{r}-\vec{r}\,'|}, \tag{3.7}$$

where $k_0 = \omega/c$ is the free space wave-number and c is the speed of light in free space. Considering now the dielectric slab; for a homogeneous dielectric region, $\vec{\nabla}\,' \cdot \vec{J}_d(\vec{r}\,') = 0$ within the dielectric, and charges only exist on the surface. The surface charge density on the dielectric, ρ_d, is given by

$$\rho_d(\vec{r}\,') = -\frac{1}{j\omega}\vec{\nabla}\,' \cdot \vec{J}_d(\vec{r}\,') = \frac{1}{j\omega}\hat{n} \cdot \vec{J}_d(\vec{r}\,') \quad \text{for } \vec{r}\,' \in S_d \tag{3.8}$$

where S_d denotes the surface of the dielectric slab and $\hat{n}$ is the outward pointing unit vector normal to the surface of the dielectric. The operator $\mathcal{L}_d$ may therefore be written as

$$\mathcal{L}_d\{\vec{J}_d\} = \frac{-j\omega\mu_0}{4\pi}\iiint_{V_d}\vec{J}_d(\vec{r}')G(\vec{r},\vec{r}')dV' - \frac{\vec{\nabla}}{j\omega\epsilon_0 4\pi}\iint_{S_d}\hat{n}\cdot\vec{J}_d(\vec{r}')G(\vec{r},\vec{r}')ds'. \quad (3.9)$$

It is necessary to solve equations 3.4 with the operator expressions given in equation 3.6 and equation 3.9 to determine the surface current distribution on the metal strip and the volume polarization current distribution in the dielectric. A method of moments solution is outlined in the next section.

3.2.3 Numerical implementation

Because of the symmetry of the antenna about the xz-plane in Figure 3.1 and the nature of the fields excited by a balanced feed, it is sufficient to analyse half the structure in one of the half spaces on either side of the xz-plane, regarded as an image plane. The centre-fed metal strip thus becomes a strip monopole fed at its base against an infinite, perfectly conducting image plane, and the current distribution on the monopole and in the remaining half of the dielectric are unaffected. The image plane and the existing ground plane are taken into account by introducing the appropriate image currents into the analysis. A source region and three image regions are identified in Figure 3.2. After determining the equivalent currents in the source region, the parameters of interest may be computed for the equivalent balanced geometry of the complete antenna. It is noted that the TE^y_{11} mode in rectangular cross-section dielectric waveguide, used to justify the idealization of the antenna geometry to that of Figure 3.1, also exhibits the required symmetry, however, no further assumptions are made regarding the field distribution in the dielectric slab.

The currents $\vec{J}_c$ and $\vec{J}_d$ are expanded using pulse basis functions and a point matching technique is used to obtain the solution. Although a pulse function approximation

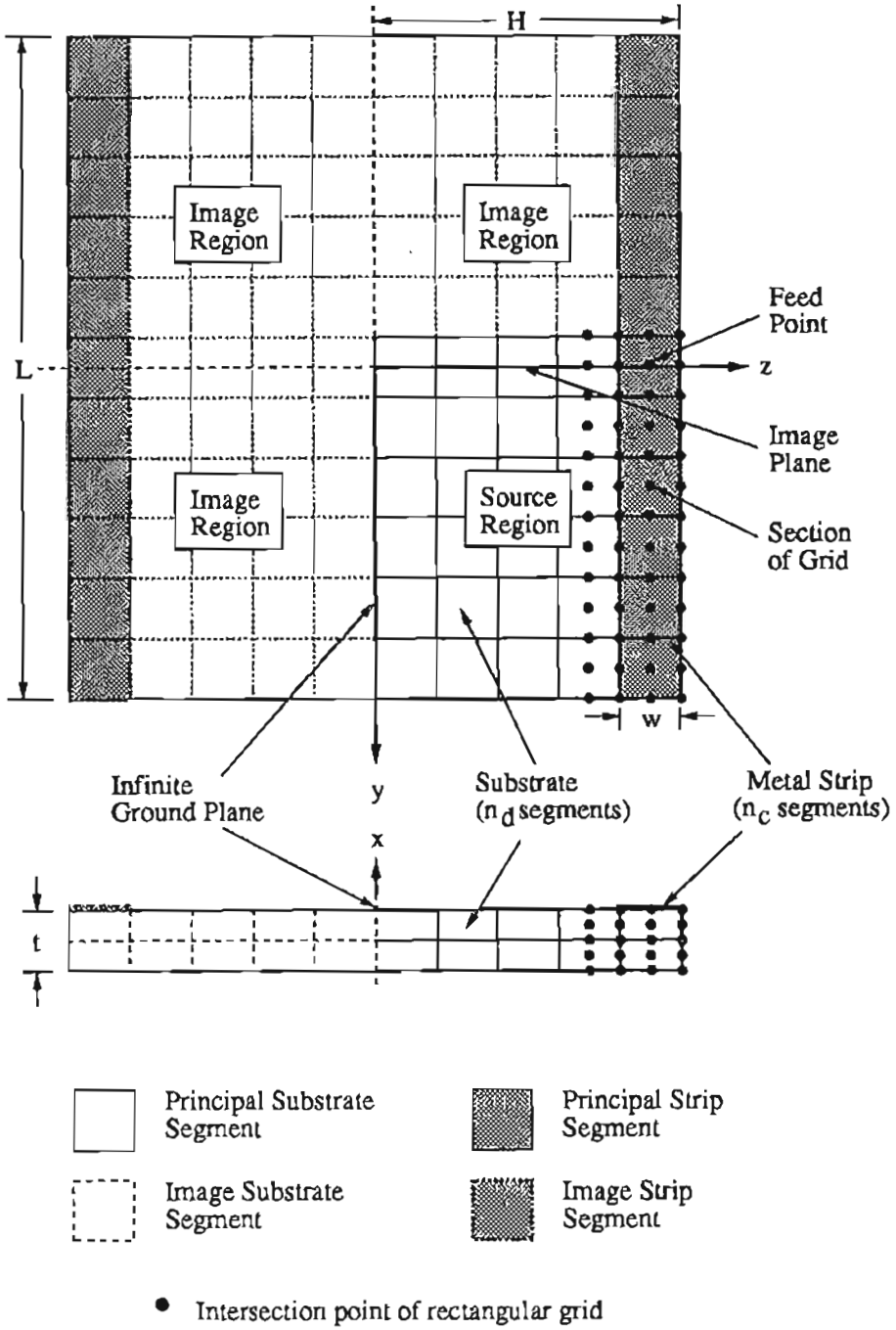

Figure 3.2: Image regions and segmentation of the metal strip and substrate.

is not strictly differentiable, where derivatives are required they may be obtained by using an offset pulse function expansion such as that used for the charge density on a wire antenna in [64] and outlined in Appendix C in the context of the modelling of wire junctions. In the source region of Figure 3.2 the strip is divided into n_c segments of equal surface area, and the dielectric slab into n_d segments of equal volume. The metal strip segments are made to align with the top surface of the dielectric segment on which they lie. Full segments about the image plane are derived from half-segments in the source region imaged about the xz-plane, and are considered to be part of the source region. It should be noted that for simplicity the boundary condition requiring that the y-directed current be zero at the end of the strip is neither negated nor strictly enforced. Comparing the results obtained from the segmentation shown in Figure 3.2 with results obtained by offsetting the metal strip segments one half-segment, and including a zero half-pulse at the end to enforce the boundary condition, has indicated that this effect is negligible. The z-directed currents on the metal strip, although included in the analysis, are expected to be small.

In the following expressions subscripts n refer to source points associated with equivalent currents and their images, and subscripts m to field points within the source region. The convention for primed and unprimed co-ordinates introduced in Section 3.2.2 is retained for consistency. A rectangular co-ordinate geometry is used such that

$$\vec{r} = \hat{x}x + \hat{y}y + \hat{z}z \tag{3.10}$$

where $\hat{x}$, $\hat{y}$ and $\hat{z}$ are unit vectors.

Using the pulse basis function expansion of the current distributions, the surface current $\vec{J}_c$ may be written as

$$\vec{J}_c(\vec{r}') = \sum_{n=1}^{n_c} \left[\hat{y}a_n + \hat{z}b_n\right] P_n(y', z') \tag{3.11}$$

where the pulse functions are

$$P_n(y',z') = \begin{cases} 1, & \text{if } y',z' \in n\text{th segment} \\ 0, & \text{otherwise} \end{cases} \tag{3.12}$$

Here a_n and b_n are the unknown constants to be determined for the surface current on the metal strip. The volume polarization current $\vec{J}_d$ may be written as

$$\vec{J}_d(\vec{r}') = \sum_{n=1}^{n_d} [\hat{x}c_n + \hat{y}d_n + \hat{z}e_n]\, Q_n(x',y',z') \tag{3.13}$$

where the pulse functions are

$$Q_n(x',y',z') = \begin{cases} 1, & \text{if } x',y',z' \in n\text{th segment} \\ 0, & \text{otherwise} \end{cases} \tag{3.14}$$

Here c_n, d_n and e_n are the unknown constants to be determined for the volume polarization currents in the dielectric slab.

Since delta-functions are used as testing functions in the point matching scheme, equation 3.4a is required to be satisfied at the centre of each metal strip segment in the source region, and equation 3.4b at the centre of each dielectric segment in the source region. The electric field at each point $\vec{r}_m$ due to sources a_n and b_n, omitting at this stage their images, may be found from

$$\begin{aligned} \mathcal{L}_c\{\vec{J}_c\} &= \frac{-j\omega\mu_0}{4\pi} \sum_{n=1}^{n_c} (\hat{y}a_n + \hat{z}b_n) \iint_{S_c} P_n(y',z') G(\vec{r}_m, \vec{r}_n')\, dy'\, dz' \\ &+ \frac{1}{j\omega\epsilon_0 4\pi} \left(\hat{x}\frac{\partial}{\partial x_m} + \hat{y}\frac{\partial}{\partial y_m} + \hat{z}\frac{\partial}{\partial z_m} \right) \cdot \\ &\quad \Big\{ \sum_{n=1}^{n_c} \iint_{S_c} \frac{\partial}{\partial y_n'} [a_n P_n(y',z') G(\vec{r}_m, \vec{r}_n')] dy'\, dz' \\ &\quad + \sum_{n=1}^{n_c} \iint_{S_c} \frac{\partial}{\partial z_n'} [b_n P_n(y',z') G(\vec{r}_m, \vec{r}_n')] dy'\, dz' \Big\}, \end{aligned} \tag{3.15}$$

and due to sources c_n, d_n and e_n, again omitting at this stage their images, from

$$\begin{aligned}
\mathcal{L}_d\{\vec{J}_d\} &= \frac{-j\omega\mu_0}{4\pi}\sum_{n=1}^{n_d}(\hat{x}c_n+\hat{y}d_n+\hat{z}e_n)\iiint_{V_d}Q_n(x',y',z')G(\vec{r}_m,\vec{r}_n')\,dx'\,dy'\,dz' \\
&- \frac{1}{j\omega\epsilon_0 4\pi}\left(\hat{x}\frac{\partial}{\partial x_m}+\hat{y}\frac{\partial}{\partial y_m}+\hat{z}\frac{\partial}{\partial z_m}\right)\cdot \\
&\Big\{\sum_{n\in S_{yz}}\alpha c_n\iint_{S_{yz}}Q_n(x',y',z')G(\vec{r}_m,\vec{r}_n')\,dy'\,dz' \\
&+\sum_{n\in S_{xz}}\beta d_n\iint_{S_{xz}}Q_n(x',y',z')G(\vec{r}_m,\vec{r}_n')\,dx'\,dz' \\
&+\sum_{n\in S_{xy}}\gamma e_n\iint_{S_{xy}}Q_n(x',y',z')G(\vec{r}_m,\vec{r}_n')\,dx'\,dy'\Big\},
\end{aligned} \tag{3.16}$$

where the sources are located at $\vec{r}_n'$. The surfaces of the dielectric segments are S_{yz}, S_{xz} and S_{xy}, and α, β and γ are found from their respective orientations as

$$\alpha=\begin{cases}1, & \text{if } \hat{n}=\hat{x}\\ -1, & \text{if } \hat{n}=-\hat{x}\end{cases}\qquad \beta=\begin{cases}1, & \text{if } \hat{n}=\hat{y}\\ -1, & \text{if } \hat{n}=-\hat{y}\end{cases}\qquad \gamma=\begin{cases}1, & \text{if } \hat{n}=\hat{z}\\ -1, & \text{if } \hat{n}=-\hat{z}\end{cases} \tag{3.17}$$

where $\hat{n}$ is again the outward pointing unit vector normal to the surfaces. For each equivalent current located in the source region there exist three associated image currents in the image regions. Equations 3.4a and 3.4b must therefore be evaluated four times at each field point and the results added. In equations 3.15 and 3.16 the field point derivatives are computed by finite differences.

A consequence of an interpretation of the rectangular pulse basis functions adopted in [66] is that surface charge is permitted, and generally occurs, on all surfaces of every dielectric segment. This has led in the past to criticism of the use of rectangular pulse basis functions to model homogeneous dielectric regions [74]. Any errors, however, are not necessarily introduced by the inherent use of pulse basis functions, as is demonstrated later by their successful adoption in the analysis described here. In reality, for a homogeneous dielectric, charges on surfaces internal to the dielectric slab are fictitious. In order to form a more appropriate representation, the polarization currents in adjacent dielectric segments are interpolated at their junction, effectively smoothing the pulse representation of the polarization current for the purpose of calculating the

surface charge. An averaged surface charge density function which is zero within the dielectric in accordance with physical reality is therefore produced. Consequently, the surface integrals in equation 3.16 need only be performed where S_{yz}, S_{xz} and S_{xy} are the outer surfaces of the dielectric slab. Interpolation is not appropriate at the outer surfaces where a discontinuity in polarization current occurs, and the relevant values of c_n, d_n and e_n at the segments adjacent to the outer surfaces are used in the calculation. By implementing equations 3.15 and 3.16 in the manner described above with equations 3.4a and 3.4b, a set of linear equations may be obtained from which the unknown constants may be found. The incident y-directed electric field is due to the voltage at the infinitesimal gap at the centre of the metal strip, which is modelled using a delta-gap generator [75] at the feed point. A sufficiently small number of segments are required for a converged solution to be obtained, so that the equations can be solved by standard matrix techniques[1].

Where a Green's function integral is required in equations 3.15 and 3.16, four cases exist: a volume integral throughout a dielectric segment and three possible surface integrals over the outer yz, xz and xy surfaces of a dielectric segment or the surface of a metal strip segment. In all cases the Green's function singularity arising when the source and field points coincide is integrable [77], and therefore numerical problems associated with the evaluation of the integrals are avoided[2]. The segmentation of the dielectric slab and metal strip is undertaken in such a way that after the segmentation is performed, a uniform three-dimensional grid extending over the entire structure can be introduced. In Figure 3.2 the points marked • indicate the intersection points of a section of this grid. The spacing between the intersection points of the grid is half the segment length in each co-ordinate direction, and the grid is aligned to the corners of the structure as shown. If the appropriate Green's function integral for each of the four cases defined above is evaluated at every intersection point of the grid for the relevant source segment closest to one corner of the structure, and the results stored in a look-up table, sufficient information is available to compute all the

[1]Double precision IMSL™ math library routines incorporating LU factorization of general complex matrices, together with iterative refinement, are employed [76].

[2]Double precision IMSL™ math library routines for multi-dimensional integration using iterated application of product Gauss formulas are used to compute all Green's function integrals [76].

Number of Integrals		
Volume Integrals	$(3n_d + 2n_c)n_t$	471,200
Dielectric Surface Integrals	$2(3n_d + 2n_c)n_s$	1,135,840
Strip Surface Integrals	$10(n_d + 2n_c) \cdot 2(2n_c - 1)$	83,600
TOTAL		1,379,040
Total Integrals in Grid Method	$4n_g$	24,320
Segmentation and definitions		
Source region strip segments	n_c	10
Source region dielectric segments	$n_d = n_x n_y n_z$	200
Total dielectric segments	$n_t = n_x(2n_y - 1)2n_z$	760
Total dielectric surface segments	$n_s = 2[(n_x+2n_z)(2n_y-1)+n_x 2n_z]$	916
Grid intersection points	$n_g = 8n_t$	6080

Table 3.1: Total number of integrations in algorithm compared with actual integrations performed using the grid method.

integrals and their derivatives required by equations 3.15 and 3.16. Redundancy in computation is thereby avoided. The significant reduction in the number of integrals to be evaluated is demonstrated in Table 3.1 for a segmentation where $n_c = 10$ and $n_d = 200$, corresponding to $n_x = 2$, $n_y = 10$ and $n_z = 10$ in the co-ordinate directions. This technique therefore allows a computationally efficient solution to be obtained.

The evaluation of the input impedance and radiation field of the antenna proceeds after the equivalent currents have been determined.

3.2.4 Modelling of antenna losses

In the foregoing development, the dielectric was assumed to be lossless. Implicit in the formulation is also the assumption that the metal strip is a perfect conductor. For practical design purposes it is useful to know the effect of any losses on the antenna performance and also the extent to which the ideal lossless model provides accurate results.

Dielectric losses can be readily included in the formulation by replacing the real permittivity, ϵ_r, with the complex permittivity, $\dot{\epsilon}_r$, where

$$\dot{\epsilon}_r = \epsilon_r(1 - j\tan\delta), \tag{3.18}$$

and

$$\tan\delta = \frac{\sigma_d}{\omega\epsilon_r} \tag{3.19}$$

is the *loss tangent* dependent on the conductivity, σ_d, of the imperfect dielectric material. Typical values of loss tangent for dielectric materials encountered in this thesis are small[3]. The dielectric losses may be represented as a feed point resistance, $R_{loss,d}$, which is obtained by subtracting the feed point resistance computed for the ideal case from that obtained for the lossy case. The extent to which the dielectric losses will affect the antenna performance depends on the magnitude of the fields excited in the dielectric substrate.

It is not a straightforward exercise to include conduction losses in the formulation described above, and a conventional perturbation method is applied using the surface currents computed for a metal strip having infinite conductivity. The power dissipated due to conduction losses, P_d, may be expressed as

$$P_d = \frac{R_s}{2}\int\int_{S_c'} |\vec{J}_y|^2\, ds, \tag{3.20}$$

where S_c' comprises both the top and bottom surfaces of the metal strip and $\vec{J}_y$ is the axially directed surface current density. The surface resistance, R_s, is defined as

$$R_s = \sqrt{\frac{\omega\mu_0}{2\sigma_c}} \tag{3.21}$$

where σ_c is the finite conductivity of the metal strip. Because the current density computed from the numerical analysis is the total current density, the distribution on the top and bottom surfaces needs to be ascertained. Denoting that part of the current

[3]Available data are $\tan\delta$=0.0023 for RT-Duroid 6010, and $\tan\delta$=0.002 for semi-insulating GaAs, both at 10GHz.

density that exist on the top surface as $\vec{J}_y^t$ and that part of the current density that exists on the bottom surface as $\vec{J}_y^b$, P_d may be written as

$$P_d = \frac{R_s}{2} \iint_{S_c} \left(|\vec{J}_y^t|^2 + |\vec{J}_y^b|^2 \right) ds \tag{3.22}$$

where S_c is the top or bottom surface of the metal strip as defined previously in the numerical analysis. Because the metal strip is narrow, the normal electric field is assumed to be continuous at the position of the metal strip, and the relevant current densities are approximately proportioned according to the resulting electric flux density normal to the metal strip surface such that

$$|\vec{J}_y^t|^2 \approx \frac{1}{(\epsilon_r + 1)^2} |\vec{J}_y|^2 \tag{3.23a}$$

$$|\vec{J}_y^b|^2 \approx \frac{\epsilon_r^2}{(\epsilon_r + 1)^2} |\vec{J}_y|^2. \tag{3.23b}$$

From the results of the numerical implementation in Section 3.2.3, the total power dissipated due to conduction losses on the metal strip may therefore be calculated from

$$P_d \approx \frac{R_s}{2} \frac{\epsilon_r^2 + 1}{(\epsilon_r + 1)^2} \left\{ |a_1|^2 \Delta S_1 + \sum_{n=2}^{n_c} 2|a_n|^2 \Delta S_n \right\}, \tag{3.24}$$

where ΔS_n is the nth strip segment surface area. The losses may be represented by a feed point resistance, $R_{loss,c}$, which is computed from the feed point current, I, as

$$R_{loss,c} = \frac{P_d}{|I|^2}. \tag{3.25}$$

The total input resistance of the lossy antenna may usefully be expressed as

$$R_{in} = R_a + R_{loss,d} + R_{loss,c} \tag{3.26}$$

where R_a is the lossless antenna radiation resistance. Provided that the losses are not large, the loss resistances $R_{loss,d}$ and $R_{loss,c}$ may be determined by separately applying the analyses for the two loss phenomena described above.

The loss computations described in this section are useful for determining the gain of a practical antenna. Given an on-axis antenna directivity, D, the on-axis gain, G, may be calculated from

$$G = \eta_r D \tag{3.27}$$

where the radiation efficiency,

$$\eta_r = \frac{R_a}{R_{in}}. \tag{3.28}$$

A method for measuring the antenna gain is described in Section 3.3.3.

3.3 Experimental verification

3.3.1 Impedance measurement

An attractive means of making impedance measurements is made possible by the symmetry of the structure described in Section 3.2.3. The image plane identified in the xz-plane of Figure 3.1 is physically replaced by a conducting metal ground plane orthogonal to the ground plane already forming a part of the structure. A monopole antenna of length $L/2$, which is contiguous with the end of the dielectric substrate, and which may be fed by a coaxial transmission line from behind the image plane, is thereby obtained. This configuration is illustrated in Figure 3.3. A Hewlett-Packard 8510B network analyser is used to perform the impedance measurements, which for the antennas constructed were taken in the frequency range approximately 2GHz to 8GHz. The ground planes are made large and the edges covered with microwave absorbing material so that the current reflection effects due to their truncation are minimal.

The reference plane for the measurement is established at the base of the monopole by introducing an electrical delay

$$t_d = \frac{2d\sqrt{\epsilon_{rc}}}{c}, \tag{3.29}$$

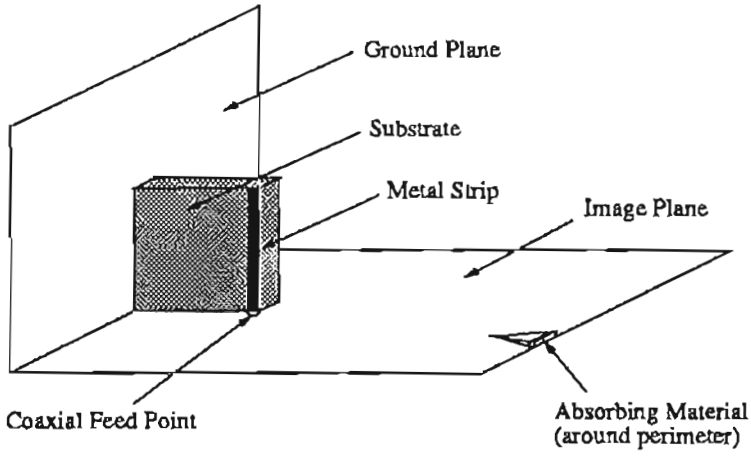

Figure 3.3: Experimental configuration for input impedance measurement. Ground plane length to tips of absorbing material = 400mm.

where ϵ_{rc} is the relative permittivity of the dielectric in the SMA coaxial connector used to feed the monopole, c is the speed of light in free space and d is the measured offset length of the calibration reference plane at the face of the SMA connector from the base of the monopole[4]. Apart from the correction for the electrical length to the reference plane at the coaxial feed port, no empirical adjustments are applied to the measured results. The measured impedance at the base of the monopole is doubled to obtain the required antenna impedance for the equivalent balanced geometry of the complete structure. All impedance results presented in this thesis relate to the complete structure without the image plane.

3.3.2 Radiation pattern measurement

Although a transmission line is required to excite a practical antenna, the analysis described above has been performed initially with no feed structure included in order to identify the influence of the substrate geometry alone on the radiation characteris-

[4]For the measurement assembly employed, $d = 9.18$mm, which for a teflon filled coaxial connector ($\epsilon_{rc} = 2.1$) gives $t_d = 88$ps.

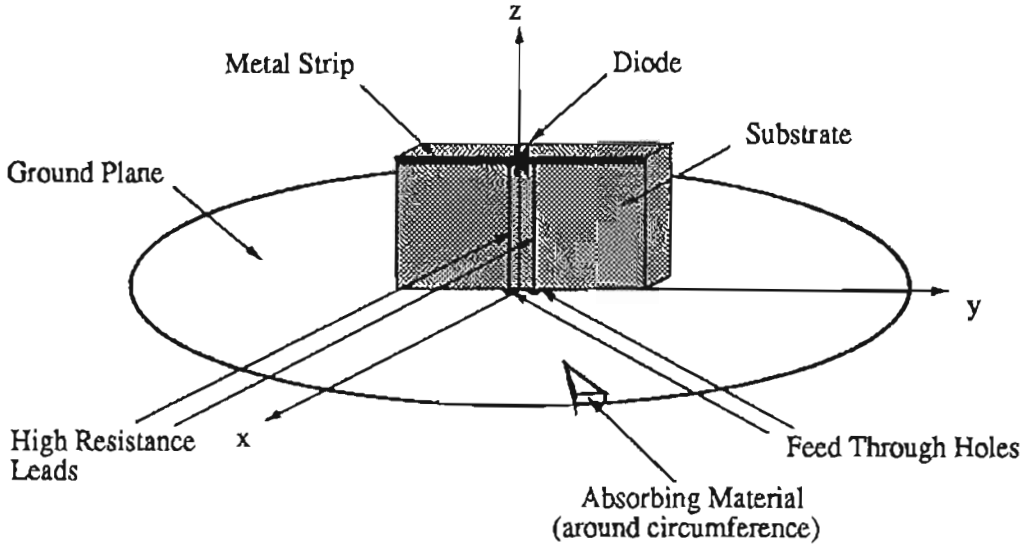

Figure 3.4: Experimental configuration for radiation pattern measurement. Ground plane diameter to tips of absorbing material = 1m.

tics. In some cases, radiation from the feed structure can have a considerable effect on the overall radiation pattern [78], and a measurement method which is not susceptible to the influence of feed radiation is needed to accurately represent the excitation conditions assumed in the analysis. It is noted that the image plane described in Section 3.3.1 for the impedance measurements cannot be used in the measurement of the radiation pattern since the truncation necessary in practice produces severe diffraction effects in the direction of the radiation maximum.

Figure 3.4 illustrates schematically the assembly used to measure the radiation patterns, where a method of designing antennas with integrated detectors [79] has been adapted to permit operation effectively without a conventional feed line and without an image plane, but of course retaining the existing ground plane of the structure. A zero-bias Schottky diode detector is connected across a small gap at the centre of the metal strip, and high resistance leads (10KΩ/cm) are used to extract the rectified voltage. The high resistance leads pass through small holes in a thick metal ground plane. The perturbation of these leads on the microwave field around the antenna will

be small [80,81]. Details of the measurement technique are given in Appendix B, where the efficacy of the method is verified for a metal strip dipole above a ground plane but without a dielectric substrate. Although it is found that the dynamic range of the measurement is limited to less than 30dB due to the mismatch between the diode and the antenna impedance, the radiation pattern is not affected. However, because of the limited dynamic range, it is not possible to measure low cross-polarization levels using this technique. Direct verification of the cross-polarization performance is reserved until Chapter 4, where the incorporation of a practical transmission line permits the use of conventional radiation pattern measurement techniques with a corresponding improvement in measurement dynamic range.

The antenna under test acts a receiving antenna and is mounted on a large circular ground plane in a microwave anechoic chamber. Measurements are conducted on antennas having dimensions scaled such that they operate at frequencies between 3GHz and 5GHz. Absorbing material is placed around the perimeter of the ground plane to reduce diffraction from the edge. This inhibits measurements at angles greater than about 80° off the z-axis, but extends the angular range over which measurements can be usefully made with a finite size ground plane such that the accuracy of the measurement is improved for angles closer to the axis of the antenna which are of greater interest.

3.3.3 Gain measurement

A measurement of antenna gain may be made by extending the image plane employed in the impedance measurement outlined in Section 3.3.1. As illustrated in Figure 3.5, a receiving monopole is positioned at a distance of 2m from the (imaged) substrate supported metal strip antenna. The feed ports of the (imaged) substrate supported metal strip antenna and the receiving monopole form a two-port network, and are denoted port 1 and port 2 respectively in Figure 3.5.

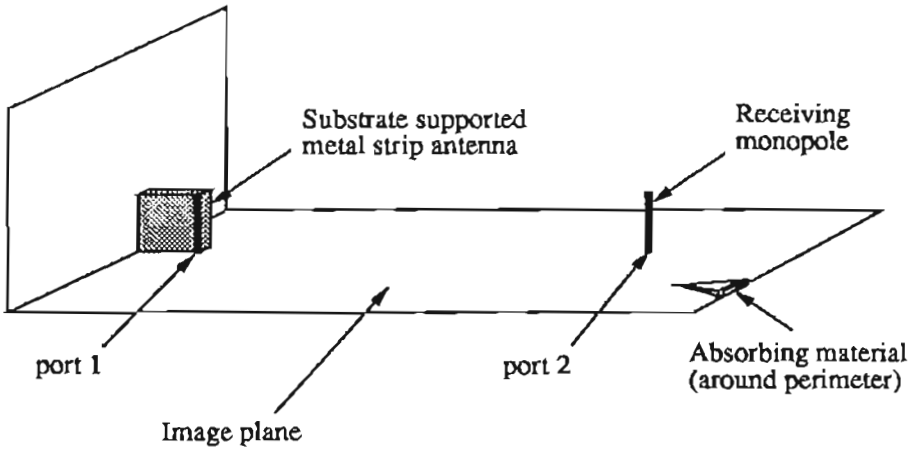

Figure 3.5: Experimental configuration for on-axis gain measurement. The separation between the substrate supported metal strip antenna and the receiving monopole is 2m.

A substitution method is used to measure the gain, for which two configurations of the antenna at port 1 are required. In the first configuration, the substrate is removed, and the antenna at port 1 becomes a monopole in front of a ground plane. This configuration is used as a reference antenna. In the second configuration, no alteration is made to the metal strip length, the substrate is restored, and the antenna at port 1 becomes the (imaged) substrate supported metal strip antenna for which the gain is to be determined. The gain of the (imaged) substrate supported metal strip antenna at a given frequency, relative to that of the reference antenna operating at the same frequency, may be determined from the two-port scattering parameters associated with port 1 and port 2 as

$$\Delta G = \frac{|S_{21}|^2}{|S_{21}|^2_{\text{ref}}} \left(\frac{1 - |S_{11}|^2_{\text{ref}}}{1 - |S_{11}|^2} \right), \tag{3.30}$$

where the subscript ref refers to the reference antenna. This substitution method inherently removes the effect of any losses due to radiation from, or imperfections in, the coaxial feed port, provided that these losses can be assumed to be the same for both configurations. In addition, losses due to conduction currents on the metal plate forming the image plane are calculated to be negligible, and the characteristics of the imaged antenna closely replicate those of the complete structure. It should be noted, however,

that for gain measurements at the resonant frequency of the substrate supported metal strip antenna, where the half-wave resonance may be substantially different from that of the reference antenna, the measurement is rather sensitive. Accurate scattering parameter measurements are therefore critical.

The relative gain, ΔG, determined from equation 3.30, is the same for the case of antennas where the image plane is not present. From the well known on-axis gain of a dipole in front of a ground plane, denoted G_{ref}, the on-axis gain of the substrate supported metal strip antenna may be calculated from

$$G = G_{\text{ref}} + \Delta G, \tag{3.31}$$

where both the measurement of ΔG and the calculation of G_{ref} are for the same frequency as the half-wave resonance of the substrate supported metal strip antenna under test. From the numerical analysis, the theoretical directivity of the substrate supported metal strip antenna may be computed, and the radiation efficiency can be calculated using equation 3.27.

3.4 Numerical and experimental results

In order to compare experimental and theoretical results and thereby test the analytical model, the substrate material of the antennas considered in this section is chosen to be RT Duroid$^{\text{TM}}$ 6010, having a relative permittivity $\epsilon_r = 10.2$. For the measurements, antennas with a metal strip length L=25.4mm were used, resulting in half-wave resonant frequencies in the range 3GHz to 4GHz. The other substrate dimensions were chosen to simulate typical MMIC antennas operating at millimetre wavelengths. The first part of Table 3.2 gives the electrical thickness, at millimetre wavelengths, of various GaAs substrates ranging in thickness from $t = 100\mu$m to 200μm. In the second part of Table 3.2 the substrate electrical thickness of some of the antennas considered in this section are shown for comparison. It is clear that a good range of the substrate

GaAs MMIC antenna			
Frequency	electrical thickness $\frac{t\sqrt{\epsilon_r}}{\lambda_0}$ (in electrical degrees)		
	100μm	150μm	200μm
40GHz	17°	26°	34°
60GHz	26°	39°	52°
90GHz	38°	58°	77°

RT Duroid 6010 antenna (at resonance)	
Physical thickness	electrical thickness $\frac{t\sqrt{\epsilon_r}}{\lambda_0}$ (in electrical degrees)
$t/L = 0.075$	25°
$t/L = 0.150$	50°

Table 3.2: Substrate electrical thicknesses for millimetre-wave GaAs MMIC antennas compared with substrate electrical thicknesses of antennas analysed and measured in this thesis.

electrical thicknesses likely to be encountered at millimetre wavelengths is covered by the antennas considered here. Because the actual substrate permittivity used for the antennas considered here is not significantly different from that of GaAs, the conclusions drawn with regard to the performance of the antennas studied in this section are readily applicable to MMIC antennas.

Two antenna geometries are considered in this section, and are denoted **Antenna A** and **Antenna B** in the discussion that follows. With reference to Figure 3.1 and the second part of Table 3.2, the normalized dimensions of each antenna are

Antenna A $H = 0.5L$, $t = 0.075L$ and $w = 0.05L$.

Antenna B $H = 0.5L$, $t = 0.150L$ and $w = 0.05L$.

Both antennas are segmented for the purpose of analysis with $n_c = 10$ and $n_d = 200$ unless otherwise stated. A total of 620 variables are therefore employed, and the solution takes approximately 30 seconds of CPU time per frequency on a Fujitsu

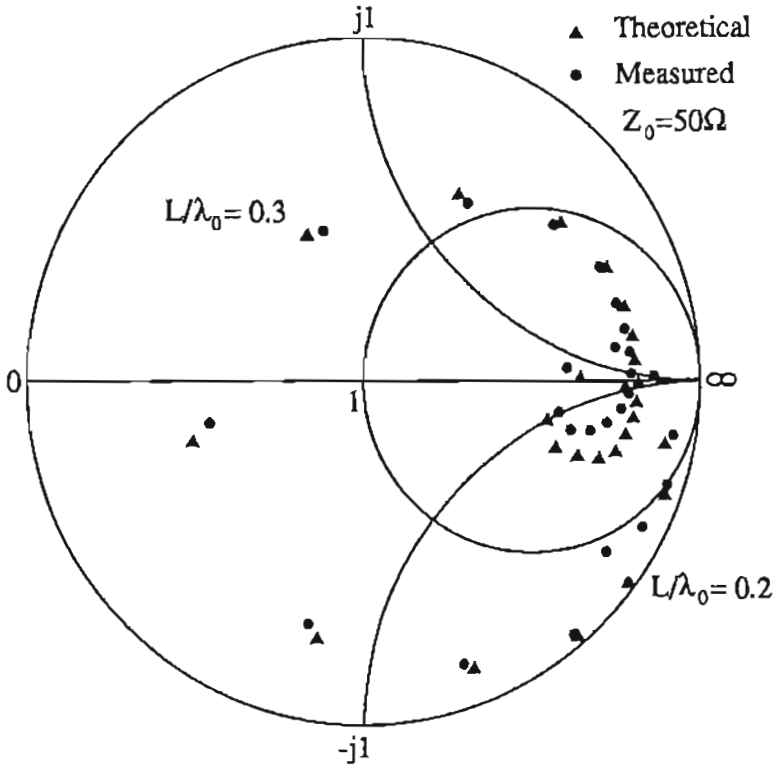

Figure 3.6: Normalized input impedance for **Antenna A**, having $t = 0.075L$ and $\epsilon_r = 10.2$. $L/\lambda_0 = 0.2$ to 0.7 in steps of 0.02.

VP2200 vector-supercomputer[5].

3.4.1 Input impedance

Theoretical and measured values of input impedance for **Antenna A** are given in Figure 3.6 and show excellent agreement. The half-wave resonance of the metal strip on the substrate occurs at $L/\lambda_0 = 0.285$ as compared with $L/\lambda_0 = 0.44$ for the case where the substrate is removed, where λ_0 in each case is the free-space wavelength. As

[5]The Fujitsu VP2200 vector-supercomputer has a scalar clock speed of 6.4ns and a vector clock speed of 3.2ns. A peak speed of 1.25GFlops is available. In the configuration used, 130MBytes of memory was available with an additional 256MBytes of swap space.

L/λ_0	Input impedance (ohms)		
	$n_d = 72, w = 0.0833L$	$n_d = 128, w = 0.0625L$	$n_d = 200, w = 0.0500L$
0.280	$13.90 - j9.88$	$14.43 - j7.80$	$14.72 - j8.35$
0.285	$15.50 - j2.14$	$16.13 - j0.48$	$16.47 - j0.37$
0.290	$17.29 + j5.74$	$18.03 + j8.93$	$18.43 + j9.26$
0.295	$19.29 + j13.78$	$20.18 + j17.58$	$20.65 + j18.36$

Table 3.3: Computed input impedance of **Antenna A** around half-wave resonance for different segment sizes (substrate $t = 0.075L, \epsilon_r = 10.2$).

expected, the physical length at which resonance occurs is significantly shortened due to the presence of the dielectric. The computed radiation resistance at resonance is found to be 16.8 ohms. A second resonant loop in the impedance characteristics clearly illustrates the effect of a dielectric resonance. Resonance of fields in the dielectric is discussed in Section 3.4.5. The effect on the analysis of increasing the segmentation size in the y- and z-directions by reducing the number of segments in the dielectric is shown in Table 3.3. The number of segments in the x-direction is maintained at $n_x = 2$, since at least two segments in this direction must be present to allow for anti-symmetrical field components in the ungrounded dielectric substrate. As the size of segments is increased in the z-direction, so too the width of the metal strip increases. From the computed input impedance shown in Table 3.3 it is found first that the results are well converged, and second that the result is relatively insensitive to the strip width. This insensitivity to strip width has also been confirmed experimentally.

Theoretical and measured values of input impedance for **Antenna B** are shown in Figure 3.7, where the agreement is again seen to be excellent. For this thicker substrate, with the same metal strip length, the half-wave resonance is computed to be at a slightly lower frequency, where $L/\lambda_0 = 0.270$. The computed resonant resistance was found to be 16.5 ohms, similar to the previous case. Clearly apparent, however, is the increasingly prominent second resonance attributed to a dielectric resonance. This effect will be discussed in Section 3.4.5.

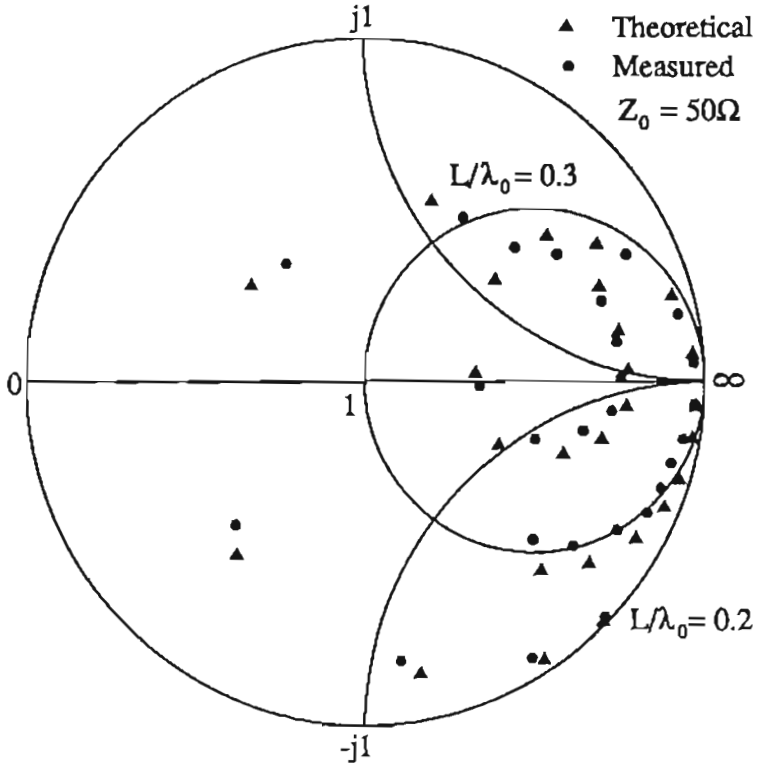

Figure 3.7: Normalized input impedance for **Antenna B**, having $t = 0.150L$ and $\epsilon_r = 10.2$. $L/\lambda_0 = 0.2$ to 0.7 in steps of 0.02.

3.4.2 Radiation pattern

The principal plane radiation patterns at the half-wave resonance of **Antenna A** are shown in Figure 3.8. The measured results for the co-polarized radiation in the yz- and xz-planes agree well with the analytical results, although the effect of diffraction due to the imperfect ground plane used in the measurement is noticeable for $\theta > 60°$ in the yz-plane. The angular spacing of the nulls in the diffraction pattern is related to the size of a 640mm square metal panel used to mount the antenna at the centre of the circular ground plane.

The influence of the dielectric substrate on the radiation pattern is most obvious in the yz-plane, which is the plane of the substrate as illustrated in Figure 3.1. At large

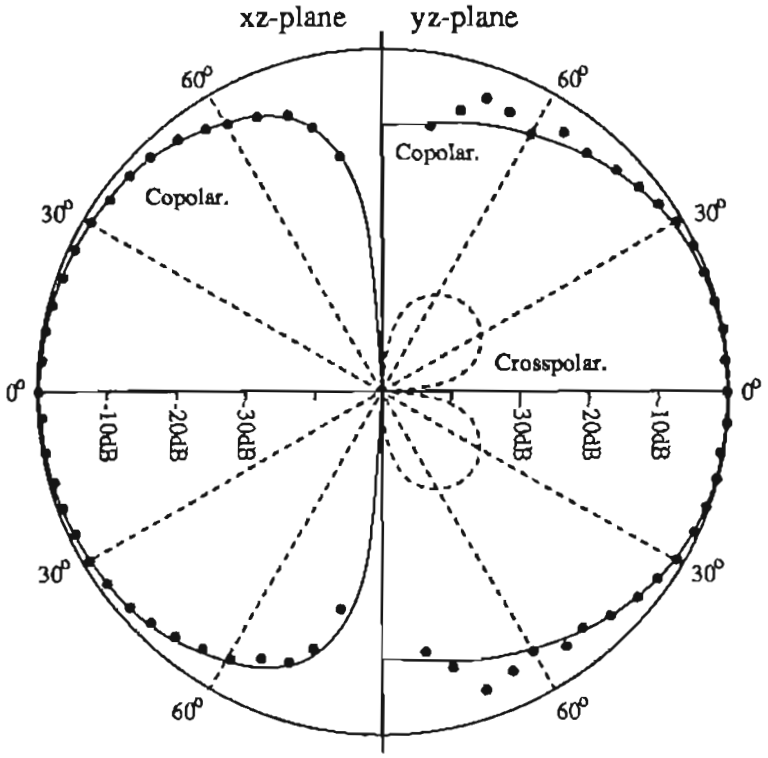

Figure 3.8: Principal plane radiation patterns at $L/\lambda_0 = 0.285$ for **Antenna A**, having $t = 0.075L$ and $\epsilon_r = 10.2$. Solid line: co-polarized, Dotted line: cross-polarized, Points: measured.

angles from the z-axis (i.e., for $\theta > 75°$) a substantial level of co-polarized radiation exists due to the presence of z-directed polarization currents in the substrate. The consequent broadening of the radiation pattern in the yz-plane is useful where arrays having a wide scan-range are to be designed, however, the effect of the radiation from the polarization currents in the dielectric on the mutual coupling between the elements needs also to be considered. The increased radiation at large angles from the z-axis is also the reason why the measured diffraction effects are prominent in the yz-plane. In addition to the increased radiation at large angles off the z-axis, significant cross-polarized radiation exists in the yz-plane, and is due to x-directed polarization currents in the substrate. No cross-polarization is predicted in the xz-plane normal to the plane of the substrate due to the balanced geometry and excitation. The effect of x-directed and z-directed polarization currents in the dielectric on the radiation characteristics in

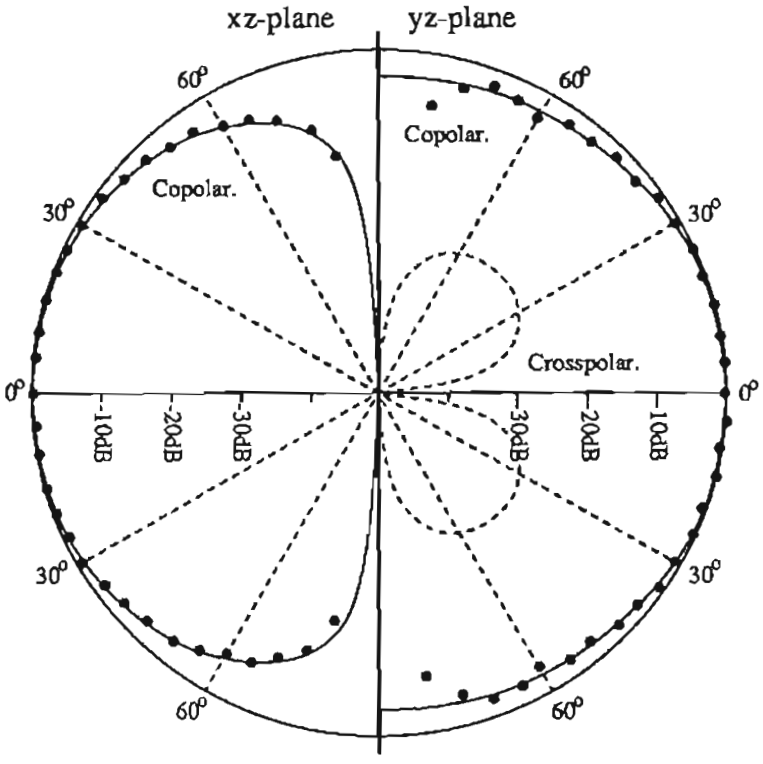

Figure 3.9: Principal plane radiation patterns at $L/\lambda_0 = 0.270$ for **Antenna B**, having $t = 0.150L$ and $\epsilon_r = 10.2$. Solid line: co-polarized, Dotted line: cross-polarized, Points: measured.

a diagonal plane at 45° to the principal planes is addressed later in Chapter 4. The marked effect of the polarization currents which are induced in the substrate on the far-field radiation pattern can be attributed to the fact that the substrate has significant electrical length, width and thickness, and is closely coupled to the near-field of the metal strip.

For **Antenna B**, the effect of the substrate on the radiation pattern is more pronounced. In Figure 3.9, both the increased cross-polarization and the increased radiation at large angles off the z-axis in the yz-plane are apparent. A slight asymmetry is becoming evident in the xz-plane radiation pattern for this thicker substrate, and is due to the fact that the substrate is present only on one side of the metal strip.

Clearly, for electrically thick substrates, the control of radiation from field components induced in the dielectric substrate is an important design issue, and methods of controlling substrate induced radiation will be addressed in Chapter 4.

3.4.3 Gain and efficiency

At the half-wave resonant frequency corresponding to $L/\lambda_0 = 0.285$, the on-axis directivity of **Antenna A** is computed to be 7.5dBi, as compared with 7.9dBi for a resonant half-wave metal strip dipole antenna having the same geometry, but with the substrate removed. The reduction of the directivity when compared to the metal strip without any substrate present is attributed to the broader co-polarized radiation pattern and increased cross-polarized radiation. In order to compute the gain of the antenna, the radiation efficiency is calculated from equation 3.28. The total input resistance at resonance is determined by adding the loss resistances $R_{loss,c}$ and $R_{loss,d}$ to the radiation resistance computed in Section 3.4.1. For an antenna resonant at 3.5GHz, $R_{loss,c} \approx .15$ ohms and $R_{loss,d} \approx .35$ ohms, resulting in a radiation efficiency $\eta_r \approx 0.97$. Application of the gain measurement described in Section 3.3.3 yields a measured radiation efficiency of 95%, in reasonably close agreement with the computed value. It is noted, however, the total measured input resistance is approximately 1.5 ohms greater than that predicted by including the calculated losses in the theoretical prediction, even though the measured and computed radiation efficiencies agree well. The difference in input impedance is attributed to feed port losses due to imperfections in the construction and materials used in the coaxial connection, and radiation from the discontinuity in the coaxial line at the base of the imaged metal strip. At millimetre wavelengths, radiation efficiencies in excess of 85% are predicted to be achievable, making these antennas attractive for application at high frequencies, and probably superior in this respect to microstrip patch type antenna elements.

For **Antenna B**, an on-axis directivity of 6.8dBi is computed. The further reduction in directivity is due to the increasing off-axis radiation and increasing cross-

polarized radiation, both due to polarization currents in the substrate. A slightly lower radiation efficiency is computed, primarily because the increased polarization currents in the substrate result in increased dielectric losses.

3.4.4 Substrate height variation

Although the substrate of a MMIC antenna is constrained to have a relatively high permittivity, variations in antenna dimensions may be useful to control antenna characteristics. Different thickness substrates have been considered in the examples above. Variations in substrate height and length for a fixed metal strip length and position above the ground plane are possible, but are found to achieve little in the way of performance enhancement. The consequent increase in substrate area usage is therefore not warranted. The effect of small overhangs in substrate height and length, such as would occur when the chip on which the MMIC antenna is fabricated is diced from the wafer after production, are described in Appendix D. For typical overhangs, a small shift in the resonant frequency of the antenna is obtained.

The remaining parameter that can be varied in the antenna geometry is the height of the metal strip above the ground plane, and the corresponding height of the substrate supporting it. Because the resonant frequency of a substrate supported metal strip antenna is found to be lower than in the case where the substrate is not present, the dimensions of **Antenna A** and **Antenna B** studied previously are such that the height of the metal strip above the ground plane is somewhat smaller that a quarter wavelength. In Table 3.4, the effect of increasing the metal strip and substrate height is illustrated for the case of a substrate thickness $t = 0.075L$. While it is clear that the radiation resistance at the half-wave resonant frequency increases with height, the decreasing on-axis gain points to the fact that the magnitudes of the polarization currents in the substrate also increase. Moreover, because the antenna impedance is required to be matched to typical transmission line characteristic impedances which may be relatively large, the small increase in radiation resistance that is obtained at

Height H	R_a (ohms)	G_0 (dBi)
$0.5000L$	16.8	7.52
$0.5625L$	19.8	7.48
$0.6250L$	23.1	7.39
$0.6875L$	26.3	7.27
$0.7500L$	29.1	7.12

Table 3.4: Variation of radiation resistance, R_a, and on-axis gain, G_0, at resonance with metal strip (and substrate) height H above ground plane. ($t = 0.075L$, $\epsilon_r = 10.2$).

the expense of a larger substrate area is not considered to be useful in practice. For this reason, the original height $H = 0.5L$ is retained in the remainder of this thesis.

3.4.5 Field distributions in the substrate

The effect of the fields which are induced in the dielectric substrate on the radiation and impedance characteristics of the antenna are clearly evident in the above results. An examination of the nature of the fields in the substrate is therefore important if they are to be exploited in engineering improvements to antenna characteristics. **Antenna A** has been found to have a half-wave resonance at $L/\lambda_0 = 0.285$. Considering the TE^y_{11} mode for rectangular dielectric waveguide, as set out in Appendix A, it is found that at $L/\lambda_0 = 0.285$ the TE^y_{11} mode is below cut-off. The field distribution in the dielectric at $L/\lambda_0 = 0.285$ is shown in Figure 3.10 by way of the computed magnitude of the components of the polarization current. An examination of the polarization current components shows that the mode structure associated with the TE^y_{11} mode is present, together with a strong excitation close to where the metal strip lies. The shape of the field distribution is, however, governed principally by the excitation since the TE^y_{11} mode is cut-off and is attenuated along the guide. The second resonance in the impedance characteristics of **Antenna A** occurs at $L/\lambda_0 = 0.620$. The magnitude of the field distribution at $L/\lambda_0 = 0.620$ is shown in Figure 3.11. In this

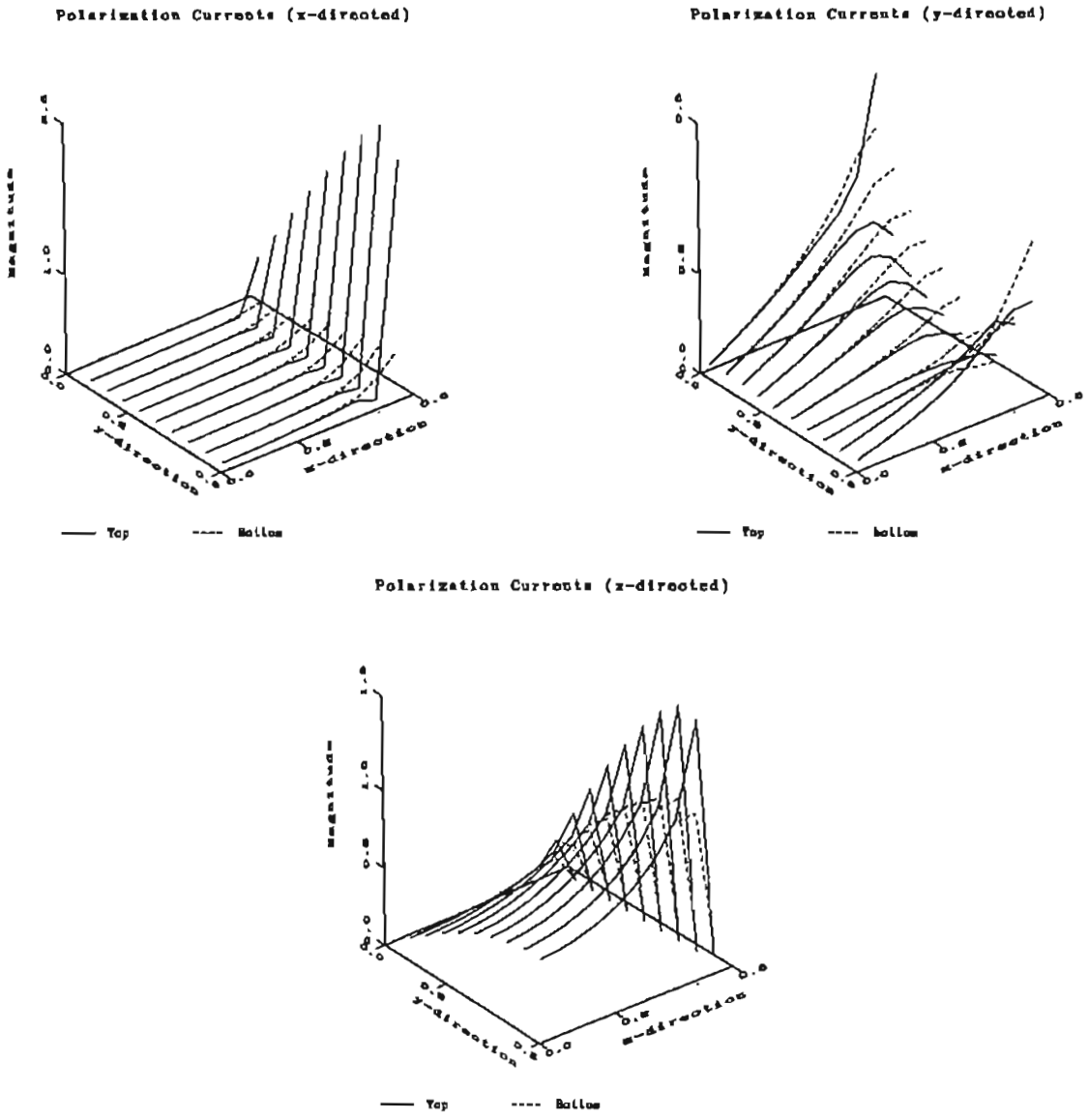

Figure 3.10: Volume polarization currents in substrate at $L/\lambda_0 = 0.285$ for **Antenna A**, hwaving $t = 0.075L$ and $\epsilon_r = 10.2$, and segmented with $n_x = 2$, $n_y = 10$ and $n_z = 10$. Note that only the quadrant corresponding to the source region is illustrated. The currents designated as "top" refer to the layer of dielectric segments closest in the x-direction to the metal strip, and "bottom" refers to the layer of dielectric segments furthest in the x-direction from the metal strip.

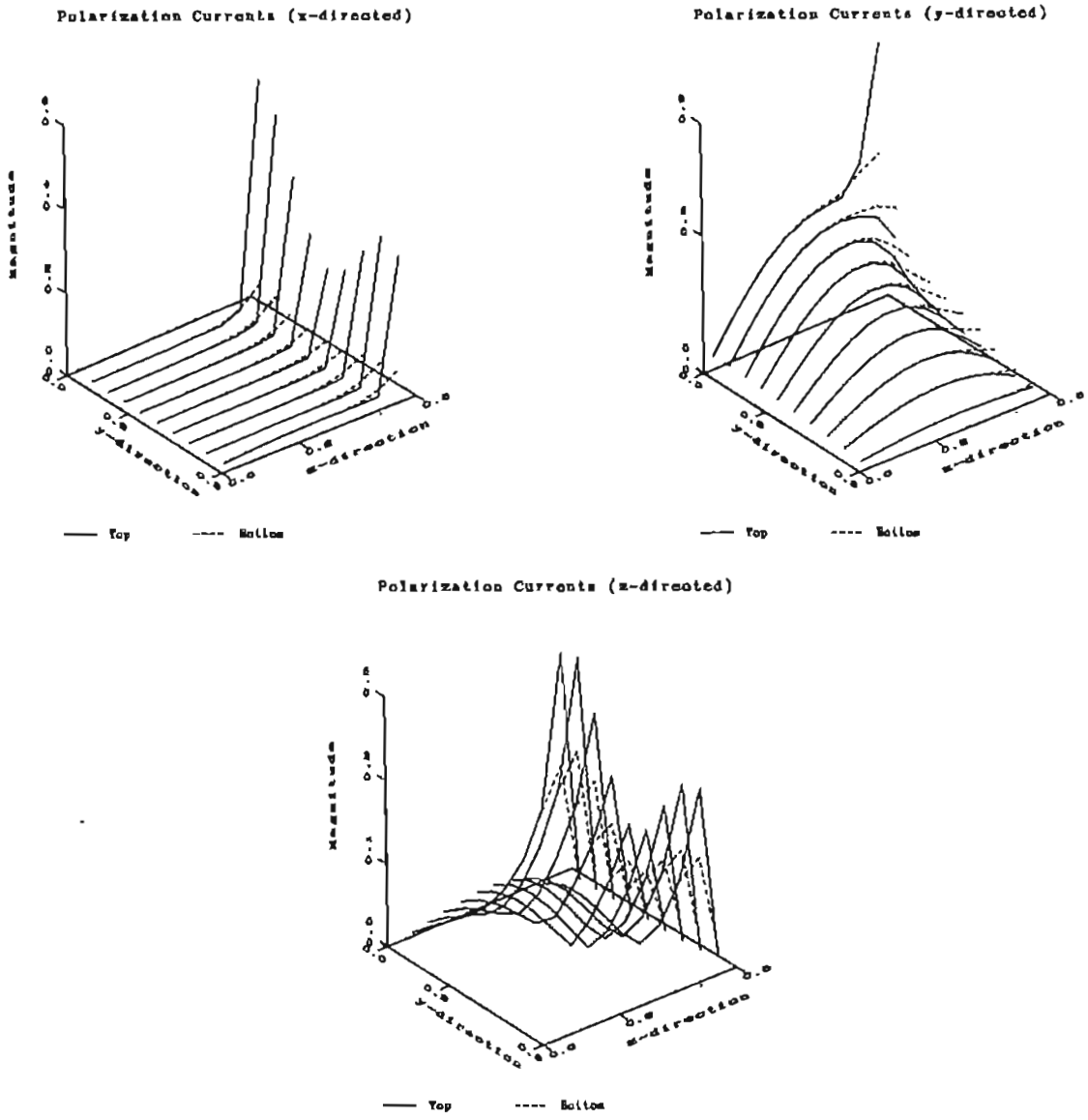

Figure 3.11: Volume polarization currents in substrate at $L/\lambda_0 = 0.620$ for **Antenna A**, having $t = 0.075L$ and $\epsilon_r = 10.2$, and segmented with $n_x = 2$, $n_y = 10$ and $n_z = 10$. Note that only the quadrant corresponding to the source region is illustrated. The currents designated as "top" refer to the layer of dielectric segments closest in the x-direction to the metal strip, and "bottom" refers to the layer of dielectric segments furthest in the x-direction from the metal strip.

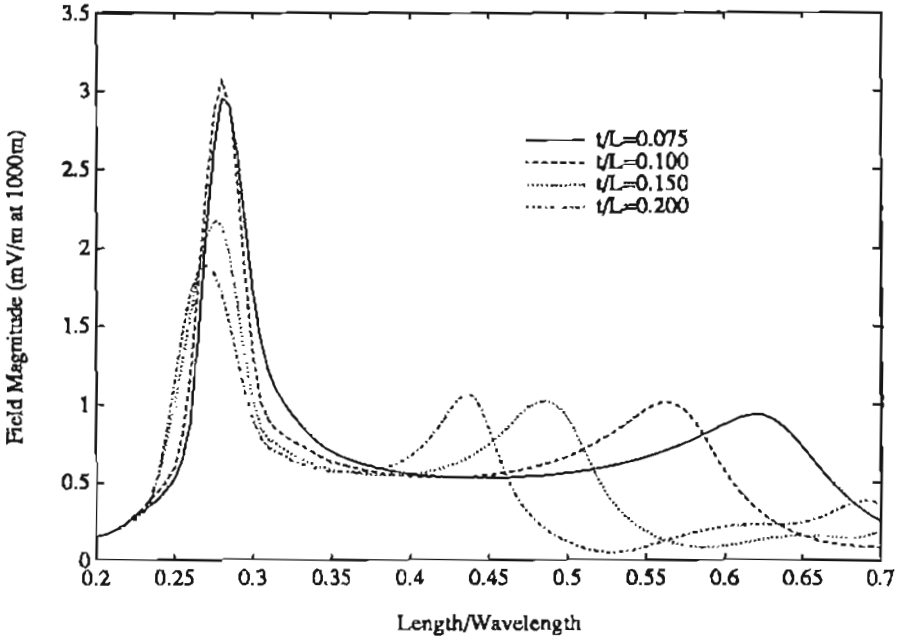

Figure 3.12: On-axis electric field strength with a feed point excitation voltage = 1v.

case, the frequency of operation is such that the TE_{11}^{y} mode may propagate, and the mode structure is clearly observed, especially for the dominant y-directed electric field component. Because a 1 volt excitation is used at both frequencies, the magnitudes of the components shown in Figure 3.11 are lower than their counterparts in Figure 3.10 due to the fact that the input power, which for a fixed excitation voltage is dependent on the antenna impedance, is 9.9dB lower at $L/\lambda_0 = 0.62$ than at $L/\lambda_0 = 0.285$. However, the radiation from the polarization currents in the substrate relative to radiation from the surface currents on the metal strip is more prominent at $L/\lambda_0 = 0.62$. This is illustrated by the fact that the maximum computed cross-polarized radiation in the yz-plane is only 22dB lower than the on-axis co-polarized radiation at this frequency.

In order to examine the effect of the fields induced in the dielectric substrate in more detail, the on-axis electric field magnitude with a 1 volt feed point excitation, for four values of substrate thickness, is shown in Figure 3.12 as a function of L/λ_0. The left-hand peak in the responses shown in Figure 3.12 corresponds to the half-wave resonance

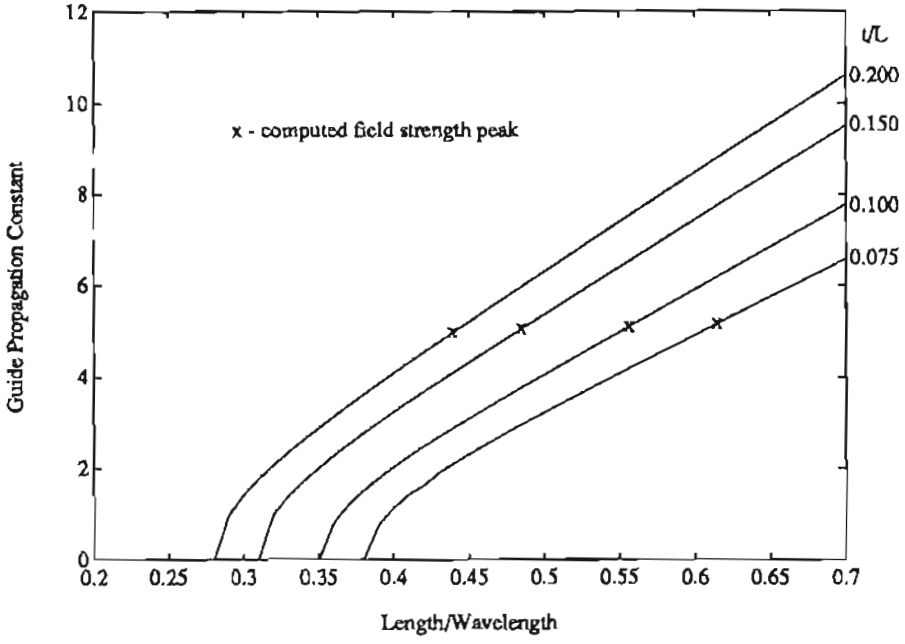

Figure 3.13: Propagation characteristics of TE_{11}^{y} mode in dielectric substrate ($\epsilon_r = 10.2$) showing, in each case, the location of the field strength peak attributed to a dielectric resonance.

of the metal strip, and the right-hand peak is attributed to the influence of a TE_{11}^{y} mode resonance in the dielectric substrate. This is verified by considering the propagation constant of the TE_{11}^{y} mode in the substrate, calculated from the expressions given in Appendix A. This propagation constant is shown in Figure 3.13 as a function of L/λ_0 for the four values of substrate thickness considered in Figure 3.12. The frequency at which the right-hand peaks occur in the responses shown in Figure 3.12 is indicated by a $\times$ on the propagation characteristics in Figure 3.13 corresponding to the appropriate thickness rectangular cross-section dielectric waveguide. Each peak can be seen to occur for a fixed value of propagation constant which corresponds approximately to that predicted by the resonator condition identified in Appendix A.

The analysis presented here has verified that the resonance effect identified in the impedance characteristics is due to fields in the dielectric substrate. Although it is not

proposed to operate the antennas at frequencies other than the half-wave resonance of the metal strip, knowledge of the occurrence of dielectric resonances is important for design purposes where the substrate is very thick. A dielectric resonance close to the half-wave resonance of the metal strip, such as may occur for thick substrates, could be undesirable from the point of view of increasing the noise bandwidth of the antenna around its operating frequency. Furthermore, if the resonance occurs within the design bandwidth of the antenna, the enhanced fields in the dielectric may significantly degrade the polarization performance. Prediction of dielectric resonances in advance from the TE_{11}^{y} mode characteristics and resonator model can help the antenna designer to identify undesirable substrate thicknesses and also avoids the use of extensive numerical computations that may be required to determine at what frequencies such resonances occur.

3.5 Summary

In this chapter, an analysis of substrate supported metal strip antennas has been presented. The geometry of the antenna has been idealized for the purpose of analysis so that the important effects associated with the dielectric substrate can be examined. Because the substrates considered are electrically thick in order to simulate a MMIC antenna for operation at millimetre wavelengths, the antenna characteristics are considerably altered from the case of a metal strip dipole antenna in free space above a ground plane. Through the use of carefully designed experimental measurements, the major effects identified by the analysis are confirmed, and the accuracy of the numerical solutions verified. Of particular significance is the demonstrated capability of the numerical method to efficiently produce accurate design information for the input impedance, radiation pattern and gain of the type of antennas of interest for application in millimetre wavelength MMIC based arrays.

Among the important contributions of the work described in this chapter are:

- The development of an accurate and computationally efficient algorithm for the analysis of a composite, finite size antenna geometry.
- The subsequent application of the analysis, over a wide frequency range, to antenna elements of practical significance to MMIC based active arrays.
- The discovery of the principal effects of the finite size, electrically thick, dielectric substrate on the radiation and impedance characteristics of substrate supported metal strip antennas.

The insight obtained and techniques developed in this chapter are expanded in the next chapter to examine problems relevant to the design of practical combinations of radiating structures and feed lines.

Chapter 4

Aspects of Practical Element Design and Analysis

4.1 Introduction and overview

Antenna design has evolved from the application of simple theoretical concepts to highly idealized structures, to the use of sophisticated design models which are capable of analysing structures having complex geometries and regions of different constitutive parameters. Many of the developments in analysis and numerical modelling have arisen directly from the need to undertake accurate engineering design of antenna elements for applications having increasingly stringent specifications. Moreover, because experimental studies are often expensive to perform, and because the performance of modern computers is continually improving, computational methods are being employed increasingly in the development of antenna design techniques and in the exploration of antenna performance through computationally conducted parametric studies. The inherent requirement for accurate design of MMIC antennas with predictable performance characteristics is addressed in this chapter with regard to metal strip antennas

on electrically thick substrates. Based on the development and testing of the analysis presented in Chapter 3, the numerical modelling of some practical MMIC antenna elements is undertaken.

In this chapter, three aspects of practical element design and analysis are considered:

- The incorporation of a feed line, and the study of its effect on the antenna performance.
- The need for impedance matching of the metal strip antenna to its feed structure.
- The control of radiation from the complete antenna structure to reduce cross-polarization.

Numerical methods which are capable of addressing these aspects of analysis are outlined, and solutions to some typical design problems are presented. Consideration is given first to a coplanar strip fed metal strip antenna, which is shown to have attractive characteristics, and second to some alternative structures having a similar geometry in order to demonstrate the application of the method outlined to a variety of problems. The validity and accuracy of the numerical analysis are again tested by means of experimental measurements.

4.2 Coplanar-strip fed substrate supported metal strip antennas

A typical MMIC antenna element, consisting of a substrate supported metal strip folded dipole together with a coplanar strip feed line, is illustrated in Figure 4.1. A microstrip line provides a feed port for connection to the MMIC electronics, and a hybrid ring power divider is employed as a *balun* to provide a balanced excitation for

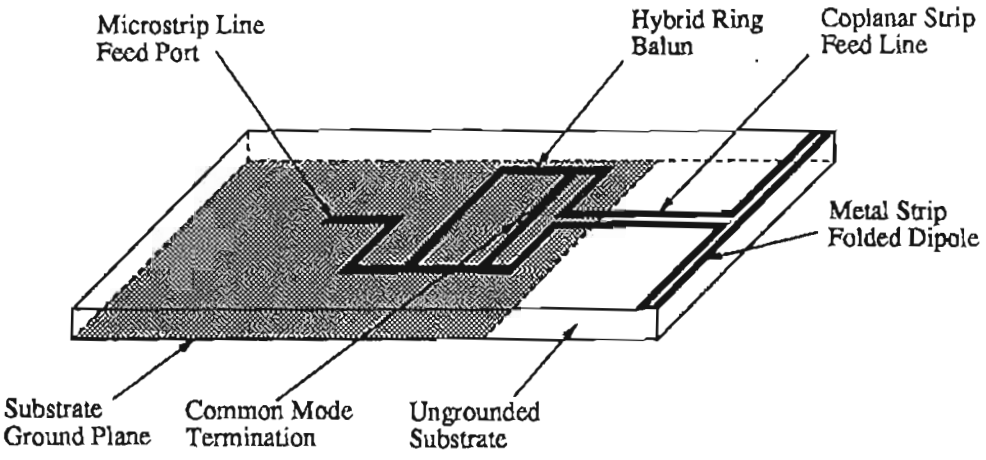

Figure 4.1: A typical MMIC antenna element with coplanar strip feed structure and balun.

the coplanar strip feed line. In this section, *coplanar strip fed substrate supported metal strip antennas* are considered, and an analysis of their performance is presented.

4.2.1 Feed line modelling

The coplanar strip fed substrate supported metal strip antenna shown in Figure 4.1 is idealized for the purpose of analysis to that shown in Figure 4.2. For the moment, the metal strip folded dipole is replaced with a single metal strip. It is assumed, as in Chapter 3, that the slot through which the antenna in Figure 4.1 would protrude is small enough so that the discontinuity that it makes in the ground plane, as well as the effect of the structure behind the ground plane, are negligible. A continuous infinite ground plane is therefore used in the analysis. Perfectly balanced, ideal feed voltages are assumed at the base of the coplanar strip feed line. Because the excitation is perfectly balanced, and the structure is symmetrical about the xz-plane, once again only half of the structure needs to be considered for the analysis, and the remaining half included as current images.

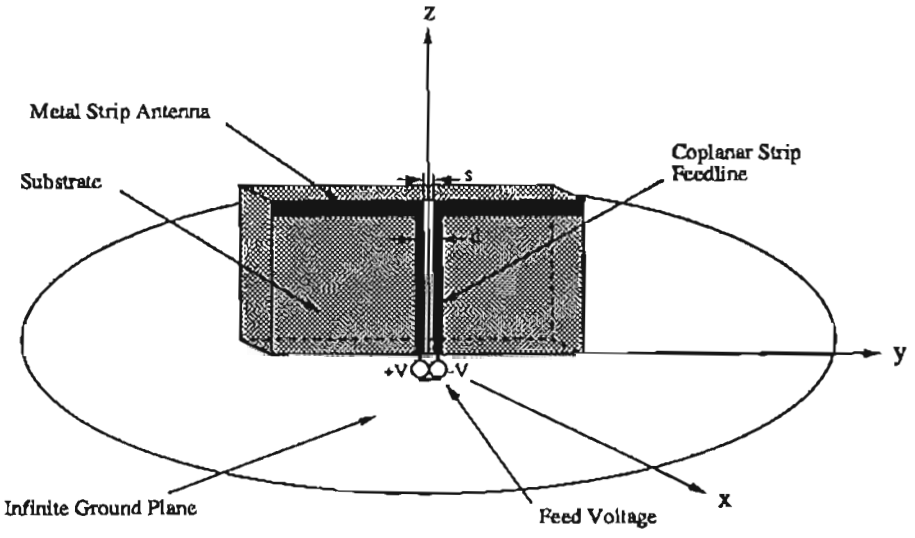

Figure 4.2: Geometry of coplanar strip fed substrate supported metal strip antenna for analysis.

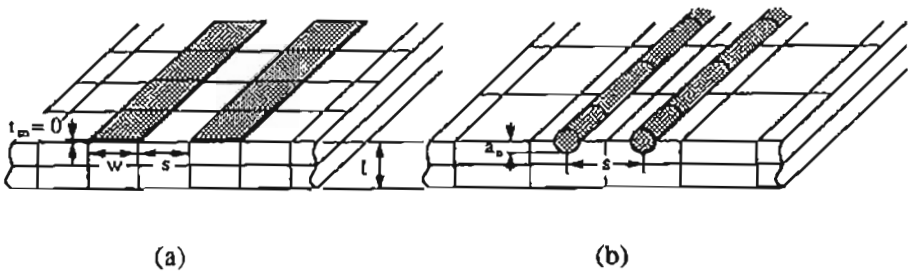

Figure 4.3: Geometries for coplanar strip line showing the strip and substrate segmentation for (a) the exact geometry, and (b) the equivalent-radius thin-wire geometry.

In Figure 4.3a, a segmentation of the two metal strips comprising the coplanar strip feed line is shown, together with the segmentation of the substrate in the region around the feed line. Because practical feed lines may require that the two metal strips forming the coplanar strip feed line be closely spaced, the uniform segmentation over the whole structure required by the grid method described in Section 3.2.3 may be very fine, and a large number of segments may be needed. Consequently, large

amounts of computer memory may be required unless the grid method is discarded in favour of an evaluation of all the necessary Green's function integrals, in which case the computational efficiency is likely to be poor. To overcome this difficulty, an equivalent-radius thin-wire approximation, as shown in Figure 4.3b, is adopted. The thin-wire approximation reduces the number of segments required in the substrate for a given separation of the metal strips forming the coplanar strip feed line. In the thin-wire approximation, only the dominant axially directed currents on the metal strips are considered. This approximation is valid since the metal strips are narrow. Each wire has an equivalent-radius, a_e, defining the surface of a cylinder on which the axially directed surface currents flow, and the field points are located on the axis of the wire, as with thin-wire antenna analysis [82]. The segmentation along the direction of the wire axis is chosen to be the same as for the two-dimensional strip representation, except that the segments are offset by half a segment, as shown in Figure 4.3b. The offset allows a single segment to traverse the ground plane at the feed point of each wire of the feed line, and a voltage at an infinitesimal gap at the centre of each of these two segments correctly positions the excitation at the base of the feed line. The pulse basis function expansion of the surface current on the wire becomes

$$\vec{J}_c(\vec{r}) = \sum_{n=1}^{n_f} P_n^1(z') f_n \hat{z} \tag{4.1}$$

where n_f is the number of segments along one wire of the feed line, f_n are the constants to be determined for the current distribution, and the one-dimensional pulse basis functions are

$$P_n^1(z') = \begin{cases} 1 & \text{for } z' \in n\text{th segment} \\ 0 & \text{otherwise.} \end{cases} \tag{4.2}$$

To be consistent, the thin-wire approximation is also applied to the metal strip antenna itself, and the two dimensional pulse basis functions, P_n, used in the analysis described in Section 3.2.3, are replaced by P_n^1 with the z-coordinate replaced by y. Only an axial current is computed for the metal strip in this case, and the constants, a_n, represent the y-directed linear current density. The constants b_n related to the z-directed metal strip current are not used since only axial currents are considered. The junctions between the feed line wires and the metal strip antenna wires are modelled as described in

Appendix C. The same equivalent-radius is used for all of the wires forming both the feed line and metal strip antenna. It is noted here that because the wire segments are offset along their axis by a half segment from the dielectric segment on which they lie, the condition that the axial current should be zero at the ends of the metal strip antenna is strictly enforced by the presence of half-pulses that are set to zero.

Conventionally, the equivalent-radius is determined by quasi-static energy considerations [83]. In the analysis described here, however, the equivalent-radius concept is a geometrical approximation which is introduced for the purpose of performing the numerical analysis efficiently. Considering first the substrate supported metal strip antenna without any feed line, the equivalent-radius may be determined by comparing the computed input impedance of an ideally fed metal strip antenna of width, w, with that computed for an antenna where the metal strip is replaced by a wire of radius, a_e. The dielectric substrate is identical in both cases, and the same substrate segmentation is used. With reference to the analysis outlined in Section 3.2.3, the Green's function integral for a two-dimensional metal strip source segment, $\mathcal{I}_1$, as required in the first case, has the form

$$\mathcal{I}_1 = \int_{y_n - l_c/2}^{y_n + l_c/2} \int_{z_n - w/2}^{z_n + w/2} G(\vec{r}_m, \vec{r}\,'_n)\, dy\, dz \tag{4.3}$$

where l_c is the y-directed length of the metal strip segment, w is the width of the metal strip, and in rectangular co-ordinates,

$$|\vec{r}_m - \vec{r}\,'_n| = \sqrt{(x_m - x'_n)^2 + (y_m - y'_n)^2 + (z_m - z'_n)^2}. \tag{4.4}$$

The Green's function integral for the equivalent-radius wire source segment, $\mathcal{I}_2$, as required in the second case, has the form

$$\mathcal{I}_2 = \frac{1}{2\pi} \int_0^{2\pi} \int_{y_n - l_c/2}^{y_n + l_c/2} G(\vec{r}_m, \vec{r}\,'_n)\, d\phi\, dy \tag{4.5}$$

where, in cylindrical co-ordinates for a wire orientated along the axial centreline of the metal strip,

$$|\vec{r}_m - \vec{r}\,'_n| = \sqrt{\rho^2 + a_e^2 - 2\rho a_e \cos(\phi_m - \phi'_n) + (y_m - y'_n)^2} \tag{4.6}$$

with $\rho^2 = (x_m - x'_n)^2 + (z_m - z'_n)^2$ [82]. It should be noted that the integrals have different dimensions, and therefore the current densities will correspond to two-dimensional or one-dimensional quantities with the application of equation 4.3 or 4.5 respectively. The Green's function integrals defined in equations 4.3 and 4.5 are applied in turn to the analysis, and the correct equivalent radius is found when the impedance characteristics are matched at the resonant frequency and over the bandwidth of interest.

In the segmentation method described in Section 3.2.3, the width of a single dielectric segment is chosen to be the same as the width, w, of the metal strip. It has been shown that the characteristics of the antenna are not sensitive to the width of the metal strip, and this allows flexibility in the choice of segment size used in the numerical implementation. In contrast, the correct equivalent-radius of the thin-wire approximation is found to be a function of the size of the dielectric segment on which it lies. This is demonstrated with respect to **Antenna A**, analysed in Section 3.4. In Figure 4.4, the variation of the impedance characteristics with the equivalent-radius is shown for frequencies around the half-wave resonance of the metal strip. It can be seen that for an equivalent-radius $a_e = 0.008L$, the characteristics agree well with the correct impedance computed in Section 3.4 by application of the two-dimensional strip formulation. Since the equivalent-radius can be chosen independently of the size of the dielectric segment, this variation does not produce difficulties. However, different segmentation schemes, such as would be used to test the convergence of the solution, require a different value of a_e to be determined. Similar considerations apply for determining the equivalent-radius of a thin-wire approximation for different substrate thicknesses. With the correct choice of a_e, all of the measurable parameters, such as the input impedance, radiation patterns and gain, computed using the thin-wire approximation, are found to be substantially the same across a wide frequency bandwidth as the corresponding parameters computed using the two-dimensional strip formulation.

Where the thin-wire approximation is used for the coplanar strip feed line, a check on the validity of the approximation may be made by considering the characteristic

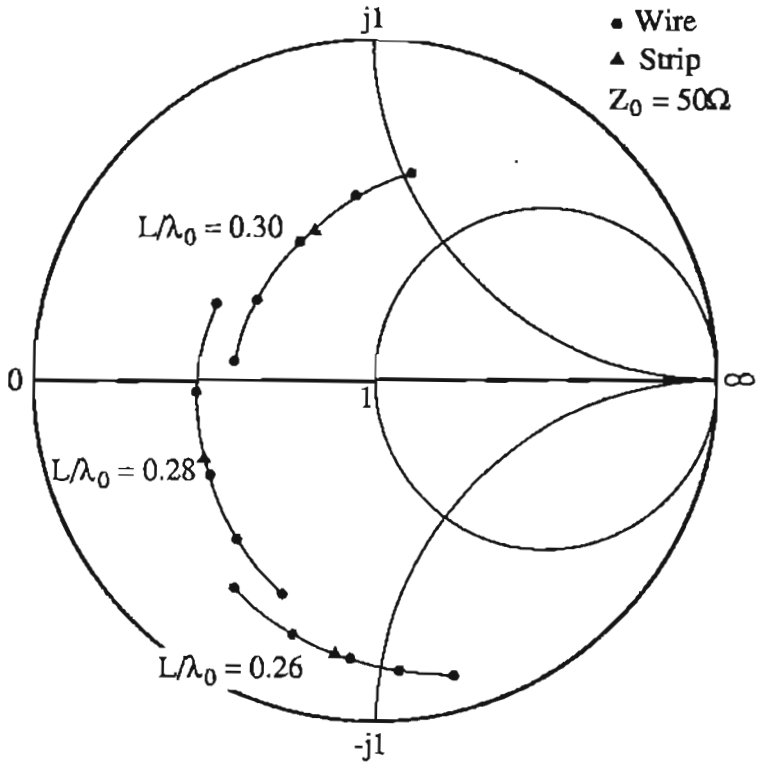

Figure 4.4: Computed input impedance of **Antenna A** from the exact strip formulation and the approximate thin-wire formulation. Substrate segmentation is $n_x = 2$, $n_y = 10$ and $n_z = 10$, corresponding to a strip width $w = 0.05L$. Impedances for a thin-wire equivalent-radius varying uniformly from $a_e = 0.0075L$ to $a_e = 0.0085L$ are shown.

impedance of the transmission line, which may be expressed as

$$Z_L = Z_{L0}/\sqrt{\epsilon_{r,\text{eff}}} \tag{4.7}$$

where $\epsilon_{r,\text{eff}}$ is the effective dielectric constant for the transmission line and Z_{L0} is the characteristic impedance of the free space line [84]. For coplanar strip line, the parameters $\epsilon_{r,\text{eff}}$ and Z_{L0} may be deduced from the geometry of the transmission line as

$$Z_{L0} = \eta_0 \frac{K(k)}{K(k')} \tag{4.8a}$$

$$\epsilon_{r,\text{eff}} = 1 + \frac{(\epsilon_r - 1)}{2} \frac{K(k_1') \cdot K(k)}{K(k_1) \cdot K(k')} \tag{4.8b}$$

where $K(k)$ is the complete elliptical integral of the first kind with modulus k, and $\eta_0 = 120\pi$ is the free space wave impedance. For infinitesimally thin metal strips ($t_m = 0$), the moduli of the elliptical integrals are related to the geometry shown in Figure 4.3a by

$$\begin{aligned} k &= \frac{s/w}{2+(s/w)} \\ k' &= \sqrt{1-k^2} \\ k_1 &= \frac{\tanh \pi s/(4t)}{\tanh \pi(s+2w)/(4t)} \\ k_1' &= \sqrt{1-k_1^2} \end{aligned}$$

and the elliptical integrals may be evaluated from series approximations as outlined in [84]. Considering now the equivalent-radius parallel wire transmission line on the same substrate, as shown in Figure 4.3b, $\epsilon_{r,\mathrm{eff}}$ must be the same as that of the coplanar strip line, and from simple transmission line theory [85]

$$Z_{L0} = \frac{\eta_0}{\pi} \cosh^{-1}\{s/(2a_e)\}\,. \tag{4.9}$$

Using the appropriate equivalent-radius parameter for the parallel wire transmission line representation, computation of the characteristic impedance of the two transmission lines reveals that the characteristic impedances of the two structures are numerically the same. The equivalent-radius thin-wire representation of the complete antenna geometry is therefore found to be valid.

After selection of the thin-wire equivalent-radius for a given segmentation, the formulation of the problem, including the feed lines, proceeds in a similar manner to that described in Chapter 3. The segmentation described for the thin-wire representation of the structure permits the use of the grid method outlined in Section 3.2.3, however, additional integrals of the form given in equation 4.5 must be computed for wire segments and half-segments orientated in the y-direction and z-direction. The approach described is applied to the numerical analysis of coplanar strip fed substrate supported metal strip antennas in Section 4.2.3.

4.2.2 Impedance matching using metal strip folded dipoles

For the substrates which have been considered so far, typical coplanar strip feed line dimensions result in feed line characteristic impedances around 100 ohms. This presents the problem of matching the low impedance of the substrate supported metal strip antenna to the feed line. A simple means of effecting this impedance match is to use a *metal strip folded dipole*, in place of the single metal strip, to increase the impedance of the antenna. An example of a substrate supported metal strip folded dipole was illustrated in Figure 4.1, where a *coplanar strip folded dipole* is employed.

With reference to the coplanar strip folded dipole shown in Figure 4.1, the metal strip closest to the end of the substrate is the *folded metal strip* and the strip parallel to it, and connected to the coplanar strip feed line, is the *driven metal strip*. The two strips forming the folded dipole are connected together at the ends. In general, the overall width of the coplanar strip folded dipole is small compared with the length, and the metal strips are narrow and closely spaced. Where the spacing between the strips is large, the structure resembles more closely a loop antenna, but this case will not be considered here. For reasons similar to those outlined for the parallel metal strips of a coplanar strip feed line, a complete analysis which incorporates the grid method is costly in terms of computer storage when the coplanar strip folded dipole is narrow. Moreover, if the folded metal strip and the driven metal strip are of unequal width, or if the spacing between the strips is not equal to the width of the strips, the grid method cannot be used. Consequently, rather than analysing the complete folded dipole structure, an alternative approach employing *decomposition* of the currents on the coplanar strip folded dipole is adopted. The currents on the coplanar strip folded dipole are separated for the purpose of analysis into a balanced (or transmission line) mode current and an unbalanced (or radiating) mode current. The radiating mode current is related to the current on a single metal strip antenna, and the transmission line current is related to the current on a coplanar strip transmission line having the same geometry as the coplanar strip folded dipole structure.

Decomposition methods for analysing folded dipoles have been found to provide accurate results for wire dipoles in free space [86], and have also been applied to asymmetrical coplanar strip folded dipoles in free space [87]. All of the analyses assume, however, that the physical environment of the folded and driven metal strips is the same. Clearly this is not the case for the antenna shown in Figure 4.1, where the coplanar strip folded dipole is in close proximity to the edge of the substrate. Two assumptions are required for the decomposition method to be applied:

1. The folded and driven metal strips must be sufficiently narrow and closely spaced so that the influence of the truncation of the dielectric substrate on the radiating mode current may be assumed to be the same for both strips.

2. The effect of the truncation of the substrate on the transmission line current must be small in order to determine the transmission line parameters for the coplanar strip folded dipole from the coplanar strip feed line equations given in Section 4.2.1.

Both of these assumptions are shown later to yield results which are sufficiently accurate for design purposes.

The input impedance of the substrate supported metal strip folded dipole is found from [87] as

$$Z_{in} = \frac{2(1+a)^2 Z_d Z_t}{(1+a)^2 Z_d + 2Z_t}, \tag{4.10}$$

where Z_d is the input impedance of a substrate supported metal strip antenna having a width, w, which is equal to the total width of the coplanar strip folded dipole, and a is the ratio of the radiating mode current on the folded metal strip to that on the driven metal strip. The balanced mode transmission line impedance, Z_t, is calculated for a short circuited coplanar strip transmission line of length, $L/2$, from

$$Z_t = jZ_L \tan\left\{\frac{\pi L\sqrt{\epsilon_{r,\text{eff}}}}{\lambda_0}\right\} \tag{4.11}$$

where Z_L and $\epsilon_{r,\text{eff}}$ are the appropriate parameters for the coplanar strip line [84],

assuming that the substrate is not truncated. At frequencies close to the half-wave resonance of the antenna, $|Z_d| \ll |Z_t|$, and hence

$$Z_{in} \approx (1+a)^2 Z_d \tag{4.12}$$

where $(1+a)^2 = \gamma^2$ is the impedance step up ratio. Since Z_t is sufficiently large, the second assumption above is no longer required. For equal strip widths, the current is equally divided between the folded and driven metal strips, and $\gamma^2 = 4$. Where other impedance step up ratios are required, a different ratio of strip widths may be used, and the resulting current ratio, a, may be determined from

$$a = \frac{\ln(4r + 2\sqrt{(2r)^2 + (w_1/2)^2}\,) - \ln(w_1)}{\ln(4r + 2\sqrt{(2r)^2 + (w_2/2)^2}\,) - \ln(w_2)} \tag{4.13}$$

where w_1 and w_2 are the widths of the driven and folded metal strips respectively, and the spacing between the centres of the metal strips is $2r$ [87]. Since equation 4.13 is derived for metal strips in free space, and is only directly applicable for an infinitely extending substrate, the second assumption is again implicit in the calculation.

Because the radiation is dominated by the unbalanced mode on the closely spaced strips forming the metal strip folded dipole, which is geometrically similar to the substrate supported metal strip antenna of width w analysed to obtain Z_d, the radiation characteristics will not be significantly different from those of the single strip case.

A second folded dipole geometry is illustrated in Figure 4.5, where the folded metal strip is constructed on the opposite side of the substrate to the driven metal strip. In contrast to the coplanar strip folded dipole described previously, this geometry is referred to as a *back-folded dipole.* The ends of the driven and folded metal strips are shown in Figure 4.5 to be connected by straps around the edge of the substrate, however, for a MMIC antenna, via hole connections close to the edges may need to be used.

For equal width strips, the back-folded dipole geometry shown in Figure 4.5, with-

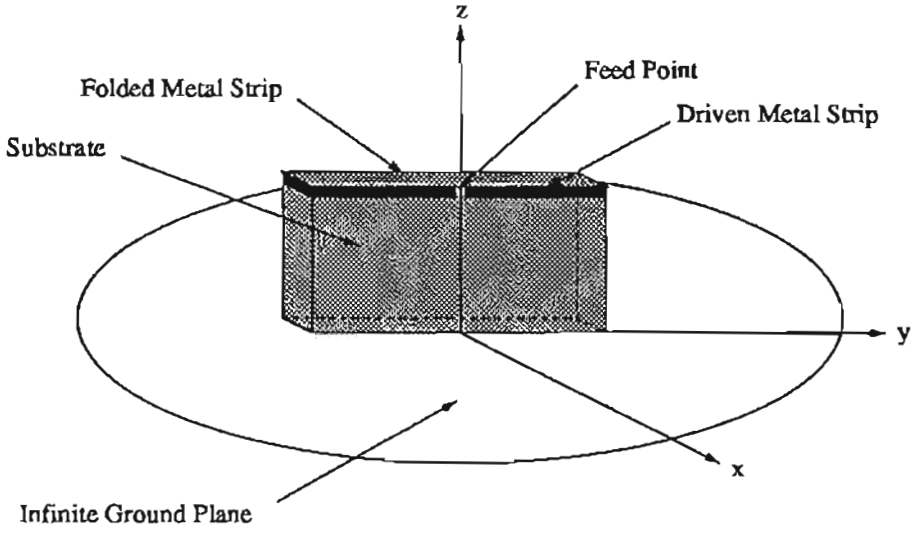

Figure 4.5: Back-folded metal strip antenna geometry for analysis.

out feed lines, lends itself to direct numerical analysis by means of the techniques described in Chapter 3. In this case, a segmentation of the substrate and both metal strips may be chosen that allows the grid method to be applied. For small straps at the ends, the analysis may be performed by neglecting the current distribution on the straps and enforcing the continuity of the current at the ends of the folded and driven metal strips [88]. A method similar to that described for a two wire junction in Appendix C is employed to enforce this condition. The computer storage for the analysis is therefore only increased by the number of pulses needed to model the folded strip, and no additional Green's function integrals are required to be computed. Finally, an image plane in the xz-plane is again identified from the symmetry of the structure and excitation, and is used in the analysis to halve the size of the problem. Using this approach, the input impedance of the substrate supported metal strip back-folded dipole is obtained directly by the numerical analysis.

The decomposition method described above for the coplanar strip folded dipole may also be applied to derive the input impedance of the back-folded dipole. The input impedance of a substrate supported metal strip antenna with a single metal strip having a width, w, which is equal to that of the driven metal strip of the back-folded

dipole is computed as in Chapter 3. The transmission line impedance may be derived from the parameters of a parallel strip transmission line [89], or an appropriately scaled microstrip line, where the microstrip ground plane produces a correctly positioned image to represent the folded metal strip. Similar considerations apply here with respect to the substrate truncation, however, it is possible to correct the parameters to allow for the edge of the substrate using data obtained for edge corrected microstrip lines [90]. A comparison of the results obtained by applying both the complete numerical analysis and the decomposition method provides a useful check on accuracy.

4.2.3 Theoretical and experimental results

A substrate supported metal strip antenna, identical to **Antenna A** in Section 3.4 except for the presence of a coplanar strip feed line, was analysed with three different coplanar strip feed line configurations arising from three different substrate segmentation sizes. The three cases, and the resulting feed line and metal strip dimensions normalized to the metal strip length, L, are

Case 1 Source region segmentation $n_x = 2$, $n_y = 10$ and $n_z = 10$

Metal strip antenna width $w = 0.05L$

Wire equivalent-radius $a_e = 0.008L$

Equivalent parallel wire feed line separation $s = 0.05L$.

Case 2 Source region segmentation $n_x = 2$, $n_y = 8$ and $n_z = 8$

Metal strip antenna width $w = 0.0625L$

Wire equivalent-radius $a_e = 0.0095L$

Equivalent parallel wire feed line separation $s = 0.0625L$.

Case 3 Source region segmentation $n_x = 2$, $n_y = 6$ and $n_z = 6$

Metal strip antenna width $w = 0.0833L$

Wire equivalent-radius $a_e = 0.0115L$

Equivalent parallel wire feed line separation $s = 0.0833L$.

Case	Z_0	Reflection Coefficient
1	92 ohms	$0.73\angle 55°$
2	94 ohms	$0.73\angle 50°$
3	99 ohms	$0.78\angle 65°$

Table 4.1: Computed reflection coefficient at the feed point of a coplanar strip feed line for substrate supported metal strip antenna with substrate parameters $t = 0.075L$ and $\epsilon_r = 10.2$.

Table 4.1 shows the results of computations for these three cases. The characteristic impedance of the coplanar strip feed line is shown for each case, together with the computed reflection coefficient at the base of the coplanar strip feed line where the balanced excitation is applied. The reflection coefficient is obtained from the impedance at the base of the coplanar strip feed line using the appropriate value of characteristic impedance shown in Table 4.1. From the input impedance calculated at the centre of the metal strip of **Antenna A** in Section 3.4, reflection coefficients having a magnitude close to 0.7 are predicted for the cases considered by assuming that the coplanar strip feed line does not perturb the impedance at the centre of the metal strip antenna. This approximate result is in close agreement with those actually obtained from the computations. As the segment size increases from *Case 1* to *Case 3*, the effect of the increase on the convergence of the solution is seen to be small, in accordance with that anticipated from the results obtained in Section 3.4 for **Antenna A**.

The computed principal plane radiation patterns for *Case 1* to *Case 3* are shown in Figure 4.6. The axially directed surface currents on the metal strips forming the coplanar strip feed line will act as a source of radiation that is polarized in the z-direction. The effect of such currents on the radiation pattern of a parallel wire fed free space dipole has been described in [78]. It is known from the results obtained in Section 3.4, however, that z-directed polarization currents are induced in the substrate by the metal strip antenna, and that these polarization currents also affect the radiation characteristics of the antenna. Moreover, additional z-directed polarization currents are induced in the substrate by the coplanar strip feed line. The distribution of currents

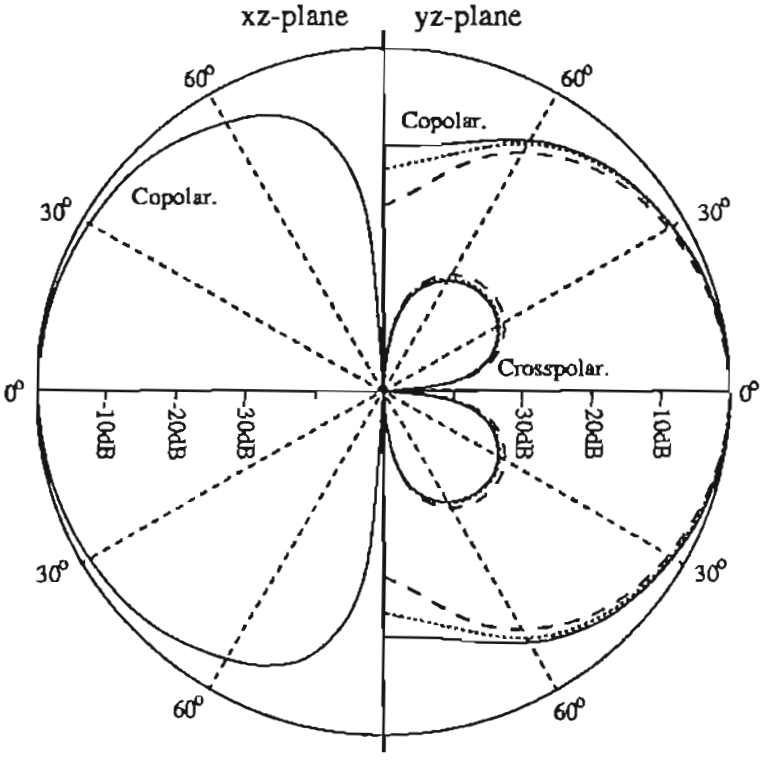

Figure 4.6: Theoretical principal plane radiation patterns for **Antenna A** with a coplanar strip feed line: *Case 1* ($s = 0.0500L$): solid line, *Case 2* ($s = 0.0625L$): dotted line, *Case 3* ($s = 0.0833L$): dashed line.

about the xz-plane of the antenna is balanced, however, it is found that the polarization currents induced in the substrate by the metal strip antenna have the opposite polarity to the surface currents on the metal strips of the coplanar strip feed line and the polarization currents that the feed line induce in the substrate. This complex source interaction results in an interference effect, causing partial cancellation of the z-directed radiation in the yz-plane. This effect is particularly noticeable for large angles from the z-axis. For wider spacings of the coplanar strips forming the feed line, the cancellation becomes greater, and consequently the yz-plane co-polarized radiation pattern becomes narrower. Conversely, for narrower spacings of the coplanar strips forming the feed line, the cancellation is not as large, and the yz-plane co-polarized radiation pattern is not substantially influenced by the presence of the feed line. Cross-polarized radiation in the yz-plane is due to x-directed polarization currents in the substrate which will be

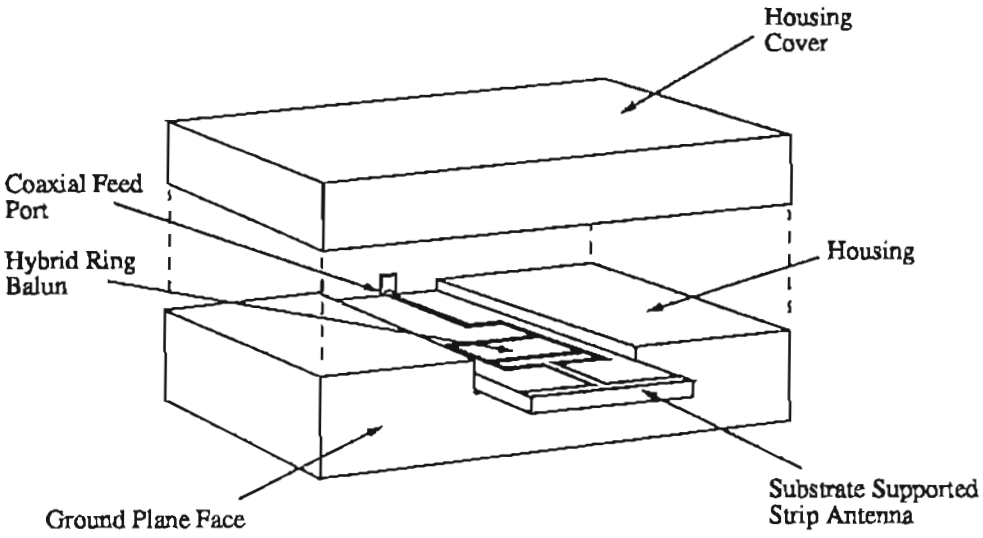

Figure 4.7: Test assembly for a substrate supported coplanar strip folded dipole with coplanar strip feed line, showing the feed port, balun and housing. The assembly mounts on a 640mm square ground plane to produce the required geometry.

induced by both the metal strip antenna and the feed line. As expected from the previous result, an increase in cross-polarized radiation in the yz-plane is noted as the separation between the metal strips forming the coplanar strip feed line is increased.

Because the antenna structure and excitation is balanced, the xz-radiation pattern is not affected by the presence of the coplanar strip feed line. Radiation in a diagonal plane at 45° to the principal planes is also of interest, since for some antennas the polarization characteristics have been found to be poor in this plane [91]. The radiation characteristics in the diagonal plane of a coplanar strip fed substrate supported metal strip antenna will be investigated in Section 4.2.4.

Measurements on a practical coplanar strip fed substrate supported metal strip antenna were performed using the test assembly shown in Figure 4.7. The antenna itself comprises a coplanar strip folded dipole and a 100 ohm coplanar strip feed line fed from the 180° phase shifted outputs of a hybrid ring power divider which is used as a balun. The use of a coplanar strip folded dipole improves the impedance match between

the antenna and the feed line. A 50 ohm microstrip line from the balanced mode input port of the power divider is fed via a coaxial-line to microstrip-line transition. The common mode port of the power divider is not terminated, and the output of the balun is designed to be matched to a 100 ohm balanced load. The predicted performance of the balun over a 10% bandwidth indicates that a return loss of better than 20dB can be achieved at the balanced mode input port. At the feed point of the coplanar strip line, an output balance of better than ± 0.2dB in magnitude and $\pm 2°$ in phase into a matched load is predicted over the bandwidth.

Two antennas of the type shown in Figure 4.1 are considered here, and are denoted **Antenna C** and **Antenna D**.

Antenna C was constructed on an RT Duroid^{TM} 6010 substrate, and was designed for a half-wave resonance at 5GHz. The dimensions of the substrate and coplanar strip feed line were those of *Case 1* above. The coplanar strip folded dipole had a length $L = 17$mm, and was fabricated with equal folded and driven strip widths and a total width corresponding to $w = 0.05L$. An impedance step up ratio of $\gamma^2 = 4$ was thereby obtained, and a decomposition method was used to calculate the impedance characteristics of the antenna using the computed impedance characteristics of **Antenna A** for Z_d. As for **Antenna A**, the half-wave resonance is predicted to occur at $L/\lambda_0 = 0.285$.

The performance of the hybrid ring power divider balun was tested by measuring the characteristics of two baluns in a back-to-back configuration. At 5GHz, a return loss of 38dB was measured, together with an insertion loss of less than 0.2dB per balun, thus verifying that an acceptable balun design had been achieved.

Assuming ideal balun performance, the predicted return loss of **Antenna C** at the coaxial feed port may be computed, and is shown in Figure 4.8 together with the measured return loss. The agreement around the design frequency is observed to be very good, and the discrepancy away from resonance is attributed to a deterioration in the performance of the balun at these frequencies.

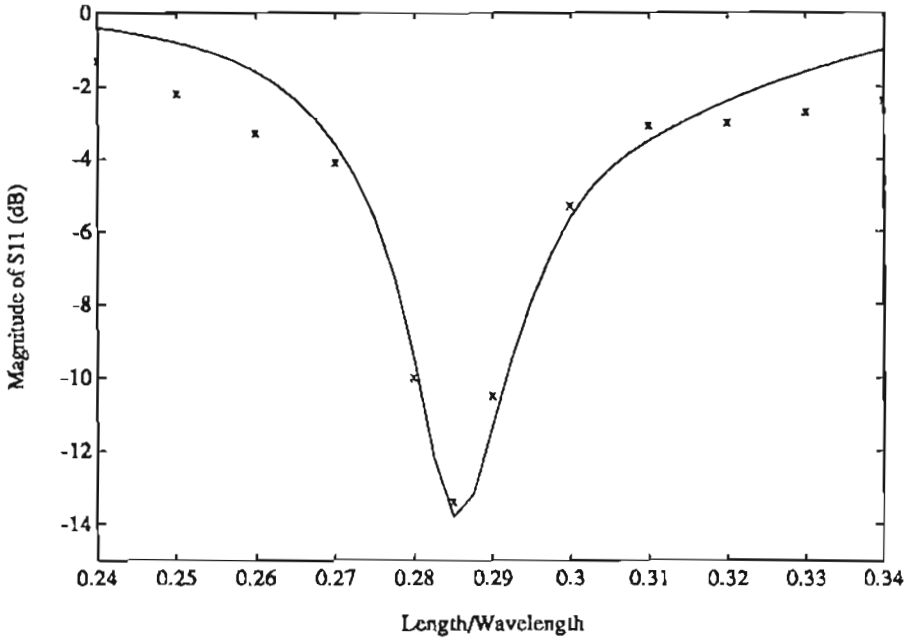

Figure 4.8: Calculated (solid line) and measured (x) return loss of a substrate supported coplanar strip folded dipole with coplanar strip feed line designed for half-wave resonance at 5GHz (**Antenna C**).

Measured principal plane radiation patterns of **Antenna C** at 5GHz are shown in Figure 4.9. Co-polarized radiation in the xz-plane and yz-plane, and cross-polarized radiation in the yz-plane agree well with the radiation patterns predicted for the coplanar strip fed antenna in *Case 1* above, which are illustrated in Figure 4.6. A low level of cross-polarized radiation, of the order of -40dB but not shown in Figure 4.9, was detected in the xz-plane measurement. This was attributed to a slight imbalance of the currents on the structure due to geometrical imperfections in the measurement assembly in the anechoic chamber. A current imbalance of only a few percent, simulated by a numerical analysis with unbalanced excitation voltages, was found to produce comparable levels of cross-polarization. The effect of diffraction from the ground plane discontinuity caused by the square mounting insert used in the measurement assembly is again apparent in the measured yz-plane co-polarized radiation pattern. Diffraction from the edges of the circular ground plane was minimized by the use of microwave

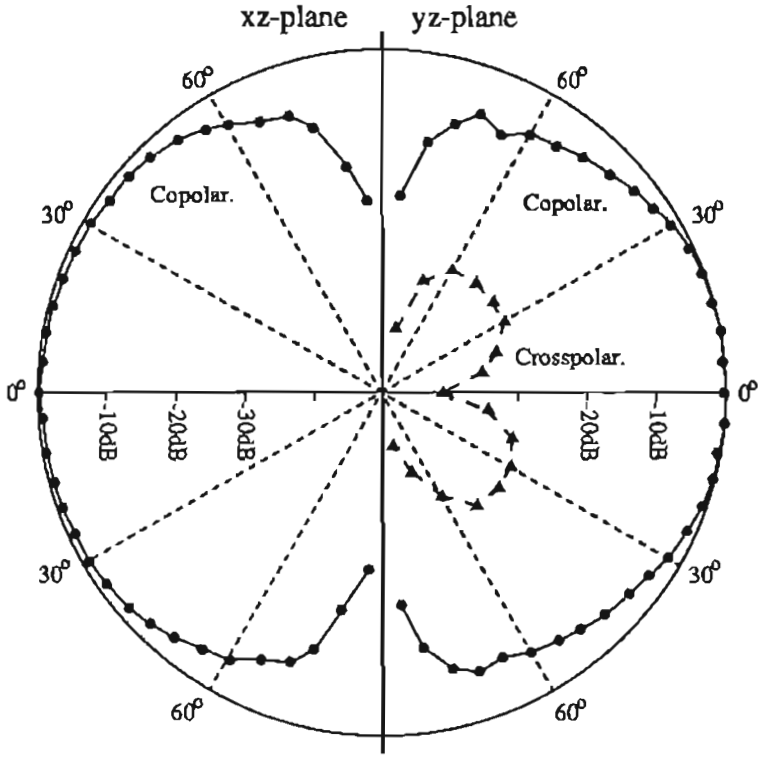

Figure 4.9: Measured principal plane radiation patterns at 5GHz for a substrate supported coplanar strip dipole with a coplanar strip feed line (**Antenna C**).

absorbing material around the circumference.

Antenna D was fabricated on a 450μm thick GaAs substrate using aluminium deposition by means of a wet etch process. The antenna was designed to be resonant at 11.8GHz. This frequency is 5% below the top of X-band, and was chosen to allow a reasonable bandwidth for measurements with X-band apparatus. A coplanar strip folded dipole antenna is again employed, and the relative widths of the folded and driven metal strips were chosen such that the impedance step up ratio $\gamma^2 = 6.9$, in order to provide a good impedance match between the coplanar strip folded dipole and a 100 ohm coplanar strip feed line, and also to maximize the bandwidth of the antenna. Allowance for fabrication errors due to trimming the substrate was made as described in Appendix D. With respect to the length, L, of the coplanar strip folded dipole, the half-wave resonance was predicted to be at $L/\lambda_0 = 0.275$. The measured return loss at

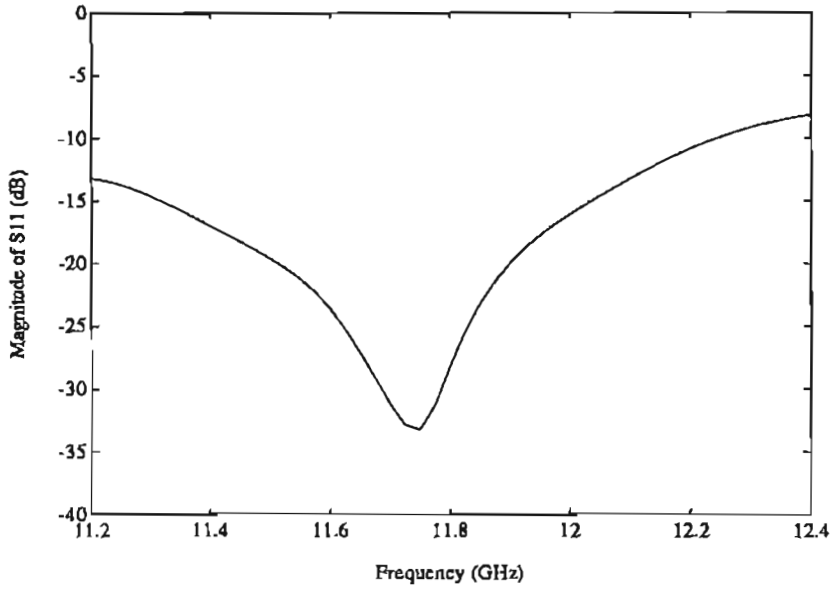

Figure 4.10: Measured return loss for an X-band GaAs substrate supported coplanar strip folded dipole with coplanar strip feed line (**Antenna D**).

the coaxial feed port of the fabricated antenna is shown in Figure 4.10. The measured resonant frequency was close to the design resonant frequency, and the low return loss confirms that good impedance matching has been achieved over a 10% bandwidth. The accuracy of the design procedure which has been developed is therefore verified.

Measured and theoretical co-polarized principal plane radiation patterns of **Antenna D** are shown in Figure 4.11. The measured radiation patterns agree well with those predicted by theory. The effect of diffraction at large angles from the z-axis is not as pronounced in the measured results at this higher frequency due to the finer angular scale and smaller range of amplitude variation in the diffraction pattern that is produced. Cross-polarized radiation was predicted to be greater than 30dB below the on-axis co-polarized radiation, and no cross-polarized radiation could be detected above this level[1].

[1]The measurement dynamic range at X-band was limited to about 30dB due to increasing path losses and cable losses in the measurement apparatus. For this reason, a detailed cross-polarized radiation pattern could not be measured.

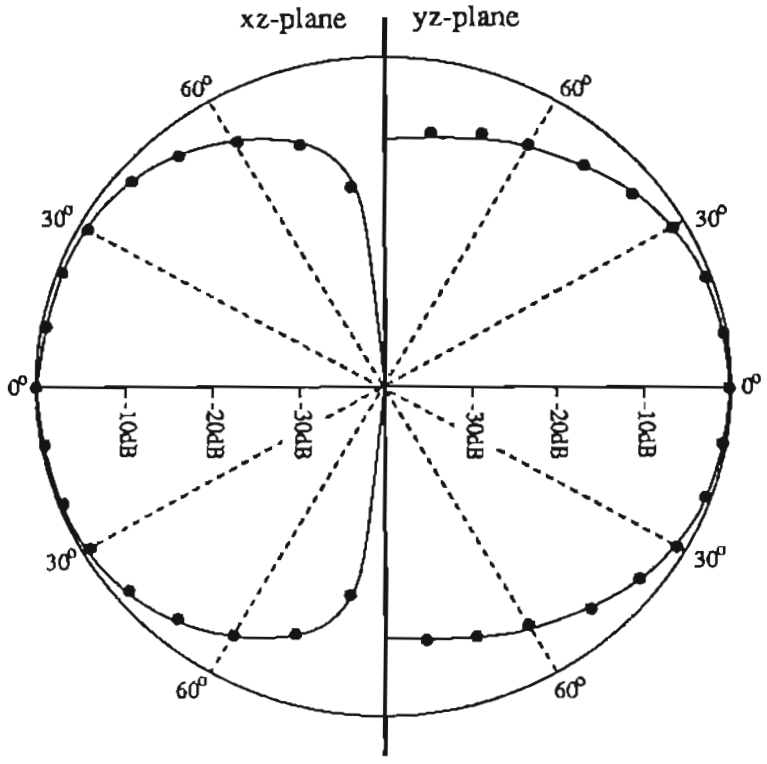

Figure 4.11: Principal plane co-polarized radiation patterns at 11.8GHz for a GaAs substrate supported coplanar strip folded dipole with coplanar strip feed line (**Antenna D**).

Finally, back-folded dipole structures described in Section 4.2.2 were studied. Results were calculated from the direct application of the numerical analysis as well as using the decomposition method. Two antennas were studied, and are denoted here as **Antenna E** and **Antenna F**. Both antennas were designed with substrates having a relative permittivity $\epsilon_r = 10.2$. **Antenna E** had dimensions identical to **Antenna A** described in Section 3.4, except that a folded metal strip, equal in width to the driven metal strip, exists on the back of the substrate, and the ends of the two strips are connected. **Antenna F** is related to **Antenna B** described in Section 3.4 in the same way. The analysis was conducted without feed lines for the purpose of determining the feed point impedance and the corresponding impedance step up ratio. For experimental measurement of the input impedance, the technique of using an image plane described in Section 3.3.1 was employed. A back-folded monopole, fed at the base of

	L/λ_0	Input impedance (ohms)		
		Numerical Analysis	Decomposition	Measured
Antenna E	0.285	$80.1 - j5.4$	$77.5 - j1.5$	-
Antenna F	0.270	$71.8 - j2.2$	$67.5 - j4.8$	$82 + j3$

Table 4.2: Computed input impedance of substrate supported back-folded metal strip dipoles using a direct numerical analysis and a decomposition method, compared with measured impedance.

the driven strip monopole and shorted to the image plane at the base of the folded strip monopole is produced, and the measured input impedance of the back-folded monopole is doubled to obtain the impedance of the complete structure. Measurements to verify the computed results were undertaken for **Antenna F**, fabricated on RT Duroid^{TM} 6010 and scaled for a half-wave resonance at 3GHz, since the wider separation between the metal strips comprising the back-folded monopole was sufficient to accommodate a SMA coaxial feed port to excite the driven metal strip without perturbing the current on the folded metal strip. The computed impedance results at the half-wave resonances of **Antenna E** and **Antenna F** are given in Table 4.2, where it can be observed that the results of two theoretical techniques agree well. The measured input resistance of **Antenna F**, also shown in Table 4.2, is slightly higher than the computed resistance since the analysis assumed a lossless antenna. Nevertheless, the agreement between the predicted and measured values is sufficient for most design purposes.

4.2.4 Controlling radiation characteristics

It is apparent from the computed and measured characteristics of the antennas considered so far that the radiation pattern of a substrate supported metal strip antenna is influenced by the volume polarization currents in the substrate as well as by currents on the feed line. The prediction of these effects is an important part of the design process, particularly where cross-polarization performance is a critical parameter and

the presence of x-directed and z-directed far-field radiation is undesirable. It is therefore important to understand the mechanisms by which such radiation occurs. Based on this understanding it is possible to choose an appropriate antenna geometry to reduce the cross-polarized radiation. Two examples are presented in this section. In the first example, a back-folded metal strip dipole is shown to reduce the x-directed polarization currents in the substrate, and therefore also the cross-polarization in the yz-plane. In the second example, a reduction in cross-polarized radiation arising from the appropriate choice of a coplanar strip feed line geometry is described.

Back-folded metal strip dipole: radiation effects

From the geometry of the back-folded metal strip dipole illustrated in Figure 4.6, it is noted that apart from the presence of the feed point excitation on the driven metal strip, the geometry exhibits an additional symmetry over the case where the metal strip (or coplanar strip folded dipole) only exists on one surface of the substrate. Recalling that the x-directed polarization current in the substrate is maximum directly under the strip, it is clear from the symmetry in the plane of the substrate that if the dominant radiating, or common mode, currents on the folded and driven metal strips are nearly equal, as is the case for equal strip widths, then the x-directed polarization current excited in the substrate by each metal strip will cancel. For this reason, the cross-polarized radiation caused by the x-directed polarization currents will be reduced by the use of a back-folded metal strip dipole. Because only the driven metal strip is excited, the symmetry is not perfect. As a result, the x-directed polarization currents will not cancel exactly, however, the reduction is found to be significant.

For **Antenna E** above, the maximum level of cross-polarization in the yz-plane is found to be reduced by 11dB over that computed for **Antenna A**. For **Antenna F** above, the reduction with respect to **Antenna B** is 18.5dB. In both cases the resulting cross-polarization is more that 40dB below the on-axis co-polarized radiation. Where the substrate is electrically thick, therefore, the back-folded dipole not only offers the advantage of increased input impedance for impedance matching to a coplanar strip

feed line, but also the advantage of significantly reduced cross-polarization in the yz-plane.

Coplanar strip feed line: radiation effects

The effect of a coplanar strip feed line on the yz-plane radiation pattern of a substrate supported coplanar strip folded dipole has been discussed in Section 4.2.3. Because the z-directed source currents are co-polarized in the yz-plane, the effect of the feed line was observed mainly as a narrowing of the co-polarized radiation pattern. In a diagonal plane at 45° to the principal planes, however, any z-directed current sources, whether they be surface currents on the metal strips forming the feed line or polarization currents in the substrate, will contribute to the cross-polarized radiation field.

Considering first the substrate supported metal strip antenna with no feed line, the computed diagonal plane co-polarized and cross-polarized radiation patterns are shown as solid lines in Figure 4.12. The z-directed polarization currents in the substrate are the primary source of the cross-polarized radiation in the diagonal plane. When a coplanar strip feed line is included in the antenna structure, the interference between the radiation from z-directed surface currents on the metal strips forming the feed line and the radiation from z-directed polarization currents in the substrate is such as to reduce the diagonal plane cross-polarized radiation. All of the current sources contributing to radiation are located within a volume $\lambda_0^3/8$, so there can be no cancellation of radiation due to the distribution of the sources. Rather, the partial cancellation that is obtained is determined by the relative phase between the z-directed sources on the feed line and those in the substrate. The resulting interference is extremely useful for controlling the diagonal plane polarization characteristics. The spacing, s, between the metal strips forming the feed line is again a factor determining the degree to which the cancellation is effective. It is found that for narrow spacings, a low level of cross-polarized radiation can be achieved. From the variation of cross-polarized radiation as the metal strip spacing is changed it is apparent that when the feed line is present, it becomes the dominant source of cross-polarized radiation in the diagonal plane. Consequently,

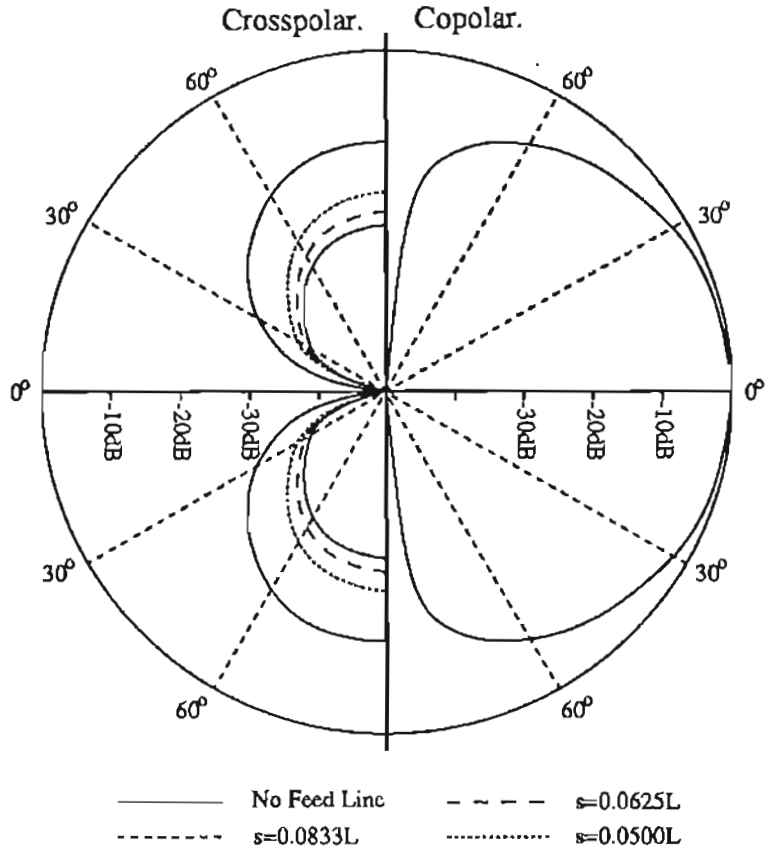

Figure 4.12: Theoretical diagonal plane radiation patterns for idealized and coplanar strip fed substrate supported metal strip antennas.

narrow spacings are preferred in order to provide the required degree of cancellation of the polarization current sources in the substrate which are due to the metal strip antenna itself. It is noted that for the range of spacings between the coplanar strips of the feed line that are considered, the co-polarized radiation pattern in the diagonal plane is essentially unaffected by the feed line.

The measured diagonal plane radiation pattern of **Antenna C** is shown in Figure 4.13. The measured results confirm the predicted results that low-level cross polarized radiation may be obtained in the diagonal plane with a well designed feed line.

This result concludes a full study of the radiation characteristics of substrate sup-

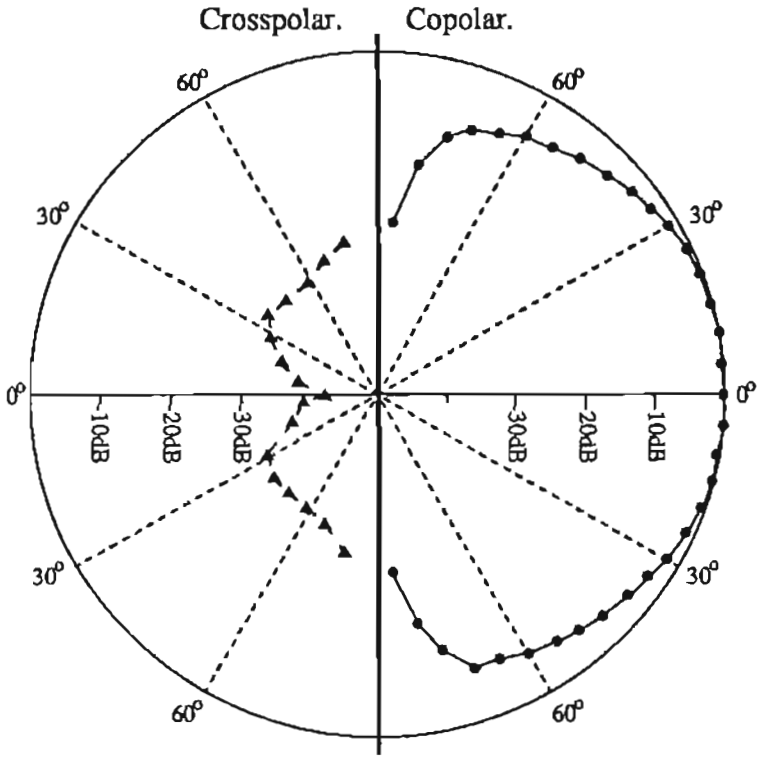

Figure 4.13: Measured diagonal plane radiation patterns for coplanar strip fed, substrate supported coplanar strip folded dipole antenna at 5GHz.

ported coplanar strip folded dipole antennas, and demonstrates that excellent performance can be achieved. Furthermore, an analysis which is capable of accurately modelling the entire antenna structure is shown to be essential if a complete theoretical investigation of the antenna performance is to be undertaken.

4.3 Alternative antenna and feed line geometries

Two alternative geometries are analysed in this section to further demonstrate the range of applicability of the numerical analysis developed above, and to investigate other possibilities for MMIC antenna elements. In Section 4.3.1, an alternative balanced

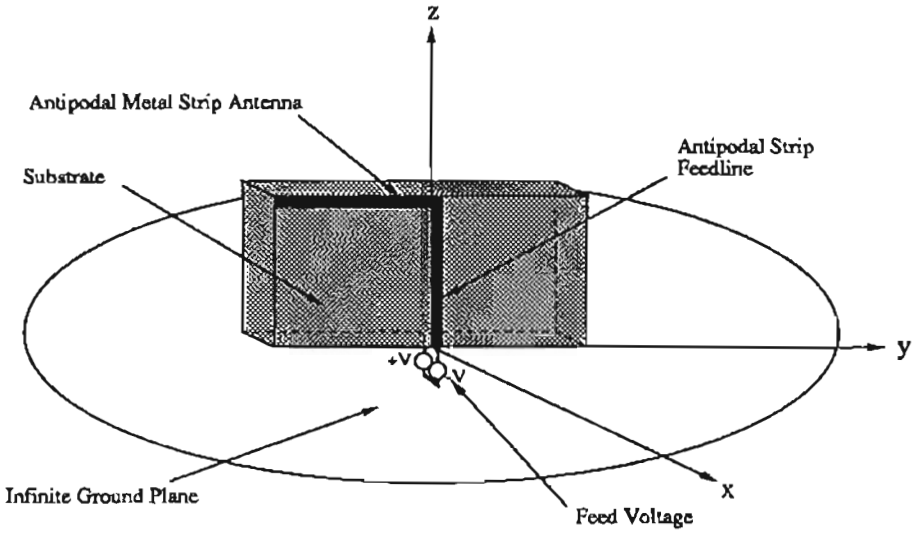

Figure 4.14: Antipodal strip fed substrate supported metal strip antenna geometry for analysis.

feed structure is studied, and in Section 4.3.2 a structure having an unbalanced feed port is studied.

4.3.1 Antipodal strip fed metal strip antenna

A transmission line consisting of two parallel metal strips separated by the dielectric substrate is referred to as an *antipodal strip* transmission line. In Figure 4.14, an antipodal strip feed line is shown for a variant of the substrate supported metal strip antenna where the two arms of the metal strip dipole are constructed on opposite sides of the substrate. The antenna itself may be referred to as an *antipodal strip dipole*, and similar antennas on electrically thin substrates have been employed in operational phased arrays [92]. For this geometry, the excitation used in the analysis consists of balanced voltages at the base of the feed line as shown in Figure 4.14. The antipodal strip feed line can be considered as a balanced form of a microstrip line, and in practice may be excited from a microstrip line by use of a tapered microstrip

balun. More general antenna geometries, such as antennas employing integral baluns [69], may be designed to have a feed structures that incorporate a form of antipodal strip feed line either directly or else as a consequence of the presence of a microstrip line on a finite size ground plane which produces an image of the microstrip line. It is therefore useful to examine the performance of antipodal strip fed substrate supported metal strip antennas, particularly for the case where the substrate is electrically thick, in order to determine their characteristics as MMIC antennas.

The antipodal strip fed substrate supported metal strip antenna shown in Figure 4.14 was analysed using an equivalent-radius thin wire approximation in a similar manner to the coplanar strip fed antennas described in Section 4.2. The dimensions of the substrate and the metal strip width were chosen to be the same as the coplanar strip fed antenna denoted as *Case A* in Section 4.2.3. In addition, the same substrate segmentation was employed, and the equivalent-radius of the thin-wire approximation of the antipodal strip antenna and the antipodal strip feed line was set to $a_e = 0.008L$ in accordance with the procedure outlined in Section 4.2.1. The characteristic impedance of the antipodal strip transmission line may be calculated as described in Section 4.2.2 for the transmission line mode of the back-folded dipole. From the impedance computed at the base of the feed line, a reflection coefficient of $0.63\angle -25°$ was obtained at $L/\lambda_0 = 0.285$, corresponding to the half-wave resonant frequency of the antenna. The computed principal plane radiation patterns of the antenna for $L/\lambda_0 = 0.285$ are shown in Figure 4.15. In contrast to the case of parallel strips comprising a back-folded dipole, where the unbalanced mode currents on the strips predominate, the antipodal strip feed line current is balanced. For this reason, the x-directed polarization current in the substrate which exists close to the position of the metal strips forming the antipodal strip feed line are enhanced rather than suppressed. An increase in cross-polarized radiation in the yz-plane is therefore generated. Moreover, because the x-directed polarization currents excited by the antipodal strip feed line and the antipodal strip dipole do not cancel in the xz-plane, the xz-plane radiation pattern is also affected by cross-polarized radiation. If the increase in cross-polarization from antipodal antenna structures on electrically thick substrates is undesirable, coplanar strip fed antenna structures offer

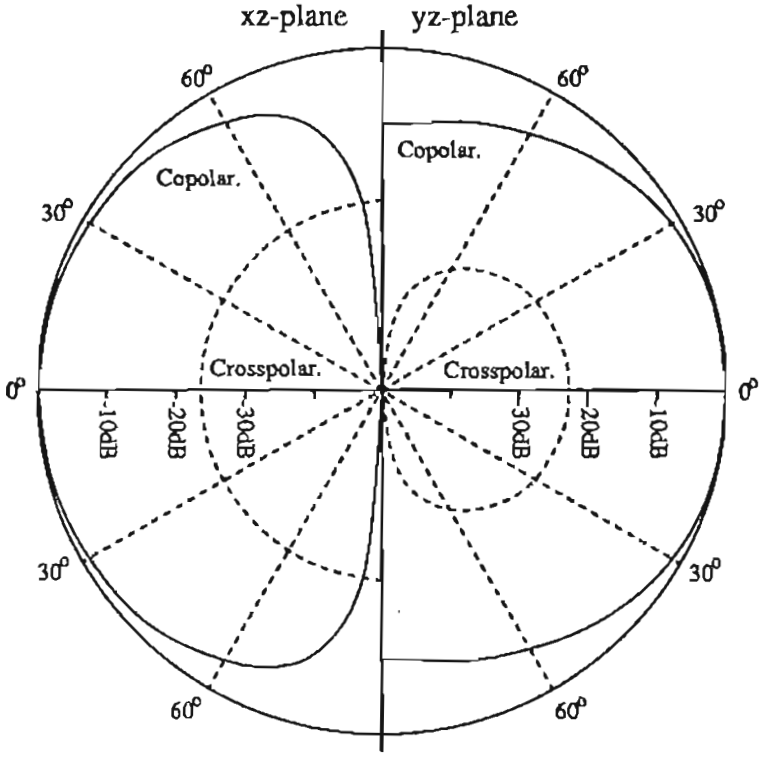

Figure 4.15: Principal plane radiation patterns for antipodal strip fed substrate supported metal strip antenna. (Substrate $t = 0.075L$, $\epsilon_r = 10.2$)

considerable advantages. The primary advantage of an antipodal strip fed structure, however, is the possibility of using a short tapered balun, thereby potentially reducing the substrate area occupied by a MMIC antenna element.

4.3.2 Single strip fed metal strip antenna

A substrate supported metal strip antenna with a single strip feed line is illustrated in Figure 4.16. The geometry consists of a substrate supported metal strip antenna, as studied in Chapter 3, together with a single z-directed metal strip which is fed against the ground plane, and which connects to the metal strip antenna at a distance p from the centre. The provision of an unbalanced feed to the antenna is attractive since it

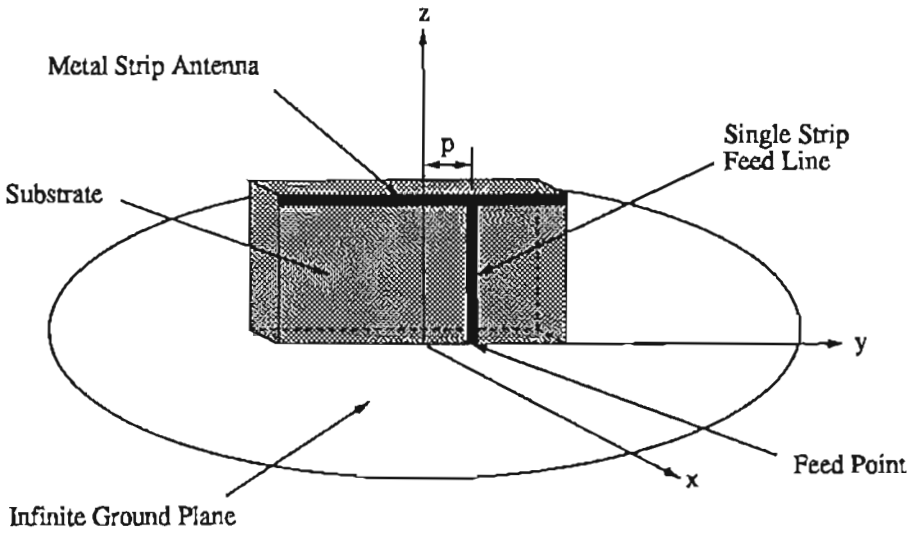

Figure 4.16: Single strip fed substrate supported metal strip antenna geometry for analysis.

eliminates the need for a balun, and thereby reduces the substrate area occupied by a MMIC antenna of this type to possibly the smallest area required for a resonant structure. A single wire fed dipole antenna, on which this structure is based, is described and analysed in detail in Appendix E. In this section, an antenna which is identical to **Antenna A** except for the presence of the single strip feed line is studied. The single strip feed line is chosen to have the same width as the metal strip antenna, and in terms of the physical length, L, of the metal strip antenna, the feed line offset is $p = 0.2L$ from the centre. This offset corresponds to the optimum case for the similarly dimensioned single wire fed resonant dipole in free space above a ground plane analysed in Appendix E, and was retained for the substrate supported antenna considered here.

For the analysis, the metal strips are modelled using the equivalent-radius thin-wire approximation adopted for all of the other feed structures considered in this chapter. The main advantage of the thin-wire approximation in this case is to expedite the modelling of the junction between the feed line and the metal strip antenna. Because only axially directed currents are considered, Kirchoff's current law can be applied at

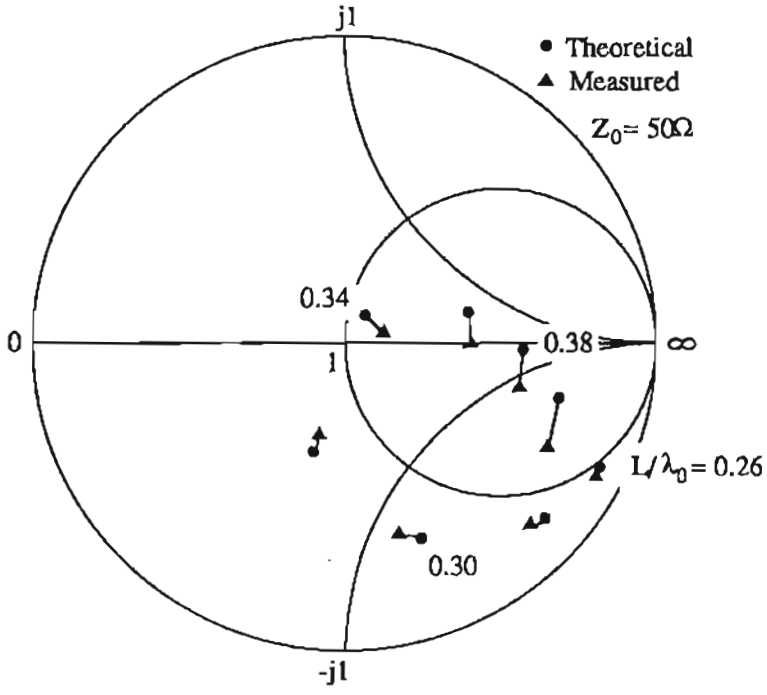

Figure 4.17: Input impedance of single strip fed metal strip antenna ($p = 0.2L$).

the junction as outlined in Appendix C. A substrate segmentation $n_x = 2$, $n_y = 10$ and $n_z = 10$ was used in the analysis, together with the corresponding equivalent-radius $a_c = 0.008L$.

An antenna for testing the analysis was constructed on a 1.9mm thick RT Duroid™ 6010 substrate with a metal strip dipole of length, $L = 25.4$mm. The remaining dimensions were scaled as for **Antenna A** and as described above for the single strip feed line. A coaxial feed port was used to excite the single strip feed from behind a large metal ground plane.

Theoretical and measured results for the feed point impedance at the base of the metal strip feed line are shown in Figure 4.17. The antenna is noted to be resonant at $L/\lambda_0 = 0.34$ (approximately 4GHz), and has a bandwidth of approximately 10%. It can be seen from the results that the input impedance at resonance is close to 50 ohms, and it is therefore feasible in the case of a MMIC antenna to excite the single strip

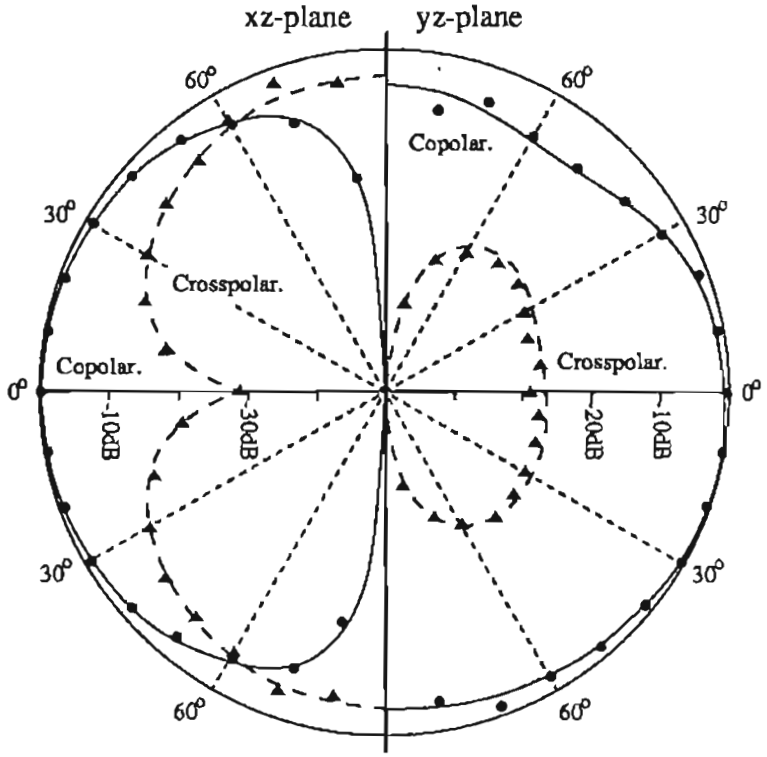

Figure 4.18: Principal plane radiation patterns for a single strip fed substrate supported metal strip antenna ($p = 0.2L$).

feed line directly from a 50 ohm microstrip line without the need for any additional impedance matching. The agreement between the numerical analysis and the measured results is also seen to be very good, which not only serves to verify the analysis of the single strip fed substrate supported metal strip antenna, but also provides confirmation of the accuracy of the equivalent-radius thin-wire approximation for a structure where it is possible to directly measure the impedance characteristics.

Principal plane radiation patterns are given in Figure 4.18. Again the agreement between the numerical analysis and the measured results is good, except for the noticeable effects of diffraction at large angles from the z-axis due to the imperfect ground plane used in the measurements. Absorbing material was again placed around the circumference of the ground plane to minimize edge diffraction. As predicted from the analysis of the single wire fed dipole in Appendix E, a significant level of cross-

polarization exists in the xz-plane due to radiation from currents on the metal strip feed line. Additional z-directed polarization currents induced in the substrate by the current on the single strip feed line also contribute to the cross-polarized radiation. The on-axis cross-polarized radiation is a consequence of the unbalanced geometry, and the cross-polarization in the yz-plane is due to x-directed polarization currents in the substrate. In addition to the cross-polarization effects noted above, a beam-squint in the yz-plane co-polarized radiation pattern due to asymmetrical interference by radiation from the currents on the single strip feed line is apparent. The null in the radiation pattern which occurs for the single wire fed dipole described in Appendix E does not appear here due to the additional radiation effects of the polarization currents in the substrate that reinforce radiation in that direction.

When the results obtained above are compared with those for the single wire fed dipole described in Appendix E, the presence of the substrate is found to have the useful effect of improving the impedance characteristics as well as improving the yz-plane co-polarized radiation pattern. Although the radiation characteristics of the single strip fed substrate supported metal strip antenna are still poor with respect to cross-polarized radiation when compared to the other antennas considered in this chapter, the possibility of small substrate area usage, and an avoidance of the requirement for balun and impedance matching structures, makes them potentially attractive for some applications. In addition, with the careful choice of an array geometry, techniques can be used to eliminate the overall beam-squint and reduce the overall cross-polarization of the array. One such geometry is outlined in Section 6.4.

4.4 Summary

In this chapter, some aspects of the design and analysis of practical MMIC antenna geometries have been described. From the consideration of several design issues, the importance of detailed and accurate numerical modelling of complex geometries has been highlighted. Although basic design information is available from the analysis

of idealized geometries, it has been shown that for a complete understanding of the characteristics of practical antenna elements, the requirement exists for all of the major features of the structure to be incorporated in the analysis.

The effect of feed lines on the radiation characteristics of substrate supported metal strip antennas is such that the inclusion of the feed line in the analysis is essential for the correct modelling of the cross-polarization performance of the antenna. A method for efficiently performing the analysis is derived, and the use of the method is demonstrated by its application to a variety of problems of practical significance. The issue of achieving an impedance match between the feed line and substrate supported metal strip antenna is resolved by the use of folded metal strip dipole structures. Finally, methods for controlling cross-polarized radiation by means of the antenna geometry are discussed. Comparisons with measured results serve to confirm the accuracy of the numerical results, and illustrate the design techniques which are developed. Sufficient information on the performance of practical substrate supported metal strip antennas can be obtained for design purposes by application of the techniques described in this chapter.

The important contributions of this chapter are therefore:

- The development of a computationally efficient analysis of complete substrate supported metal strip antennas incorporating feed lines and impedance matching.
- The development of an accurate numerical design approach for metal structures on electrically thick substrates, which is essential for MMIC antennas.
- The application of computed design data to practical structures consisting of feeding and radiating parts, and verification by experimental measurements that an appropriate design has been achieved.
- The discovery of the relationship between the various sources of cross-polarized radiation in substrate supported metal strip antennas with feed lines, and the exploitation of the feed line geometry to control the cross-polarization performance.

- The use of back-folded dipole geometries to control the cross-polarization performance of the antenna.
- The study of the characteristics of various basic feed structures on electrically thick substrates.

It has therefore been demonstrated that the substrate supported metal strip antennas proposed for application to monolithically fabricated millimetre wavelength active arrays are capable of good performance with regard to important design parameters. The research presented in this chapter has elucidated engineering design opportunities for MMIC antennas not previously understood or available.

Although it is now possible to accurately model the characteristics of single antenna elements in isolation, further application of the analysis to the problems of mutual coupling and the scanning performance of arrays is required. These problems are considered in the following chapters.

Chapter 5

Mutual Coupling Between Substrate Supported Metal Strip Antennas

5.1 Introduction and overview

Where a substrate supported metal strip antenna exists in isolation, the results obtained in Chapters 3 and 4 completely characterize the antenna performance. In the case of an array of several or many substrate supported metal strip antennas, however, the radiation from nearby elements can affect the individual resultant excitation. For proper operation of each element of the array, the influence of the nearby elements must be computed in advance as part of the design process. An understanding of the effect of mutual coupling with nearby antenna elements is therefore an important requirement for array design. Mutual coupling data is also useful for synthesis problems relating to small arrays, where the elements operate in different environments due to their relative positions in the array [93,94].

While an infinite array technique, such as that described later in Chapter 6, allows the characteristics of elements of large arrays which are far from the array boundaries to be determined under excitation conditions corresponding to a uniform magnitude and predetermined phase gradient over the array aperture [27], more fundamental information on the interaction between elements is obtained from the self and mutual impedances associated with all of the elements of the array. The self and mutual impedances make up an *impedance matrix* which relates the voltage excitation at the feed port of each element to the current at each feed port. For the case of a general excitation, or where the array is small, the complete impedance matrix is usually required, and may be obtained theoretically or experimentally. Due to the wide variety of antenna elements and array geometries which may be considered in a realistic design study, and the high cost of experimentally obtaining the required self and mutual impedances for each specific case, a theoretical approach is preferred. For small arrays, this usually means that all of the terms of the impedance matrix must be calculable from accurate models of the antenna element and the array. Even in the case of larger arrays, the study of mutual coupling between elements is useful for determining the effect of non-uniformities in geometry or excitation for which infinite array techniques are not correct, for example as is the case with antenna elements close to the edge of an array.

The calculation of all of the self and mutual impedances for an array of substrate supported metal strip antennas is limited in practice by the computational requirements imposed by the numerical analysis, and as a consequence is restricted to arrays of only a few elements. In spite of the fact that the complete environment of a large array cannot be modelled, useful results can still be obtained, particularly for cases where it can be shown that close neighbour interactions dominate the mutual coupling effects.

In this chapter, two-element and three-element arrays of substrate supported metal strip antennas are analysed. The analytical method described in Chapter 3 is applied to determine the current distributions on the elements of the arrays for various feed port terminations which allow the mutual impedances to be calculated. Because the computational requirements for the solution of the electric-field integral equations

representing the arrays are large, high-performance large-scale computer resources are needed. Although more general cases may be considered, the use of symmetry constraints serves to reduce the computational burden required for the solution. Results obtained from this analysis are compared with experimental measurements on collinear and collateral three-element arrays as a test of the analytical model and numerical method, and show good agreement. The test assemblies used in the measurements are fabricated in such a way that the assumptions in the analytical model are accurately satisfied, and consequently the agreement between the numerical results and the measurements is a validation of the analysis as an accurate design method. Extending the analysis to include feed structures, it is shown that it is possible to predict the mutual coupling between the elements of three-element arrays of substrate supported coplanar strip folded dipoles with coplanar strip feed lines. Comparisons are also made with typical arrays of wire dipoles without substrates to further investigate the effect of the substrate on the mutual coupling.

The aim of this chapter, therefore, is to show how accurate information with regard to mutual coupling between the elements of practical MMIC antenna arrays can be obtained by extending the analytical model and numerical method outlined for isolated antennas in Chapter 3.

5.2 Formulation and numerical implementation

Collinear and collateral arrays of substrate supported metal strip antennas are illustrated in Figures 5.1 and 5.2 respectively. Two-element and three-element arrays are considered in this study, where the two-element arrays are obtained for both the collinear and the collateral cases by omitting element 3. The geometry of the substrate supported metal strip antenna elements is that of the idealized antenna considered in Chapter 3, where the ground plane is continuous and infinite in extent, and no feed lines are included. The voltages applied at the infinitesimal gap feed ports of the elements are denoted by V_1, V_2 and V_3, and the feed port currents I_1, I_2 and I_3 are obtained from

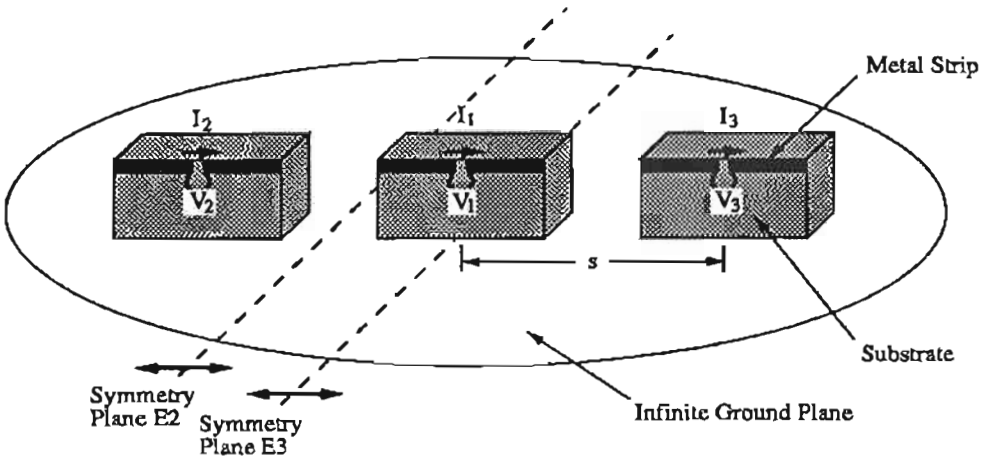

Figure 5.1: Collinear array geometry, idealized for analysis.

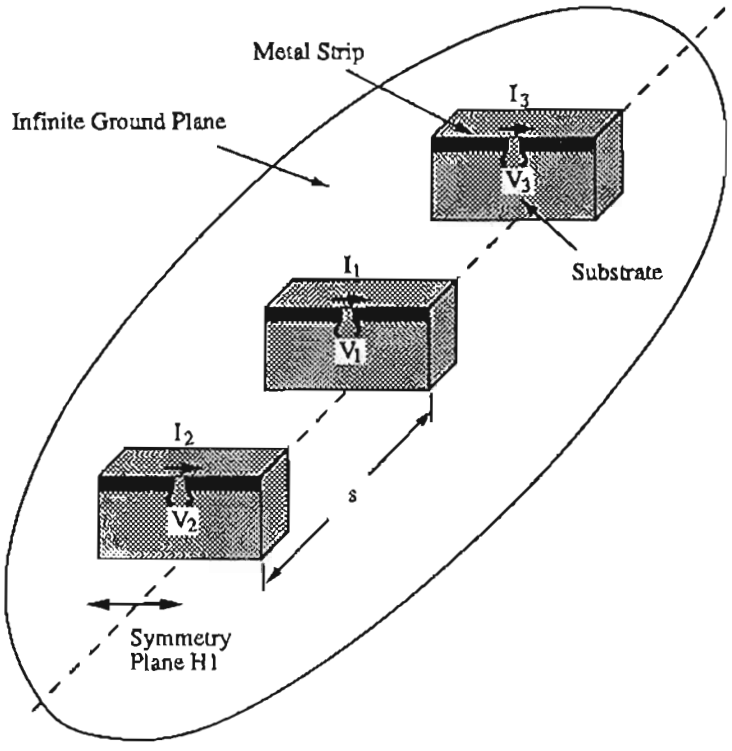

Figure 5.2: Collateral array geometry, idealized for analysis.

the resulting current distributions on the metal strips. These currents are computed from the electric field integral equations using the method developed in Chapter 3. In this way, no assumptions regarding the current distributions are made beyond those which are justified by any symmetry which exists in the geometry and excitation. Because up to 1800 pulse basis functions are used in the calculation, a grid method is again employed to improve the computational efficiency. An appropriate segmentation is first chosen for the antenna elements using the convergence of the computed input impedance of a single, isolated antenna as a guide. In the collinear array configuration, the separation between the elements, not occupied by dielectric, is constrained to an integral number of segment lengths in the y-direction, and the required Green's function integrals are computed for all intersection points of a grid extending over the entire array for the widest spacing required. Only one look-up table is computed for the entire range of element spacings considered. Because the space between the element which is not filled by dielectric is large for the collateral array configuration, this method produces a look-up table with a large number of unrequired entries, and for this reason separate look-up tables for each element spacing are computed. The moment matrix that relates the electric field scattered by the current sources at each segment to the incident electric field at the centre of each segment for the complete array is filled from the appropriate look-up table. Where symmetry can be identified it is exploited to reduce the number of basis functions, and hence the size of the moment matrix, required for the solution.

The analysis that follows is presented in terms of the impedance matrices related to the feed ports of the antenna elements considered. This approach is taken for two reasons: First, from the point of view of the theoretical development, the consideration of the impedance matrices associated with the feed ports provides a self-contained description of the problem without the need to involve the details of the numerical analysis. The details of the numerical analysis are readily ascertained by applying the numerical technique described in Chapter 3 to the appropriate geometry. Second, the approach provides a nexus between the theoretical formulation in this section and the experimental verification in the next. Using this description, the feed port voltages

and currents are related by the matrix equation

$$\mathbf{Z_n I_n} = \mathbf{V_n} \tag{5.1}$$

where the impedance matrix $\mathbf{Z_n}$ is a $n \times n$ matrix for an n-element array.

Considering first the collinear arrays; for the two-element array

$$\mathbf{Z_2} = \begin{bmatrix} Z_{11} & Z_{12} \\ Z_{21} & Z_{22} \end{bmatrix}, \quad \mathbf{I_2} = \begin{bmatrix} I_1 \\ I_2 \end{bmatrix} \quad \text{and} \quad \mathbf{V_2} = \begin{bmatrix} V_1 \\ V_2 \end{bmatrix}. \tag{5.2}$$

By reciprocity $Z_{21} = Z_{12}$ and with identical elements $Z_{22} = Z_{11}$. For a structure that exhibits symmetry in its geometry and feed port conditions, two independent equations must be obtained by applying two independent feed port conditions. For the two-element array, the conditions are chosen to be firstly $V_1 = 1$ and $V_2 = 1$, and secondly $V_1 = 1$ and $V_2 = -1$, and a symmetry plane appropriate for these excitations is identified as E2 in Figure 5.1. The presence of such a symmetry plane makes it possible to determine the current distributions for the entire structure economically by solving for currents on one of the elements and treating the currents on the other element as dependent sources or images. For the first excitation the symmetry is even, and the feed port current on element 1 is denoted $I_{1,\text{even}}$. For the second excitation the symmetry is odd, and the feed port current on element 1 is denoted $I_{1,\text{odd}}$. The self impedance Z_{11} may therefore be obtained from the solution of equation 5.1 as

$$Z_{11} = \frac{V_1}{2}\left(\frac{1}{I_{1,\text{even}}} + \frac{1}{I_{1,\text{odd}}}\right), \tag{5.3}$$

and similarly the mutual impedance Z_{12} as

$$Z_{12} = \frac{V_1}{2}\left(\frac{1}{I_{1,\text{even}}} - \frac{1}{I_{1,\text{odd}}}\right). \tag{5.4}$$

For the three element collinear array,

$$\mathbf{Z_3} = \begin{bmatrix} Z_{11} & Z_{12} & Z_{13} \\ Z_{21} & Z_{22} & Z_{23} \\ Z_{31} & Z_{32} & Z_{33} \end{bmatrix}, \quad \mathbf{I_3} = \begin{bmatrix} I_1 \\ I_2 \\ I_3 \end{bmatrix} \quad \text{and} \quad \mathbf{V_3} = \begin{bmatrix} V_1 \\ V_2 \\ V_3 \end{bmatrix}. \tag{5.5}$$

Again by reciprocity $Z_{12} = Z_{21} = Z_{13} = Z_{31}$ and $Z_{23} = Z_{32}$, and with identical outer elements $Z_{22} = Z_{33}$. A symmetry plane is identified as E3 in Figure 5.1 for the analysis, and the central element is excited with $V_1 = 1$. The outer elements are terminated in turn by a short-circuit resulting in $V_2 = V_3 = 0$, and an open-circuit resulting in $I_2 = I_3 = 0$. From the symmetry of the geometry and excitation, it can be seen that only the current on one half of the array as divided by the symmetry plane E3 need be computed, with the remaining currents treated as dependent sources or images. It is also apparent that only two independent feed ports exist under these conditions, and the matrix equation 5.1 can be reduced to

$$\mathbf{Z_2'}\mathbf{I_2'} = \mathbf{V_2'} \tag{5.6}$$

where

$$\mathbf{Z_2'} = \begin{bmatrix} Z_{11} & 2Z_{12} \\ Z_{21} & Z_{22} + Z_{23} \end{bmatrix}, \quad \mathbf{I_2'} = \begin{bmatrix} I_1 \\ I_2 \end{bmatrix} \quad \text{and} \quad \mathbf{V_2'} = \begin{bmatrix} V_1 \\ V_2 \end{bmatrix}. \tag{5.7}$$

It should be noted that in 5.7, the full feed port voltage V_1 has been retained, and as a consequence $\mathbf{Z_2'}$ is asymmetrical. Replacing V_1 with $V_1/2$ to allow for the presence of the symmetry plane would result in a symmetrical form for $\mathbf{Z_2'}$. The self impedance Z_{11} of the central element of the three-element array is obtained directly from the case where the outer elements are terminated by open-circuits, such that

$$Z_{11} = \frac{V_1}{I_{1,\text{open}}}, \tag{5.8}$$

and the mutual impedance Z_{12} between adjacent elements of the three-element array is obtained by using the first of equations 5.7 for each of the two outer element

terminations, such that

$$Z_{12} = \frac{V_1}{2} \frac{I_{1,\text{open}} - I_{1,\text{short}}}{I_{1,\text{open}} I_{2,\text{short}}} \tag{5.9}$$

where *open* and *short* refer to the outer element feed port conditions for which the feed port currents are computed.

The self impedance of the outer elements of the three-element collinear array, and the mutual impedance between the outer elements of the three-element collinear array, may be obtained in the manner described above for a two-element array, where the excitation conditions are firstly $V_2 = 1$ and $V_3 = 1$, and secondly $V_2 = 1$ and $V_3 = -1$. Element 1 is terminated in an open circuit, as required by the definition of the impedance matrix, such that $I_1 = 0$. The symmetry plane for this case is again E3 in Figure 5.1, and the currents are therefore required to be computed for half the structure comprising the whole of element 2 and half of element 1, with the currents on element 3 and the remaining half of element 1 treated as dependent sources or images. Denoting the current at the feed port of element 2 as $I_{2,\text{even}}$ for the first excitation, and $I_{2,\text{odd}}$ for the second excitation, the self impedance Z_{22} of the outer elements may be found from

$$Z_{22} = \frac{V_2}{2} \left(\frac{1}{I_{2,\text{even}}} + \frac{1}{I_{2,\text{odd}}} \right), \tag{5.10}$$

and the mutual impedance between the outer elements from

$$Z_{23} = \frac{V_2}{2} \left(\frac{1}{I_{2,\text{even}}} - \frac{1}{I_{2,\text{odd}}} \right). \tag{5.11}$$

Considering now the collateral array as shown in Figure 5.2, a symmetry plane shown as H1 is present for both the two-element and the three-element arrays, and the current distributions need only be determined on half of each element with the remaining currents treated as dependent sources or images. The analysis of the two-element and three-element collateral arrays then proceeds as described above for the collinear arrays. It is noted, however, that the equalities $Z_{11} = Z_{22}$ for a two-element array and $Z_{22} = Z_{33}$ for a three-element array, identified above in relation to collinear arrays, are not strictly correct for collateral arrays because of the relative position of

the substrates. Where the element spacing is much larger than the substrate thickness, as is the case for the arrays which will be considered here, the actual conditions for the collateral arrays are closely approximated by the assumed equalities. The validity of this assumption has been verified by comparing the self impedances of each element of the array, which are available from the computation.

For both the two-element and three-element arrays the excitation voltages and feed port terminations are applied explicitly at the relevant feed ports, and the feed port currents are obtained in each case with approximately the same computational burden as for the collinear arrays. The self impedance of the elements of a two-element collateral array may be obtained from equation 5.3, and the mutual impedance between the elements of a two-element collateral array from equation 5.4. Similarly, the self-impedances of the central element and outer elements of a three-element collateral array may be obtained from equations 5.8 and 5.10 respectively, and the mutual impedances between adjacent elements, and between the outer elements, of a three-element collateral array from equations 5.9 and 5.11 respectively.

Using the approach outlined above, all of the terms of the impedance matrices related to the feed ports of two-element and three-element arrays of substrate supported metal strip antennas may be computed theoretically.

5.3 Experimental verification

Access to a well defined feed port that allows direct connection to microwave impedance measuring equipment, such as a network analyser test set equipped with a 50 ohm coaxial input port, is necessary for accurate experimental measurements. For both the collinear and collateral three-element arrays, a coaxial feed port is obtained for the central element by replacing the symmetry planes identified as E3 in Figure 5.1 and H1 in Figure 5.2 with large metal ground planes, in a similar manner as for the impedance measurement outlined in Section 3.3.1. In this way, the central element

of both arrays is a monopolar element. A collinear two-element array does not have the symmetry required for creating a coaxial feed point at either element, and for this reason only three-element arrays are subjects for experimental testing of the numerical analysis. For the collinear array, a single dipolar element and its image, open-circuited or short-circuited at the feed port at the centre of the metal strip as required, provide the outer elements. For the collateral array, two monopolar outer elements, open-circuited or short-circuited to the metal image plane as required, are used. It would be possible to measure the mutual coupling between the elements of the collateral array directly by providing a coaxial feed port to all three elements, however, extensive mechanical modifications would be required to the experimental assembly for different spacings. For this reason, the method employing open-circuited and short-circuited outer elements is adopted.

In the measurement assembly, the central element is excited from a SMA connector as in the impedance measurements described in Section 3.3.1, and illustrated in Figure 3.3. The single outer element of the collinear array, or the two imaged outer elements of the collateral array are positioned to give the required element spacings. Arrays scaled to operate at microwave frequencies are tested, and impedance measurements are made at the coaxial feed port of the central element using a Hewlett-Packard 8510B network analyser. The impedance at the base of the central metal strip monopole is obtained by applying the computed reference plane offset delay, t_d, to the measured results, as described in Section 3.3.1. As in those measurements, no further empirical adjustments are made to the measured impedance.

To determine the self impedance Z_{11} of the central element of the arrays, and the mutual impedance Z_{12} between adjacent elements of the arrays, a measurement of the monopolar input impedance of the central element is required for the two conditions of open-circuited and short-circuited outer elements. The measured monopolar impedances are denoted by Z_{oc} and Z_{sc} for the open-circuit and short-circuit cases respectively.

The self impedance Z_{11} of the central element of the arrays is simply obtained from

the measured monopolar impedance with the outer elements open-circuited, and

$$Z_{11} = 2Z_{oc}. \tag{5.12}$$

The measurement will be affected by antenna losses, as well as by the losses associated with the coaxial feed port described in Section 3.3.3, and is anticipated to be somewhat higher than that predicted by the analysis.

Since the outer elements are identical in each array, the interpretation of the measured results and the calculation of Z_{12} can proceed in a similar manner to that presented in [95] for a two-element array. All of the terms of the impedance matrices in 5.5 and 5.7 are dipolar, and in addition to those assumptions already justified by reciprocity or by the identical nature of the elements, the following assumptions are made:

$$Z_{22} = Z_{11} \quad \text{and} \quad Z_{23} = 0. \tag{5.13}$$

The implications of these assumptions will be addressed later. Under these assumptions, the matrix equation 5.6 can be used to deduce Z_{12} from Z_{oc} and Z_{sc}, and for both the collinear and collateral arrays

$$Z_{12} = \sqrt{2Z_{oc}(Z_{oc} - Z_{sc})}. \tag{5.14}$$

Since equation 5.14 will have two solutions, the correct sign may be determined by considering the limiting case for close spacing and preserving continuity at each zero crossing. It is noted that the measured mutual impedance may be sensitive to experimental errors when the $Z_{oc} - Z_{sc}$ factor of equation 5.14 is small, as is anticipated for wide element spacings. Fortunately, the errors which are associated with the element positioning and measurement procedure are small, and the resulting scatter of measured data is found to be correspondingly small.

One of the assumptions 5.13 which was inherent in the derivation of equation 5.14 is that $Z_{22} = Z_{11}$. There are two ways in which this assumption is not strictly correct for the measurement. Firstly, the environment of the outer elements is different from

that of the central element, particularly for close element spacings. This will affect the first occurrence of the measured Z_{oc} factor of equation 5.14, since this factor relates to the outer elements. Since it is not possible to determine Z_{22} directly from the experiment, no correction can be applied. Secondly, the losses due to radiation from, and imperfections in, the coaxial feed port are not considered in the assumption that $Z_{22} = Z_{11}$. In the experimental procedure, only the central element is excited, and therefore any losses associated with the coaxial feed should be eliminated from the first occurrence of the measured Z_{oc} factor of equation 5.14 since this factor again relates to the outer (unfed) elements. A correction for this effect can be applied where the feed port resistance attributable to the feed losses is known.

From the above discussion it can be seen that a carefully designed experimental procedure can be developed to verify the mutual impedances computed by the numerical analysis in Section 5.2.

5.4 Numerical and experimental results

Results are presented here for substrate supported metal strip antenna elements having dimensions, normalized to the metal strip length L, of height $H = 0.5L$ above the ground plane, strip width $w = 0.05L$, and substrate thickness $t = 0.075L$. The relative permittivity of the substrate was $\epsilon_r = 10.2$. These dimensions correspond to **Antenna A**, analysed in Section 3.4, which in isolation has a half-wave resonance corresponding to $L/\lambda_0 = 0.285$. The substrate segmentation in the analysis was such that for each full element, $n_x = 2$, $n_y = 19$ and $n_z = 10$. A total of 1178 variables are required to compute the current distributions for a two-element collinear array, and 1240 variables for a two-element collateral array. For three-element collinear and collateral arrays, 1798 and 1860 variables are required respectively. The convergence of the solution is confirmed by re-evaluating the current distributions for a coarser segmentation. Because computer storage and run-time considerations permit it, the finer segmentation was retained for all of the computations. An average CPU time per element spacing was approximately

100 seconds on a Fujitsu VP2200 vector-supercomputer.

For the measurements on the collinear and collateral three-element arrays, the imaged and complete antenna elements were constructed on RT-Duroid^{TM} 6010 substrates, and were scaled to obtain a half-wave resonance at approximately 3.4GHz. The computed and measured results that follow are for the half-wave resonant frequency of the substrate supported metal strip antennas.

The computed self impedance Z_{11} of the elements of a two-element collinear array, and of the central element of a three-element collinear array, are shown in Figure 5.3 for element spacings, s, between $0.35\lambda_0$ and $0.8\lambda_0$. Self impedances of the corresponding elements of two-element and three-element collateral arrays are shown in Figure 5.4. For close collinear array element spacings, the self impedances are influenced by the presence of the other elements, however, for wide spacings the self impedances approach those of the isolated antenna element. For the range of collateral array element spacings, the self impedances are essentially constant. For both the three-element collinear and collateral arrays, the measured self impedance of the central element for element spacings, s, between $0.40\lambda_0$ and $0.75\lambda_0$ in steps of $0.05\lambda_0$ is also shown in Figures 5.3 and 5.4. The losses associated with the antenna elements and coaxial feed, as described in Section 3.4, are found to account for the discrepancy between the measured and theoretical self resistance. The small discrepancy between the measured and theoretical self reactance is attributed to the feed point modelling in the numerical analysis. The coaxial feed structure used in the measurement will have parasitic effects associated with the open end feeding the metal strip monopole, however, in the numerical analysis an ideal delta-gap generator is used.

The computed mutual impedances Z_{12} between the elements of collinear and collateral two-element arrays, and between adjacent elements of collinear and collateral three-element arrays, are shown in Figures 5.5 and 5.6 for element spacings, s, between $0.35\lambda_0$ and $0.8\lambda_0$. The results reveal that the mutual coupling between adjacent elements of a three-element array is almost identical to that between the elements of a two-element array. This is true for both the collinear and collateral cases, although for

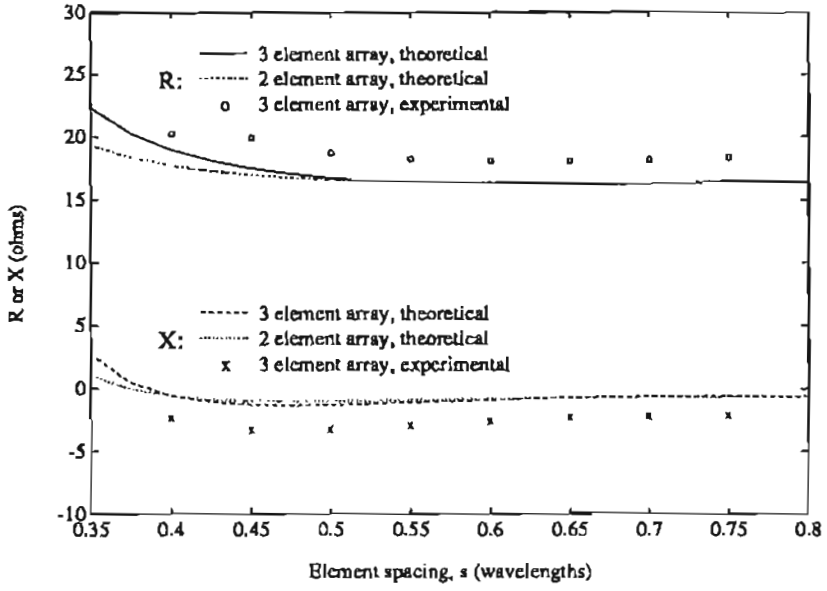

Figure 5.3: Self impedance Z_{11} of the central element of the three element collinear array, and of the elements of a two element collinear array ($L/\lambda_0 = 0.285$).

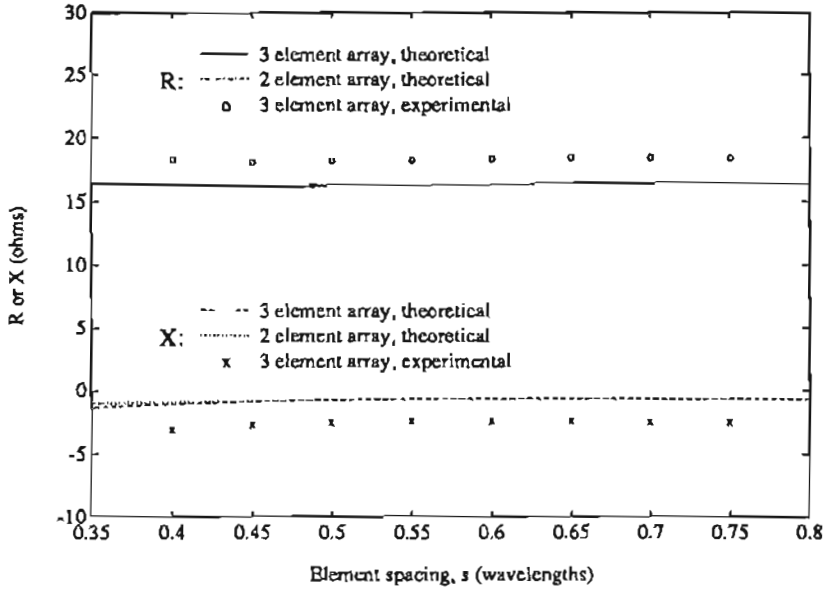

Figure 5.4: Self impedance Z_{11} of the central element of the three element collateral array, and of the elements of a two element collateral array ($L/\lambda_0 = 0.285$).

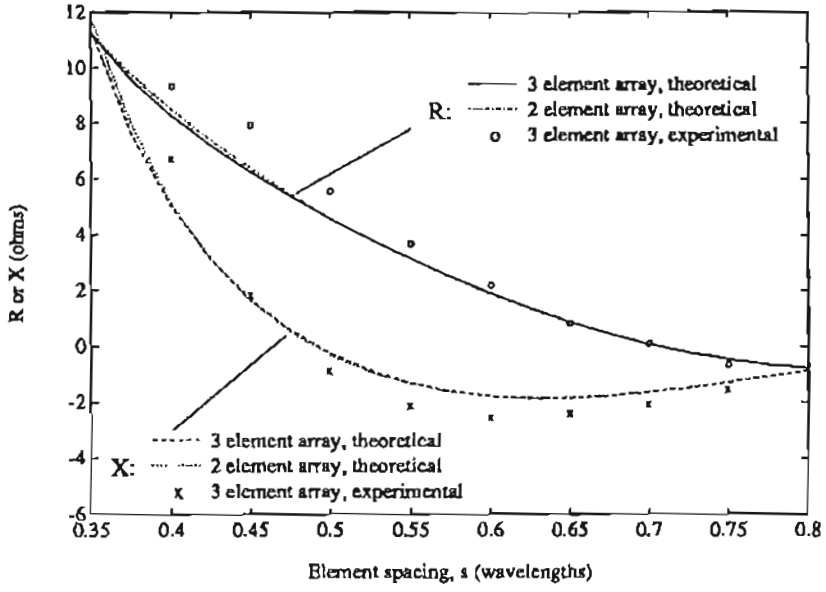

Figure 5.5: Mutual impedance Z_{12} for adjacent elements of the three element collinear array, and for elements of a two element collinear array ($L/\lambda_0 = 0.285$).

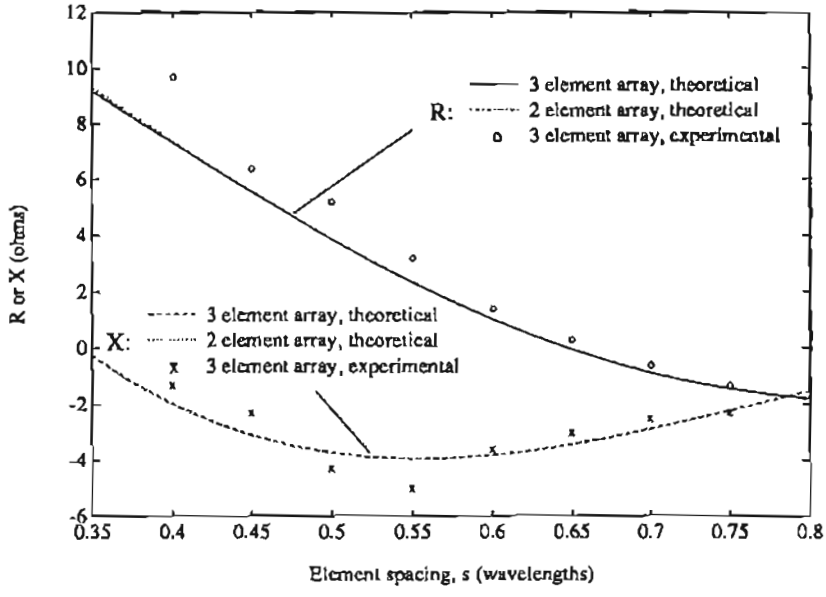

Figure 5.6: Mutual impedance Z_{12} for adjacent elements of the three element collateral array, and for elements of a two element collateral array ($L/\lambda_0 = 0.285$).

closer element spacings a small departure is observed for the collinear array where the effect of the third element becomes more pronounced. Measured results for the mutual impedance between adjacent elements of the three-element arrays for element spacings, s, between $0.40\lambda_0$ and $0.75\lambda_0$ in steps of $0.05\lambda_0$, obtained using the technique described in Section 5.3, are also shown in Figures 5.5 and 5.6. In general good agreement is obtained with the theoretical results, the scatter in experimental data being attributed to the experimental errors introduced as described in Section 5.3. In addition, it has been computed that the effect of the coaxial feed losses, which are not included in the analysis, accounts for up to 0.25 ohms of the discrepancy between the measured and theoretical mutual resistance, with the mutual reactance being unaffected by the applied correction. Furthermore, for close element spacings of the three-element collinear array, the difference between the outer element and central element self-impedance becomes more pronounced, and the assumption of equal self-impedances therefore affects the accuracy of the mutual impedance calculated from the measured results.

For the three-element collinear and collateral arrays, the computed self impedances Z_{22} of the outer elements, as a function of the outer element spacing $s' = 2s$, are given in Figures 5.7 and 5.8 respectively. The central element in each case is terminated in an open-circuit as required by the definition of the impedance matrix. Also shown are the self impedances of two-element collinear and collateral arrays formed from the corresponding three-element arrays with the central elements removed. For close collinear array element spacings, the influence of the central element is apparent in the results.

The computed mutual impedances Z_{23} between the outer elements of collinear and collateral three element arrays are shown in Figures 5.9 and 5.10 respectively, again as a function of the outer element spacing s'. In both cases the central element is terminated in an open-circuit as required by the definition of the impedance matrix. For comparison, Figures 5.9 and 5.10 also present the results of analyses of two-element collinear and collateral arrays formed from the corresponding three-element arrays with the central element removed. It is clear from the results that for close spacings, the mutual coupling between the outer elements of the three-element arrays is affected by

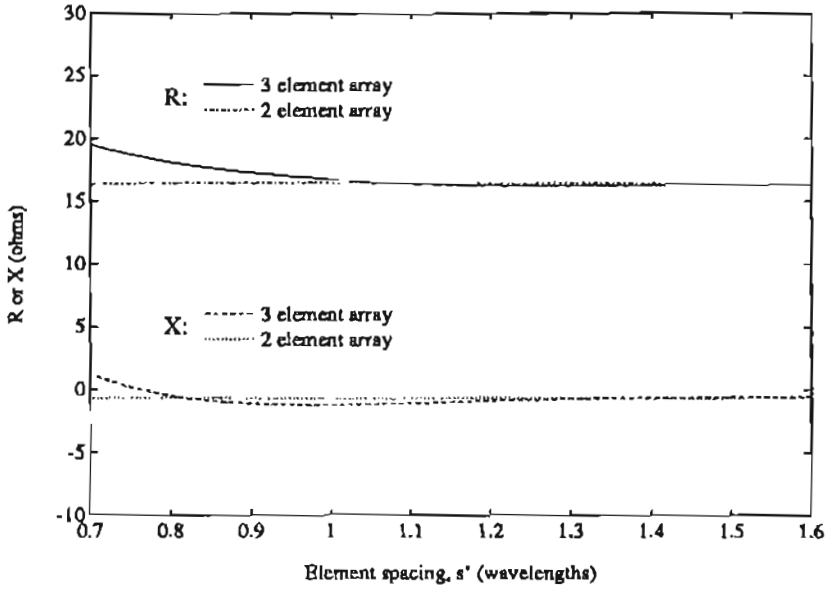

Figure 5.7: Self impedance Z_{11} of the outer elements of the three element collinear array, and of the elements of a two element collinear array formed by removing the central element ($L/\lambda_0 = 0.285$).

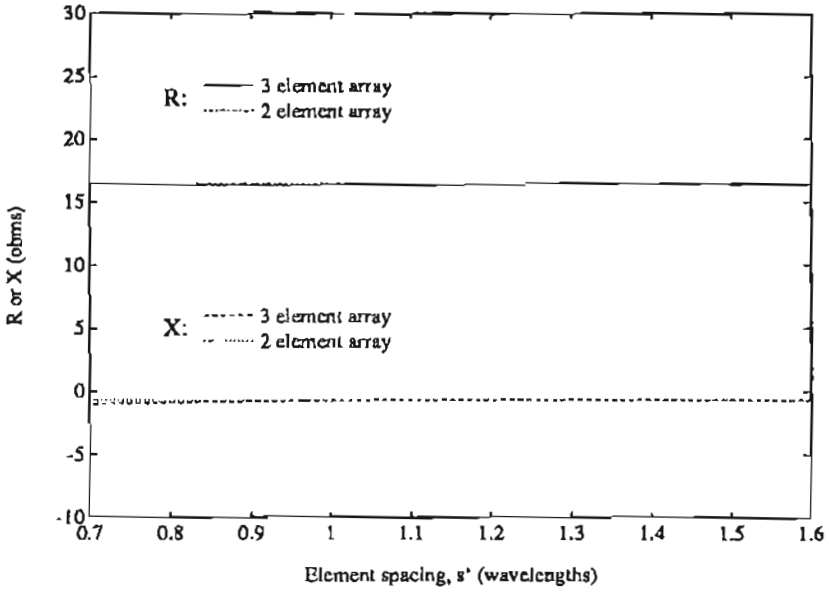

Figure 5.8: Self impedance Z_{11} of the outer elements of the three element collateral array, and of the elements of a two element collateral array formed by removing the central element ($L/\lambda_0 = 0.285$).

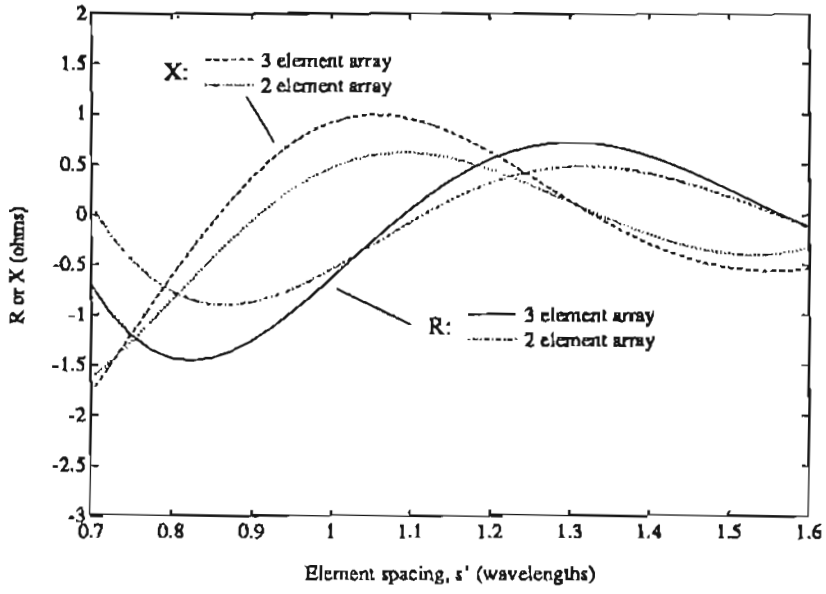

Figure 5.9: Mutual impedance Z_{23} for outer elements of the three element collinear array, and for elements of a two element collinear array formed by removing the central element ($L/\lambda_0 = 0.285$).

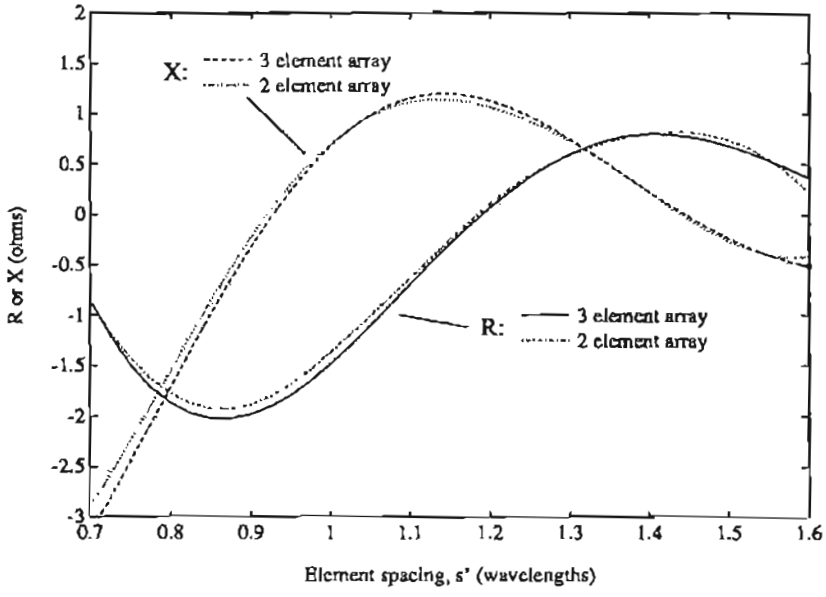

Figure 5.10: Mutual impedance Z_{23} for outer elements of the three element collateral array, and for elements of a two element collateral array formed by removing the central element ($L/\lambda_0 = 0.285$).

the presence of the central element, particularly for the collinear array.

The self and mutual impedances derived and experimentally verified above allow the complete impedance matrices related to the feed ports of two-element and three-element collinear and collateral arrays to be obtained. The resulting impedance matrices may be employed in the analysis of practical arrays. Examples of two-element and three-element arrays of substrate supported coplanar strip folded dipoles, fed by coplanar strip feed lines, are given in the next section.

5.5 Three-element substrate supported metal strip folded dipole arrays

Collinear and collateral three-element arrays of substrate supported coplanar strip folded dipole antennas with coplanar strip feed lines were designed and constructed with element spacings $s = 0.5\lambda_0$ in each case. The dimensions and substrate parameters chosen for the design were the same as those of **Antenna C** in Section 4.2.3, and are related also to the dimensions and parameters of the idealized antennas for which the self and mutual impedances were computed in Section 5.4. For the array construction, each of the elements was housed in the assembly shown in Figure 4.18. Coaxial feed ports were therefore available at each element, and the elements and their housings were assembled in the manner shown in Figure 5.11 for a collateral array. A collinear array was similarly assembled, but is not illustrated. The antenna elements were resonant at 5GHz, and the ground plane was made 400mm square with absorbing material on the edges to reduce the current reflection effects caused by its truncation. For **Antenna C**, it is known that the impedance step up ratio $\gamma^2 = 4$, and the coplanar strip feed line has a characteristic impedance $Z_0 = 100$ ohms. Given a three-element impedance matrix $\mathbf{Z_3}$, with the self and mutual impedances computed above for element spacings $s = 0.5\lambda_0$, the scattering matrix, relative to reference planes at the terminals of the

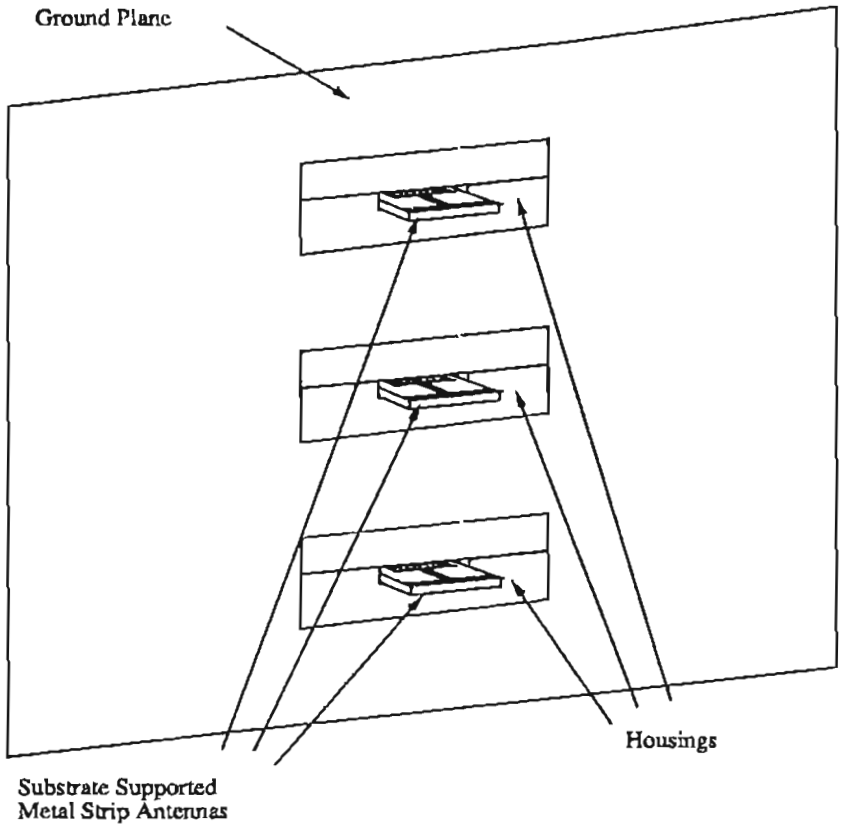

Figure 5.11: Three-element collateral array assembly.

coplanar strip folded dipoles, may be computed as

$$\mathbf{S_3} = (\gamma^2 \mathbf{Z_3} - Z_0 \bar{\mathbf{I}}_3)(\gamma^2 \mathbf{Z_3} + Z_0 \bar{\mathbf{I}}_3)^{-1} \tag{5.15}$$

where $\bar{\mathbf{I}}_3$ is the 3×3 identity matrix. For two-element collinear and collateral arrays, equation 5.15 may be re-written with 2×2 matrices, and a two-element impedance matrix $\mathbf{Z_2}$, as computed in Section 5.4, is used to determine $\mathbf{S_2}$. For substrate supported metal strip antennas fed from coplanar strip feed lines, the analysis in Section 4.2.1 indicates that where the metal strips forming the feed line are closely spaced, the impedance characteristics and the dominant radiation characteristics of the antenna are not significantly altered. Provided that this condition is met, the self and mutual terms of the impedance matrices can be computed for antenna elements with no feed lines. The analysis of the arrays considered in this section assumes that the presence

of the feed lines does not affect the mutual coupling. Assuming that the impedances of the balun and coplanar strip feed line are perfectly matched, and that the feed structure is lossless, the magnitude of the scattering parameters at the coaxial feed ports of the elements can be predicted from the relevant terms of $\mathbf{S_2}$ or $\mathbf{S_3}$.

The return loss of **Antenna C** in isolation was found in Section 4.2.3 to be -13.4dB, and the computed and measured return loss of each of the elements in the collinear and collateral arrays was within ± 0.2dB of this value for the element spacing considered. The computed and measured mutual coupling results for the collinear and collateral arrays are given in Table 5.1 for the following three parameters in each of the two array configurations:

1. the mutual coupling between adjacent elements of the collinear and collateral three-element arrays,
2. the mutual coupling between the outer elements of similar three-element arrays, and
3. the mutual coupling between the elements of two-element arrays formed by removing the central element from each configuration.

The agreement between the theoretical and measured mutual coupling is very good, suggesting that the analysis without feed lines outlined in Section 5.2 is adequate for practical antenna structures of the type considered in this section.

Further significance of the results obtained here and in Section 5.4 will be discussed in the next section.

	Collinear Array		Collateral Array	
	theoretical	measured	theoretical	measured
Mutual coupling between adjacent elements	-19.1dB	-18.9dB	-16.0dB	-16.3dB
Mutual coupling between outer elements (central element terminated)	-27.9dB	-27.6dB	-24.5dB	-24.6dB
Mutual coupling between outer elements (central element removed)	-33.0dB	-33.1dB	-33.6dB	-33.6dB

Table 5.1: Theoretical and measured mutual coupling for arrays of substrate supported coplanar strip folded dipoles with coplanar strip feed lines (at $L/\lambda_0 = 0.285$).

5.6 Substrate effects on mutual coupling

The effect of the electrically thick dielectric substrate on the performance of isolated antenna elements has been examined in detail in Chapters 3 and 4. By comparing the mutual coupling results obtained in this chapter with the mutual coupling between simple half-wave resonant dipole antennas in similar arrays, it is possible to make some observations about the effect of the dielectric substrate on the mutual coupling. Three-element collinear and collateral thin-wire folded dipole arrays spaced at $s = 0.5\lambda_0$ were analysed using an established moment method technique [64] for comparison. No feed lines were included in the computation of the self and mutual impedances, and no dielectric substrates were present in the geometry. The results for a folded dipole array with the elements fed by parallel wire transmission lines were calculated in the manner described in Section 5.5 for arrays of substrate supported coplanar strip folded dipoles fed by coplanar strip feed lines. The appropriate parameters used to obtain the scattering matrix in this way were $Z_0 = 300$ ohms and $\gamma^2 = 4$, and the self and mutual impedances were computed for arrays of thin-wire dipoles having length L and radius $a = 0.01L$ positioned above an infinitely extending ground plane at a height $H = 0.5L$,

	Collinear Array		Collateral Array	
	straight	45° bend	straight	45° bend
Mutual coupling between adjacent elements	-11.7dB	-18.5dB	-14.7dB	-15.5dB
Mutual coupling between outer elements (central element terminated)	-19.4dB	-27.6dB	-22.8dB	-23.8dB
Mutual coupling between outer elements (central element removed)	-29.5dB	-29.6dB	-29.2dB	-26.1dB

Table 5.2: Theoretical mutual coupling for arrays of folded wire dipole antennas with no substrates (at $L/\lambda_0 = 0.44$). Comparisons are shown for straight dipoles and dipoles with 45° downward arm bends.

at their resonant frequency corresponding to $L/\lambda_0 = 0.44$.

Theoretical results for the mutual coupling between these thin-wire folded dipole antennas without substrates are given in Table 5.2, set out to aid direct comparisons with Table 5.1 for substrate supported elements. The mutual coupling is computed for both straight wire folded dipoles described above, and also for folded dipoles with each arm bent 45° downwards towards the ground plane. For the downward bent dipoles, the driven and folded element radii are proportioned so that $\gamma^2 = 8$, since the self impedance without such adjustment is found to be lower due to the bend. Downward bent dipoles have been used previously to reduce the effect of mutual coupling and feed line scattering in arrays [53]. It can be seen by comparing the results given in Tables 5.1 and 5.2 that the mutual coupling between the straight folded dipoles without substrates is higher than that between the substrate supported coplanar strip folded dipoles. This is especially apparent for collinear arrays. The arrays of downward bent folded dipoles without substrates can be seen to exhibit comparable mutual coupling to the arrays of substrate supported coplanar strip folded dipoles.

These comparisons with arrays of thin-wire folded dipoles without substrates in-

dicate that the substrates have a significant effect on the mutual coupling. This is especially the case for the collinear arrays, where the mutual coupling is reduced substantially over that calculated for arrays of straight wire folded dipoles without substrates. The reduction is due to the shorter physical length of the metal strip required for resonance when the substrate is present, and the consequent increase in the physical separation between the elements which, for the practical elements considered here, is not occupied by dielectric substrate. It is noted in support of this that the physical separation between the downward bent thin-wire folded dipoles is comparable to that of the substrate supported coplanar strip folded dipoles for the same element spacing. While the substrate supported coplanar strip folded dipole has been shown to have good cross-polarization performance, the improvement in the mutual coupling between thin-wire folded dipoles without dielectric substrates, obtained by means of the downward arm bend, is achieved at the expense of an increase in the cross-polarized radiation of the elements.

It is also interesting to note the effect of the central element on the mutual coupling between the outer elements of the arrays. For both the collinear and collateral arrays, the mutual coupling is higher with the central element present, due to surface currents excited on the metal strip, and polarization currents in the substrate, of the central element. This implies that in estimating the mutual coupling between elements of a larger array from computations relating to pairs of elements, the effect of any interposed elements should be considered. While this increases the computational burden in obtaining the required design information it is observed that the mutual coupling between the outer elements of the three-element arrays of substrate supported coplanar strip folded dipole arrays is small, and in most applications can be considered to be close to the lower limit for which mutual coupling information is useful. For larger arrays, therefore, the further complexity associated with the computation of mutual coupling between pairs of elements having more than one interposed element does not arise because the result would be so small as to be of negligible consequence.

Finally, from the measured results on practical arrays having elements with well designed feed and impedance matching structures, it is clear that for the cases consid-

ered, the effect of any feed line radiation is small, as is the effect of any polarization currents induced in the substrate by currents on the feed structures. In addition, since the substrate supported metal strip antennas described in this thesis are intended to be used in MMIC arrays where each element has its own associated driving electronics, coupling effects between elements introduced by way of interactions in the feed paths of some corporate feed networks [96] are eliminated. The computational method and the results obtained, as outlined in this chapter, may therefore be applied directly to practical synthesis and analysis problems.

5.7 Summary

In this chapter, the issue of mutual coupling between elements in arrays of substrate supported metal strip antennas has been addressed. An efficient numerical analysis was developed which enabled the self and mutual impedance terms of the impedance matrices to be determined. The analysis was applied to two-element and three-element collinear and collateral arrays with element spacings between $0.35\lambda_0$ and $1.6\lambda_0$. In the case of the three-element arrays, the results obtained were verified experimentally. Using the theoretical results, practical antenna array assemblies were analysed, and the accuracy of the predicted mutual coupling was demonstrated by the close agreement shown with measured values of mutual coupling for the cases considered.

The benefits associated with the presence of the electrically thick, finite size substrate in the geometry of each antenna element have been shown to extend to the mutual coupling between elements in arrays of substrate supported metal strip antennas. It has been computed that such arrays exhibit lower mutual coupling than similar arrays of resonant dipole antennas where the substrates are not present. Furthermore, measurements on small arrays of substrate supported metal strip antennas with coplanar strip feed lines has indicated that an analysis which omits the feed lines from the computation of the impedance matrices can still provide accurate results for the mutual coupling, provided that the feed line dimensions are chosen appropriately.

The level of mutual coupling between the elements of the arrays studied has shown that while the mutual coupling between widely spaced elements is small, the effect of a single element interposed between two other elements must be taken into account in the analysis.

The contributions described in this chapter are therefore:

- The analysis of mutual coupling for the class of MMIC antenna elements under consideration,
- The discovery of a reduction in mutual coupling brought about by the use of electrically thick, finite size dielectric substrates,
- The successful application of the computed mutual impedance results to the analysis of small arrays of practical MMIC antenna elements incorporating feed lines and impedance matching.

Finally it is noted here that the results obtained for self and mutual impedances relating to small arrays of substrate supported metal strip antennas may be more widely applicable in phased array design, where larger arrays are to be employed. Because the mutual coupling is shown to be very small for widely separated elements, many mutual impedance terms may be assumed to be zero. In such situations, an approximation of the impedance matrix for larger arrays may be made, and because the mutual impedance terms are not of themselves a function of the array excitation the results may be used in the study of finite size phased arrays [5].

Chapter 6

Infinite Arrays of Substrate Supported Metal Strip Antennas

6.1 Introduction and overview

An important parameter in the design of antenna elements for phased arrays is the *active impedance* at the feed port of each element when operating in an array environment. The active impedance is defined as the impedance at the feed port of an antenna element under conditions where all of the elements of the array are excited to produce a given radiation pattern, and is dependent on both the environment in which the element operates and the particular excitation used throughout the array. Each element must be excited so that a known current distribution is produced with the required amplitude and phase. Since in practice finite impedance sources will be used to drive the elements, methods for determining the active impedance of each element of an array are essential for the accurate design and analysis of phased array systems. Because of the high cost associated with experimental development, particularly where MMICs are involved, precise numerical techniques are required as design

tools. Moreover, since the radiation pattern of a practical phased array is dependent on the excitations applied to the feed ports of the elements, the final result of combining all of the element contributions relies upon an accurate knowledge of the active impedance. Detailed measurement and adjustment is not practical, and for this reason accurate modelling of the active impedance characteristics is important.

The numerical analysis of substrate supported metal strip antennas as described in the preceding chapters is limited by the computational requirements of the models used, and a complete analysis of arrays of more than a few elements is impractical. However, useful information can be obtained by assuming that uniform infinite array conditions apply [27], where each element of the array operates in an identical environment. For an infinite array analysis, the elements of the array are excited by known voltages with a uniform magnitude and linear phase gradient across the array aperture. The phase gradient is related to the beam-steer angle of the array, and the current distributions on each element are identical except for the linear phase gradient imposed by the excitation. In practice, uniform infinite array conditions are closely approximated for the majority of elements in large arrays because these do not lie near the edge of such an array.

Arrays of printed dipoles on dielectric sheets perpendicular to a ground plane, which are similar to the antennas considered here, have been analysed recently using infinite array techniques [24]. The geometry of these antennas differs from that of the antennas considered in this thesis since the dielectric sheets which are described in [24] are continuous, are of infinite extent in the aperture plane, and are sufficiently thin that they cause only a small perturbation to the active impedance characteristics of the array. Related work on antennas which include feed lines has also been reported [97], however, the metal strips which comprise the feed line are widely spaced, and because the dielectric sheet is electrically thin the effect of radiation from the feed line dominates the characteristics. Nevertheless, the work reported demonstrates the increasing interest in arrays having geometries similar to those considered here. For the electrically thick substrates considered in this thesis, the polarization currents in the individual substrates, as well as the fields scattered by currents on the feed lines,

will have an important effect on the active impedance characteristics. Because the individual substrates considered here are of finite size, and are separated from each other in the aperture plane, the analysis described in [24] and [97] cannot be used. In this chapter the numerical techniques derived in earlier chapters are expanded to treat the case of infinite arrays of the more general substrate supported metal strip antennas and their feed lines which have been identified in this thesis as useful MMIC antennas.

An infinite array analysis for the class of MMIC antennas which are of interest is formulated in Section 6.2.1 in such a way as to be suitable for efficient numerical implementation. A complete formulation is obtained for an infinite array of substrate supported metal strip antennas without feed lines extending from them. In the initial analysis the antenna elements are fed by idealized voltage sources applied at an infinitesimal gap at the centre of the metal strip. The use of idealized, zero-impedance voltage sources imposes a known excitation, but in practice excitation has to be achieved by considering the active impedance of the antenna element and the internal impedance of the source. Because the radiation resistance of substrate supported simple metal strip antennas at half-wave resonance are found to be small, substrate supported coplanar strip folded dipole antennas are chosen for study as the array element, and a decomposition method, similar to that described in Section 4.2.2, is used to obtain the active impedance from the radiating mode currents.

In Section 6.2.2 the analytical model is extended to include a feed line to each metal strip folded dipole. It is well known that feed line induced scan blindness effects can impair the performance of an array [53]. In order to study the effect of feed line scattering, a coplanar strip feed line is introduced into the analysis. Section 6.2.2 describes how the analysis is expanded from the initial case where no feed line is considered to the case where a coplanar strip feed line is present, and appropriate feed models are developed. To reduce the computational burden and simplify the application of Kirchoff's current law at metal strip junctions, an equivalent-radius thin-wire approximation has been outlined in Section 4.2.2 to analyse in isolation the substrate supported coplanar strip folded dipole elements, fed by coplanar strip feed lines. The equivalent-radius thin-wire approximation is retained for the analysis here,

and the radiating mode currents on the coplanar strip folded dipole and coplanar strip feed line are again determined by a decomposition method.

In Section 6.2.3, numerical results for the active impedance of the substrate supported coplanar strip folded dipole elements of an infinite array, both with and without coplanar strip feed lines, are presented. The effect of the common mode current which is induced on the feed line as the array is scanned is discussed, together with the effect of radiation from polarization currents in the finite size substrates. Scan blindness effects are identified, and a method of reducing the scan blindness caused by radiation from the common mode current on the feed line is presented.

Experimental data is obtained by means of phased array simulator measurements which are described in Section 6.3, and good agreement is obtained with the results of analysis.

To completely characterize the performance of substrate supported metal strip antennas in an infinite array environment, the radiation characteristics of the antenna elements can be computed from the numerically determined currents. From the radiation characteristics the effect of scan blindness evident in the active impedance characteristics can be observed, together with any additional effects on the antenna element directivity and cross-polarization performance that are caused by the beam-steer angle of the radiation.

In the case of finite size arrays, the effect of locating elements near the edge of the array cannot be predicted directly from the infinite array analysis, and the impedance characteristics of such elements may differ from those of the elements in the central area of the array. In addition, the radiation characteristics of the outer elements of a finite array may also differ from those of the centrally located elements. For large arrays, the effect of such discrepancies may be small. Finite size arrays also allow the possibility of surface wave excitation, which for infinite arrays may only occur at beam steer angles corresponding to scan blindness. It has been shown, however, that for all but small arrays, the effect of surface wave excitation is not significant other than

at beam-steer angles corresponding to the introduction of scan blindness. Although finite size arrays are not considered in this thesis, techniques for approximating the radiation patterns of a finite array, such as methods for convolving the infinite array results with the actual current amplitude window on the array [98], may be adopted for their analysis. Consequently, the results obtained in this chapter may be used as a basis for the analysis of finite size arrays as well as very large arrays.

Finally, an array of single strip fed, substrate supported metal strip antennas, which has applications to integrated spatial power combining arrays and integrated imaging arrays, is described in order to illustrate how an infinite array analysis for a fixed-beam array may be used in the analysis of its characteristics. From the results obtained in Section 4.3.2 for such antennas operating in isolation, the radiation pattern is known to have some deficiencies. With an appropriate choice of subarray geometry it is shown that an array with good radiation characteristics can be designed.

6.2 Infinite array analysis

6.2.1 Formulation of infinite array analysis for simple strip elements

A section of an infinite array of substrate supported simple metal strip antennas is illustrated in Figure 6.1. The antenna elements have been idealized to simple metal strips supported by dielectric slabs above a ground plane of infinite extent, as shown in Figure 6.1. The elements are excited by ideal voltage sources at the centre of each metal strip, and in this section, no feed lines are included in the analysis.

Considering first the analysis of a single antenna element, as described in Chapter 3, the metal strip is modelled by equivalent surface currents $\vec{J}_c$ and the dielectric substrate by equivalent volume polarization currents $\vec{J}_d$. The coupled equations describing the

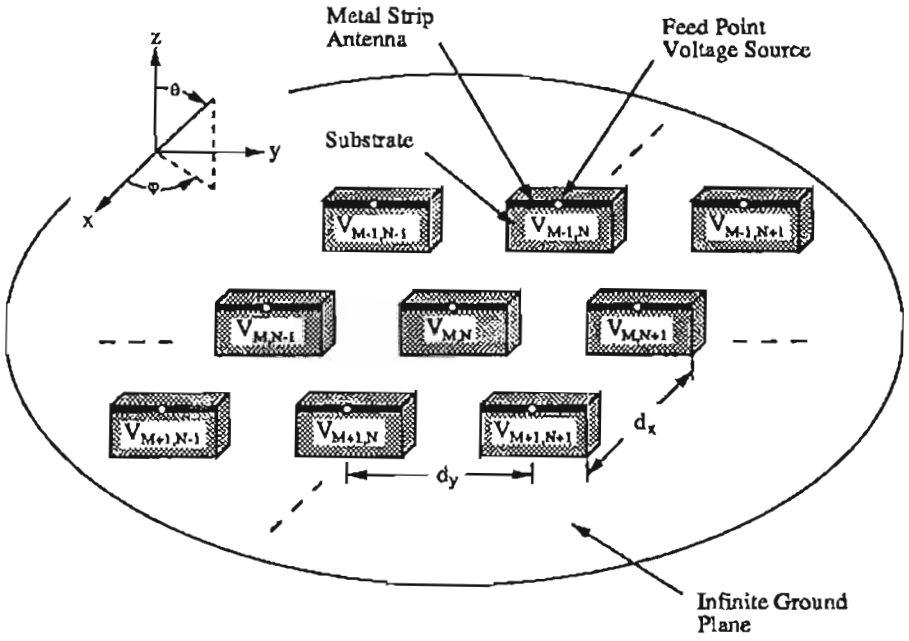

Figure 6.1: Array geometry.

relationship between the equivalent currents and the incident electric field $\vec{E}^i$ at a point $\vec{r}$, given previously as equations 3.4a and 3.4b and reproduced here for convenience, are

$$-\left[\mathcal{L}_c\left\{\vec{J}_c\right\}\right]_{\tan} - \left[\mathcal{L}_d\left\{\vec{J}_d\right\}\right]_{\tan} = \left[\vec{E}^i(\vec{r})\right]_{\tan}, \quad \text{for } \vec{r} \in S_c, \tag{6.1a}$$

$$\frac{\vec{J}_d(\vec{r})}{j\omega\epsilon_0(\epsilon_r - 1)} - \mathcal{L}_c\left\{\vec{J}_c\right\} - \mathcal{L}_d\left\{\vec{J}_d\right\} = \vec{E}^i(\vec{r}), \quad \text{for } \vec{r} \in V_d. \tag{6.1b}$$

Image theory is used again to account for the infinite ground plane in the analysis. Unlike the analysis described in Chapter 3, for the formulation described here an image plane in the xz-plane cannot be used since the required symmetry does not exist where a phase gradient occurs across the array aperture, except for the special case where the phase gradient results in the excitation of a plane-wave corresponding to beam steer angles in the xz-plane. Consequently, the entire metal strip is divided into a total of N_c segments and the entire substrate into a total of N_d segments, with separately chosen segment lengths in each of the coordinate directions. The surface currents on the metal strip are then expanded in terms of two-dimensional pulse basis functions

P_n and the volume polarization currents in the substrate in terms of three-dimensional pulse basis functions Q_n giving

$$\vec{J}_c(\vec{r}) = \sum_{n=1}^{N_c} P_n(y,z)(a_n\hat{y} + b_n\hat{z}) \tag{6.2}$$

and

$$\vec{J}_d(\vec{r}) = \sum_{n=1}^{N_d} Q_n(x,y,z)(c_n\hat{x} + d_n\hat{y} + e_n\hat{z}) \tag{6.3}$$

where a_n, b_n, c_n, d_n and e_n are the unknown constants to be determined for the current distributions, and having units corresponding appropriately to $\vec{J}_c$ or $\vec{J}_d$.

Current subvectors $\mathbf{J_c}$ and $\mathbf{J_d}$, comprising the constants describing the current distributions, are defined by

$$\mathbf{J_c} = [a_1, \ldots, a_{N_c}, b_1, \ldots, b_{N_c}]^T \tag{6.4}$$

$$\mathbf{J_d} = [c_1, \ldots, c_{N_d}, d_1, \ldots, d_{N_d}, e_1, \ldots, e_{N_d}]^T \tag{6.5}$$

where T denotes the vector transpose, and the subscripts $\mathbf{c}$ and $\mathbf{d}$ refer to surface currents on the metal strip and volume polarization currents in the substrate respectively. A point matching method is used to obtain the matrix equation

$$\mathbf{ZJ} = \mathbf{E} \tag{6.6}$$

where

$$\mathbf{Z} = \begin{bmatrix} \mathbf{Z_{cc}} & \mathbf{Z_{cd}} \\ \mathbf{Z_{dc}} & \mathbf{Z_{dd}} \end{bmatrix} + \frac{1}{j\omega\epsilon_0(\epsilon_r - 1)} \begin{bmatrix} \mathbf{0} & \mathbf{0} \\ \mathbf{0} & \bar{\mathbf{I}} \end{bmatrix} \tag{6.7a}$$

$$\mathbf{J} = \begin{bmatrix} \mathbf{J_c} \\ \mathbf{J_d} \end{bmatrix} \tag{6.7b}$$

$$\mathbf{E} = \begin{bmatrix} \mathbf{E_c} \\ \mathbf{E_d} \end{bmatrix}. \tag{6.7c}$$

Here, $\mathbf{Z}$ is the moment matrix with elements determined by the action of each source

current and its image about the array ground plane at the points in space for which the equations 6.1 are to be enforced to find the solution, $\mathbf{J}$ is the vector of constants representing the currents to be determined, and $\mathbf{E}$ is the vector corresponding to the electric field excitation. In the partitioning of the first term of the matrix $\mathbf{Z}$, $\mathbf{Z_{cc}}$ and $\mathbf{Z_{dc}}$ relate to the action of the surface currents $\mathbf{J_c}$, and $\mathbf{Z_{dd}}$ and $\mathbf{Z_{cd}}$ relate to the action of the volume polarization currents $\mathbf{J_d}$. The partitions of the second term of the matrix $\mathbf{Z}$ have the same sizes as the corresponding partitions of the first term, and $\mathbf{0}$ denotes a zero submatrix and $\bar{\mathbf{I}}$ denotes an identity matrix. A delta-gap voltage generator is used at the feed point of the metal strip antenna, so the elements of the subvector $\mathbf{E_c}$, denoted by E_{cm}, are

$$E_{cm} = \begin{cases} E_0, & \text{for a feed point at } m \\ 0, & \text{otherwise} \end{cases} \tag{6.8}$$

where E_0 is the impressed electric field caused by a feed point voltage of one volt. There is no incident electric field in the substrate, so

$$\mathbf{E_d} = \mathbf{0}. \tag{6.9}$$

The elements of $\mathbf{Z_{cc}}$ and $\mathbf{Z_{dc}}$ have the same form, and are denoted by Z_{cmn}, and the elements of $\mathbf{Z_{dd}}$ and $\mathbf{Z_{cd}}$ have the same form, and are denoted by Z_{dmn}, where Z_{cmn} and Z_{dmn} may be obtained from equations 6.1a and 6.1b respectively, and represent the interaction between the n^{th} source point, located at $\vec{r}_n$ and the m^{th} field point, located at $\vec{r}_m$. In this chapter, the primed and unprimed co-ordinate notation adopted in Chapter 3 is not used, since the position vectors are unambiguously defined by their subscripts. An examination of the way in which the point matching procedure is carried out shows that it is possible to determine the matrix elements by means of operators $\mathcal{F}_c$ and $\mathcal{F}_d$, described below, on a dyadic Green's function, $G(\vec{r}_m, \vec{r}_n)$, and the components of the basis function expansions, P_n and Q_n, of the current distributions. The matrix elements may therefore be written as

$$Z_{cmn} = \mathcal{F}_c \{P_n G(\vec{r}_m, \vec{r}_n)\} \tag{6.10a}$$

$$Z_{d\,mn} = \mathcal{F}_d\left\{Q_n G(\vec{r}_m, \vec{r}_n)\right\}. \tag{6.10b}$$

Because the equivalent currents exist in free space, the Green's functions in equation 6.10 are the free space dyadic Green's function. The numerical implementation of equation 6.10a has the form

$$\begin{aligned}\mathcal{F}_c\left\{P_n G(\vec{r}_m, \vec{r}_n)\right\} &= \frac{-j\omega\mu_0}{4\pi}\iint_{S_{cn}} P_n(y,z) G(\vec{r}_m, \vec{r}_n)\, dS_n \\ &\quad + \frac{1}{j\omega\epsilon_0 4\pi}\frac{\partial}{\partial v_m}\iint_{S_{cn}} \frac{\partial}{\partial u_n}\left\{P_n(y,z) G(\vec{r}_m, \vec{r}_n)\right\} dS_n \end{aligned} \tag{6.11}$$

where S_{cn} is the surface of the n^{th} metal strip segment. The source and field point spatial variables are denoted u_n and v_m, with u and v assuming the appropriate x, y or z coordinate such that a unit vector $\hat{u}$ corresponds to the polarization of the source current vector and a unit vector $\hat{v}$ corresponds to the polarization of the electric field component at the field point. Derivatives of the pulse basis function expansions with respect to the source point and field point spatial variables u_n and v_m are computed by finite differences. Because the problem is solved by means of pulse basis functions and point matching, the source point derivative in the first term of equation 6.11 may be taken outside the integral with no effect on the computation. In practice, it is also permissible to compute both derivatives at the field point, since the basis functions are symmetrical. The implementation that results from this procedure is numerically identical to the offset pulse function representation of the charge density described in Section 3.2.3. For each source point, equation 6.11 is applied to both the source current and its image and the results added. The numerical implementation of equation 6.10b has the form

$$\begin{aligned}\mathcal{F}_d\left\{Q_n G(\vec{r}_m, \vec{r}_n)\right\} &= \frac{-j\omega\mu_0}{4\pi}\iiint_{V_{dn}} Q_n(x,y,z) G(\vec{r}_m, \vec{r}_n)\, dV_n \\ &\quad - \frac{1}{j\omega\epsilon_0 4\pi}\frac{\partial}{\partial v_m}\iint_{S_{dn}} \tau_u Q_n(x,y,z) G(\vec{r}_m, \vec{r}_n)\, dS_n \end{aligned} \tag{6.12}$$

where V_{dn} is the volume of the n^{th} dielectric segment and S_{dn} is the entire surface of the n^{th} dielectric segment. The value of τ_u is related to the unit vector $\hat{u}$, representing

the polarization of the source current, in such a way that

$$\tau_u = \begin{cases} 1, & \text{where } S_{dn} \text{ is an outer surface and } \hat{u} \cdot \hat{n} = 1 \\ -1, & \text{where } S_{dn} \text{ is an outer surface and } \hat{u} \cdot \hat{n} = -1 \\ 0, & \text{otherwise,} \end{cases} \tag{6.13}$$

where $\hat{n}$ is the outward pointing unit vector normal to the outer surface. As a consequence, τ_u serves to ensure that surface charges internal to the homogeneous dielectric substrate are not introduced into the problem. This procedure is numerically the same as the averaging approach described in Section 3.2.3 for avoiding internal surface charge in the homogeneous dielectric substrate. Again, at each source point equation 6.12 is applied to both the source current and its image and the results added.

A segmentation scheme similar to that described in Section 3.2.3 is employed so that a grid can be defined with intersection points at both the centres and junctions of the segments. This relationship between the grid and the segmentation allows the computation of the finite differences required for the partial derivatives in equations 6.11 and 6.12. The grid intersection points form the geometric basis for a lookup table containing all the necessary Green's function integrals required by the operators $\mathcal{F}_c$ and $\mathcal{F}_d$, and an efficient numerical algorithm is again obtained for the determination of the moment matrix $\mathbf{Z}$.

A two-dimensional array of elements, infinite in both the x and y directions, is now considered. A rectangular array geometry with uniform element spacings d_x and d_y is illustrated in Figure 6.1. The position of each element in the array is denoted by (M, N), where M and N are integers extending from $-\infty$ to $+\infty$, and a reference element is defined at $M = 0$, $N = 0$. Source and field points on element (M, N) are denoted by $\vec{r}_{n,MN}$ and $\vec{r}_{m,MN}$ respectively. For the purpose of determining the active impedance under the desired excitation conditions, the elements of the array are excited by voltage sources V_{MN}, as shown in Figure 6.1, where each voltage source has unity magnitude, but the phase is adjusted to produce a plane wave corresponding to a beam-steer angle in the direction (θ, φ). The excitation subvectors, corresponding to

the applied voltages for element (M, N), are therefore given by

$$\mathbf{E_{c,MN}} = \mathbf{E_{c,00}} \exp\{-j(Mk_0 d_x \sin\theta\cos\varphi + Nk_0 d_y \sin\theta\sin\varphi)\} \quad (6.14a)$$

$$\mathbf{E_{d,MN}} = 0 \quad (6.14b)$$

As a consequence of the identical environment of each element in a uniform infinite array, the current subvectors of the element (M, N) are related to the current subvectors of the reference element by

$$\mathbf{J_{c,MN}} = \mathbf{J_{c,00}} \exp\{-j(Mk_0 d_x \sin\theta\cos\varphi + Nk_0 d_y \sin\theta\sin\varphi)\} \quad (6.15a)$$

$$\mathbf{J_{d,MN}} = \mathbf{J_{d,00}} \exp\{-j(Mk_0 d_x \sin\theta\cos\varphi + Nk_0 d_y \sin\theta\sin\varphi)\}. \quad (6.15b)$$

It is therefore only necessary to compute $\mathbf{J_{c,00}}$ and $\mathbf{J_{d,00}}$. By taking the field points only on the reference element, and summing the contributions of all the elements for each source point, equations 6.10a and 6.10b may be written for the infinite array case as

$$Z_{c\,mn} = \mathcal{F}_c\Big\{ \sum_{M=-\infty}^{\infty} \sum_{N=-\infty}^{\infty} P_{n,MN} G(\vec{r}_{m,00}, \vec{r}_{n,MN}) \cdot \exp\{-j(Mk_0 d_x \sin\theta\cos\varphi + Nk_0 d_y \sin\theta\cos\varphi)\} \Big\} \quad (6.16a)$$

$$Z_{d\,mn} = \mathcal{F}_d\Big\{ \sum_{M=-\infty}^{\infty} \sum_{N=-\infty}^{\infty} Q_{n,MN} G(\vec{r}_{m,00}, \vec{r}_{n,MN}) \cdot \exp\{-j(Mk_0 d_x \sin\theta\cos\varphi + Nk_0 d_y \sin\theta\cos\varphi)\} \Big\} \quad (6.16b)$$

where $P_{n,MN}$ and $Q_{n,MN}$ are the two-dimensional and three-dimensional pulse basis functions on element (M, N). The double summation and the exponential factor of equation 6.16a and 6.16b are included in the calculation of the Green's function integrals for the look up table. Although the double summation of the free space Green's functions associated with pulse basis functions on each element of the array is more computationally intensive than the computation required for the evaluation of equations 6.10a and 6.10b for a single, isolated element, the lookup table has the same

size in both cases, and the improvement in computational efficiency achieved by the use of the grid is preserved. Where a source point lies on the reference element, an accurate Gauss-Kronrod numerical integration is performed. For source points on the remaining elements, an approximation is made where $|\vec{r}_m - \vec{r}_n|$ is considered constant in the integration, thereby increasing the computational speed of the integration, and hence also the required double summation. In the numerical analysis, the limits of the double summation must be finite but sufficiently large for the solution to be well converged. In the next section, a method for applying the infinite array computation to substrate supported coplanar strip folded dipole elements both with and without coplanar strip feed lines is described.

6.2.2 Folded dipole and feed line modelling

An idealized feed model for a substrate supported metal strip antenna is shown in Figure 6.2a. The idealized feed structure shown was assumed for the elements considered in Section 6.2.1. No feed line is present, and the source consists of a one volt delta-gap voltage generator at the centre of the metal strip. The metal strip is segmented such that there are N_c pulses along the length of the strip, and each pulse supports both y-directed and z-directed surface currents distributed uniformly over the entire width of the segment. For the excitation shown in Figure 6.2a, the active admittance, Y, at the feed point of the substrate supported metal strip antenna in the infinite array environment can be calculated using the method described in Section 6.2.1 from

$$Y = i_d, \tag{6.17}$$

where i_d is the y-directed current at the feed point, obtained from the appropriate element of the subvector $\mathbf{J}_{c,00}$.

If instead of a single metal strip, a substrate supported coplanar strip folded dipole is formed as described in Section 4.2.2, the admittance is a function of the radiating

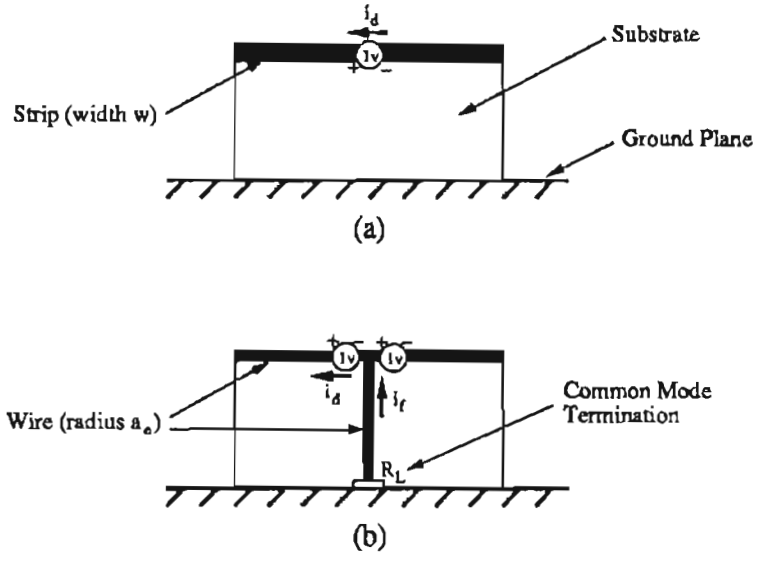

Figure 6.2: Radiating mode equivalent models for active impedance computation: (a) idealized feed, (b) coplanar strip feed line.

mode and transmission line mode currents on the two metal strips comprising the folded dipole, and is given by

$$Y = \frac{i_d}{\gamma^2} + \frac{i_t}{2}, \tag{6.18}$$

where i_t is the transmission line mode current at the feed point and γ^2 is the impedance step up ratio of the folded dipole. The derivation of equation 6.18 follows that of [99] and is given in Appendix F. The substrate is modelled exactly as described in Section 6.2.1, however, only the radiating mode currents on the coplanar strip folded dipole are considered in the analysis, and the radiating mode current, i_d is computed from the current at the feed point of the single metal strip shown in Figure 6.2a. Where the transmission line mode currents are required they would be calculated by a transmission line analysis of the parallel strip structure comprising the metal strip folded dipole. The impedance step up ratio γ^2 is related to the ratio, a, between the radiating mode currents on the folded and driven arms of the folded dipole, as described in Section 4.2.2, where $\gamma^2 = (1+a)^2$. The impedance step up ratio is useful in practice for achieving an impedance match to typical coplanar strip feed line characteristic

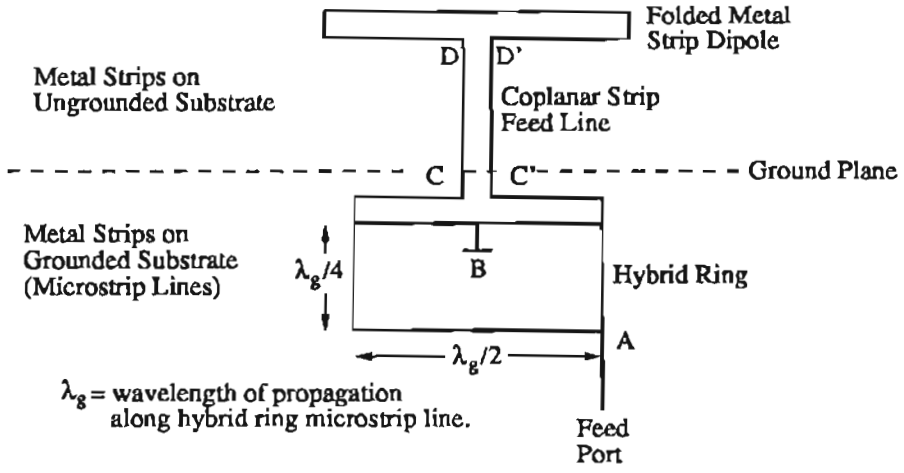

Figure 6.3: Schematic view of metal strip parts of a substrate supported metal strip antenna, showing the balun and feed line geometry.

impedances. At the half-wave resonance of the antenna, it is found that $i_t/2 \ll i_d/\gamma^2$, and hence

$$Y \approx \frac{i_d}{\gamma^2}. \tag{6.19}$$

Although the metal strip folded dipole is contiguous with the edge of the substrate, and is therefore not physically symmetrical, for equal width folded and driven metal strips a current ratio $a = 1$ is assumed in the analysis, resulting in $\gamma^2 = 4$. The two-dimensional pulse function representation of the surface current on a single metal strip may be employed for the computation of the radiating mode currents with the width, w, of the single strip set equal to the total width of the coplanar strip folded dipole. Both of these assumptions have been validated by experiment for single, isolated antenna elements in Section 4.2.3.

A practical antenna element may consist of a substrate supported coplanar strip folded dipole fed by a coplanar strip feed line, as described in Section 4.2. In order to develop an infinite array analysis for such elements, it is necessary to consider the feed line and balun structure. A schematic view of a hybrid ring power divider used as a balun to feed a coplanar strip feed line is shown in Figure 4.13. The currents on the

coplanar strip feed line may be divided into a transmission line (or balanced) mode, and a common (or radiating) mode. By using a hybrid ring power divider as a balun, each mode has an independent feed port (or termination). The transmission line mode will be excited from a feed port connected to port A of the hybrid ring as shown in Figure 6.3. Although a common mode is not deliberately excited, any common mode currents will be terminated at port B of the hybrid ring. The impedance presented by the balun terminals at the base of the coplanar strip feed line, shown as C–C′ in Figure 6.3, is matched to the characteristic impedance of the coplanar strip feed line for the balanced mode. The voltage at C–C′ excited from port A will be transferred to the antenna input terminals, shown as D–D′, by the transmission line. In contrast, the common mode at the terminals C–C′ will be terminated in an impedance that is determined by the actual value of the termination at port B of the hybrid ring. A facility thereby exists to adjust the common mode termination at the terminals C–C′ to some chosen value. This feature, associated with the use of a hybrid ring power divider as a balun, has not been previously exploited. More conventional balun structures do not have a separate port available to terminate the common mode, and are designed to present an open circuit to the common mode in order to prevent such currents affecting the electronics connected to the feed port [99]. The feed structure shown in Figure 6.3 has been used successfully with substrate supported metal strip antennas operating in isolation and in small arrays. In this chapter, infinite arrays of substrate supported metal strip antennas with coplanar strip feed lines are analysed, where the coplanar strip line is assumed to be excited from the balun as described above.

The characteristics of substrate supported metal strip antennas with coplanar strip feed lines have been investigated in Section 4.2.3 using an equivalent-radius thin-wire approximation for the metal strips comprising a metal strip antenna and coplanar strip feed line. The thin-wire approximation was introduced as a means of analysing the structure without substantially increasing the complexity of the geometry, and therefore the computer run time and storage requirements, as would be necessary for a full representation of the metal strips of the feed line and metal strip dipole. Details of the thin-wire approximation are given in Section 4.2, and the results obtained from an

analysis of substrate supported coplanar strip folded dipoles with coplanar strip feed lines are verified by experimental measurements. Because the thin-wire approximation simplifies the application of Kirchoff's current law to the junctions between the feed line strips and the arms of the metal strip antenna, it has been retained for the analysis presented here.

Using the thin-wire approximation for the substrate supported coplanar strip folded dipoles with coplanar strip feed lines, the radiating mode currents can be modelled as shown in Figure 6.2b, where two one-volt sources are employed. The derivation of this model follows that given in [99], and is described in detail in Appendix F. The currents on the metal strips associated with both the feed line and the folded dipole have been decomposed to obtain the radiating mode currents on single wires. The wires have an equivalent-radius, a_e, determined as described in Section 4.2. In the model shown, the equivalent-radius of the wires representing the feed line and metal strip folded dipole are assumed to be the same throughout the analysis since the overall widths of the coplanar strip feed line and metal strip folded dipole are usually comparable in practice. Although the radiation from the transmission line mode currents on the coplanar strip feed line has been shown to have an effect on the cross-polarized radiation of the antenna, the radiating mode currents still dominate the performance of the antenna, and the effect on the array performance caused by neglecting the transmission line currents on the feed line is predicted to be minimal. The active admittance is determined at the feed point of the metal strip antenna, since the transmission line mode on the feed line, which transforms the excitation applied at the base of the feed line via a balun to the feed point at the centre of the metal strip, is not considered in the radiation problem. It is assumed that the active impedance computed in this way can be transferred back to the balun input using the appropriate known feed line parameters. The measurements on substrate supported coplanar strip folded dipoles fed with coplanar strip feed lines outlined in Section 4.2.3, which show that the reflection coefficient at the input port of the balun can be accurately predicted in this way, have validated these assumptions. The active admittance at the feed point

of the half-wave resonant antenna, as derived in Appendix F, is given by

$$Y \approx \frac{i_d}{2\gamma^2} - \frac{i_f}{4\gamma} \tag{6.20}$$

where $i_f/2$ is the common mode current at the metal strip dipole end of each of the two strips comprising the coplanar strip feed line, and again the transmission line mode current on the folded dipole can be neglected at resonance. Since only axially directed currents are considered in the thin-wire approximation of the structure, Kirchoff's current law is valid at the junction between the wires representing the metal strip antenna and coplanar strip feed line in the radiating mode model, and is applied as described in Appendix C.

In the radiating mode model shown in Figure 6.2b, the common mode on the feed line is terminated at the base of the feed line by a resistance R_L. Although only balanced mode currents are excited on the feed line by a well designed balun, common mode currents are induced as the array is steered from boresight due to the resulting asymmetry of the current distributions, and R_L is used in the model to simulate the impedance presented to the common mode at the base of the feed line, the terminals of which are shown as C–C′ in Figure 6.3. The value of R_L will be determined by the type of balun employed. As described above, for many balun structures the common mode is prevented from entering the module and affecting the electronics by isolating the common mode at the terminals C–C′. Where the common mode is completely isolated, R_L corresponds to an open circuit. If the balun has the property that some form of common mode termination is present, then R_L is finite. A further specific case exists, where $R_L = 0$. Although there can be no physical connection of the feed line to the array ground plane at the terminals C–C′ for the coplanar strip feed lines considered, it is possible in practice to closely create this condition by means of the hybrid ring power divider employed in the coplanar strip fed antennas considered in this thesis, since the facility exists to discriminate between the balanced mode and common mode currents, and thereby present appropriate terminations to each. In all of the above cases, common mode currents may still be induced along the length of the feed line regardless of the common mode termination chosen.

From equations 6.17, 6.19 or 6.20 the active impedance of each type of antenna element described above, operating in a uniform infinite array array environment, can be determined as a function of the beam-steer angle (θ, φ) of the array by

$$Z = \frac{1}{Y}. \tag{6.21}$$

Some examples are described in the next section.

6.2.3 Design examples

The antenna element chosen for initial calculations was based on **Antenna A** described in Section 3.4. This antenna has the dimensions, expressed in terms of the metal strip length L, of height $H = 0.5L$, substrate thickness $t = 0.075L$ and metal strip width $w = 0.05L$, with a substrate relative permittivity $\epsilon_r = 10.2$. The antenna has been shown to have a half-wave resonance at a frequency corresponding to $L/\lambda_0 = 0.285$ when operated in isolation from other elements, and the numerical results in this section are computed at this frequency. Since the radiation and impedance characteristics of this antenna element in isolation have been described in detail, an assessment of the effect of the substrate and the feed line on the impedance and radiation characteristics of an array of such elements can be undertaken.

Element spacings $d_x = 0.5\lambda_0$ and $d_y = 0.5\lambda_0$ were chosen for the array in order to preclude the existence of grating lobes over the entire range of beam-steer angles. Three different examples are considered. In the first, an array of substrate supported coplanar strip folded dipole antennas is analysed in the manner described in Section 6.2.1 for the case where no feed line is present, using the idealized feed model for a folded dipole structure outlined in Section 6.2.2. The arms of the folded dipole are assumed to be proportioned so that the impedance step up ratio $\gamma^2 = 4$. In the second and third examples, the elements are fed by coplanar strip feed lines, which are introduced into the analysis as described in Section 6.2.2. The physical geometry of the antenna element

in these two examples is that of **Antenna C** in Section 4.2.3. The two examples consist of analyses for two different common mode terminations at the base of the feed line. In all three cases results for the active impedance of the elements are presented for three scan-planes, $\varphi = 0°$, $45°$ and $90°$. Finally, the element factors of the principal plane radiation patterns are obtained for the three cases.

The accuracy of the numerical solution is dependent on both the fidelity of the pulse basis function representation of the current distributions, and the actual size of the array considered in the double summations of equations 6.16a and 6.16b. Two segmentations were tested for the array of substrate supported coplanar strip folded dipoles without feed lines over a range of beam-steer angles, the first having $N_c = 15$ and $N_d = 240$, and the second $N_c = 19$ and $N_d = 380$. The results obtained for the second segmentation were sufficiently close to those of the first segmentation for the current distributions to be regarded as accurate. Since computer storage and run time considerations permitted it, the second segmentation scheme was retained in the examples that follow. For the second segmentation, wires with an equivalent-radius of $a_e = 0.008L$ are required in the radiating mode model for computations relating to antennas with feed lines.

The size of the array which can be regarded as sufficient for an approximation to an infinite array varies depending on the beam-steer angle, however, the results for the planes $\varphi = 0°$ and $\varphi = 45°$ converged well for small arrays. Array sizes of 21×21 and 41×41 were used to test for convergence of the solution, and examples of such tests are shown in Table 6.1, for antennas without feed lines, and in Table 6.2, for antennas with feed lines.

For the $\varphi = 90°$ plane, convergence was reasonably good for beam-steer angles $\theta < 60°$, however, depending on the performance of the array, larger arrays were required for beam steer angles where substrate induced scan blindness effects exist, and also for beam steer angles where feed line induced scan blindness effects are present. An example of convergence close to a feed line induced scan blindness is shown in Table 6.2 for a feed line with the common mode isolated from the balun, where the

Scan Plane	Active Impedance (ohms)	
	21 × 21 elt.	41 × 41 elt.
$\varphi = 0°$	$102.1 + j19.7$	$102.6 + j20.9$
$\varphi = 45°$	$80.8 - j7.8$	$81.0 - j9.5$
$\varphi = 90°$	$62.6 - j23.2$	$65.0 - j21.6$

Table 6.1: Active impedance of substrate supported coplanar strip folded dipole antenna with idealized feed for array sizes 21 × 21 elements and 41 × 41 elements (at $\theta = 45°$).

Scan Plane	Active Impedance (ohms)	
	21 × 21 elt.	41 × 41 elt.
common mode isolated		
$\varphi = 0°$	$86.2 + j0.8$	$87.0 + j2.1$
$\varphi = 45°$	$56.3 - j26.8$	$57.0 - j28.1$
$\varphi = 90°$	$10.7 - j34.4$	$34.8 - j28.7$
common mode terminated		
$\varphi = 0°$	$86.2 + j0.8$	$87.0 + j2.1$
$\varphi = 45°$	$72.4 - j19.2$	$73.3 - j21.1$
$\varphi = 90°$	$67.6 - j31.1$	$67.5 - j28.9$

Table 6.2: Active impedance of substrate supported coplanar strip folded dipole antenna with coplanar strip feed for array sizes 21 × 21 elements and 41 × 41 elements (at $\theta = 45°$).

active impedance varies rapidly with beam-steer angle. In such cases, the numerical results were tested using larger size arrays to ensure that they were accurate.

A Fujitsu VP2200 vector-supercomputer was again used to perform the numerical computations. With $N_c = 19$ and $N_d = 380$, the computer storage required is 45MBytes, and a typical run-time per beam-steer angle for a 41×41 element array amounts to approximately 230 seconds. Some 70% of this time is taken up in filling the matrix $\mathbf{Z}$, and techniques for accelerating the convergence of the double summation of the Green's function could be adopted if a reduction in run-time is desired [100]. Because the program is relatively inexpensive to run for the design examples considered, such enhancement was not implemented.

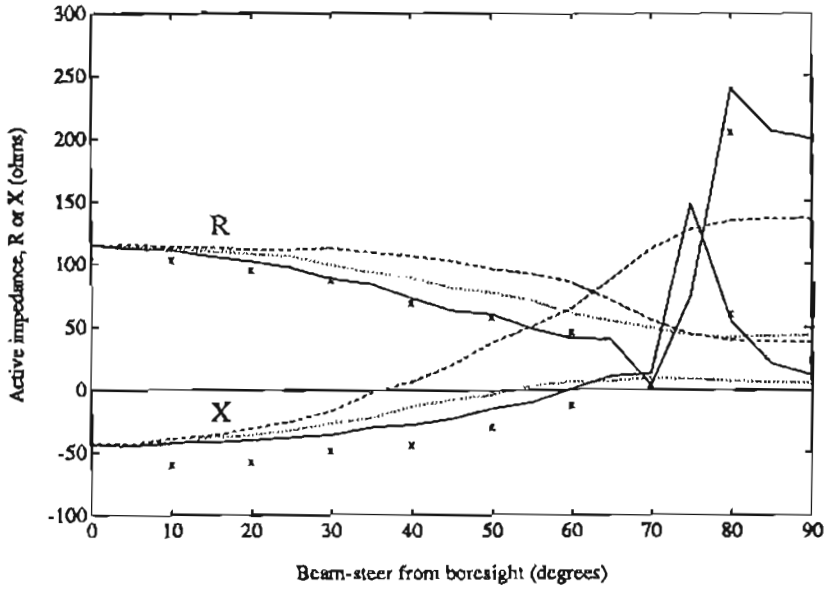

Figure 6.4: Active impedance $R + jX$ for an infinite array of substrate supported coplanar strip folded dipoles with idealized feeds. Dashed line: $\varphi = 0°$ plane, Dotted line: $\varphi = 45°$ plane, Solid line: $\varphi = 90°$ plane. Points marked x are the results of an equivalent-radius thin-wire analysis for the $\varphi = 90°$ plane.

Active impedance results

A: Substrate Supported Coplanar Strip Folded Dipole Without Feed Line

For the first example, a substrate supported coplanar strip folded dipole with no feed line was analysed using the idealized feed model of Figure 6.2a. The active impedance was computed from equation 6.19, and the results are shown in Figure 6.4. The active impedance exhibits a gradual change with beam-steer angle, θ, until relatively large angles from boresight in the $\varphi = 90°$ plane are approached.

At about 70° from boresight in the $\varphi = 90°$ plane a rapid variation in impedance is noted, and the resistive part of the impedance approaches zero, suggesting a scan blindness effect. Similar effects have been observed for a number of microstrip antenna arrays, including arrays of aperture coupled microstrip patch antennas where the power

is trapped in the substrate as resonant surface-wave modes, and no real power is radiated [101]. In addition, printed dipoles on relatively thin dielectric sheets have been observed to exhibit similar scan blindness [24]. Because the substrates used in those investigations are electrically thin, the scan blindness occurs at angles approaching 90° from boresight.

For the substrate supported metal strip antennas considered here, the substrate is again identified as the cause of the scan blindness. In Section 3.4 it was shown for antennas operating in isolation with a balanced excitation, that a polarization current distribution is induced in the substrate. The distribution was further shown to exhibit the features of a balanced mode in dielectric waveguide. Because of their distributed nature, the z-directed polarization currents contribute to the radiation from the antenna, and in the yz-plane the z-directed polarization currents are co-polarized with respect to the radiation due to the y-directed surface currents on the metal strip and y-directed polarization currents in the substrate. For an infinite array with element spacings $d_y = \lambda_0/2$ the condition of a balanced polarization current distribution is only achieved in the $\varphi = 90°$ plane for $\theta = 0°$, corresponding to the boresight direction, and for $\theta = 90°$, resulting in radiation across the array aperture. In the latter case, although the y-directed radiation must be zero due to the presence of the ground plane, it has been shown that a z-directed co-polarized radiation field is present due to the z-directed polarization currents in the substrate. As a consequence of this, the resistive part of the active impedance of the substrate supported metal strip antenna does not vanish for a beam-steer angle $\theta = 90°$, however, the value of the resistance is substantially different to that at boresight because of the different radiation mechanism. At beam-steer angles in the $\varphi = 90°$ plane other that $\theta = 0°$ or $\theta = 90°$, the distribution of polarization currents in the substrate can be thought of as a combination of a balanced mode and a common mode. The scan blindness at $\theta = 70°$ where the resistive part of the active impedance approaches zero is caused by interference between the radiation from the y-directed sources and the z-directed sources which results in field cancellation in this direction. When this scan blindness occurs, the energy that would otherwise be radiated away from the array aperture is transferred between the elements of the

infinite array as a so-called surface wave. Surface wave propagation has been shown for periodic arrays of dielectric sheets [102], and the array of finite size dielectric slabs present in the structures considered in this chapter is anticipated to support similar modes of propagation. It is noted that the resistance, although small, is not zero at the beam-steer angle corresponding to scan blindness, since there is no mechanism for cancellation of the x-directed cross-polarized radiation that occurs in the yz-plane.

The prediction of scan blindness effects caused by the presence of polarization currents in the finite size, electrically thick substrates is an important part of the design process for large millimetre wave arrays of this type. Numerical experiments conducted with similar antennas having substrate thicknesses $t/L = 0.15$ have revealed similar effects. In spite of the introduction of substrate induced scan blindness, the results shown in Figure 6.4 indicate that the variation in active impedance is manageable from a design point of view for beam-steer angles other than those greater than approximately $\theta = 60°$ in the $\varphi = 90°$ plane.

The active impedance of the substrate supported coplanar strip folded dipole antenna without feed line was also computed with the metal strip in the radiating mode model shown in Figure 6.2a replaced by a thin-wire with an equivalent-radius $a_e = 0.008L$, located on the axis of the metal strip. The results obtained for a $\varphi = 90°$ scan-plane are presented in Figure 6.4 as points marked $\times$, with a 10 degree angular step used for the computation. The results clearly demonstrate that for the purpose of computing the active impedance as a function of beam-steer angle, the equivalent-radius thin-wire model for the metal strip is acceptable. In the cases that follow, this equivalent-radius thin-wire representation of the metal strip parts of the antenna is employed.

B: Substrate Supported Metal Strip Folded Dipole With Coplanar Strip Feed Line

For the second example, a coplanar strip feed line is included with the element, and is introduced into the analysis using the feed model shown in Figure 6.2b. The common mode termination is chosen to correspond to an open-circuit in this example, such that

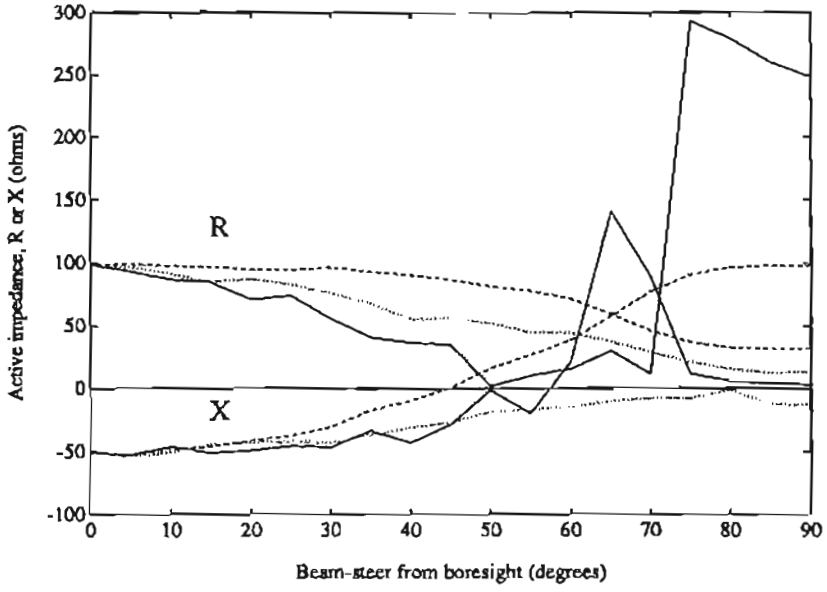

Figure 6.5: Active impedance $R + jX$ for an infinite array of substrate supported coplanar strip folded dipoles with coplanar strip feed lines, (common mode isolated). Dashed line: $\varphi = 0°$ plane, Dotted line: $\varphi = 45°$ plane, Solid line: $\varphi = 90°$ plane.

the common mode current is isolated by the balun. Equation 6.20 was used to calculate the active impedance at the centre of the metal strip from the computed current distributions, and the results are shown in Figure 6.5. While the active impedance in the $\varphi = 0°$ and $\varphi = 45°$ planes again shows a gradual change with beam-steer angle, the active impedance in the $\varphi = 90°$ plane changes rapidly with beam-steer angle beyond about $\theta = 45°$. A scan blindness which is due to feed line scattering is identified at $\theta = 50°$ in the $\varphi = 90°$ plane, and the substrate induced effects for larger beam-steer angles are more pronounced than in the previous example due to the additional polarization currents excited in the substrate by common mode currents on the feed line. The mechanism for the scan blindness effects observed in this case is again due to the presence of both y-directed and z-directed radiation sources, and is similar to that described previously. It is clear from these results that feed line scattering is an important consideration in the design of the antenna element, and consequently the array.

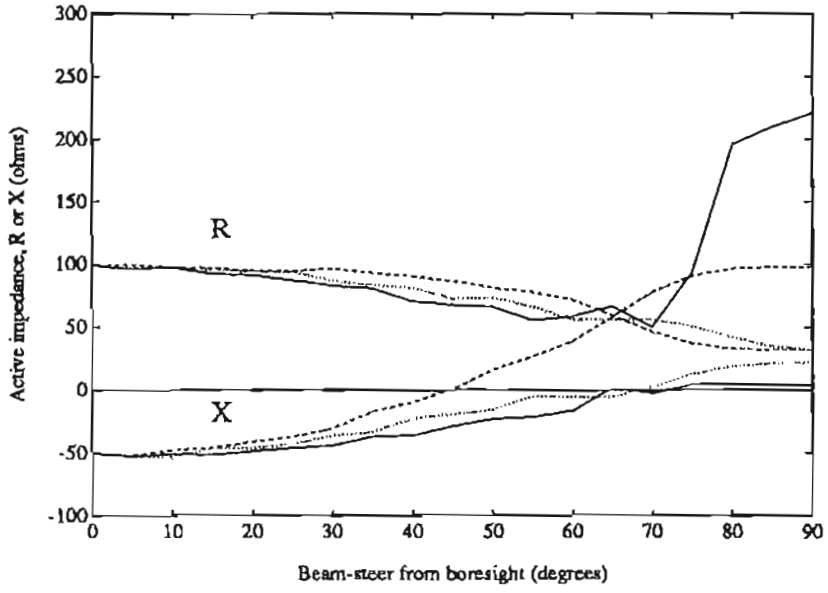

Figure 6.6: Active impedance $R+jX$ for an infinite array of substrate supported metal strip antennas with coplanar strip feed lines, (common mode terminated). Dashed line: $\varphi = 0°$ plane, Dotted line: $\varphi = 45°$ plane, Solid line: $\varphi = 90°$ plane.

Because of the large variations in the active impedance caused by feed line scattering, a larger array is required if the computation is to exhibit convergence at all beam-steer angles of interest in the $\varphi = 90°$ plane. The number of elements in the y-direction was increased to a maximum of 81 for critical beam-steer angles where rapid variations in the active impedance are observed. The results presented are indicative of the magnitude of the effects around regions of scan blindness and for the angular range $\theta > 60°$ in the $\varphi = 90°$ plane. They illustrate the difficulties that may be encountered in practical element design. Inclusion of the feed line in the analysis is clearly essential for an accurate understanding of antenna performance.

For the third example, the common mode on the base of the feed line is terminated by a resistance, as described in Section 6.2.2. The analysis proceeds as in the second example, and the active impedance results are shown in Figure 6.6. Low values of resistance were employed for the common mode termination, and the results have been

found to be insensitive to the choice R_L for values that were tested between zero and 100 ohms. The common mode current on the feed line is found to be significantly reduced when these terminations are used, as compared with the case of an open-circuit termination. In all scan planes, a gradual change of the active impedance over a wide range of beam-steer angles is obtained. In particular, there is no evidence of feed line induced scan blindness in the $\varphi = 90°$ plane, and the variation in active impedance due to substrate induced effects for large beam-steer angles in the $\varphi = 90°$ plane are less pronounced. The results have been shown for this case to be well converged over the entire range of beam-steer angles considered for a 41×41 element array.

The active impedance results shown in Figure 6.6 demonstrate how the termination at the base of the feed line may be used to obtain a wider range of useful beam-steer angles in the yz-plane. An examination of the current distribution on the single wire representing the feed line in the radiating mode model reveals that when a low resistance termination is applied at the base of the feed line, the common mode current on the feed line is reduced compared with the case of an open-circuit termination. With reference to the schematic view of the metal strip parts of the antenna and feed line, shown in Figure 6.3, it may be noted that the distance between one of the terminals at the base of the feed line and the end of the metal strip antenna arm to which it is connected is approximately $\lambda_0/2$. When the condition of an open-circuit common mode termination is achieved at the base of the feed line, the length of metal strip identified above is free to resonate. If the termination is altered to achieve a low impedance or short-circuit common mode termination at the base of the feed line, the resonance is suppressed. Since the common mode will radiate, the quality factor of any resonance so induced is low. Consequently, common mode currents may be induced on the feed line for a wide bandwidth about the resonant frequency, and therefore cannot be suppressed by altering the antenna geometry to change the metal strip lengths unless substantial changes are also accepted in the radiation characteristics. The common mode termination has the effect of changing the condition at the balun end of the feed line metal strip without altering the antenna geometry in such a way that, at the frequency of operation of the antenna, common mode currents are suppressed.

Recalling that the scan blindness effects are caused by interference between radiation from y-directed and z-directed sources, the modification of the common mode current on the feed line achieved by the use of a low impedance common mode termination is such that the radiation from the interfering sources reinforces, rather than cancels, at beam-steer angles for which scan blindness would otherwise occur. This effect gives rise to the improved active impedance characteristics. An additional design parameter has therefore been made available by the use of a hybrid ring power divider as a balun, through which it is possible to control the feed line scattering in such a way as to enhance the active impedance characteristics of the phased array.

Radiation characteristics

In classical array analysis, the overall radiation pattern of an array is a function of both the distribution of the elements in the array aperture and the radiation characteristics of the elements. In the case of the distribution of the elements in the aperture, an *array factor* can be identified, which may be determined from the position and excitation of each element. The array factor is then multiplied by an *element pattern factor*, which is the radiation pattern of an individual antenna element for a particular excitation across the array aperture. In the case of an infinite array, the element pattern factor will be the same for each element. A useful illustration of the radiation characteristics of an antenna element in a phased array is therefore obtained by considering the field radiated by a single element at angles corresponding to the beam-steer angle of the array. Although a complete radiation pattern is not obtained for each beam-steer angle, it is assumed that the array factor is such that the most significant effect of the element pattern factor on the overall radiation pattern of a practical array will be in the direction of maximum radiation as defined by the array factor.

Principal plane element pattern factors at angles corresponding to the beam steer angle of the array are shown in Figure 6.7 for the three substrate supported metal strip antennas analysed above. The results are obtained directly from the current distributions computed in the numerical analysis. Figure 6.7 shows the principal plane

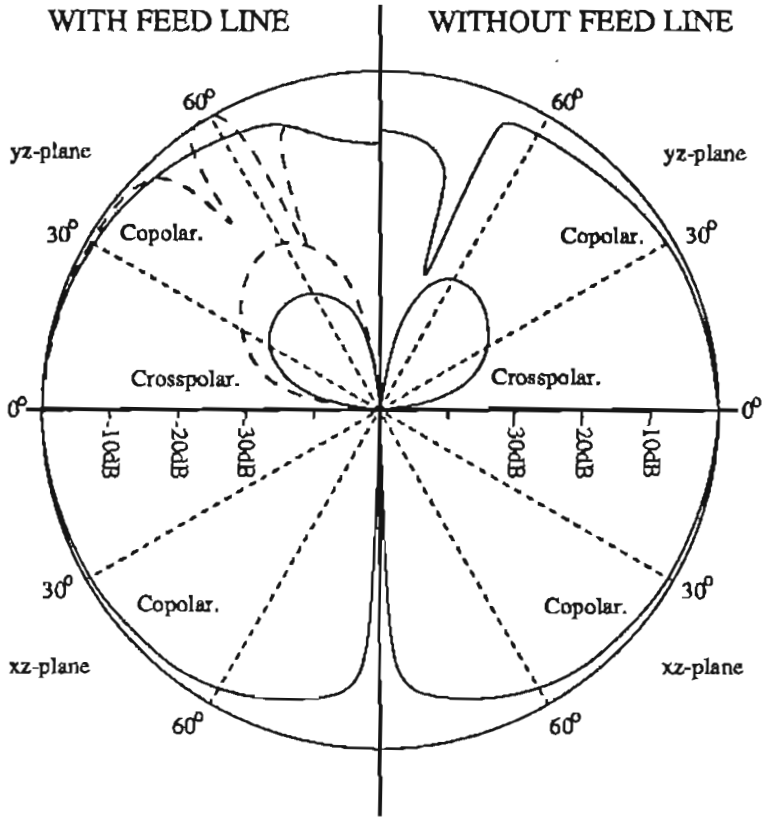

Figure 6.7: Element pattern factor in infinite array array environment. Right hand side: without feed line. Left hand side: with feed line (solid line: common mode terminated, dashed line: common mode isolated). The yz-plane patterns correspond to $\varphi = 90°$ beam steer angles and the xz-plane patterns to $\varphi = 0°$ beam steer angles.

radiation characteristics for one quadrant from $\theta = 0°$ to $\theta = 90°$ in each plane, since the yz-plane is symmetrical and the asymmetry in the xz-plane, due to the location of the substrate only on one side of the metal strip, is small. On the right hand side of Figure 6.7, the principal plane element pattern factors of the substrate supported coplanar strip folded dipole without feed line are shown. The effect of the scan blindness near $\theta = 70°$ in the yz-plane ($\varphi = 90°$ scan-plane) is clearly apparent from the radiation pattern minima in the co-polarized field. For an infinite array, scan blindness is complete, and a complete null should exist, however, because a large but finite array size is used in the numerical analysis, a complete null is not obtained. In addition, the five degree angular resolution of the data used to obtain the fitted curves

shown in Figure 6.7 is such that the actual depth of the null is only approximately determined. Nevertheless, the detail shown illustrates the effect of the scan blindness on the radiation characteristics. Another feature of interest in the principal plane element pattern factor is the cross-polarization in the yz-plane, which is increased over that of the isolated element, shown in Figure 4.6, for angles approaching the scan blindness. This is caused by the asymmetry in the x-directed polarization currents in the substrate introduced by the phase shift across the array aperture to produce the required beam-steer angle. Because there is no mechanism for field cancellation of the x-directed radiation, no scan blindness effects are observed in the cross-polarized radiation. In the xz-plane, the co-polarized radiation exhibits the expected smooth variation with angle. The left hand side of Figure 6.7 shows the principal plane element pattern factors for the substrate supported coplanar strip folded dipole with a coplanar strip feed line for the two common mode terminations described above. Although the polarization currents in the substrate are completely modelled, only the radiating mode currents on the metal strips comprising the folded dipole and feed line are considered in the analysis. It is noted, however, from the results for isolated elements of this type presented in Section 4.2.3 that the transmission line mode currents on the feed line and folded dipole have little effect on the principal plane radiation patterns. The effect of neglecting these currents in the computation of the principal plane element pattern factors is therefore small. The scan blindness effects noted in the active impedance results for the case where the terminals at the base of the feed line are open-circuit to the common mode are again clearly observed in the yz-plane co-polarized field. Moreover, the beneficial effect of an alternative termination presenting a low resistance termination to the common mode at the base of the feed line is again apparent. Of additional note, however, is the fact that even for small angles, θ, in the yz-plane, the cross-polarized field is significantly increased in the case where the common mode at the base of the feed line is terminated in an open-circuit. This is due to the fact that the common mode current excited on the feed line as the beam is steered excites additional x-directed field components in the substrate. Where the common mode on the feed line is suppressed by means of an appropriate termination, the cross-polarization performance, as well as the overall scanning performance, is found to be

improved. Once again, because symmetry about the xz-plane is maintained, the xz-plane element pattern factor is unaffected by the beam-steering.

The three examples considered above suggest that the numerical analysis outlined in this thesis can provide useful design information concerning the impedance and radiation characteristics of large phased arrays constructed using MMIC antennas. At the present time there appear to be few techniques reported in the literature which are capable of providing results with which to compare those presented here for antenna structures incorporating finite size, electrically thick dielectric substrates. Some recent work on endfire tapered slot antennas, however, shows some promise for application to the problem of finite size elements [57].

6.3 Phased array simulator studies

Three-element phased array simulators were used to test the accuracy of the theoretical results in the $\varphi = 0°$ plane for two beam-steer angles. The simulators were "looking-out" simulators as described in Appendix G, where each of the three elements is either excited or terminated in a matched load, while a waveguide that simulates the infinite array environment at specific beam-steer angles encloses the elements and is terminated in an absorbing load so that only modes propagating outward from the array aperture exist. The substrate supported metal strip antennas used in the simulators were designed so that the substrate permittivity and all of the relevant dimensions correspond to those in the numerical examples of the previous section.

The first phased array simulator considered has the geometry shown in Appendix G as Figure G.1b, where each of the three antenna elements is imaged about the broad wall of the waveguide and is fed via a coaxial connector. Substrate supported metal strip antennas, each comprising a single metal strip, were used in the experiment. The elements dimensions were chosen so that an isolated antenna was resonant at 2.56GHz, and the waveguide dimensions were chosen to be 175×29mm, resulting in an array

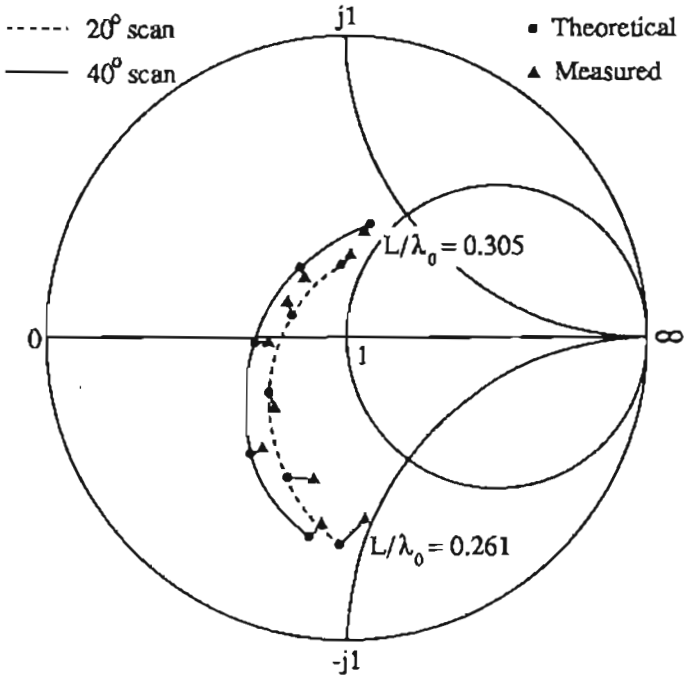

Figure 6.8: Theoretical and measured active impedance in $\varphi = 0°$ plane for unbalanced feed point simulator. $Z_0 = 50\Omega$.

spacing $d_x = d_y = 0.5\lambda_0$ at the design resonant frequency. Using this phased array simulator geometry, the scattering-parameters can be measured for reference planes at the base of the strip monopoles by introducing an electrical delay corresponding to the offset between the calibration reference plane and the base of the strip monopoles. As in the measurements on single imaged antennas described in Section 3.3, no empirical adjustment is made to the measured results. Reflection coefficients for two beam-steer angles in the $\varphi = 0°$ plane, which at 2.56GHz are $\theta = 19.5°$ and $\theta = 41.8°$, are obtained as described in Appendix G. The corresponding active impedances are shown in Figure 6.8. It is noted that the beam steer angle which is simulated is a function of the frequency of operation, however, over the measured bandwidth the beam-steer angles for the two cases are close to 20° and 40°. The agreement between the theoretically predicted active impedance and that measured using the phased array simulator is very good. Multiplying the impedances shown in Figure 6.8 by $\gamma^2 = 4$ produces the impedance levels illustrated previously for substrate supported coplanar

strip folded dipoles.

A second phased array simulator was constructed with substrate supported coplanar strip folded dipole antennas having coplanar strip feed lines. The elements used were identical to those described as **Antenna C** in Section 4.2.3, and consist of a coplanar strip folded dipole having equal width folded and driven arms and a coplanar strip feed line fed by a hybrid ring power divider used as a balun. The relative dimensions of the antenna element were identical to those in the previous phased array simulator example, but were scaled so that an isolated antenna element was resonant at 5GHz. The phased array simulator geometry is shown in Appendix G as Figure G.1a, and the waveguide cross-section dimensions were chosen to be 30mm×90mm to produce the same beam-steer angles as the previous simulator. The feed ports in this simulator arrangement are coaxial to microstrip line transitions connected to the 50 ohm microstrip lines that feed the hybrid ring baluns. The experimental assembly can be visualized by considering the three-element array shown in Figure 5.11 enclosed by the waveguide as described above. As indicated in Appendix G, for a given beam-steer angle, only the calculation from the measurement procedure of the magnitude of the reflection coefficient at the feed port of an element in an infinite array environment is meaningful. The effect of the balun and feed line would otherwise need to be de-embedded, and the approximations required for such a de-embedding procedure to be adopted are likely to outweigh any benefits.

The theoretical active impedance at the feed point of the metal strip folded dipole, obtained by applying the analysis described in Sections 6.2.1 and 6.2.2 over the bandwidth of interest, may be used to predict the magnitude of the reflection coefficient at the coaxial feed port reference plane used in the experiment. The calculation of the reflection coefficient at the feed port reference plane from the active impedance at the centre of the metal strip folded dipole proceeds in a similar manner to that described for a three-element array in Section 5.5, except that only a single impedance term is considered. For this calculation, the balun and feed line are considered to be lossless and perfectly matched. The measured and predicted magnitude of the reflection coefficients for the two beam-steer angles of the phased array simulator are given

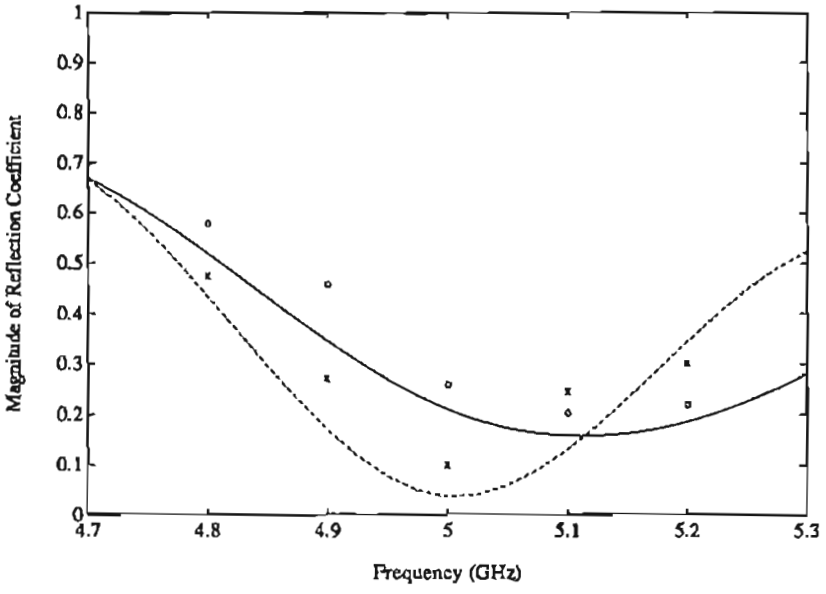

Figure 6.9: Theoretical and measured magnitude of reflection coefficient for balanced feed point simulator. Solid line: 20°, $n = 1$ (x - measured), Dashed line: 40°, $n = 2$ (o - measured).

in Figure 6.9 for frequencies near the antenna resonance. Good agreement between theory and experiment is again obtained for both of the beam-steer angles over the bandwidth considered.

The phased array simulator experiments described here indicate that, for the beam-steer angles measured, the theoretical results are sufficiently accurate for use in the design of practical array elements. Validation of the theoretical results is, however, limited by the range of beam-steer angles that may be considered. The use of larger simulators presents one option for further experimental investigation, however phased array simulators do not permit measurements to be taken in the $\varphi = 90°$ plane where the more significant dielectric and feed line effects occur.

6.4 A single strip fed antenna array

In addition to phased arrays, MMIC antennas have applications in other millimetre wave systems where the benefits of MMIC technology are desired. Examples include transmitting arrays for spatial power combining applications [33], and imaging arrays where preamplification is beneficial to increase the sensitivity of the system [103]. In these cases, phase shifting is not usually a requirement, and the complexity of the electronics may be significantly less than for phased arrays. An antenna design that occupies the minimum possible substrate area is therefore desirable to maintain a high packing density on the MMIC wafer, and consequently reduce the cost associated with integration of the antenna element. For this reason, the single strip fed substrate supported metal strip antenna described in Section 4.3.2 offers attractive advantages, since the unbalanced feed removes the requirement for a balun. Although a minimum substrate area design is achieved, and a good impedance match is obtained to a 50 ohm microstrip line, the radiation characteristics have been shown to have some shortcomings. The analysis of arrays of single strip fed substrate supported metal strip antennas in this section is aimed at demonstrating how acceptable radiation performance may be obtained for applications where beam squint and cross-polarized radiation are undesirable by special subarray arrangements within the overall array.

A method for reducing the degradation of the radiation characteristics caused by feed line radiation in arrays of rectangular microstrip patch antennas designed to obtain circularly polarized radiation by selecting an appropriate array geometry has been described in the literature [104]. Similar considerations can be applied to a linearly polarized array of single strip fed antennas, and an array exhibiting good radiation characteristics may be constructed using the unit cell shown in Figure 6.10. Two pairs of elements, mirror imaged in the xz-plane make up the unit cell, which forms a subarray that is replicated to form the complete array. Although a unit cell comprising a single pair of elements could be conceived, subsequent analysis reveals that the radiation in the diagonal planes at 45° to the principal planes has a high cross-polarized component caused by currents on the single strip feed lines, and consequently the four

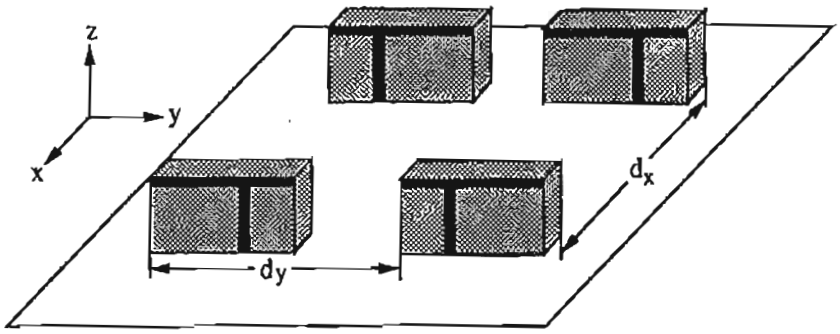

Figure 6.10: Single strip fed substrate supported metal strip antenna array unit cell.

element unit cell is chosen for consideration here. Symmetry considerations require that for in-phase currents to be achieved on the metal strip dipoles comprising either pair of elements, the currents on the single strip feed lines must be anti-phase. This in turn requires that the MMIC modules associated with these elements must be able to produce a 180° phase inversion alternately from element to element. In practice this phase inversion may be achieved in a variety of ways, depending on the MMIC electronics employed and the particular application. For example, a differencing scheme may be applied to signals received by alternate elements in an imaging array.

An infinite array of the unit cells shown in Figure 6.10 may be analysed using the techniques described in the previous section. Because no beam steering is required, relatively small arrays provide well converged results. By considering the unit cell of Figure 6.10 and its adjacent cells, it is noted that except for changes in polarity due to the required symmetry, the current on every element of the unit cell, and hence the array, will be same. A reference element is chosen close to the centre of the array, and the current distribution on the reference element is computed for an excitation at the base of the single strip feed line. The currents on the remaining elements of the array are included by summing their contribution to the total field at the segments of the reference element as described in Section 6.2.1, and well converged results are obtained for an array of 5×5 unit cells.

For analysis, the single strip fed substrate supported metal strip antenna elements

were chosen to be identical to the element analysed in isolation in Section 4.3.2. The array spacings were chosen to be $d_x = d_y = 0.5\lambda_0$ at the half-wave resonance of the elements, which occurs at $L/\lambda_0 = 0.34$. The computed input impedance of $88+j1$ ohms at the half-wave resonance may be compared with the isolated antenna impedance of $56+j11$ ohms computed at the same frequency. The principal plane radiation patterns for the complete 5×5 unit cell array are shown in Figure 6.11. It is recognized that for finite size arrays, identical currents on all elements will not be obtained, however, the results presented illustrate the performance that would be achievable where the 5×5 unit cells form part of a much larger array where the edge effects can be neglected. The principal plane radiation patterns reveal that the introduction of the symmetry associated with the unit cell results in a symmetrical beam and low cross-polarization in both planes. The remaining cross-polarization in the yz-plane is due to x-directed field components induced in the substrate. The radiation characteristics in a diagonal plane at 45° to the principal planes are shown in Figure 6.12. It is important to investigate the characteristics in the diagonal plane because the array factor caused by the non-uniform feed line spacing and unusual phase relationship between the currents on the feed lines may introduce significant cross-polarized side lobes into the radiation pattern. From Figure 6.12 it is clear that the cross-polarized side lobes are small for the array geometry under consideration. Improved side lobes, both co-polarized and cross-polarized, may be obtained in all planes by including an appropriate amplitude taper in the excitation [105]. Provided that the taper is gradual, over a large array the infinite array analysis should still provide a good indication of the anticipated radiation and impedance characteristics.

The analysis of this novel array of single strip fed substrate supported metal strip antennas has further demonstrated how the techniques developed in this thesis may be applied to MMIC antenna geometries to provide design information useful in the of development complex integrated antenna structures and arrays. Because the complete antenna and feed line have been included in the analysis, the numerical results obtained in this section are expected to provide a useful prediction of the performance of such millimetre wave arrays.

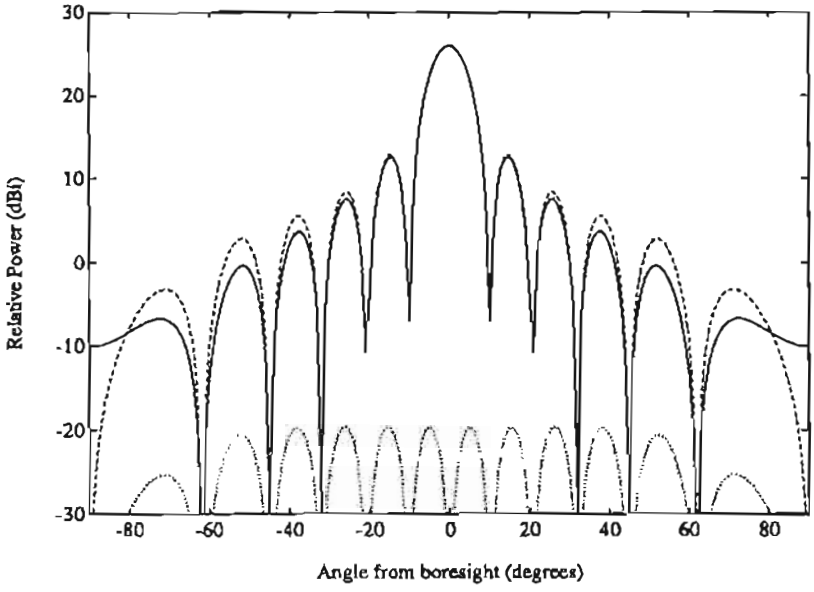

Figure 6.11: Principal plane radiation patterns for an array comprising 5×5 unit cells. Solid line: yz-plane copolar., Dashed line: xz-plane copolar., Dotted line: yz-plane cross-polar.

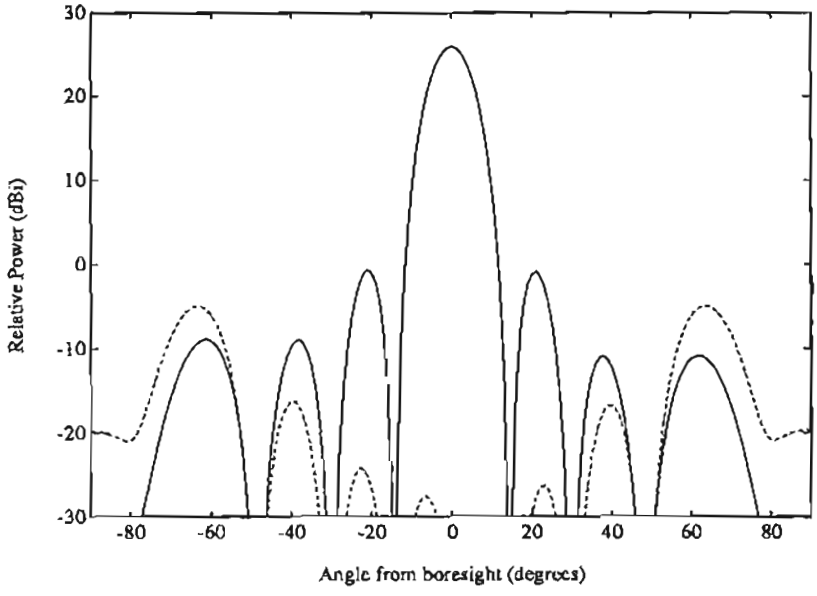

Figure 6.12: Diagonal plane radiation patterns for an array comprising 5×5 unit cells. Solid line: copolar., Dashed line: cross-polar.

6.5 Summary

In this chapter, the analysis of substrate supported metal strip antennas has been expanded to an investigation of an infinite array of elements in order to assess their performance as elements in large phased arrays, and to determine the characteristics of such arrays. The environment of the infinite array provides a good approximation to the environment in which the majority of elements of the millimetre wave MMIC arrays are expected to operate. A numerical method for introducing the conditions required for an infinite array is developed, and applied to several antenna geometries. As well as the modelling of the electrically thick, finite size dielectric substrate and the metal strip antenna itself, techniques are developed for including the effect of feed lines in the analysis. The final formulation of the problem has the advantage that the complete geometry may be analysed with high computational efficiency.

The methods developed for infinite array analysis have exhibited well behaved numerical characteristics, and have been used to study practical design problems. In particular, the development of a substrate supported coplanar strip folded dipole with a coplanar strip feed line has been undertaken, and a structure which exhibits good impedance and radiation characteristics over a wide range of beam-steer angles has been developed. Supporting the analytical techniques are two phased array simulator experiments, the results of which show good agreement with the numerical computations. Further to the study of practical element geometries is the development of a novel single strip fed substrate supported metal strip antenna array for fixed-beam applications requiring the antenna element to occupy the minimum possible substrate area. Solutions to such practical problems of MMIC antenna element and array design have been made possible by the analytical methods developed in this chapter.

The contributions described in this chapter are therefore

- The inclusion of the infinite array conditions with the finite size, composite dielectric and conducting structure formulation.

- The development of efficient methods for modelling practical phased array elements comprising folded dipoles and feed lines.

- A description and explanation of substrate induced scan blindness effects for substrates which are electrically thick.

- An understanding of the manner in which feed line induced scan blindness affects the antenna performance, and the development of a technique of modifying the common mode termination at the base of the feed line, by the novel use of a hybrid ring power divider as a balun, to suppress the common mode current excited on the feed line as the beam is steered.

- The exploitation of the interference between radiation from polarization currents in the substrate and radiation from common mode currents on the feed line to eliminate feed line induced scan blindness and improve the polarization characteristics of the array as the beam is steered.

- The analysis and design of a novel single strip fed substrate supported metal strip antenna array.

In summary, this chapter has described, as the culmination of the present work on the analysis of substrate supported metal strip antennas, its application to the design of large steerable arrays. The analysis that has been developed and applied takes account of all of the practical details of the antenna geometry, and has revealed that arrays of such MMIC antennas have the potential to offer excellent performance. Of particular significance is the fact that the presence of the electrically thick substrate which arises naturally in the fabrication of MMIC antennas can substantially improve the beam-steering characteristics of the array. The thrust towards producing cost-effective arrays using MMIC technology therefore has the additional benefit of increased array performance by virtue of the inherently good characteristics of the type of antenna element that has been studied in detail in this thesis.

Chapter 7

Conclusions and Recommendations

7.1 Conclusions

The motivation for the research described in this thesis is the strong possibility that millimetre wavelength phased arrays that fully exploit MMIC technology by incorporating antenna elements as part of the MMIC chip offer perhaps the greatest promise as a means of fabricating reliable, cost-effective systems. Although the bulk of the work reported in the literature has focussed on TILA arrays, in particular emphasizing the use of microstrip antenna elements, the work described in this thesis has considered an alternative, LITA architecture, for the array. By examining the principal factors governing the choice of an array architecture, and considering the recognized limitations of TILA arrays, it may be concluded that the LITA architecture offers some significant benefits for MMIC based arrays. The advantages may be clearly perceived in technological areas such as operating efficiency, heat removal, signal routing, yield control and substrate area utilization. It is also apparent that these advantages are obtained with either less or comparable complexity in the array construction. It is likely, however, that the technological advances that are being made in the effort to

realize multilayer TILA active arrays are also applicable to LITA array construction, and that the resulting materials and techniques can be employed to develop methods for assembling LITA arrays from MMIC chips incorporating antenna elements or even subarrays. Given that in principle the construction of a LITA array is feasible, a key factor that may have limited their development to date has been the dearth of design information pertaining to appropriate antenna elements. The original contribution of this thesis relates to the comprehensive analysis of a class of antenna elements which are identified as being particularly suitable as MMIC antennas for LITA arrays.

Substrate supported metal strip antennas, consisting of narrow metal strips contiguous with the ends of ungrounded extensions of the MMIC substrates, are ideally suited for application to millimetre wave arrays because of their simple geometry and small chip area usage. As analysed in this thesis, each metal strip is supported by a finite size, electrically thick dielectric substrate. The range of electrical thicknesses chosen in this research correspond at millimetre wavelengths to typical MMIC chip thicknesses. The presence of the substrate is found to significantly affect the antenna characteristics, and for this reason a numerical analysis of the antenna, required for design purposes, has been developed which accurately takes account of the substrate. An electric field integral equation approach is described where the substrate is modelled using a volume formulation, and a computationally efficient algorithm is obtained that provides the basis for a design tool. Initially the basic antenna geometry, without any feed structure, is analysed. The results of this analysis are compared with carefully designed experimental measurements in order to verify the numerical implementation. These comparisons show excellent agreement between the theoretical and measured results.

From the results obtained for the basic antenna geometry, several important characteristics which are due to the presence of the substrate are identified. The analysis accurately predicts the resonant frequency of the antenna and the radiation resistance. When compared with a half-wave resonant metal strip dipole without a substrate, both of these characteristics are found to be reduced due to the presence the substrate. The impedance characteristics also reveal that resonances may be excited within the sub-

strate, and these may affect the antenna performance. Furthermore, from the radiation characteristics, it is evident that when the substrate is electrically thick and has finite dimensions, polarization currents excited in the substrate contribute to the far-field radiation of the antenna, particularly in the form of cross-polarized components. The discovery of these effects, and the understanding of their origin, arises directly from the application of the accurate and efficient numerical analysis which has been developed.

Following elucidation of the role of the basic antenna geometry, practical details pertaining to feed lines and impedance matching are addressed. The numerical method is expanded to include a coplanar strip feed line by using thin-wire approximations for the metal strip components of the structure. Impedance matching is achieved by means of a coplanar strip folded dipole, and a decomposition analysis, used to obtain the antenna impedance, is demonstrated to provide accurate results. The analysis of the substrate supported coplanar strip folded dipole antenna, fed with a coplanar strip feed line, provides the basis for a design procedure for practical antenna structures. Design information is obtained from a numerical model which represents all of the essential details of the geometry, thereby ensuring that all of the important effects of the feed line and substrate are considered. In this way, the radiation characteristics of the complete antenna can be studied with the aim of finding structures that reduce the substrate-induced cross-polarized radiation, which is found to be significant in the yz-plane and in the diagonal planes at 45° to the principal planes. In the case of the yz-plane , a back-folded dipole is developed which increases the symmetry inherent in the overall antenna geometry and thereby reduces the excitation of polarization currents that contribute to cross-polarized radiation in this plane. In the case of the diagonal plane, an interesting interference effect is found to occur between the radiation from the balanced mode currents on the coplanar strip feed line and the radiation from the polarization currents in the substrate. It is found that these two mechanisms of cross-polarized radiation result in far-field components that partially cancel each another, thereby reducing the overall cross-polarization in the diagonal planes. A correctly dimensioned coplanar strip folded dipole, used in conjunction with a coplanar strip feed line, is found to present a good impedance match to the coplanar strip feed line

over a 10% bandwidth. Practical coplanar strip fed, substrate supported coplanar strip folded dipole antennas are therefore shown to exhibit excellent characteristics. They have been derived using the numerical technique developed, and verified experimentally. It is concluded that these antennas have characteristics that would satisfy relatively stringent specifications on performance in MMIC based applications.

Because substrate supported metal strip antennas exhibit good characteristics when operated in isolation, further development of the numerical analysis was undertaken to consider mutual coupling in small arrays. Collinear and collateral two-element and three-element arrays were studied to determine the mutual coupling between elements as the element spacing was altered. Impedance matrices for the antenna input ports were computed, and the results were used to predict the mutual coupling between substrate supported coplanar strip folded dipoles fed with coplanar strip feed lines. The results, reinforced by experiments, reveal that for the collinear arrays, the mutual coupling is substantially lower for substrate supported metal strip antennas than for the corresponding metal strip dipoles without substrates. This appears to be due to the shortening of the metal strip antenna at resonance caused by the presence of the substrate. Significantly, the lower mutual coupling is comparable with the case of a metal strip dipole, without substrate, bent downwards at 45°; a commonly used method to reduce mutual coupling in dipole arrays. In the case of substrate supported metal strip antennas, however, the reduced mutual coupling is achieved without degradation of the cross-polarization performance as would be the case with the bent dipole arrays. The collateral arrays were found to exhibit comparable performance whether or not the substrate was present. The low mutual coupling reinforces the promise of good array performance, and also suggests that wider use of electrically thick substrates at lower frequencies may be beneficial in some applications.

To gain a detailed understanding of the characteristics of substrate supported metal strip antennas in large phased arrays, an infinite array analysis is undertaken. The infinite array environment is introduced by summing the contributions of all of the elements to the electric field at a specified reference element. The result of this summation is approximated when the Green's function integrals for the structure are computed.

After formulating the problem for the basic geometry, a method of including the effect of coplanar strip feed lines is developed so that again all of the essential parts of a practical antenna can be modelled. To begin with, results are computed for the basic geometry, without feed lines, to study the influence of the substrate on the scanning performance of the array. Both active impedance results and element radiation pattern factors are computed for beam-steer angles in various scan-planes. For results in the $\varphi = 0°$ plane, phased array simulator experiments were performed to verify that the analysis yields the correct results. Subsequent studies using the validated model reveal a scan blindness in the $\varphi = 90°$ plane. An understanding of the nature of the fields induced in the substrate indicates that interference between the radiation from currents on the metal strip and polarization currents in the substrate is the cause of the scan blindness. Because the substrate considered in the analysis is electrically thick, the scan blindness occurs for beam-steer angles around 70° from boresight, suggesting that for thick substrates substrate induced scan blindness will present a problem that may have to be overcome by suitably engineered modifications or additions to this idealized radiating element.

When feed lines are included in the analysis, additional effects arise in the characteristics of the array as the beam is steered in the $\varphi = 90°$ plane. These are due to scattering from the common mode current induced on the feed line as the beam is steered. Feed line induced scan blindness effects are shown by further analysis to occur when the terminals at the base of the feed line present an open circuit to the common mode current. Since they occur for scan angles only 40° to 50° from boresight they present a more serious problem to the array designer than the substrate induced scan blindness. However, to alleviate the scan blindness problems, a method making use of the properties of a hybrid ring power divider as a balun is developed, whereby the terminals at the base of the feed line present a low resistance to the common mode current. This has the effect of reducing the common mode on the entire feed line to the extent where the interference between the radiation from the various current sources reinforces the total co-polarized radiation at beam-steer angles where scan blindness would otherwise occur. The resulting antenna characteristics are shown

to be devoid of scan blindness, and excellent scanning performance is obtained for the array over almost the entire range of beam-steer angles. This result is of particular significance. Provided that the common mode current on the feed line is controlled by an appropriate common mode termination at the base of the feed line, the presence of polarization currents in the electrically thick, finite size substrate inherent in the MMIC antennas under consideration reduces or eliminates the feed line induced scan blindness effects that would otherwise seriously degrade the array performance. Moreover, unlike conventional methods for eliminating scan blindness by bending the metal strip arms downwards, the improvement in scanning performance is achieved without increasing the cross-polarized radiation.

As a further example of substrate supported metal strip antenna arrays, a single strip fed substrate supported metal strip antenna array is developed and analysed. Such an array has applications to millimetre wave imaging systems and spatial power combining, and the single strip fed antenna element offers an attractive feature of occupying minimal substrate area. The computed results for a single isolated element have been verified by experiment, and confirm that the thin-wire approximation for the metal strip parts of the antenna structure is accurate. An analysis of the array illustrates further the application of the numerical techniques that have been developed to solve design problems.

Based on the numerical techniques in this thesis, a design procedure can be established to meet a set of specifications for an array, assuming that LITA architecture is accepted. From the general characteristics of substrate supported metal strip antennas obtained in this research, their suitability for use in a particular system, for example in terms of bandwidth or gain, may be assessed. Given that substrate supported metal strip antennas are then identified as being able to satisfy the basic system specifications, a particular MMIC fabrication process must be identified, and the parameters associated with that process ascertained. From these parameters it is then possible to study basic antenna geometries and compute radiation and impedance characteristics. Using the radiation and impedance characteristics of an idealized antenna element as a guide, the design of an impedance matching and feed network may be undertaken, and

the resulting structure analysed to test its overall performance. At this stage, modifications to the antenna and feed geometry may be made to optimize performance. After arriving at a suitable element geometry, computations to obtain mutual coupling data as well as the active impedance and radiation characteristics of an element in an infinite array environment may be made to achieve a suitable array design. The method described in this thesis for eliminating scan blindness effects may be employed to achieve satisfactory performance over the required range of beam-steer angles. Further corrections to the antenna geometry may also be necessary to allow for the effect of mutual coupling on the antenna impedance. A methodical sequence of steps, as described above, reduces the degree of iteration needed in the design procedure. At the conclusion of the above procedure, a satisfactory element will have been designed. Furthermore, since the element is designed with the array performance taken into account, it is anticipated that for the large, practical arrays envisaged, the design procedure will also allow useful performance predictions to be made for the array. Further work to assess the effect of the array edges or amplitude tapers across the array aperture, not undertaken in the research described in this thesis, may be required to determine the detailed array radiation pattern and sidelobe levels. It is noted, however, that this problem is common to almost all procedures used to design phased array elements.

In summary this thesis presents a study of a class of MMIC antenna elements suitable for application to millimetre wave active arrays. The original contribution of the work presented is outlined at the end of each chapter, however, the broader aims of the work that have been achieved are

- An objective review of MMIC based array architectures with a view to understanding the merits and limitations of the available options.
- The identification of a class of MMIC antennas for assemblies that orientate MMICs normal to the array aperture compared with the more commonly favoured arrangement of MMICs parallel to the aperture.
- The development of efficient computational tools to aid the electromagnetic design of LITA arrays of MMIC antennas.

- An understanding of the fundamental effects of the finite size, electrically thick substrate associated with substrate supported metal strip antennas for MMIC integration.
- The exploitation of particular characteristics of substrate supported metal strip antennas to develop elements and arrays that exhibit good performance.

The research presented has therefore been able to make substantial advances in the analysis and design of MMIC antenna elements suitable for LITA arrays, and widens the possibilities available for cost-effective implementation of MMIC technology active arrays for millimetre wavelength applications.

7.2 Recommendations for Future Work

The stimulus for future millimetre wave system development will be provided by commercial applications as well as the traditional military orientated applications [106], and for this reason trends toward cost-effective, readily manufacturable components will increase. Further development of LITA arrays based on the work of this thesis is likely to proceed on four fronts.

Firstly, for the promise of LITA arrays employing substrate supported metal strip antennas to be fulfilled, elements and subarrays need to be fabricated using MMIC technology to implement subsystems that convincingly demonstrate the practical viability of the approach. Such subsystems may demonstrate some or all of the functions of a phased array, however, equally important is the development of the appropriate technology for packaging and housing the MMIC modules and for constructing the overall array with the required interconnections for control and signal routing. The advances being made in planar array technology suggest that this is achievable.

Secondly, while antenna geometries having good characteristics have been described,

and array performance has been predicted by analysis, it is inevitable that alternative element and array geometries will need to be investigated. The cost-effective fabrication of millimetre wave phased arrays has implications for a large number of applications, including within-building high-speed data communications and inter-satellite communications, collision avoidance and tracking radars, and imaging systems. Antennas offering wide bandwidth, and arrays with dual polarization capability are two areas worthy of consideration, these being driven by contemporary trends in polarimetric radar and remote sensing. Arrays which offer a lightweight, open construction and a ready means of heat removal from active components may well be considered from a technological standpoint to be desirable for satellite or portable systems. The resulting geometries, however, also require analytical tools to be developed in order to obtain a satisfactory design. Many challenging issues of analysis are opened up when alternative antennas and array geometries are considered, but common to all of them is the need to accurately model finite size, composite conducting and dielectric structures. The foundation provided by the work recorded in this thesis offers a starting point for such further development.

Thirdly, the question of system design remains unanswered. The promise of spatial power combining in active lens or active reflector structures is widely recognized as a means of reliably distributing millimetre wave energy, and compartmentalising various system functions. It is encouraging that the MMIC arrays considered in this thesis are at least compatible with this approach to system design, since by integrating antenna elements at both ends of a substrate, a chip can be used to receive spatially distributed millimetre wave energy, perform whatever functions are needed, and then re-radiate the energy in space. Analysis of such systems, using the design data obtained by the techniques described in this thesis, may provide solutions which predict the basic performance that is achievable.

Finally, when economies of scale permit it, MMIC antenna technology may be useful in systems requiring much smaller arrays than those considered in this thesis. Where this is the case, neither the small array analysis nor the infinite array analysis are currently capable of providing reliable design information. The two possibilities to

redress this are, first to compute all of the self and mutual impedances for elements of larger arrays using more powerful computers and algorithms that are able to efficiently handle problems that may be several orders of magnitude larger in computational terms than those considered so far, and second to develop and make use of approximation techniques for obtaining data for finite size arrays from the analysis of an infinite array.

As the technology available for millimetre wave MMIC arrays becomes more advanced and more widely available, it is almost certain that the development of MMIC antenna elements and their application in arrays will flourish. The areas suggested above form areas for profitable and stimulating study.

Appendix A

Rectangular Cross-Section Dielectric Waveguide

The propagation of electromagnetic waves in dielectric guiding structures has been widely investigated for applications ranging from antenna design to opto-electronics. An exact solution exists for modes propagating along grounded and ungrounded dielectric slab waveguides, where the dielectric slab has a finite thickness but infinite lateral dimensions [107]. Such guided waves are often referred to as *surface waves*, and have been shown to be of importance in the analysis and design of planar printed circuit antennas [18,19,20]. Dielectric waveguides having rectangular cross-section may be analysed using approximate methods developed initially for integrated optics [108,109]. In these approximate methods, assumptions regarding the field distribution outside the dielectric are made such that the propagation constants of the guided wave may be determined by field matching at the dielectric boundaries. More recently, numerical methods have been applied to precisely model the field distributions and compute the propagation coefficients [110,111].

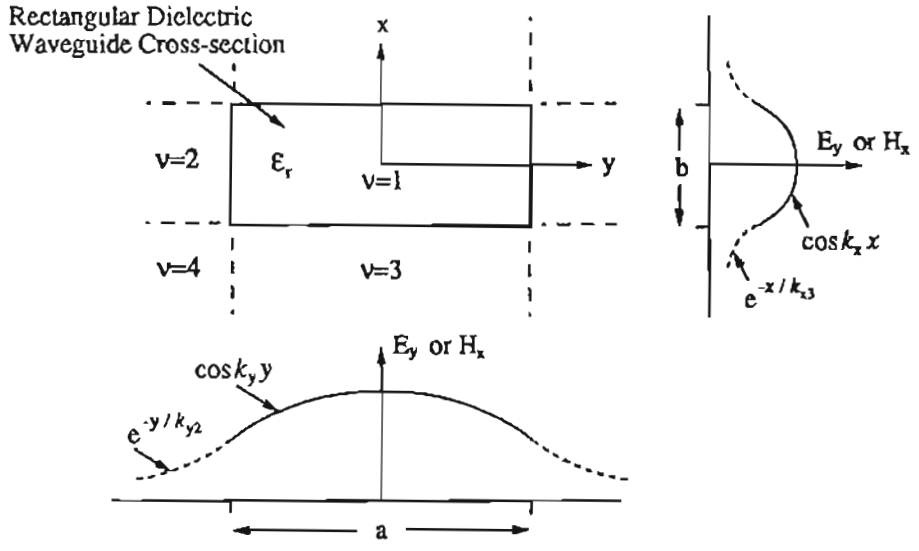

Figure A.1: Geometry and principal field distributions for rectangular cross section dielectric waveguide

Propagation Constants of Rectangular Cross-Section Dielectric Waveguide

Because the permittivity of the substrates used in this thesis is relatively large, the approximate method of Marcatili [108] is found to be adequate for the calculation of the propagation constants required for the analysis in Section 3.4.5. The dominant mode in the guiding structure formed by the rectangular cross-section ungrounded substrate of the antennas described in this thesis is the TE^{y}_{11} mode[1], having the principal field components E_y and H_x. Because of the orientation of the principal electric field component, the y-directed axial current on the metal strip antenna readily couples to this mode.

For the geometry shown in Figure A.1, the field distribution may be derived from

[1] Because of a rotation in the coordinate axes, this mode is identified as the TE^{x}_{11} mode in Marcatili's analysis.

the hybrid (or LSE) mode equations using the electric vector potential

$$F_{x\nu} = \begin{cases} C\cos k_x x \cos k_y y e^{-jk_z z} & \nu = 1, \text{for } |y| \le a/2 \text{ and } |x| \le b/2 \\ C\cos k_x x e^{-k_{y\nu} y} e^{-jk_z z} & \nu = 2, \text{for } |y| > a/2 \text{ and } |x| \le b/2 \\ C\cos k_y y e^{-k_{x\nu} x} e^{-jk_z z} & \nu = 3, \text{for } |y| \le a/2 \text{ and } |x| > b/2 \\ 0 & \nu = 4, \text{for } |y| > a/2 \text{ and } |x| > b/2 \end{cases} \tag{A.1}$$

where $\nu = 1, 2, 3, 4$ denotes the cross-section region, k_x, k_y and k_z are the propagation constants inside the waveguide ($\nu = 1$), $k_{x\nu}$ and $k_{y\nu}$ are the propagation constants outside the waveguide ($\nu = 2, 3$) and C is a complex constant. For the region $\nu = 1$ inside the dielectric, the permittivity $\epsilon_{r\nu} = \epsilon_r$, and for the regions $\nu = 2, 3$ outside the dielectric, the permittivity $\epsilon_{r\nu} = 1$. It is assumed in Marcatili's analysis that the fields do not extend into the region $\nu = 4$. The field components of the TE^y_{11} mode are

$$E_{y\nu} = \frac{-jk_z}{\epsilon_0 \epsilon_{r\nu}} F_{x\nu} \tag{A.2a}$$

$$E_{x\nu} = 0 \tag{A.2b}$$

$$E_{z\nu} = \frac{1}{jk_z} \frac{\partial E_{y\nu}}{\partial y} \tag{A.2c}$$

$$H_{y\nu} = \frac{1}{\omega \mu_0 k_z} \frac{\partial^2 E_{y\nu}}{\partial x \partial y} \tag{A.2d}$$

$$H_{x\nu} = \frac{k_{y\nu}^2 + k_x^2}{\omega \mu_0 k_z} E_{y\nu} \tag{A.2e}$$

$$H_{z\nu} = \frac{1}{j\omega \mu_0} \frac{\partial E_{y\nu}}{\partial x} \tag{A.2f}$$

By matching the internal and external fields tangential to the dielectric boundaries $y = \pm a/2$ and $x = \pm b/2$, the propagation constants may be determined, and the relevant solutions are obtained from

$$k_y a = \pi - 2\tan^{-1} \frac{k_y}{\epsilon_r \sqrt{(\epsilon_r - 1)k_0^2 - k_y^2}} \tag{A.3a}$$

$$k_x b = \pi - 2\tan^{-1} \frac{k_x}{\sqrt{(\epsilon_r - 1)k_0^2 - k_x^2}} \tag{A.3b}$$

where

$$k_z = \sqrt{\epsilon_r k_0^2 - k_y^2 - k_x^2} \tag{A.4}$$

and

$$k_0 = \omega^2 \epsilon_0 \mu_0 \tag{A.5}$$

It may be noted that when $a \rightarrow \infty$, and hence $k_y \rightarrow 0$, the solution becomes that of the TE_0 characteristic mode for ungrounded dielectric slab waveguide [107]. A comparison of the field component distributions of the TE_{11}^y mode in the rectangular cross-section dielectric waveguide with those for the TE_0 mode in the ungrounded dielectric slab waveguide reveals that although the principal components are similar, in contrast to the TE_0 mode the TE_{11}^y mode has a low-frequency cut-off characteristic. In addition, because $F_{x\nu}$ exhibits even symmetry about the yz-plane, neither the TE_{11}^y rectangular cross-section dielectric waveguide mode nor the TE_0 dielectric slab waveguide mode will propagate in grounded substrates typically used for MMICs.

Resonance Conditions

In the case of the substrate supported metal strip antennas described in this thesis, the rectangular cross-section dielectric waveguide formed by the substrate has a finite length. This introduces the possibility of resonances in the fields guided by the substrate. A transmission line model of the finite-length dielectric waveguide, formed by the ungrounded extension of the MMIC substrate and its image about the array ground plane, is given in Figure A.2b. The transmission line has a characteristic impedance Z_0 and a guide wavelength $\lambda_g = 2\pi/k_z$. The guide wavelength can be readily obtained from the computed propagation constants for the TE_{11}^y mode. Voltages sources, V, are shown in Figure A.2b to recognize that the TE_{11}^y mode is excited by the metal strips contiguous with the end of the substrate and its image. It has been shown in Section 3.2.1 that the antenna structures considered in this thesis can be idealized in such a way that the ungrounded part of the MMIC substrate forms a dielectric slab on a continuous ground plane. A side view of this arrangement is shown in Figure A.2a,

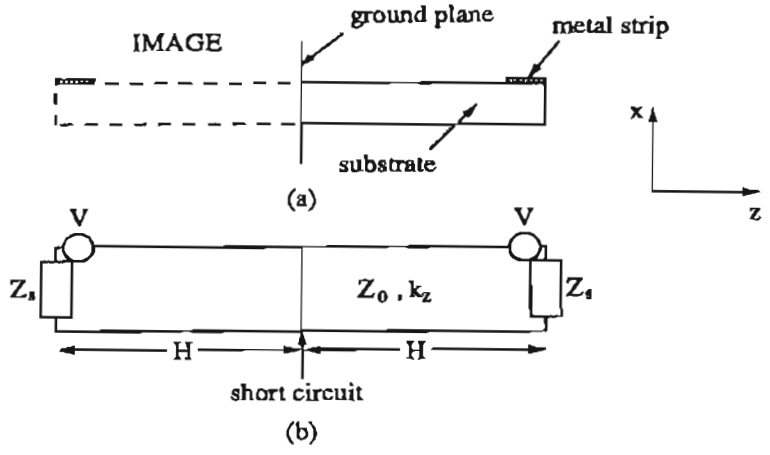

Figure A.2: (a) Side view of substrate supported metal strip antenna, and (b) transmission line model of the dielectric substrate.

where the image of the substrate and metal strip antenna about the ground plane is also shown. At the centre of the transmission line model, therefore, a short circuit exists since the total electric field tangential to the ground plane is zero. Due to the short circuit condition at the centre, only one half of the transmission line structure shown in Figure A.2b, having a physical length H from the array ground plane to the end of the substrate immediately beneath the metal strip, needs to be considered. The condition for resonance is therefore dependent on the end impedance, shown as Z_s in Figure A.2b.

Various methods have been developed for numerically determining the natural resonant frequencies of isolated dielectric resonators, and several of these are described in [112]. Techniques for calculating the end impedance (or admittance) of truncated dielectric slab waveguides have also been applied to microstrip dipole antennas to investigate the effect of the truncation on the radiation efficiency of the antenna [23]. For the antennas considered in this thesis, however, calculation of the end impedance is complicated by the presence of the metal strip antenna contiguous with the end of the substrate forming the dielectric waveguide, because the boundary conditions on the surface of a conductor must be satisfied at the top face of the substrate where the

metal strip is fabricated. It has been found that for dielectric waveguide cross-sections where $b/a \leq 0.2$, an end impedance $Z_s = 0$, corresponding to a short circuit, provides a satisfactory approximation. For a given waveguide length H, corresponding to the height above the ground plane that the ungrounded substrate of the antenna extends, dielectric resonances may be predicted to occur for propagation constants

$$k_z = \frac{n\pi}{H}, \tag{A.6}$$

where $n = 1, 2, \ldots$ corresponds to the integral number of half-wavelengths along the transmission line at resonance. The agreement between the resonances predicted by equation A.6 for $n = 1$, and those noted in the antenna characteristics computed in Section 3.4.5, suggests that this transmission line model is sufficiently accurate for most design purposes.

Appendix B

Radiation Pattern Measurement Using Integrated Diode Detectors

A method for measuring the radiation pattern of a substrate supported metal strip antenna without a feed line was described in Section 3.3.2. The method is based on a technique used for non-perturbing field measurements [80,81], and the details involved, together with a verification of the method, are outlined in this appendix.

For the analysis and measurements described here, a metal strip dipole antenna of length, L, and strip width, w, is supported in free space at a height, H, above a conducting ground plane. In practice polystyrene foam can be used to support the metal strip, thereby providing a good approximation to free space. The input impedance of such an antenna is readily calculated using a method of moments analysis for a thin wire dipole of radius $a = w/4$ [83].

In the measurement technique, a zero-bias Schottky Barrier Diode (SBD) is connected across a gap at the centre of the metal strip dipole. A small, packaged stripline SBD was used, such that the gap size was small compared with the strip length L. High

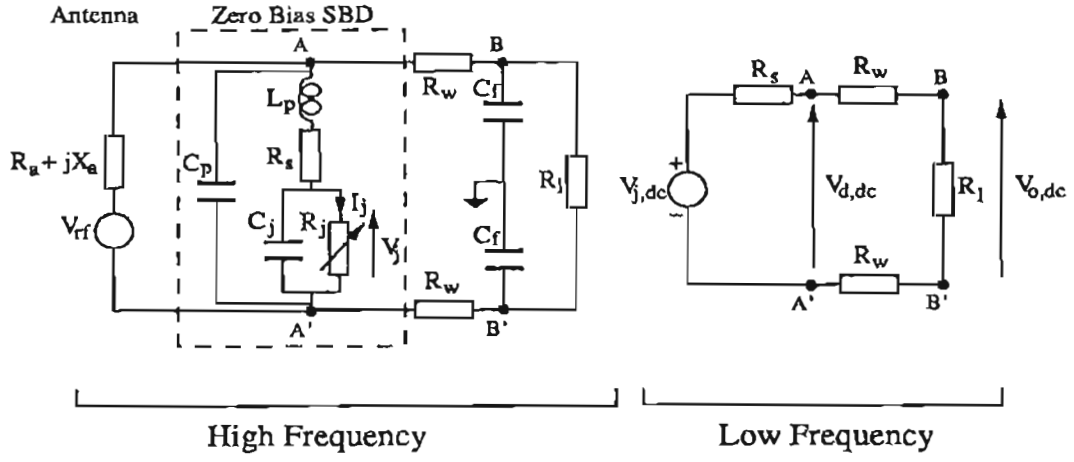

Figure B.1: Equivalent circuit of dipole antenna and integrated diode detector.

resistance leads extending through small holes in the ground plane to either side of the SBD provided the connection to the measurement instrumentation. As outlined in Section 3.3.2, these high resistance leads are such that they produce a negligible effect on the microwave fields around the antenna. The small holes in the ground plane also act as feed-through capacitors to ensure that any small microwave currents that may be induced on the high resistance leads are prevented from reaching the measurement instrumentation.

The equivalent circuit for the structure described above is shown in Figure B.1. The metal strip dipole antenna is modelled as its frequency dependent impedance, $R_a + jX_a$, in series with a voltage, V_{rf}. A uniform illuminating electric field is established, having a power density, P_{av}, that is the same for each frequency of interest, and the voltage V_{rf} may be expressed as

$$V_{rf} = V_0 \cos(\omega t + \zeta), \tag{B.1}$$

where ζ is an arbitrary phase angle, V_0 is the magnitude of the received voltage given by

$$V_0 = \frac{c}{\omega}\sqrt{8\pi R_a G P_{av}} \tag{B.2}$$

and G is the antenna gain. The components of the SBD equivalent circuit shown

Junction Resistance	(R_j)	5000Ω
Junction Capacitance	(C_j)	0.35pF
Series Resistance	(R_s)	30Ω
Packaging Capacitance	(C_p)	0.07pF
Packaging Inductance	(L_p)	0.4nH

Table B.1: Zero Bias Schottky Diode Parameters

in Figure B.1 are defined in Table B.1. Graphite coated card was used to construct narrow high resistance leads, which had a measured resistance greater that 10kΩ/cm. The total resistance of each lead is represented by a resistance R_w, where $R_w > 20\text{k}\Omega$ for the assembly employed. The input resistance of the measurement instrumentation is denoted by R_l, and with the high input resistance instrumentation employed, $R_l = 10\text{M}\Omega$. The value of the feed-through capacitance, C_f, is such that it can be assumed to present a short circuit directly to ground at the point where the high resistance leads pass through the ground plane, and can also be neglected in the low frequency analysis of the diode assembly. No external bias is applied to the diode, and as a result of the high resistance in the direct current path of the equivalent circuit, the direct current that flows through the diode by way of rectification of the input signal is small.

In the measurement system described above, the rectified direct current through the diode at the centre of the metal strip dipole is used to provide an indication of the relative power received by the antenna for each incident angle of incoming radiation. It is therefore necessary to establish that the diode exhibits a square law response. It is also clear that both the diode impedance, determined from the equivalent circuit of the SBD, and the antenna impedance, are frequency dependent. Consequently, a frequency dependent mismatch exists between the impedance at the diode terminals and that of the antenna, and the available dynamic range of the measurement will be affected by the transfer of power from the antenna terminals to the diode junction. Because the measurement is required to be conducted at the half-wave resonant frequency of the ideal metal strip dipole, to maximize the dynamic range it is desirable for the peak response of the diode and metal strip dipole assembly to occur close to the half-wave

resonant frequency of the ideal metal strip dipole. The following analysis is undertaken to demonstrate that the required conditions may be obtained.

The relationship between the junction voltage V_j and the junction current I_j is given by the ideal diode equation,

$$I_j = I_s \left[\exp\left(\frac{eV_j}{nkT}\right) - 1 \right], \tag{B.3}$$

where I_s is the saturation current, e is the magnitude of the electron charge, k is Boltzmann's constant, n is the ideality factor (typically $n \approx 1$) and T the temperature. Assuming that the applied voltage is small, such that $eV_j/(nkT) \ll 1$, a two term Taylor series expansion of equation B.3 may be used to obtain the ideal diode equation in the form

$$\begin{aligned} I_j &\approx I_s \left(\frac{eV_j}{nkT} + \frac{1}{2}\left(\frac{e}{nkT}\right)^2 V_j^2 + \cdots \right) \\ &\approx \frac{V_j}{R_j} + \frac{I_s}{2}\left(\frac{e}{nkT}\right)^2 V_j^2, \end{aligned} \tag{B.4}$$

where the junction resistance, $R_j = nkT/(eI_s)$. From the low frequency equivalent circuit, the direct current component of the junction current, denoted $I_{j,dc}$, must also satisfy the expression

$$I_{j,dc} = \frac{-V_{j,dc}}{R_s + R_0} \tag{B.5}$$

where $V_{j,dc}$ is the direct current component of the junction voltage and $R_0 = 2R_w + R_l$ is the resistance in the direct current path external to the diode. To obtain the direct current characteristics it is assumed that I_j and V_j have the form

$$I_j(t) = I_{j,dc} + I_{j,\omega} \cos \omega t \tag{B.6a}$$

$$V_j(t) = V_{j,dc} + V_{j,\omega} \cos \omega t \tag{B.6b}$$

where the time origin has been chosen to give zero relative phase, and higher order harmonics are not considered. The magnitudes of the fundamental frequency components of the junction current and junction voltage are denoted by $I_{j,\omega}$ and $V_{j,\omega}$ respectively.

Substituting the expressions in equations B.6a and B.6b for the junction current and voltage in equation B.4 yields

$$I_{j,dc} + I_{j,\omega}\cos\omega t = \frac{V_{j,dc}}{R_j} + \frac{V_{j,\omega}\cos\omega t}{R_j} + \frac{I_s}{2}\left[\frac{e}{nkT}V_{j,dc} + \frac{e}{nkT}V_{j,\omega}\cos\omega t\right]^2. \qquad \text{(B.7)}$$

Noting that $eV_{j,dc}/nkT \ll 1$, and making use of equation B.5, results in

$$(R_j+R_s+R_0)I_{j,dc}+I_{j,\omega}R_j\cos\omega t = V_{j,\omega}\cos\omega t+\frac{R_jI_s}{2}\left(\frac{eV_{j,\omega}}{nkT}\right)^2\left(\frac{1}{2}+\frac{1}{2}\cos 2\omega t\right), \qquad \text{(B.8)}$$

and finally, by matching the direct current and fundamental frequency components, the pertinent terms of the junction current may be expressed as

$$I_{j,\omega} = \frac{V_{j,\omega}}{R_j} \qquad \text{(B.9)}$$

$$I_{j,dc} = \frac{e}{4nkT}\frac{V_{j,\omega}^2}{R_j + R_s + R_0}. \qquad \text{(B.10)}$$

From equation B.5, and noting that $R_0 \gg R_j + R_s$, the direct current voltage across the diode junction may be expressed as

$$V_{j,dc} = -\frac{e}{4nkT}\frac{V_{j,\omega}^2(R_s + R_0)}{R_j + R_s + R_0} \approx -\frac{e}{4nkT}V_{j,\omega}^2, \qquad \text{(B.11)}$$

from which the required square law response is evident. Because the resistance in the direct current path is large, the voltage $V_{d,dc}$ at the diode terminals, and the output voltage $V_{0,dc}$ at the measuring instrument, are approximately equal to the diode junction voltage $V_{j,dc}$. The output voltage at the measuring instrument is therefore also proportional to the square of the magnitude $V_{j,\omega}$ of the high frequency voltage at the junction. The value of $V_{j,\omega}$ may be calculated from the applied voltage V_{rf} using the high frequency equivalent circuit shown in Figure B.1.

At a given frequency, the power received by the antenna is proportional to the power, P_d, absorbed in the diode, and may be obtained from the diode direct current

output voltage and voltage sensitivity, Γ, by

$$P_d = \frac{V_{0,dc}}{\Gamma}, \tag{B.12}$$

where Γ, in units of microvolts per microwatt, is determined from the SBD equivalent circuit and characteristics [113], as

$$\Gamma = \frac{e}{2nkT} \frac{R_j}{\left(1 + \frac{R_s}{R_j}\right)^2} \frac{1}{1 + \frac{\omega^2 C_j^2 R_s R_j^2}{R_j + R_s}}. \tag{B.13}$$

The variation in P_d with frequency yields the power response of the diode and metal strip dipole assembly. Provided that the impedance presented to the antenna terminals by the diode is such that the total impedance characteristics are dominated by the variation of antenna impedance with frequency, the frequency response of the metal strip dipole will be closely approximated by P_d.

The radiation pattern of a metal strip dipole with dimensions $L = 25.4$mm, $H = 12.7$mm and $w = 1.0$mm, resulting in a half-wave resonant frequency of 5.2GHz, was measured using the method described above. In Figure B.2 the theoretical frequency response of the diode detector at the centre of the metal strip dipole is compared with the measured response. In practice the microwave signal was modulated at 1kHz, and the measurement instrumentation was a Stanford Research Systems lock-in amplifier. A dynamic range of approximately 30dB was obtained in the measurement at 5.2GHz, and is limited primarily by the impedance mismatch between the diode and the metal strip dipole. The diode response in Figure B.2 is also compared with the theoretical power received by the ideal metal strip dipole antenna without the diode, normalized to the same peak value. The similar responses confirm that the diode detector does not detune the dipole resonance sufficiently to reduce the dynamic range of the measurement beyond that already imposed by the impedance mismatch. Radiation pattern results for the metal strip dipole antenna at its half-wave resonant frequency are shown in Figure B.3, and demonstrate that an accurate measurement is obtained.

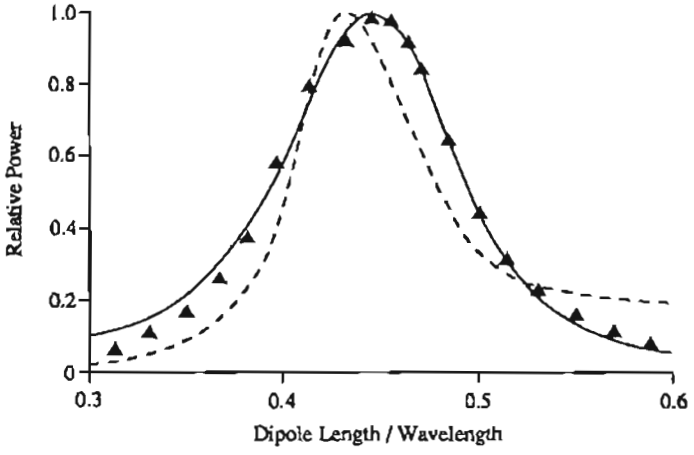

Figure B.2: Normalized response of diode detector for a uniform illuminating electric field E_y of constant power. Solid line: Theoretical response of diode detector at dipole gap, Dashed line: Theoretical power received by dipole with infinitesimal gap feed point, Points: Measured response of diode detector at dipole gap.

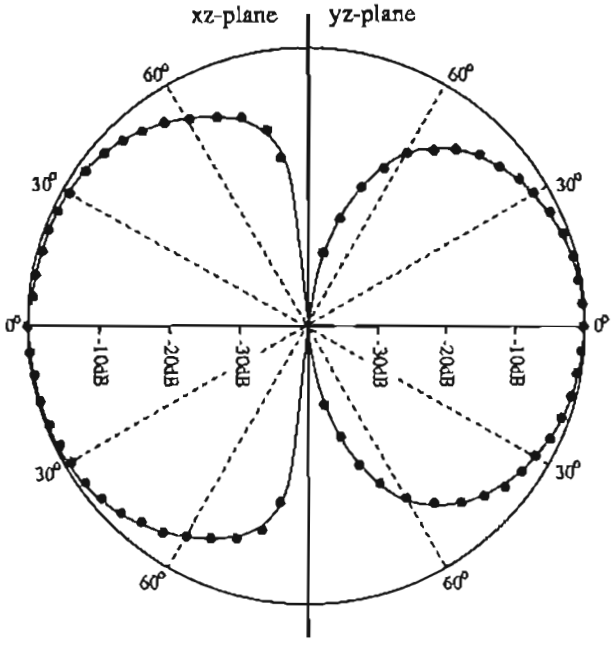

Figure B.3: Theoretical and measured principal plane radiation patterns of a metal strip dipole above a conducting ground plane. (Measured data shown as points.)

Appendix C

Numerical Modelling of Wire Junctions

The analysis of antenna geometries involving junctions between metal strips is performed throughout this thesis using an equivalent-radius thin-wire representation of the metal strips. The analysis assumes that the strips are sufficiently narrow so that only currents in the axial direction are significant. Pulse basis functions on cylindrical wire segments are used to expand the current distribution, with the boundary conditions being satisfied on the wire axis for an axially directed current distribution located on the wire surface at a radius a_e. Offset pulse basis functions are used for the charge density distribution, with the charge density on each offset pulse given by

$$\rho_{n+\frac{1}{2}} = -\frac{1}{j\omega}\frac{I_n - I_{n+1}}{l_n} \tag{C.1}$$

where I_n is the current of the nth pulse, l_n is the length of the nth pulse, and the current is assumed to have a reference direction corresponding to increasing n [64].

Two types of wire junction are illustrated in Figure C.1. The geometries shown result in half-size charge density pulses adjacent to the junction. It is well known that

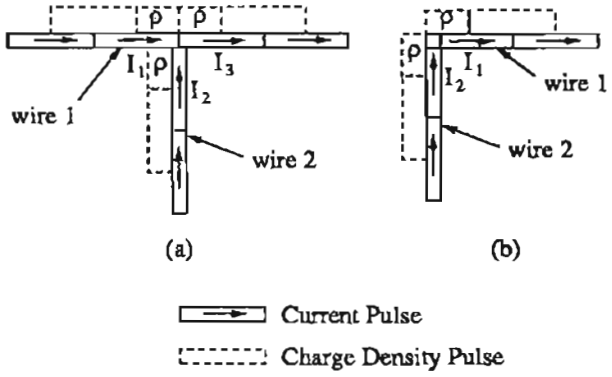

Figure C.1: Junction current and charge density pulses.

Kirchoff's current law applies at junctions of thin wires [114,115]. Because a point matching scheme with the matching points at the centre of each current pulse is used, however, direct application of Kirchoff's current law is not convenient. Since Kirchoff's current law is an expression of the continuity equation

$$\iint \vec{J} \cdot \vec{ds} = \iiint \vec{\nabla} \cdot \vec{J}\, dV = -j\omega Q, \tag{C.2}$$

it can be seen that in the limit where the second integral is taken over an infinitesimal volume around the junction, the wires become the same and consequently the same charge, Q, exists at the end of each wire. Assuming that all of the wires have the same radius, for the case shown in Figure C.1a all of the charge density half-pulses at the junction must be

$$\rho = \frac{1}{j\omega}\left(\frac{I_1 - I_3}{l_1} + \frac{I_2}{l_2}\right), \tag{C.3}$$

where l_1 and l_2 are the length of the current pulses on wires 1 and 2 respectively. Similarly, for the case shown in Figure C.1b,

$$\rho = \frac{1}{j\omega}\left(-\frac{I_1}{l_1} + \frac{I_2}{l_2}\right). \tag{C.4}$$

An appropriate model for wire junctions is therefore obtained by enforcing Equation C.3 or Equation C.4 at the charge density half-pulses adjacent to the junction.

Frequency	This model	Reference [114]
102 MHz	$146 + j298\Omega$	$143 + j297\Omega$
114 MHz	$383 + j454\Omega$	$386 + j461\Omega$
126 MHz	$1024 + j189\Omega$	$1067 + j157\Omega$
138 MHz	$631 - j590\Omega$	$590 - j613\Omega$
150 MHz	$223 - j489\Omega$	$203 - j483\Omega$

Table C.1: T-antenna feed point impedance.

Frequency	This model	Reference [114]
102 MHz	$118 + j209\Omega$	$107 + j193\Omega$
114 MHz	$326 + j335\Omega$	$287 + j321\Omega$
126 MHz	$801 + j11\Omega$	$779 + j100\Omega$
138 MHz	$394 - j431\Omega$	$443 - j438\Omega$
150 MHz	$157 - j329\Omega$	$169 - j347\Omega$

Table C.2: L-antenna feed point impedance.

Two wire-antennas in free space were analysed to determine the accuracy of the junction model. The first antenna was a T-antenna, comprising a horizontal wire 1m long and 0.5m above an infinite conducting ground plane, and a vertical wire 0.5m long between the centre of the horizontal wire and a feed point on the surface of the ground plane. The second antenna was an L-antenna, comprising a horizontal wire 0.5m long and 0.5m above an infinite conducting ground plane, and a vertical wire 0.5m long between one end of the horizontal wire and a feed point on the surface of the ground plane. All of the wires had a radius 0.01m. For the analysis, a delta-gap generator was used at the feed point, and the wires were segmented to give 16 pulses per metre.

Tables C.1 and C.2 show the results obtained using the junction model described here and the results obtained using an alternative method of junction modelling described in [114]. Good agreement is obtained between the results of the two methods, the small discrepancies being attributed to differences in the feed point models employed.

Appendix D

Substrate Dimension Variations

During the monolithic fabrication of substrate supported metal strip antennas, the parts of the MMIC wafer which are not required must be removed from the antenna surroundings by laser scribing or some other means. In order that the metalization is not disturbed, some clearance between the cut and the metal strip antenna is inevitable, and the extent to which the resulting overhang of the substrate affects the antenna characteristics needs to be determined. While small dimensional changes in the substrate have been found to produce little effect on the radiation characteristics, the resonant frequency of the antenna is altered. Correction for this effect is required in the design of the antenna element.

The effect of substrate overhang is illustrated in Figure D.1, where the measured resonant frequency of an antenna is shown in (a) as a function of the substrate extension above the metal strip height and in (b) as a function of the substrate extension beyond both ends of the metal strip length. Measurements were made on antennas resonant at around 5GHz, having a substrate thickness $t = 0.075L$ and permittivity $\epsilon_r = 10.2$. The metal strip of length L was supported above the ground plane at a fixed height $H = L/2$.

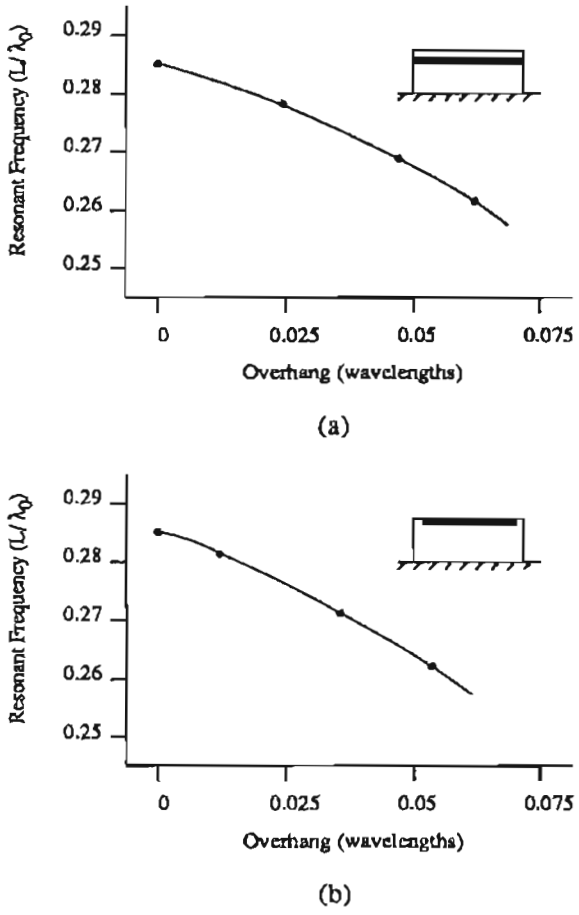

Figure D.1: Variation in resonant frequency, (a) with substrate extending above the metal strip height and (b) with substrate extending beyond the metal strip length at both ends. (Substrate $t = 0.075L$, $\epsilon_r = 10.2$.)

From the results, variations of approximately 1% in resonant frequency are anticipated for typical fabrication tolerances, and have been incorporated into the design of the X-band antenna element, fabricated on a GaAs substrate, studied in Section 4.2.3.

Appendix E

The Single Wire Fed Resonant Dipole Antenna

A half-wave resonant dipole above a ground plane, fed by a single wire which is offset from the centre of the dipole, was first described by W.L. Everitt and J.F. Byrne in 1929 [116]. In this early work, the single wire feed line was considered to be a type of transmission line, and efforts were made to describe the correct manner of matching the line to the antenna impedance. Perhaps because subsequent work on guided wave theory showed that a single wire could not properly be treated as a transmission line, little interest seems to have been generated in the antenna since that time, although in the amateur radio community the concept has been preserved [117]. The single wire feed does, however, have some useful features, the most significant being the utilization of an unbalanced feed point which eliminates the need for a balun in many applications. With the availability of modern numerical techniques, a more detailed analysis can be undertaken to investigate its radiation and impedance characteristics.

The single wire fed dipole antenna, as described above, is illustrated in Figure E.1. The current on the dipole is found using a moment method solution with the basis

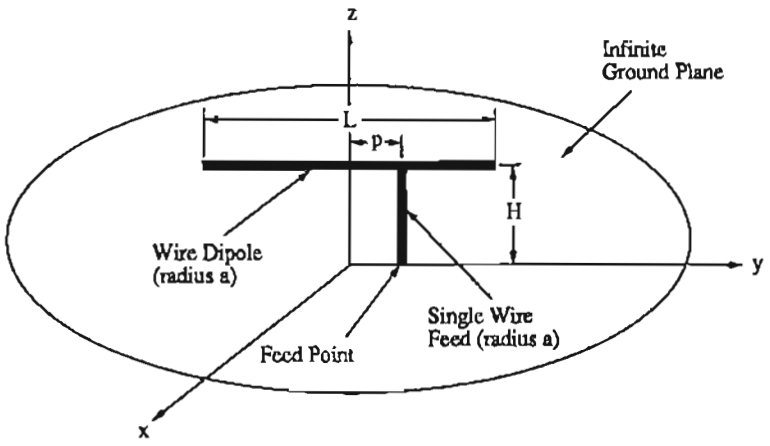

Figure E.1: Geometry of the single wire fed dipole antenna above a ground plane.

functions, $I(y)$, for the current on the segments given by

$$I(y) = A + B \sin k_0 y + C \cos k_0 y, \tag{E.1}$$

where $k_0 = 2\pi/\lambda_0$ and y is the axial distance from the centre of the segment. A, B and C are constants to be determined. Similar basis functions are used for the z-directed single wire feed. A divergent transmission line method is used in this analysis to model the junction between the single wire feed line and the dipole [114]. The analysis is performed for a dipole of length L and height H above the ground plane, where $H = L/2$, and the wire radius is chosen to be $a = 0.01L$. For these dimensions, the dipole has a half-wave resonance at a frequency corresponding to $L/\lambda_0 = 0.44$. The radius of the single wire feed line is also chosen to be $a = 0.01L$.

The input impedance at the antenna feed point is shown in Figure E.2 for varying values of the single wire feed offset, p. From the results, it is apparent that the lower values of input resistance, which are of practical use, are obtained for larger offsets. The capacitance associated with the input impedance at the feed point is due to fringing fields to the ground plane from the single wire feed line and fringing fields from the dipole to the single wire feed line. A value of p may be selected whereby the current distribution on the feed line has essentially a constant magnitude. This phenomenon is

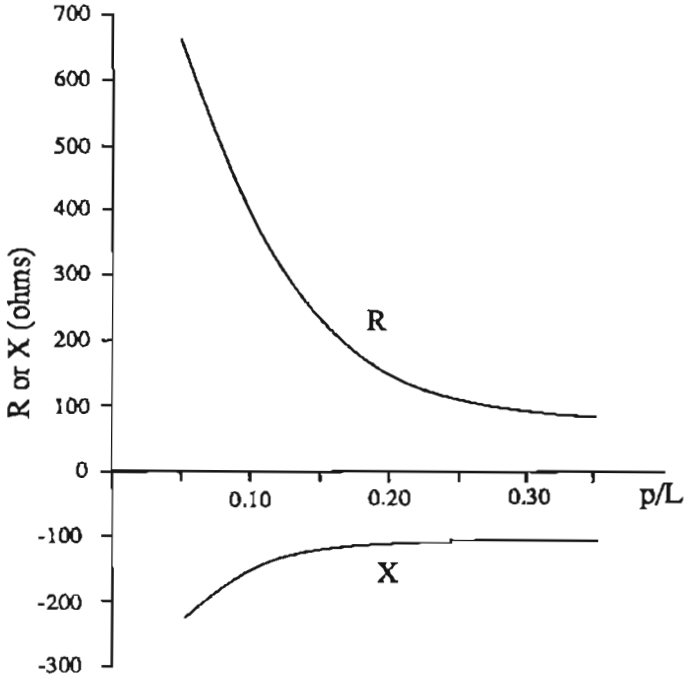

Figure E.2: Feed point input impedance at resonance as a function of junction position ($L/\lambda_0 = 0.44$).

illustrated in Figure E.3, where the magnitude of the current on the dipole and the feed line is shown for three values of p/L. For an offset $p/L = 0.2$, the feed line appears to carry a uniform travelling wave, and this travelling wave excites the resonant current distribution on the dipole. A small discontinuity in the current distribution on the dipole at the junction with the feed line is noted. When considered along with the relative phases of the currents, the discontinuity is found to be related to the current at the end of the single wire feed line by the need to satisfy Kirchoff's current law at the junction. These general characteristics of the current distributions were noted in earlier work [116].

The variation of the impedance at the feed point with wavelength is shown in Figure E.4. It is clear that because of the capacitive loading of the single wire feed, and the large input resistance, impedance matching techniques are required for most applications. The presence of a dielectric slab, as described in Section 4.3.2, is found to

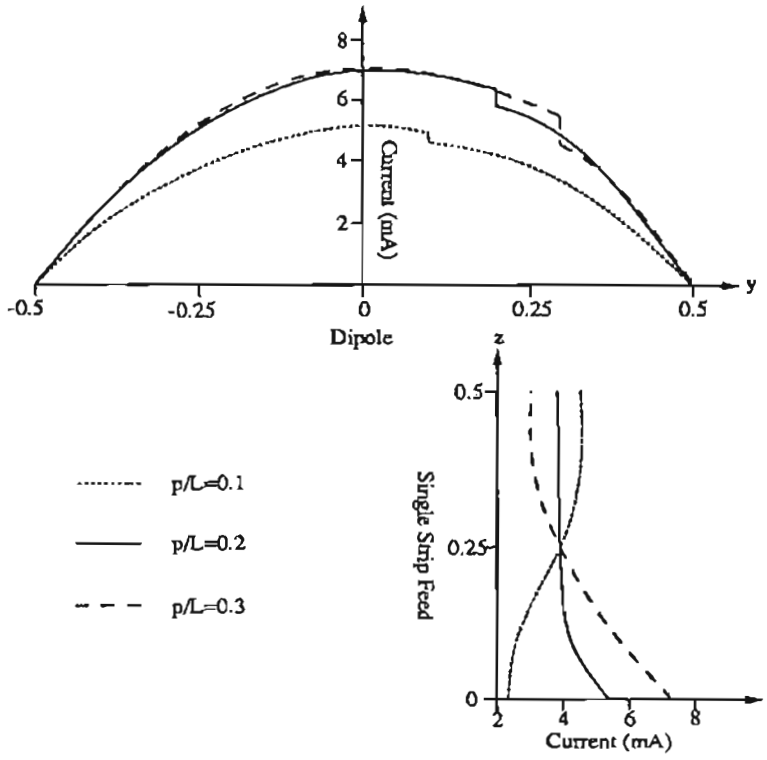

Figure E.3: Magnitude of the current distributions on the dipole and single-wire feed at resonance ($L/\lambda_0 = 0.44$).

improve the impedance characteristics and yield an element that is a reasonable match to 50 ohm microstrip line.

Because the single wire feed line carries a significant current which is not balanced by a nearby return current as in a transmission line, the presence of the feed line can be expected to significantly influence the radiation of the antenna. However, an analysis of the radiation characteristics does not appear to have been previously undertaken. The computed radiation patterns of the single wire fed dipole antenna for the three single wire feed line offsets considered previously are shown in Figure E.5, where the xz-plane pattern is on the left and the yz-plane pattern on the right. The value of the spherical coordinate ϕ for each quadrant of the radiation pattern is indicated to assist visualizing the radiation patterns with reference to the dipole and single wire feed line positions shown in Figure E.1. A null in the yz-plane radiation pattern, and

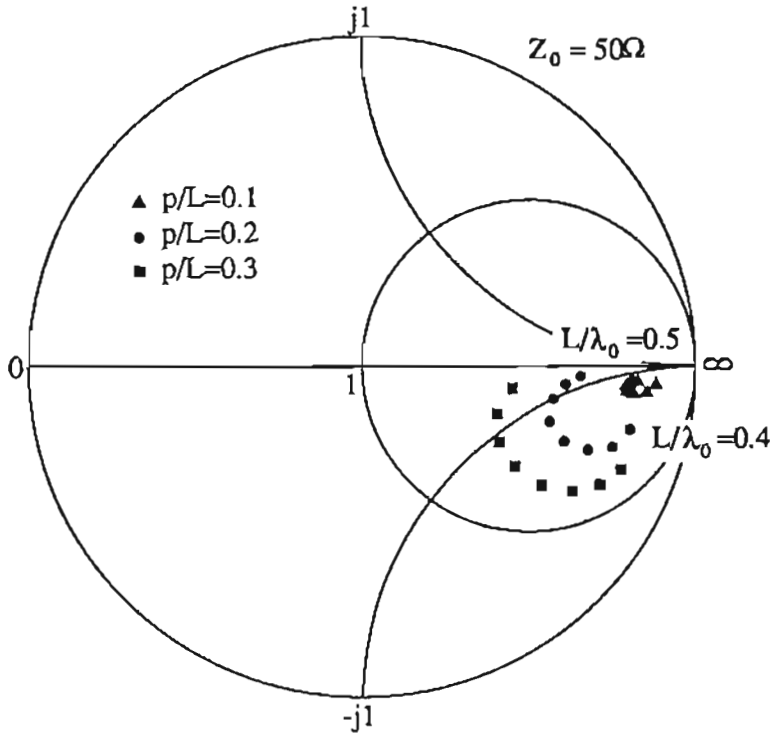

Figure E.4: Input impedance as a function of wavelength.

the associated beam-squint, is caused by the interference of the feed line radiation with that of the dipole. Furthermore, the significant cross-polarized component of radiation in the xz-plane is also attributable to radiation from the feed line.

The analysis described in this appendix forms a foundation for investigating the properties of the single wire fed, substrate supported metal strip antenna described in Section 4.3.2, and the arrays considered in Section 6.4.

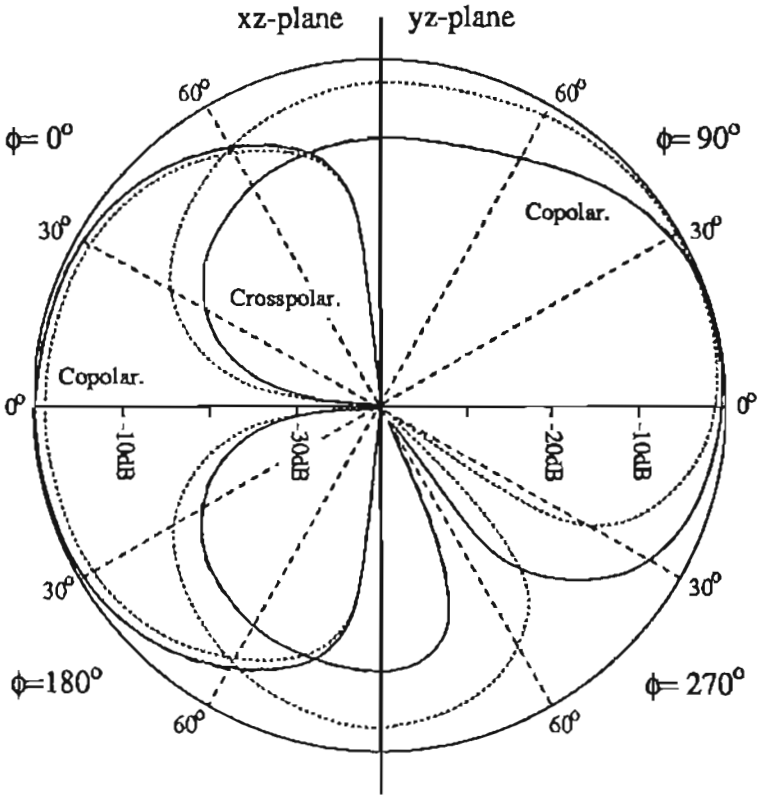

Figure E.5: Principal plane radiation patterns of single wire fed dipoles. Dotted line: $p/L = 0.1$, Solid line: $p/L = 0.2$, Dashed line: $p/L = 0.3$.

Appendix F

Derivation of Radiating Mode Models for Array Analysis

The radiation from various metal strip folded dipole and feed line configurations is computed in Chapter 6 from simplified models of the antenna geometry that, for the metal parts of the structure, include only the radiating currents. In this appendix, the radiating mode models are derived for both a metal strip folded dipole and a metal strip folded dipole fed from a coplanar strip feed line. The derivation follows that of [99], where comparisons with an exact analysis for resonant free-space folded dipoles above a ground plane have validated the accuracy of the approach. The manner in which the models are applied to the substrate supported metal strip antennas considered in this thesis is described in Section 6.2.2.

A metal strip folded dipole of length, L, without a feed line as shown in Figure F.1a, is considered first. The widths of the folded and driven arms are not assumed to be equal. For the antennas considered, the folded dipole is located above a ground plane, however, the ground plane does not enter into the analysis presented here. A voltage, V, is applied to the input terminals on the driven arm of the folded dipole, and a

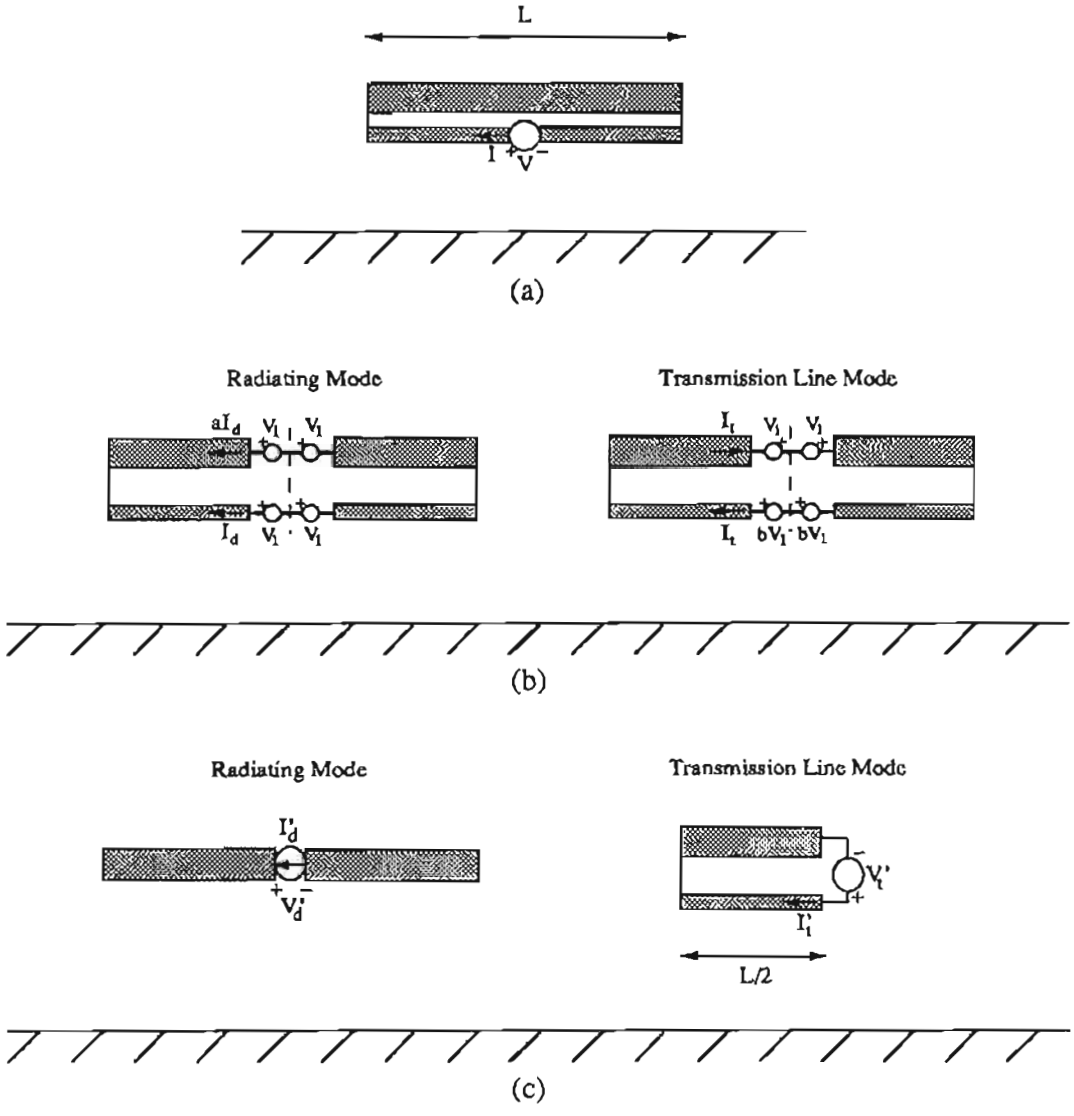

Figure F.1: Folded dipole decomposition procedure: (a) folded dipole terminal voltage and current, (b) decomposition into radiating and transmission line modes, and (c) equivalent radiating mode and transmission line mode models used to compute the currents associated with each mode.

current, I, that flows through the positive terminal is identified. The admittance, Y, of the folded dipole at its input terminals is therefore

$$Y = \frac{I}{V}. \tag{F.1}$$

In Figure F.1b, two separate modes are identified. The currents and voltages forming a so-called *radiating mode* are shown on the left hand structure, and those forming a so-called *transmission line mode* are shown on the right hand structure. Because the currents associated with the transmission line mode are closely spaced and are equal opposites, the transmission line mode contributes negligible radiation, and the folded dipole radiates predominantly by way of the radiating mode currents. The relationship between the separate modes in Figure F.1b and the complete folded dipole shown in Figure F.1a is such that the currents and voltages associated with the complete folded dipole can be viewed as the sum of the corresponding currents and voltages associated with each of the two modes. A pair of terminals between the centre of the folded metal strip and the centre of the driven metal strip for each half of the folded dipole are identified for the two modes. For both modes, a reference potential to which all of the voltage sources are referenced is shown as a dashed line in Figure F.1b.

The voltage sources, V_1, exciting the radiating mode are arranged so that the voltage at each terminal of the radiating mode model is the same, and as a consequence, no transmission line currents can be excited by these sources. The radiating mode currents are proportioned on the folded and driven arms in the ratio aI_d:I_d, where the value of a is determined by the relative widths of the folded and driven metal strips as described in Section 4.2.2. The voltage sources exciting the transmission line mode are arranged so that i) the sum of the radiating mode and transmission line mode voltage sources on the folded arm is zero, and ii) the transmission line currents, I_t, excited on the folded and driven arm have the same magnitude but opposite phase. To obtain the second condition, the voltages on the driven arm are scaled by a factor, b, in the transmission line model, and the total voltage at the input terminals of the complete folded dipole obtained by combining the radiating and transmission line mode sources

is $V = 2V_1(1+b)$. Furthermore, a voltage $V/2$ appears across the terminals on each half of the transmission line mode as required, and this voltage does not excite radiating mode currents.

In order to determine b, the admittance matrix relating the terminal voltages and currents of the two modes is considered. The following conditions are known to apply:

1. the radiating and transmission line modes are orthogonal,
2. reciprocity applies for voltages and currents associated with a given mode, and
3. the co-located voltages and currents for each mode are related by the same admittance term, since the geometry is the same for both cases.

As a result, the voltages and currents at the mode terminals are related by

$$\begin{bmatrix} Y_{dd} & Y_{fd} & 0 & 0 \\ Y_{fd} & Y_{ff} & 0 & 0 \\ 0 & 0 & Y_{dd} & Y_{fd} \\ 0 & 0 & Y_{fd} & Y_{ff} \end{bmatrix} \begin{bmatrix} V_1 \\ V_1 \\ bV_1 \\ -V_1 \end{bmatrix} = \begin{bmatrix} I_d \\ aI_d \\ I_t \\ -I_t \end{bmatrix}, \tag{F.2}$$

where Y_{dd}, Y_{ff} and Y_{fd} are the self and mutual admittances for sources at the terminals of the radiating and transmission line models. By obtaining expressions for a and b from equation F.2 in terms of the various admittances, it can be shown that $b = a$, and consequently the total voltage at the folded dipole input terminals is

$$V = 2V_1(1 + a). \tag{F.3}$$

It is noted that for equal width strips, $Y_{dd} = Y_{ff}$, and the well known result that $a = 1$ is obtained for this case.

The admittance, Y, at the folded dipole input terminals may be found by considering the total current flowing through the positive terminal. From Figure F.1b, the total current is made up of I_d from the radiating mode and I_t from the transmission

line mode, and therefore

$$Y = \frac{I_d + I_t}{2V_1(1+a)}. \tag{F.4}$$

For the purpose of analysis, radiating and transmission line mode currents may be computed for the models shown in Figure F.1c, and the admittances $Y_d = I_d'/V_d'$ and $Y_t = I_t'/V_t'$ obtained. The models in Figure F.1c are equivalent to those in Figure F.1b when

$$Y_d = \frac{(1+a)I_d}{2V_1} \tag{F.5}$$

$$Y_t = \frac{I_t}{V_1(1+a)}, \tag{F.6}$$

and the input admittance of a folded dipole may therefore be obtained from equation F.4 as

$$Y = \frac{Y_d}{(1+a)^2} + \frac{Y_t}{2}. \tag{F.7}$$

The admittance Y_d is obtained from a numerical analysis of the radiating mode equivalent model shown in Figure F.1c, and the admittance Y_t from an analysis of the the short circuited length of parallel strip transmission line in Figure F.1c as

$$Y_t = -jY_0 \cot\left(\frac{kL}{2}\right), \tag{F.8}$$

where Y_0 is the characteristic admittance of the transmission line and k is the propagation constant of the transmission line mode.

Considering now the same metal strip folded dipole antenna fed from a coplanar strip feed line, as shown in Figure F.2a, the voltage, V, at the input terminals of the folded dipole is excited by the balanced mode on the feed line. Because the balanced mode currents on the feed line are closely spaced, they are assumed not to affect the radiation of the antenna and are therefore omitted from the analysis. It is possible in a phased array, however, for common mode currents to be excited on the feed line as the beam of the array is steered in space, due to the resulting asymmetry of the overall array excitation, and these common mode currents will affect the radiation

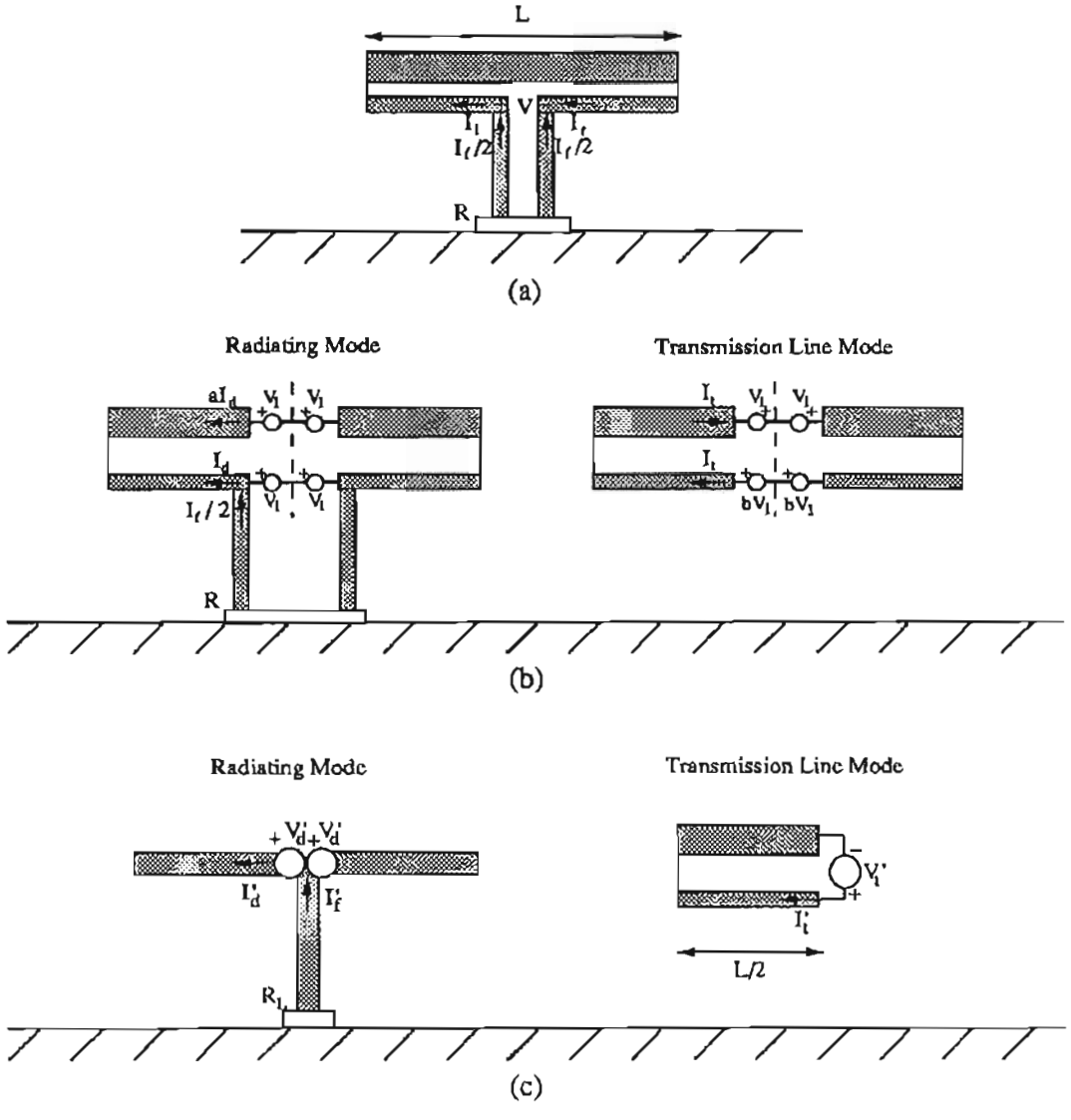

Figure F.2: Folded dipole and feed line decomposition procedure: (a) folded dipole terminal voltage and current and feed line common mode current, (b) decomposition into radiating and transmission line modes, and (c) equivalent radiating mode and transmission line mode models used to compute the currents associated with each mode.

characteristics and impedance of the elements. In Figure F.2a, common mode currents $I_f/2$ are shown at the junctions between the metal strips of the feed line and the folded dipole. Furthermore, the common mode currents on the feed line are terminated at the ground plane by a common mode resistance R, which is determined by the properties of the balun network that connects the feed line to the driving electronics. The details of the common mode termination are discussed in Section 6.2.3 of this thesis. When a common mode current is excited on the feed line, the current, I_l, flowing through the positive terminal, and the current, I_r, flowing through the negative terminal, will be unequal. This is due to the fact that the common mode currents feed anti-symmetrical currents in addition to the existing radiating mode currents on the folded dipole. For the analysis here, it is chosen to compute the feed port admittance by considering the current I_l flowing through the positive terminal[1].

The separation of the voltages and currents into the radiating mode and transmission line mode of the folded dipole, as shown in Figure F.2b, follows that presented above for the case where the feed line is not present. In this case, the voltage sources at the antenna input terminals represent the voltage transferred to the terminals by the balanced mode on the feed line. At the positive terminal of Figure F.2a, the current, I_l, may be expressed as

$$I_l = I_d - \frac{I_f}{2} + I_t \tag{F.9}$$

and consequently the admittance, Y, at the folded dipole input terminals is

$$Y = \frac{I_l}{2V_1(1+a)} = \frac{I_d - I_f/2 + I_t}{2V_1(1+a)}. \tag{F.10}$$

For the purpose of analysis, radiating and transmission line mode currents may be computed from the models shown in Figure F.2c. Because the metal strips of the feed line are closely spaced, the common mode currents on the feed line are summed to give a current I_f on a single metal strip that connects to the folded dipole at the

[1]A similar analysis considering the current I_r flowing through the negative terminal would produce the same result, provided that the convention for the direction of the currents and the polarity of the voltage sources is preserved in the numerical analysis used to determine the radiating mode currents.

junction between the radiating mode sources at the dipole input terminals. A common mode termination R_L at the base of the single metal strip representing the feed line is included in the model. Admittances Y_d and Y_t may be computed as in the previous case for a folded dipole without a feed line, however, when the single strip representing the feed line is included an additional admittance $Y_f = I_f'/V_d'$ is also identified. The models in Figure F.2c are equivalent to those in Figure F.2b when

$$Y_d = \frac{(1+a)I_d}{2V_1} \tag{F.11}$$

$$Y_t = \frac{I_t}{V_1(1+a)} \tag{F.12}$$

$$Y_f = \frac{I_f}{V_1}, \tag{F.13}$$

and the input admittance at the terminals of the folded dipole is obtained from equation F.10 as

$$Y = \frac{Y_d}{2(1+a)^2} - \frac{Y_f}{4(1+a)} + \frac{Y_t}{2}. \tag{F.14}$$

The admittances Y_d and Y_f are computed from a numerical analysis of the radiating mode equivalent model shown in Figure F.2c, and the transmission line admittance Y_t is computed in the same way as for a folded dipole without a feed line.

In Section 6.2.2, sources $V_d' = 1$ volt and $V_t' = 1$ volt are employed so that the numerical values of the required admittances correspond to the appropriate currents at each source. The impedance step up ratio of the folded dipole is denoted as γ^2 in Section 4.2.2, and is defined as $\gamma^2 = (1+a)^2$.

Appendix G

Phased Array Simulator Measurements

Phased array simulators are used to measure the performance of antenna elements in an infinite array environment for various beam-steer directions. A waveguide surrounding several antenna elements simulates the array environment by imaging the enclosed antenna elements about the conducting walls of the waveguide. The waveguide is terminated in a reflectionless load such that only waves propagating away from the array aperture exist. A "looking-out" type of phased array simulator as described in [118] is used for the measurements in Section 6.3. The front and side views of two phased array simulators are illustrated in Figure G.1. The simulator in Figure G.1a is used for complete substrate supported metal strip antennas having a balanced coplanar strip feed line. The simulator in Figure G.1b is used for half elements which have themselves been imaged about one of the waveguide walls, thereby giving access to a well defined feed point suitable for connection to a coaxial line. In both simulators, beam-steer angles in the xz-plane (or $\varphi = 0°$ plane) are obtained. The symmetry of the simulator geometry, and the balanced excitation and current distributions on the antenna elements for beam-steer angles in the xz-plane, is such that all of the

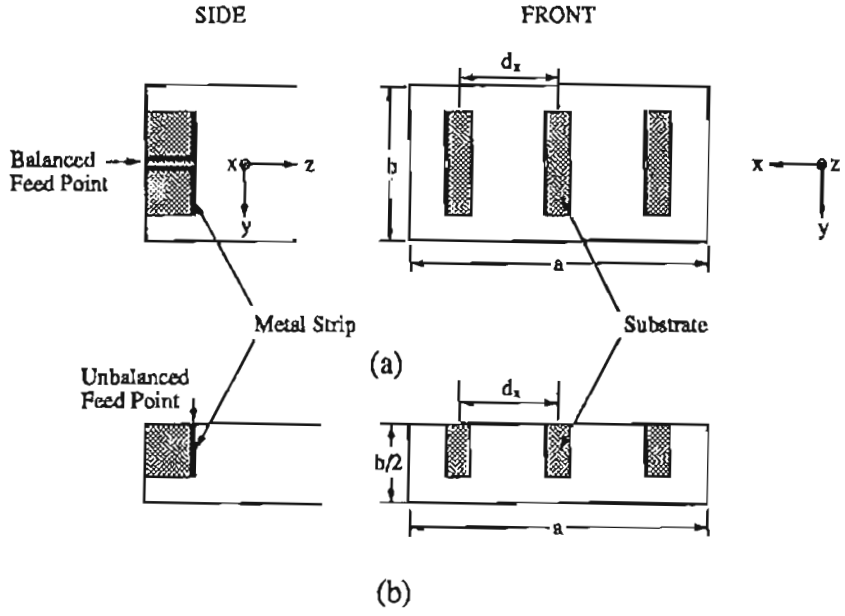

Figure G.1: Simulator geometry: (a) complete elements (b) imaged elements

currents are correctly imaged, however, the position of the substrates is shifted with respect to the position of the metal strips for the images in the narrow wall of the waveguide. Because the spacing between the elements is large compared with the substrate thickness, this effect is not expected to have a significant influence on the results.

The three-element simulators employed are dimensioned such that the element spacings d_x and d_y are

$$d_x = \lambda_r/2 = \frac{a}{3}$$
$$d_y = \lambda_r/2 = b$$

where λ_r is the free-space wavelength at the half-wave resonance of the antenna elements. Half-wavelength spacing is chosen to preclude the existence of grating lobes. From the analysis in [118], solutions exist for two beam-steer angles in the $\varphi = 0°$ scan

plane, which are determined from

$$\theta_n = \sin^{-1} \frac{n\lambda_0}{6d_x} \qquad \text{for } n = 1, 2 \tag{G.1}$$

and the corresponding reflection coefficients at the feed points are

$$\Gamma_n = \sum_{r=1}^{3} S_{1r} \frac{\sin \frac{n\pi}{3}(r - \frac{1}{2})}{\sin \frac{n\pi}{6}} \qquad \text{for } n = 1, 2 \tag{G.2}$$

where S_{1r} are the measured scattering parameters at the measurement reference planes of the three-port network comprising the three antenna feed ports.

For the phased array simulator in Figure G.1a, the need to provide a balanced feed by means of a balun normally results in only the magnitude of the reflection coefficient being determined at the antenna terminals in order to avoid a complicated de-embedding problem. However, for such simulators, complete substrate supported metal strip antenna elements and their feed lines are included in the measurement. For the phased array simulator in Figure G.1b, the magnitude and phase of the reflection coefficient at the unbalanced antenna feed point may be directly determined, and the active impedance at the feed point calculated. Reference planes at the bases of the metal strip monopoles in the simulator are obtained by introducing time delays, t_d, as described in Section 3.3.1, to allow for the offset distance from the calibration reference planes. No other empirical adjustments are made to the measured results. The measured scattering parameters at the required reference planes are used to determine the reflection coefficients Γ_n for the two beam steer angles available. The active impedance at the centre of complete substrate supported metal strip antennas without feed lines, for each beam steer angle, is obtained by doubling the impedance corresponding to the appropriate Γ_n.

Bibliography

[1] J. C. Wiltse, *Introduction and overview of millimeter waves*, vol. 4 of *Infrared and millimeter waves*, pp. 1–21. New York: Academic Press, 1981.

[2] P. Bhartia and I. J. Bahl, *Millimeter wave engineering and applications.* New York: John Wiley and Sons, 1984.

[3] N. C. Currie and C. E. Brown, *Principles and applications of millimeter wave radar.* Boston: Artech House, 1987.

[4] A. A. Oliner and G. H. Knittel, *Phased array antennas.* Dedham: Artech House, 1972.

[5] D. M. Pozar, *Analysis and design of considerations for printed phased array antennas*, vol. 1 of *Handbook of Microstrip Antennas*, ch. 12, pp. 693–753. London: Peter Perigrinus, 1989.

[6] D. M. Pozar, "Microstrip antennas," *Proceedings of the IEEE*, vol. 80, pp. 79–81, Jan. 1992.

[7] P. Bradsell, "Phased arrays in radar," *Electronics and Communications Engineering Journal*, pp. 45–51, Apr. 1990.

[8] M. I. Herman, G. Lan, J. C. Chen, and C. Pao, "Multifunction W-band MMIC receiver technology," *Proceedings of the IEEE*, vol. 79, pp. 342–354, Mar. 1991.

[9] J. Mondal, J. Geddes, J. Dentry, and D. Carlson, "Ka band MMIC receiver with ion implanted technology for high volume, low cost application," *IEEE Microwave and Guided Wave Letters*, vol. 1, pp. 278–281, Oct. 1991.

[10] D. H. Schaubert, "Printed circuit antenna technology," in *Advisory Group for Aerospace Research and Development Lecture Series 151*, NATO, 1987.

[11] W. W. Lam, C. F. Jou, N. C. Luhmann, and D. B. Rutledge, "Diode grids for electronic beam steering and frequency multiplication," *International Journal of Infrared and Millimeter Waves*, vol. 7, pp. 27–41, Jan. 1986.

[12] G. M. Rebeiz, D. P. Kasilingam, Y. Guo, P. A. Stimson, and D. B. Rutledge, "Monolithic millimeter-wave two-dimensional horn imaging arrays," *IEEE Transactions on Antennas and Propagation*, vol. 38, pp. 1473–1482, Sept. 1990.

[13] R. J. Mailloux, "Phased array architecture for millimeter wave active arrays," *Microwave Journal*, pp. 117–124, July 1986.

[14] L. R. Whicker, J. J. Zingaro, M. C. Driver, and R. C. Clarke, "A new approach to active phased arrays through RF-wafer scale integration," in *IEEE Microwave Theory and Techniques Symposium*, (Dallax, Texas), pp. 1223–1226, May 1990.

[15] D. W. Griffin, "Studies of concepts for the design of space-based phased-array radar systems at 60GHz," tech. rep., Southeastern Centre for Electrical Engineering Education, St. Cloud, Florida, May 1986.

[16] D. W. Griffin, "New architectures for millimeter wave phased array radar antennas that use monolithic modules," in *IEEE Antennas and Propagation Symposium*, pp. 1198–1201, June 1987.

[17] J. A. Kinzel, B. J. Edwards, and D. Rees, "V-band space based phased arrays," *Microwave Journal*, vol. 30, pp. 89–102, Jan. 1987.

[18] N. G. Alexopoulos, P. B. Katehi, and D. B. Rutledge, "Substrate optimization for integrated circuit antennas," *IEEE Transactions on Microwave Theory and Techniques*, vol. 31, pp. 550–557, July 1983.

[19] D. B. Rutledge, D. P. Niekirk, and D. P. Kasilingam, *Integrated circuit antennas*, vol. 10 of *Infrared and Millimetre Waves*, ch. 1, pp. 1–90. New York: Academic Press, 1983.

[20] D. M. Pozar, "Considerations for millimeter wave printed antennas," *IEEE Transactions on Antennas and Propagation*, vol. 31, pp. 740–747, Sept. 1983.

[21] J. R. James and P. S. Hall, eds., *Handbook of Microstrip Antennas*. London: Peter Peregrinus, 1989.

[22] J. R. James, "Printed antennas: new research frontiers," in *Proceedings of the Asia Pacific Microwave Conference*, vol. 1, (Adelaide, Australia), pp. 21–26, 1992.

[23] A. K. Bhattacharyya, "Effects of ground plane and dielectric truncations on the efficiency of a printed structure," *IEEE Transactions on Antennas and Propagation*, vol. 39, pp. 303–308, Mar. 1991.

[24] J. R. Bayard, M. E. Cooley, and D. H. Schaubert, "Analysis of infinite arrays of printed dipoles on dielectric sheets perpendicular to a ground plane," *IEEE Transactions on Antennas and Propagation*, vol. 39, pp. 1722–1732, Dec. 1991.

[25] E. H. Newman, "Strip antennas in a dielectric slab," *IEEE Transactions on Antennas and Propagation*, vol. 26, pp. 647–653, Sept. 1978.

[26] T. K. Sarkar, E. Arvas, and S. Ponnapalli, "Electromagnetic scattering from dielectric bodies," *IEEE Transactions on Antennas and Propagation*, vol. 37, pp. 673–676, May 1989.

[27] N. Amitay, V. Galindo, and C. P. Wu, *Theory and analysis of phased array antennas.* New York: John Wiley and Sons, 1972.

[28] H. Zebker and J. J. Van Zyl, "Imaging radar polarimetry: a review," *Proceedings of the IEEE*, vol. 79, pp. 1583–1606, Nov. 1991.

[29] D. B. Rutledge and M. S. Muha, "Imaging antenna arrays," *IEEE Transactions on Antennas and Propagation*, vol. 30, pp. 535–540, July 1982.

[30] K. S. Yngvesson, *Near millimeter imaging with integrated planar receptors: general requirements and constraints*, vol. 10 of *Infrared and Millimeter Waves*, pp. 91–110. New York: Academic, 1983.

[31] S. J. Nightingale, M. A. G. Upton, B. K. Mitchell, U. K. Mishra, S. C. Palmateer, and P. M. Smith, "A 30GHz monolithic single balanced mixer with integrated dipole receiving element," *Microwave Journal*, pp. 103–106, Aug. 1985.

[32] V. D. Hwang, T. Uwana, and T. Itoh, "Quasi-optical integrated antenna and receiver front end," *IEEE Transactions on Microwave Theory and Techniques*, vol. 36, pp. 80–85, Jan. 1988.

[33] Z. B. Popovic, R. M. Weikle, M. Kim, and D. B. Rutledge, "A 100 MESFET planar grid oscillator," *IEEE Transactions on Microwave Theory and Techniques*, vol. 39, pp. 193–200, Feb. 1991.

[34] F. C. Jain and R. Bansal, *Semiconductor antennas for millimeter-wave integrated circuits*, vol. 15 of *Infrared and Millimetre Waves*, pp. 263–286. New York: Academic Press, 1986.

[35] L. J. Baca and J. G. McInerney, "Design of a broadband high-frequency antenna on GaAs using the effective index method," *Electronics Letters*, vol. 26, pp. 1083–1085, July 1990.

[36] J. A. Kinzel, "GaAs technology for millimeter wave phased arrays," *IEEE Antennas and Propagation Society Newsletter*, pp. 12–14, Feb. 1987.

[37] J. McIlvenna, "Monolithic phased arrays for EHF communication terminals," *Microwave Journal*, pp. 113–125, Mar. 1988.

[38] R. J. Mailloux, "Array elements and architectures of printed circuit array antennas," *IEEE Microwave Theory and Techniques Society Newsletter*, no. 122, pp. 29–32, 1988.

[39] J. A. Kinzel, "Recent advances in monolithic millimeter-wave arrays," in *IEEE Antennas and Propagation Symposium*, (Dallas, Texas), pp. 1402–1405, May 1990.

[40] A. J. Parfitt and D. W. Griffin, "Monolithic microwave and millimetre wave integrate circuit antennas," in *Proceedings of IREECON International Convention*, (Melbourne Australia), pp. 169–172, Sept. 1989.

[41] A. J. Parfitt and D. W. Griffin, "Integrated antenna elements for MMIC phased array radar modules: constraints and options," in *Proceedings of RADARCON90*, (Adelaide Australia), pp. 391–397, Apr. 1990.

[42] R. J. Mailloux, "Antenna array architecture," *Proceedings of the IEEE*, vol. 80, pp. 163–172, Jan. 1992.

[43] D. R. Decker, *GaAs monolithic microwave integrated circuits*, vol. 11 of *VLSI Electronics - Microstructure Science*, pp. 87–132. Orlando: Academic Press, 1985.

[44] D. N. McQuiddy, R. L. Gassner, P. Hull, J. S. Mason, and J. M. Bedinger, "Transmit/receive module technology for X-band active array radar," *Proceedings of the IEEE*, vol. 79, pp. 308–341, Mar. 1991.

[45] C. R. Seashore, "MIMIC for millimeter wave integrated circuits," in *SPIE Millimeter Wave Technology IV and Radio Frequency Power Sources*, vol. 791, pp. 104–108, 1987.

[46] F. K. Schwering, "Millimeter wave antennas," *Proceedings of the IEEE*, vol. 80, pp. 92–102, Jan. 1992.

[47] A. J. Parfitt, D. W. Griffin, and P. H. Cole, "A chip scale approach to monolithic microwave integrated circuit design for millimetre wavelengths," in *IEEE Antennas and Propagation Symposium*, (Chicago Illinois), pp. 1914–1918, July 1992.

[48] P. B. Katehi and N. G. Alexopoulos, "On the modeling of electromagnetically coupled microstrip antennas - the printed strip dipole," *IEEE Transactions on Antennas and Propagation*, vol. 32, pp. 1179–1186, Nov. 1984.

[49] R. H. Jansen, R. G. Arnold, and I. G. Eddison, "A comprehensive CAD approach to the design of MMICs up to mm-wave frequencies," *IEEE Transactions on Microwave Theory and Techniques*, vol. 36, pp. 208–219, Feb. 1988.

[50] M. Priolo, G. St. Onge, W. Coughlin, J. Bugeau, and D. Meharry, "Transmit/receive modules for 6 to 18GHz multifunction arrays," in *IEEE Microwave Theory and Techniques Symposium*, (Dallas, Texas), pp. 1227–1230, May 1990.

[51] N. Fourikis, "Antenna elements for wide-band multifunction active phased arrays," in *International Conference on Millimeter Wave and Far Infrared Technology*, (Beijing, China), Aug. 1992.

[52] A. A. Oliner, "Surface wave effects and blindness in phased array antennas," in *Phased array antennas*, pp. 107–111, Dedham: Artech House, 1972.

[53] H. K. Schuman, D. R. Pflug, and L. D. Thompson, "Infinite planar arrays of arbitrarily bent thin wire radiators," *IEEE Transactions on Antennas and Propagation*, vol. 32, pp. 364–377, Apr. 1984.

[54] D. R. Shostak, E. C. Smith, and R. A. Price, "Array backplate architecture for monolithic microwave integrated circuits," in *IEEE Antennas and Propagation Symposium*, (Dallas, Texas), pp. 1413–1416, May 1990.

[55] R. Tang, A. Popa, and J. J. Lee, "Applications of photonic technology to phased arrays," in *IEEE Antennas and Propagation Symposium*, (Dallas Texas), pp. 758–761, May 1990.

[56] K. S. Yngvesson, J. Johansson, and E. L. Kollberg, "A new integrated array for multi-beam systems with application to millimeter imaging," in *IEEE Antennas and Propagation Symposium*, pp. 895–898, 1986.

[57] M. E. Cooley, D. H. Schaubert, N. E. Buris, and E. A. Urbanik, "Radiation and scattering analysis of infinite arrays of endfire slot antennas with a ground plane," *IEEE Transactions on Antennas and Propagation*, vol. 39, pp. 1615–1625, Nov. 1991.

[58] A. C. Buck and D. M. Pozar, "An aperture coupled microstrip antenna with a perpendicular feed," *Electronics Letters*, vol. 22, pp. 125–126, 1986.

[59] S. Kobayashi, R. Mittra, and R. Lampe, "Dielectric tapered rod antennas for millimeter-wave applications," *IEEE Transactions on Antennas and Propagation*, vol. 30, pp. 54–58, Jan. 1982.

[60] C. Yao, S. E. Schwarz, and B. J. Blumenstock, "Monolithic integration of a dielectric millimeter-wave antenna and mixer diode: an embryonic millimeter-wave IC," *IEEE Transactions on Microwave Theory and Techniques*, vol. 30, pp. 1241–1247, Aug. 1982.

[61] A. J. Parfitt, D. W. Griffin, and P. H. Cole, "On the modeling of metal strip antennas contiguous with the edge of electrically thick finite size dielectric substrates," *IEEE Transactions on Antennas and Propagation*, vol. 40, pp. 134–140, Feb. 1992.

[62] M. W. McAllister, S. A. Long, and G. L. Conway, "The rectangular dielectric resonator antenna," in *IEEE Antennas and Propagation Symposium*, pp. 696–699, 1983.

[63] J. R. James and A. Henderson, *Planar millimeter wave antenna arrays*, vol. 14 of *Infrared and Millimeter Waves*, pp. 189–247. Orlando: Academic Press, 1985.

[64] R. F. Harrington, *Field computation by moment methods.* New York: Macmillan, 1968.

[65] J. Jin, J. L. Volakis, and J. D. Collins, "A finite-element–boundary integral method for scattering and radiation by two- and three-dimensional structures," *IEEE Antennas and Propagation Magazine*, vol. 33, pp. 22–32, June 1991.

[66] T. K. Sarkar and E. Arvas, "Scattering cross section of composite conducting and lossy dielectric bodies," *Proceedings of the IEEE*, vol. 77, pp. 788–795, May 1989.

[67] T. K. Sarkar, S. M. Rao, and A. R. Djordjevic, "Electromagnetic scattering and radiation from finite microstrip structures," *IEEE Transactions on Microwave Theory and Techniques*, vol. 31, pp. 1568–1575, Nov. 1990.

[68] T. K. Sarkar and E. Arvas, "An integral equation approach to the analysis of finite microstrip antennas: volume/surface formulation," *IEEE Transactions on Antennas and Propagation*, vol. 38, pp. 305–312, Mar. 1990.

[69] S. M. Rao, T. K. Sarkar, P. Midya, and A. R. Djordjevic, "Electromagnetic radiation and scattering from finite conducting and dielectric structures: surface/surface formulation," *IEEE Transactions on Antennas and Propagation*, vol. 39, pp. 1034–1037, July 1991.

[70] B. J. Rubin and S. Daijavad, "Radiation and scattering from structures involving finite-size dielectric regions," *IEEE Transactions on Antennas and Propagation*, vol. 38, pp. 1863–1873, Nov. 1990.

[71] B. J. Rubin, "General solution for propagation, radiation and scattering in arbitrary 3D inhomogeneous structures," *IEEE Antennas and Propagation Magazine*, vol. 34, pp. 17–25, Feb. 1992.

[72] J. S. Kot, "Computer modelling of mm-wave integrated circuit antennas using the Nystrom method," in *IEE International Conference on Computers in Electromagnetics*, (London), 1991.

[73] C. A. Balanis, *Advanced Engineering Electromagnetics*, pp. 394–414. New York: John Wiley and Sons, 1989.

[74] R. A. York, R. C. Compton, and B. J. Rubin, "Experimental verification of the 2-D rooftop approach for modeling microstrip patch antennas," *IEEE Transactions on Antennas and Propagation*, vol. 39, pp. 690–694, May 1991.

[75] W. L. Stutzman and G. A. Thiele, *Antenna theory and design*, pp. 336–339. New York: John Wiley and Sons, 1981.

[76] IMSL Inc., Houston, Texas, *IMSL math/library: Users Manual*, 1987.

[77] A. D. Yaghjian, "Electric dyadic Green's functions in the source region," *Proceedings of the IEEE*, vol. 68, pp. 248–263, Feb. 1980.

[78] E. Mendelovicz, A. T. Adams, K. Siarkiewicz, and A. Mendelovicz, "Feedline interference with dipole performance theory and experiment," *IEEE Transactions on Electromagnetic Compatibility*, vol. 16, pp. 90–97, May 1974.

[79] K. Mizuno, Y. Daiku, and S. Ono, "Design of printed resonant antennas for monolithic-diode detectors," *IEEE Transactions on Microwave Theory and Techniques*, vol. 25, pp. 470–472, June 1977.

[80] R. W. P. King and G. S. Smith, *Antennas in matter: fundamental theory and applications*, pp. 224–239. Cambridge: MIT Press, 1981.

[81] T. E. Batchman and G. Gimpelson, "An implantable electric field probe of submillimeter dimensions," *IEEE Transactions on Microwave Theory and Techniques*, vol. 31, pp. 745–751, Sept. 1983.

[82] C. A. Balanis, *Advanced Engineering Electromagnetics*, pp. 718–722. New York: John Wiley and Sons, 1989.

[83] B. D. Popovic and A. Nesic, "Generalisation of the concept of equivalent radius thin cylindrical antennas," *IEE Proceedings Part H*, vol. 131, pp. 153–158, June 1984.

[84] R. K. Hoffman, *Handbook of microwave integrated circuits*. Norwood: Artech House, 1987.

[85] C. W. Davidson, *Transmission lines for communications*. London: Macmillan Press, 1978.

[86] G. A. Thiele, E. P. Ekelman, and L. W. Henderson, "On the accuracy of the transmission line model of the folded dipole," *IEEE Transactions on Antennas and Propagation*, vol. 28, pp. 700–703, Sept. 1980.

[87] R. W. Lampe, "Design formulas for an asymmetric coplanar strip folded dipole," *IEEE Transactions on Antennas and Propagation*, vol. 33, pp. 1028–1031, Sept. 1985. (Corrected vol. 34, p. 611, Apr. 1986).

[88] M. C. Elias and C. T. Carson, "Direct analysis of folded dipole by method of moments," *Electronics Letters*, vol. 9, pp. 520–521, Nov. 1973.

[89] H. A. Wheeler, "Transmission line properties of parallel strips separated by a dielectric sheet," *IEEE Transactions on Microwave Theory and Techniques*, vol. 13, pp. 172–185, Mar. 1965.

[90] E. Yamashita, H. Ohashi, and K. Atsuki, "Characterization of microstrip lines near a substrate edge and design formulas of edge compensated microstrip lines," *IEEE Transactions on Microwave Theory and Techniques*, vol. 37, pp. 890–896, May 1989.

[91] D. H. Schaubert, "Radiation characteristics of linear tapered slot antennas," in *IEEE Antennas and Propagation Symposium*, (San Jose, California), pp. 1324–1327, June 1989.

[92] P. J. Kharilas, "HAPDAR - An operational phased array radar," *Proceedings of the IEEE*, vol. 56, pp. 1967–1975, Nov. 1968.

[93] Y. Kang and D. M. Pozar, "Correction of error in reduced sidelobe synthesis due to mutual coupling," *IEEE Transactions on Antennas and Propagation*, vol. 33, pp. 1025–1028, Sept. 1985.

[94] H. Steyskal and J. S. Herd, "Mutual coupling compensation in small array antennas," *IEEE Transactions on Antennas and Propagation*, vol. 38, pp. 1971–1975, Dec. 1990.

[95] W. L. Stutzman and G. A. Thiele, *Antenna theory and design*, pp. 154–160. New York: John Wiley and Sons, 1981.

[96] K. M. Lee and R. S. Chu, "Analysis of mutual coupling between a finite phased array of dipoles and its feed network," *IEEE Transactions on Antennas and Propagation*, vol. 36, pp. 1681–1689, Dec. 1988.

[97] J. P. Bayard, M. E. Cooley, and D. H. Schaubert, "A general method for treating infinite arrays of antennas printed on protruding dielectric substrates," in *IEEE Antennas and Propagation Symposium*, (London, Ontario), pp. 600–603, June 1991.

[98] A. K. Skrivervik and J. R. Mosig, "Finite phased array of microstrip patch antennas: the infinite array approach," *IEEE Transactions on Antennas and Propagation*, vol. 40, pp. 579–582, May 1992.

[99] H. K. Schuman, "Modeling folded dipoles and feedlines for radiation and scattering," *IEEE Transactions on Antennas and Propagation*, vol. 38, pp. 30–39, Jan. 1990.

[100] K. E. Jordan, G. R. Richter, and P. Sheng, "An efficient numerical evaluation of the Green's function for the Helmholtz operator on periodic structures," *Journal of Computational Physics*, vol. 63, pp. 222–235, 1986.

[101] D. M. Pozar, "Analysis of an infinite phased array of aperture coupled microstrip patches," *IEEE Transactions on Antennas and Propagation*, vol. 37, pp. 418–425, Apr. 1989.

[102] L. R. Lewis and A. Hessel, "Propagation characteristics of periodic arrays of dielectric slabs," *IEEE Transactions on Microwave Theory and Techniques*, vol. 19, pp. 276–286, Mar. 1971.

[103] W. Lam, P. Lee, L. Yujiri, T. Berenz, and J. Pearlman, "Millimeter wave imaging using preamplified diode detector," *IEEE Microwave and Guided Wave Letters*, vol. 2, pp. 276–277, July 1992.

[104] J. Huang, "A technique for an array to generate circular polarization with linearly polarized elements," *IEEE Transactions on Antennas and Propagation*, vol. 34, pp. 1113–1124, Sept. 1986.

[105] J. F. Ramsay, "Lambda functions describe antenna/diffraction patterns," *Microwaves*, pp. 69–107, June 1967.

[106] J. Browne, "Millimeter waves and commercial applications," *Microwaves and RF*, vol. 31, pp. 113–120, July 1992.

[107] R. F. Harrington, *Time harmonic electromagnetic fields*, pp. 163–171. New York: McGraw Hill, 1961.

[108] E. A. J. Marcatili, "Dielectric rectangular waveguide and directional coupler for integrated optics," *Bell Systems Technical Journal*, vol. 48, pp. 2071–2102, Sept. 1969.

[109] J. E. Goel, "A circular harmonics computer analysis of rectangular dielectric waveguide," *Bell Systems Technical Journal*, vol. 48, pp. 2133–2160, Sept. 1969.

[110] K. Ogusu, "Numerical analysis of the rectangular dielectric waveguide and its modifications," *IEEE Transactions on Microwave Theory and Techniques*, vol. 25, pp. 874–885, Nov. 1977.

[111] K. Solbach and I. Wolff, "The electromagnetic field and the phase constants of dielectric image lines," *IEEE Transactions on Microwave Theory and Techniques*, vol. 26, pp. 266–274, Apr. 1978.

[112] R. E. Collin and D. A. Ksienski, "Boundary element method for dielectric resonators and waveguides," *Radio Science*, vol. 22, pp. 1155–1167, Dec. 1987.

[113] H. A. Watson, ed., *Microwave semiconductor devices and their circuit applications*, pp. 330–381. New York: McGraw Hill, 1969.

[114] J. L. Pages, "Numerical modelling of feed points at wire junctions," *Journal of Electrical and Electronics Engineering, Australia*, vol. 7, pp. 257–260, Dec. 1987.

[115] J. C. Logan, "A comparison of techniques for treating radiation and scattering by bent wire configurations with junctions," National Science Foundataion Grant GK-4223 TR-73-10, Syracuse University, Aug. 1973.

[116] W. L. Everitt and J. F. Byrne, "Single wire transmission lines for short-wave antennas," *Proceedings of the IRE*, vol. 17, pp. 1840–1867, Oct. 1929.

[117] J. J. Nagle, "Windom antennas," *Ham Radio*, pp. 10–19, May 1978.

[118] J. J. Gustincic, "The determinaation of active array impedance with multielement waveguide simulators," *IEEE Transactions on Antennas and Propagation*, vol. 20, pp. 589–595, Sept. 1972.